NTNU
Norwegian University of
Science and Technology

Analysis and Design Bjørnefjorden Floating Cable-Stayed Bridge subjected to Large Ship Collisions and Extreme Environmental Loads

Aleksander Aalberg

MASTER THESIS 2017

For

Stud. Techn. Aleksander Aalberg

Analysis and Design Bjørnefjorden Floating Cable-Stayed Bridge subjected to Large Ship Collisions and Extreme Environmental Loads

Analyse og dimensjonering Bjørnefjorden flytende skråstagbro utsatt for støt fra store skip og ekstreme miljølaster

The Norwegian Public Roads Administration (NPRA) is running a project "Ferry free coastal route E39", where suspension bridges, floating bridges or submerged tunnels would be installed across fjords in Western Norway. The straits are up 5 kilometres wide and will call for significant extension of present technology. Several innovative crossing concepts have been proposed. One of them is the combined floating-cable stayed bridge concept.

The bridge has to resist extreme environmental loads and accidental actions with acceptable safety levels. One of the concerns are accidental ship collisions with energies 100-1500 MJ. The proposed concepts cannot be designed adequately using existing methods and design rules. Consequently, advanced scenario-based analyses have to be conducted based on accurate simulation of the governing physical processes.

For crossing of Bjørnefjorden one of the most relevant concept is floating bridge with a cable stayed section in the south end.

The purpose of the project and (later) master thesis work is to perform scenario-based and advanced analysis of ship collision with the bridge and to assess the response of the bridge exposed to extreme environmental loads, both in intact and damaged condition.

.

Scope of work:

1. The global finite element model of the bridge developed in the project period for USFOS analysis revisited. As far as possible identify the sources for all deviations in the results obtained with USFOS and those reported form use of alternative software.

2. Perform parametric study of ship collision analysis for selected scenarios against the pontoons and the bridge girder. Pontoons fabricated in both concrete and steel should be considered. For bridge girder impact the effect of local damage on the global girder resistance should be modelled ain USFOS as far as possible. Assess the criticality of the bridge response wrt to global integrity.

3. By means of analysis with LS-DYNA propose a pontoon steel design that is highly resistant against ship collision.

4. Simulate non-central impacts with the pontoons where the ship may be deflected away from the pontoon

5. Establish relevant environmental conditions for the bridge. To what extent can USFOScalculate the environmental loads? If need be, use alternative software (e.g. WADAM) to calculate the environmental loads, notably wave loads including drift forces. Reference is made to the master thesis by Ole Harald Moe. Turbulent wind may be created with the program WINDSIM.

6. Analyse the bridge subjected to extreme environmental loads, using e.g. the contour line method. Establish the extreme characteristic response and compare with relevant resistance criteria.

7. For selected damage condition as concerns girder damage or pontoon flooding, assess the residual strength of the bridge subjected to relevant environmental loads

8. Conclusions and recommendations for further work.

Literature studies of specific topics relevant to the thesis work may be included.

The work scope may prove to be larger than initially anticipated. Subject to approval from the supervisor, topics may be deleted from the list above or reduced in extent.

In the thesis the candidate shall present his personal contribution to the resolution of problems within the scope of the thesis work.

Theories and conclusions should be based on mathematical derivations and/or logic reasoning identifying the various steps in the deduction.

The candidate should utilise the existing possibilities for obtaining relevant literature.

The thesis should be organised in a rational manner to give a clear exposition of results, assessments, and conclusions. The text should be brief and to the point, with a clear language. Telegraphic language should be avoided.

The thesis shall contain the following elements: A text defining the scope, preface, list of contents, summary, main body of thesis, conclusions with recommendations for further work, list of symbols and acronyms, references and (optional) appendices. All figures, tables and equations shall be numerated.

The supervisor may require that the candidate, in an early stage of the work, presents a written plan for the completion of the work. The plan should include a budget for the use of computer and laboratory resources, which will be charged to the department. Overruns shall be reported to the supervisor.

The original contribution of the candidate and material taken from other sources shall be clearly defined. Work from other sources shall be properly referenced using an acknowledged referencing system.

The report shall be submitted in two copies:
- Signed by the candidate
- The text defining the scope included
- In bound volume(s)
- Drawings and/or computer prints which cannot be bound should be organised in a separate folder.

Supervisor:
Prof. Jørgen Amdahl

Co-supervisor:
Postdoc Yanyan Sha

Deadline:, June 16,   2017
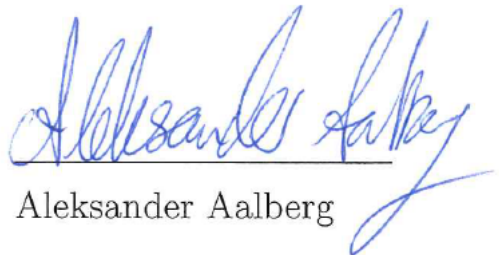
Trondheim, January 10 2017

Jørgen Amdahl

Preface

This report is intended for presenting the work and findings which have been achieved during the master thesis in the spring of 2017 at the Norwegian University of Science and Technology, Department of Marine Technology.

Working with the master thesis have proven to be a demanding task where some part of the work reviled to be more time consuming than expected. As a consequence of this it was not possible to study all parts in the problem description. It would have been interesting to study ship collision more in depth, but less attention had to be put on these analysis due to time limitations. This was decided in agreement with Supervisor Professor Jørgen Amdahl. Though challenging, it have been a quite interesting task working with the scope of this thesis.

I would like to thank Supervisor Professor Jørgen Amdahl and Co-supervisor Postdoc Yanyan Sha for helpful guidance with the master thesis during the spring semester. Further, I would also thank my brother Johannes Aalberg for help and support during the five years.

Aleksander Aalberg

Abstract

The purpose of this master thesis is to analyse one of the proposed bridge design for the Bjørnafjorden crossing, exposed to extreme environmental loads and large ship impacts. This is a floating cable-stayed bridge with a total length of nearly 5 kilometers, where the floating part is supported by 19 pontoons. The main focus was put on studying the response caused by wind and waves, while ship collision was limited to analysing the global integrity of the bridge.

Wave induced response was investigated for two different wave directions, which had the largest 100-year significant wave height. Both linear wave loads and slowly-varying drift forces was accounted for and introduced as time-varying load histories, established from the corresponding transfer functions. Due to the large length of the bridge it could be relevant to study how the bridge behaviour is affected by the correlation between the wave loads acting on the pontoons. This was done using two different approaches, one with fully uncorrelated heave force and a second correlation established from the position of each pontoon. The two wave directions and correlations was further analysed in order to find the worst condition, which should be used to establish the characteristic response. For the worst sea state 90 1-hour simulations was conducted in order to approximate the characteristic wave response from 30 3-hour simulations. This was done by fitting 30 maximum values to a Gumbel distribution and using the 90% fractile as the characteristic response. The effect from wind was studied together with fully correlated waves from west, where the total wind field consisted of both a mean and turbulent component established using WindSim.

Ship collision was simulated by use of spring elements with assigned vessel strength properties and applied at two different impact locations, where both pontoon and bridge girder collision was investigated. The vessel strength was modelled using a force-deformation curve for the bulb and forecastle, assuming strength design of the bridge. Different impact energies was studied in order to analyse the effect of impact speed.

The analysis with environmental loads showed that linear waves induces large moments in the bridge girder, while slowly-varying drift forces and wind are important for horizontal motions. Waves from north-west in combination with the correlation obtained by accounting for the different pontoon positions proved to give the largest response in the bridge girder. This condition was therefore used to establish the characteristic wave response, which showed that the design capacity with regard to yielding was exceed for one of the box girders and column. According to these results the strength against bending must be increased.

The ship collisions gave rise to large utilizations in the bridge girder with values close to fully utilized, for the largest impact energies. For pontoon collision this resulted in permanent displacements of the bridge girder, due to plastic rotations in the cross beams. This may not necessarily be critical for the design as long as the permanent displacement do not impair the global integrity. Further, as long as the bridge is able to maintain the stress level in the fully utilized parts the current design appears to have sufficient resistance against ship impact. On the other hand if collision with the bridge girder results in extensive damage to one of the box girders, it may be critical in connection with surviving 100-year environmental loads.

On a late stage of the master thesis it was discovered that the cross sectional properties of the cross beams about the local y- and z-axis appears to be switched. This is something that may affect the result both with regard to environmental loads and ship collision. It is therefor recommended to study the effect of this discrepancy further.

Sammendrag

Hensikten med denne masteroppgaven er å analysert en av de foreslåtte brukonstruksjonene for fjordkryssingen over Bjørnafjorden, utsatt for ekstreme miljølaster og kollisjon fra store skip. Dette konseptet er en flytende skråstagbro med en total lengde på nesten 5 kilometer, hvor den flytende delen holdes oppe av 19 pontonger. Hovedfokuset i oppgaven har vært oppførselen som følger av vind- og bølgelaster, mens skipskollisjon ble begrenset til analyse av den globale integriteten til broen.

Broens oppførsel på grunn av bølgelaster har blitt undersøkt for to bølgeretninger, begge valgt ut i fra hvilke retninger som har de største 100-års signifikante bølgehøyde. Både lineære bølgelaster og saktevarierende bølgedriftkrefter ble tatt hensyn til og påført som tidsvarierende lasttilfeller, etablert ved bruk av de tilhørende transferfunksjoner. På grunn av lengden til broen vil det kunne være relevant å studere hvordan oppførsel blir påvirket av korrelasjonen mellom bølgelastene på de ulike pontongene. Dette ble gjort med to ulike tilnærminger, hvor den ene hadde fullt ukorrelerte hiv-krefter, mens den andre tok utgangspunkt i posisjonen til hver enkelt pontong. De to bølgeretningene og metodene for korrelasjon ble deretter analysert for å kunne finne det mest ekstreme tilfellet, som videre ble brukt til å bestemme broens karakteristiske respons fra bølger. For den verste sjøtilstanden ble 90 simuleringer med lengde på 1 time utført, slik at man kunne oppnå en tilnærming til den karakteristiske oppførselen som tilsvarer 30 tretimers-simuleringer. Dette ble gjort ved å tilpasset en Gumbel-fordeling til 30 maksimalverdier, og bruke 90% fraktil som den karakteristiske responsen. Effekten av vindlaster ble studert sammen med bølger påført fra vest, hvor det totale vindfeltet bestod av både en gjennomsnittlig og en turbulent komponent etablert ved bruk av WindSim.

Skipskollisjon ble simulert ved å benytte et fjærelement med tildelt samme styrkeegenskaper som et skip, hvor både kollisjon med pontong og brobane ble studert. Styrkeegenskapene til skipet ble modellert ved bruk av kraft-deformasjons kurver til både forskip og bulb, hvor broen er antatt sterkere en skipet, tilsvarende såkalt styrke-design. Ulike kollisjonenergier ble studert for å analysere effekten av kollisjonshastighet.

Analysene med miljølaster viste at de lineære bølgekreftene gir store moment i de to brobjelkene, mens de saktevarierende bølgedriftkreftene og vindlaster gir betydelig bidrag til bevegelse i horisontalplanet. Bølger fra nord-vest i kombinasjon med korrelasjon mellom bølgekreftene skapt av pontongenes ulike plassering gav de største kreftene i brobjelkene. Denne sjøtilstanden ble derfor brukt for å definere karakteristisk respons fra bølger, noe som viste at broens kapasitet med tanke på materialtets flytgrense ble oversteget i en av brobjelkene og søyle. I henhold til disse resultatene bør derfor broens bøyemostand økes.

Analysene av skipskollisjon viste at brobanen fikk høy utnyttelse med verdier i nærheten av fullstendig plastisk tilstand i enkelte områder, for kollisjon med høy energi. Ved kollisjon mot pontongene viste resultatene at hele brobanen fikk permanent forskyvning på grunn av plastisk rotasjon i tverrbjelkene. Dette resultatet er ikke nødvendigvis kritisk for broens design så lenge den permanente forskyvning ikke svekker den globale integriteten til broen. Så lenge komponentene med høyest utnyttelse klarer å holde det høye spenningsnivået tilsier dette at nåværende design har tilstrekkelig motstandsdyktighet mot skipskollisjon. På en annen side, hvis kollisjon mot brobanen resulterer i omfattende skade i en av brobjelkene, vil dette kunne være kritisk med tanke på å motstå 100-års miljølaster.

På et sent stadium i arbeidet med masteroppgaven ble det oppdaget at tverrsnittegenskapene til tverrbjelkene om de lokale y- og z-aksene virker å være byttet om på i bromodellen. Dette kan ha innvirkning på resultatene både fra miljølaster og skipskollisjon. Det anbefales derfor at effekten av dette avviket blir studert videre.

Table of Contents

List of Figures

List of Tables

Abbreviations

Symbol	=	Definition
ALS	=	Accidental Limit State
DAF	=	Dynamic Amplification Factor
ULS	=	Ultimate Limit State
NPRA	=	Norwegian Public Roads Administration
TLP	=	Tension Leg Platform

Symbols

Latin symbols

A	$=$	Cross sectional area
$\boldsymbol{C}$	$=$	Damping matrix
$c_{d,ii}$	$=$	Diagonal term of the drag force coefficient matrix
C_D	$=$	Drag coefficient
C_L	$=$	Lift coefficient
C_M	$=$	Moment coefficient
$c_{m,ii}$	$=$	Diagonal term of the added mass coefficient matrix
$c_{r,ii}$	$=$	Diagonal term of the potential damping coefficient matrix
c_u	$=$	Decay coefficient for the u-component in the wind velocity field
c_v	$=$	Decay coefficient for the v-component in the wind velocity field
c_w	$=$	Decay coefficient for the w-component in the wind velocity field
D	$=$	Diameter
E	$=$	Elastic modulus
E_s	$=$	Strain energy
E_t	$=$	Effective elastic modulus accounting for catenary effect of cables
f	$=$	Frequency component in turbulent wind
f_{H_s,T_p}	$=$	Joint probability function of H_s and T_p
f_k	$=$	Characteristic strength
$\boldsymbol{F}$	$=$	Applied force
F_d	$=$	Drag force
$F_{exc,i}$	$=$	Excitation load in degree of freedom i
F_i^{SV}	$=$	Slowly-varying wave drift excitation load in degree of freedom i
$F(X)$	$=$	Cumulative distribution function
g	$=$	Acceleration of gravity
$|H|$	$=$	Transfer function
H_s	$=$	Significant wave height
I_t	$=$	Torsional moment of inertia
I_y	$=$	Moment of inertia about local y-axis
I_z	$=$	Moment of inertia about local z-axis
k	$=$	Wave number

$\boldsymbol{K}$	=	Stiffness matrix
L	=	Length
m	=	Mass
$\boldsymbol{M}$	=	Mass matrix
p	=	Pressure, and momentum
Q_k	=	Characteristic load
R_d	=	Design resistance
R	=	Radius
s	=	Distance between two points in space
S_d	=	Design load
S_{hy}	=	Shear area directed in local y-axis
S_{hz}	=	Shear area directed in local z-axis
$S(\omega_)$	=	Used for wave and wind spectrum
t	=	Time
T	=	Temperature, wave period
T_{jj}	=	Second order transfer function
T_p	=	Peak period
$U_m(z)$	=	Mean wind velocity component
v	=	Velocity
v_b	=	Basic wind speed
w	=	Unit weight of cables
W_{pt}	=	Plastic torsional section modulus
W_{py}	=	Plastic section modulus about local y-axis
W_{pz}	=	Plastic section modulus about local z-axis
x	=	Coordinate axis
x_c	=	Characteristic response
y	=	Coordinate axis
z	=	Vertical distance, and vertical coordinate axis

Greek symbols

α	=	Scale parameter, and mean wind shape parameter
α_1	=	Coefficient for the mass matrix in Raylaigh damping equation
α_2	=	Coefficient for the stiffness matrix in Raylaigh damping equation
β	=	Location parameter, and wave heading
γ	=	Parameter for the peak of JONSWAP spectrum
γ_f	=	Partial safety factor
γ_m	=	Material factor used in design
δ	=	Phase angle between the response and the surface elevation
Δ	=	Represents the change in a value
ϵ	=	Random phase angle
λ	=	Thermal expansion coefficient, wave length
ϕ	=	Eigenmode, and phase spectum
Φ	=	Velocity potential
Ψ_i	=	Correlation factor
ρ	=	Mass density
σ	=	Stress, standard deviation
σ_w	=	Parameter for the width of JONSWAP spectrum
σ_Y	=	Yield stress
ζ_a	=	Wave amplitude
ζ	=	Wave elevation
θ	=	Phase angle
ω	=	Wave frequency in [rad/s]
ξ	=	Damping ratio

Chapter 1

Introduction

As a part of the National Transport Plan, the Norwegian Public Road Administration (NPRA) have ambitions of establish a continuous coastal highway between Kristiansand and Trondheim during the next 20 years (Statens vegvesen, 2016b). The present layout includes ferries that are used to cross many of the fjords, which are to be replaced with so called fixed links in order to achieve this goal. Due to the large width and depth of these crossings, conventional bridge designs are not adequate and thus new concepts are needed (Statens vegvesen, 2016a).

For Bjørnafjorden there are three main concepts that have been under considerations, which include a suspension bridge combined with Tension Leg Platform (TLP) technology, a submerged floating tunnel and a floating bridge (Garathun, 2016). Moe (2016) analysed the global behaviour of the first concept, while in this thesis a floating bridge developed by a project group consisting of COWI, Aas-Jakobsen, Johs Holt and Global Maritime is assessed. This concept consists of a curved bridge girder supported by pontoons and a cable stayed part, with a total length of approximately 5 kilometers (COWI, Aas Jakobsen, Global Maritim, & Johs. Holt, 2016, p.8). Due to the large size of this bridge, and the fact that it is floating, the response pattern is expected to be complex. This increases the importance of understanding the behaviour of the bridge when subjected to different loading conditions for assuring a good and safe design. A bridge at this locations will be exposed to environmental loads such as wind and waves in addition to possible large ship impacts, which puts requirements to the design.

Previous work on this concept includes Sha and Amdahl (2016a) which studied the local behaviour of the bridge girder exposed to ship collision, while the global behaviour of the same collision event is presented by Sha (2016). COWI et al. (2016) performed a detailed analysis of this bridge including loads from wind and waves, though the bridge girder was

modelled as one single box girder. This deviates from the actual design which consists of two box girders in parallel.

1.1   Objective and description of the report

The objective of this thesis is to use time domain simulation to analyse the response of the floating cable-stayed bridge design proposed by COWI et al. (2016), exposed to extreme environmental loads in addition to large ship impacts. A global bridge model received from Postdoc Yanyan Sha is used for the analysis.

First, theory on how to analyse the response from waves and wind will be presented together with simplified approaches for ship collision analysis. This is followed by a description of the methodology behind the simulations and a review of the global bridge model, with focus on the updates made to this model. The choice of which environmental loads that are applied, and how these are established, is then presented before the modelling of ship impact is discussed. The final chapters include the results, with a discussion of their meaning, then a more overall discussion of the results, before a conclusion and recommendations for further work is made.

1.2   Scope and limitations

The scope of work as defined in the problem description proved to be too comprehensive. This because more time then expected had to be spent on verifying that the wave loads was applied correctly, and among other things the initial wave analysis reviled that some parts of the bridge model had to be updated. After consulting this with supervisor Professor Jørgen Amdahl it was agreed to put the main focus on extreme environmental loads, and to only study the global bridge response caused by ship impacts. This means that the effect of having concrete or steel pontoons and the "effect of local damage" in the bridge girder as stated in the second point in the problem description are not considered. Also the third point concerning a local analysis of a pontoon steel design is not a part of the thesis, by the same reason. Further, simulations with non-central impact was only to be performed if such a model came available during the work and since this was not the case the fourth point could not be studied. As a consequence the collision analysis in this thesis are limited to head on collision, where the ship follows a straight line, and global behaviour only. When the actual local properties of the hit pontoon or bridge girder is not accounted for it could give errors in the local behaviour, but the global behaviour

should be captured correctly.

Chapter 2

Theory

2.1 The dynamic equation of motion

The dynamic behaviour of a structure is defined by the equation of motion as expressed in Equation 2.1, where the $\boldsymbol{M}$, $\boldsymbol{C}$ and $\boldsymbol{K}$ denotes the mass, damping and stiffness matrices for the structure, respectively. Futhermore, $\boldsymbol{F}(t)$ is the applied load, while $\ddot{\boldsymbol{x}}$, $\dot{\boldsymbol{x}}$ and $\boldsymbol{x}$ is the acceleration, velocity and displacement.

$$\boldsymbol{M}\ddot{\boldsymbol{x}} + \boldsymbol{C}\ddot{\boldsymbol{x}} + \boldsymbol{K}\boldsymbol{x} = \boldsymbol{F}(t) \tag{2.1}$$

For a structure exposed to a time varying load one normally distinguishes between three cases. These are presented below, and describes the structural behaviour based upon the difference between the applied frequency ω and the relevant eigenfrequency ω_n for the structure (Langen & Sigbjörnsson, 1979, p.178).

- Stiffness dominated system, when $\frac{\omega}{\omega_n} << 1$

- Resonance dominated system, when $\frac{\omega}{\omega_n} \approx 1$

- Inertia dominated system, when $\frac{\omega}{\omega_n} >> 1$

As illustrated above, the structural response is to a large degree dependent of the eigenfrequenies of the structure, together with the corresponding eigenmodes. It is therefor important to calculate these properties to get an impression of how the bridge may behave under different loading conditions. According to Langen and Sigbjörnsson (1979) both eigenfrequencies and the corresponding eigenmodes can be estimated solving Equation

2.2, where $\boldsymbol{M}$ and $\boldsymbol{K}$ still are the mass and stiffness matrices, while ω_i and ϕ_i is the eigenfrequency and eigenmode for mode number "i", respectively. This equation is often solved using an iterative approach, where the eigenfrequency and eigenmode is solved simultaneously. For more information about such methods it is referred to literature such as Langen and Sigbjörnsson (1979).

$$\left(\boldsymbol{K} - \omega_i^2 \boldsymbol{M}\right)\phi_i = \boldsymbol{0} \tag{2.2}$$

2.2 Environmental loads

2.2.1 Wave induced loads

A structure that is located in sea will be exposed to a dynamic pressure distribution caused by the presence of waves, which gives a resulting force acting on the structure when integrated over the wet surface. Knowing this pressure distribution is therefor an important property when wave forces are to be calculated. One procedure for establishing this property is to introduce curtain assumptions about the behaviour of the water surrounding the structure. By assuming that the water is irrotational it is possible to express the fluid velocity vector $\boldsymbol{v}$ by a single scalar function Φ as presented in Equation 2.3 (Panton, 2013, p.283). If the fluid also can be regard as incompressible the pressure can be determined by the unsteady form of the Bernoulli equation (Panton, 2013, p.284). In Equation 2.4 the Bernoulli equation is presented in the form as found in Faltinsen (1990, p.14), where ρ is the water density, g the acceleration of gravity, z the vertical position, $C(t)$ a time dependent arbitrary value and p is the water pressure.

$$\boldsymbol{v} = \nabla\Phi \tag{2.3}$$

$$\rho \cdot \frac{\partial\Phi}{\partial t} + \rho \cdot \frac{1}{2} \cdot \nabla\Phi \cdot \nabla\Phi + \rho \cdot g \cdot z + p = C(t) \tag{2.4}$$

One of the important features with equation 2.4 is that the pressure at any point in water due to surface waves can be calculated as long as the velocity potential is known. The work is therefor to determine this velocity potential which, due to the assumptions regarding the fluid behaviour, must satisfy a differential equation with corresponding boundary conditions along the fluid domain (Faltinsen, 1990, p.13-17). At the free surface there are two boundary conditions that applies, a dynamic and kinematic condition respectively.

The first condition states that the water pressure and the atmospheric pressure should be equal at the free surface, while the latter condition is related to the particles on the free surface which always should stay on the free surface (Faltinsen, 1990, p.15). These conditions are in general non-linear, but by introducing the assumption of small wave amplitudes it is possible to derive an simple analytically expression of the velocity potential. This is often termed linear wave theory and could be used to establish loads and motions of large-volume structures from waves (Faltinsen, 1990, p.37).

2.2.2 Linear wave induced loads

Within the assumption of linear wave theory the total wave force acting on a structure could be divided into two parts, namely radiation and diffraction (DNV GL, 2015, p.2-47). These components describes different causes of pressure in the fluid and therefor corresponds to different velocity potentials. According to Faltinsen (1990) one way of describing the properties of these contribution is that the diffraction, as defined in DNV GL (2015), illustrates a situation where the structure is kept fixed and exposed to regular waves. This gives the excitation wave force and includes the effect from pressure in the undisturbed wave in addition to modifications of the wave caused by the fixed structure. The radiation term describes the waves that are generated when the structure oscillates with the same frequency as the incident waves. The motions of the structure causes pressure in the fluid which are proportional to the structures acceleration, velocity and displacement. These are therefor handled on the left hand side of the equation of motion, see equation 2.1, and the contributions are often termed added mass, damping and restoring, respectively (Faltinsen, 1990, p.39). The excitation forces is on the other hand the applied force on the right hand side of this equation system. By including both of these contributions interaction between the incident waves and the presence of a structure is accounted for, within linear theory.

To establish the total excitation forces and moment in addition to added mass, potential damping and restoring one may use numerical methods. One example of such methods is the panel method, where the wet surface of a structure is divided into smaller parts, so called panels (Faltinsen, 1990, Ch.4). The basis of this method is to assume a form of the velocity potential of each panel, and then approximate the total velocity potential by the taking the sum of all these contributions. For more information about such methods see e.g. Faltinsen (1990, Ch.4). Outputs from such an analysis could be one the form of frequency dependent properties such as excitation forces and moments, added mass and damping. In this case the total excitation wave force-time history $F_{exc,i}(t)$ could be estimated using Equation 2.5, where the wave elevation $\zeta(t)$ is assumed to follow Equation

2.6 which is similar to the definition in DNV GL (2015, p.2-31). In these equations ζ_a is the wave amplitude, ω_j is the wave frequency component, t is the time instant and ϵ_j is a random phase angle. The additional symbols in Equation 2.5 are the phase angel between the force and the wave elevation δ_j together with the transfer function of the wave force $\left|H_i(\omega_j)\right|$. Furthermore, the subscript i and j designates the degree of freedom and frequency component numbers, respectively. Both equations assumes that the irregular waves can be expressed by a superposition of all regular wave components in a sea state, which is a result of linear wave theory (Faltinsen, 1990, p.37). The random phase angle ϵ_j is included for each wave component to retain some of the randomness in the resulting wave forces and elevation, and is assumed to be "uniformly distributed between 0 and 2π" (Haver, 2013, p.144). By using different sets of random phase angles one will obtain unique sets of the wave force-time histories.

$$F_{exc,i}(t) = \sum_{j=1}^{N} \zeta_{a,j} \cdot \left|H_i(\omega_j)\right| \cdot \cos\left(\omega_j \cdot t + \delta_j(\omega_i) + \epsilon_j\right) \tag{2.5}$$

$$\zeta(t) = \sum_{j=1}^{N} \zeta_{a,j} \cdot \cos\left(\omega_j \cdot t + \epsilon_j\right) \tag{2.6}$$

Provided that the transfer function and the phase angle in Equation 2.5 are established, the only unknown parameter is the wave amplitude ζ_a. This could be calculated using a wave spectrum $S(\omega_j)$ by the relation expressed by Equation 2.7, where $\Delta\omega$ is the frequency increment (Faltinsen, 1990, p.23). According to Faltinsen (1990, p.23-24) a wave spectrum represents the transformation of the wave elevation into frequency domain, and could be established by performing measurements in the area of interest. There exists on the other hand different parameterizations of such spectrum, which could be valid approximations for use in connection with analysing design of structures (Myrhaug, 2007, p.6). Some of the main assumptions behind these spectrum is that the parameters describing the sea state can be regarded as constant within a short term period. According to DNV (2014b, p.46) this is possible with the assumption of a stationary process, meaning that the variance and mean value of the surface elevation are constant during this period of time (Myrhaug, 2007, p.2). One parameterization is the JOSWAP spectrum which describes a sea state that is not fully developed (DNV, 2014b, p.46), this spectrum will be presented more in detail in Chapter 5.2.

$$\zeta_a = \sqrt{2 \cdot S(\omega_j) \cdot \Delta\omega} \tag{2.7}$$

2.2.3 Slowly-varying drift forces

In the previous section it was described how one may calculate wave forces using linear wave theory. This gives only loads having the same frequency as the incident waves, but a structure exposed to waves will in general also experience non-linear wave forces. These includes mean drift forces in addition to loads oscillating with so called sum and difference frequencies (Faltinsen, 1990, p.131). According to Faltinsen (1990) the additional components reviles by accounting for higher order terms when deriving the wave forces, in addition to a better representation of the boundary conditions. Difference frequency is caused by the presence of different frequency components in an irregular sea state. This effect causes a slowly-variation in the mean wave loads and may be relevant for floating structures with eigenperiods in the range of 1-2 minutes (Faltinsen, 1990, p.133). Some of the theory behind slowly-varying drift forces will be presented in the following, within second order wave theory.

To obtain the mean and slowly-varying drift forces it is in general required to introduce a second order velocity potential, which is used as a correction to the linear. Thus, if these are known the second order wave force could be calculated from the pressure when inserting the velocity potentials into the Bernoulli equation (Pinkster, 1979). Another approach is to introduce a similar formulation of the slowly-varying drift forces as used for the linear excitation force and calculate the non-linear effect by Equation 2.8 (Faltinsen, 1990, p.155). In this equation F_i^{SV} is the slow-drift wave load, ζ_a is the wave amplitude, t the time instant, ω is wave frequency and ϵ is the random phase angle. T^{ic} and T^{is} are the second-order transfer functions connected to the cosine and sine functions, respectively. Further, the subscripts j and k refer to the wave component number, where N is the total amount of components. Equation 2.8 has the same form as the second-order correction of the surface elevation in DNV (2014b, p.41). Therefor, as pointed out by Pinkster (1979) T_{jk}^{ic} and T_{jk}^{is} will be the in phase and out of phase components, respectively, of the slowly-varying correction. This provided that the surface elevation is expressed as a cosine function, as used in this thesis.

$$
\begin{aligned}
F_i^{SV} = \sum_{j=1}^{N} \sum_{k=1}^{N} \zeta_{a,j} \cdot \zeta_{a,k} \Big[& T_{jk}^{ic} \cdot \cos\left((\omega_k - \omega_j) \cdot t + (\epsilon_k - \epsilon_j)\right) + \\
& T_{jk}^{is} \cdot \sin\left((\omega_k - \omega_j) \cdot t + (\epsilon_k - \epsilon_j)\right) \Big]
\end{aligned}
\tag{2.8}
$$

According to Faltinsen (1990) one of the benefits of using Equation 2.8 to calculate the slow-drift loads is that the expression can be further simplified by introducing curtain

assumptions. By using Newman's approximation it is possible to express the off-diagonal terms of the second-order transfer functions by the diagonal ones, which is illustrated by Equation 2.9 and 2.9. The benefit of doing this is that the diagonal terms corresponds to the mean drift coefficients, which can be calculated using only the linear velocity potential. The linear velocity potential is much easier to solve, and using this approximation will therefor save computational effort (Faltinsen, 1990, p.157). Further, equation 2.8 can be simplified into a single summation using the formulation presented in Equation 2.11, where only the diagonal terms of cosine transfer functions are required (Faltinsen, 1990, p.158). According to Faltinsen (1990, p.158) this expression will produce components with high frequency which are non physical. On the other hand it is stated that these should not affect the response due to slowly-varying loads.

$$T_{jk}^{ic} = T_{jk}^{ic} = 0.5 \cdot \left(T_{jj}^{ic} + T_{kk}^{ic} \right) \tag{2.9}$$

$$T_{jk}^{is} = T_{jk}^{is} = 0 \tag{2.10}$$

$$F_i^{sv}(t) = 2 \cdot \left[\sum_{j=1}^{N} \zeta_{a,j} \cdot T_{jj}^{ic}(\omega_j)^{1/2} \cos(\omega_j \cdot t + \epsilon_j) \right]^2 \tag{2.11}$$

Due to the square root term of the second-order transfer function in Equation 2.11, using this formulation requires that this property is positive Faltinsen (1990, p.158). According Standing, Brendling, and Wilson (1987, p.311) one may account for the sign of the mean drift coefficients using Equation 2.12. Thus using this approach the contribution from the off-diagonal drift terms will be zero if the mean drift coefficients for frequency j and k are different (Standing et al., 1987, p.311). By inserting Equation 2.12 into the equation for the slow-drift force, see Equation 2.8, Equation 2.13 is obtained.

$$T_{jk}^{ic} = \frac{1}{2} \cdot \left(\text{sgn}(T_{jj}^{ic}) + \text{sgn}(T_{kk}^{ic}) \right) \cdot \sqrt{\left| T_{jj}^{ic} \cdot T_{kk}^{ic} \right|} \tag{2.12}$$

$$
\begin{aligned}
F_i^{sv} = &\sum_{j=1}^{N} \zeta_{a,j} \cdot \text{sgn}(T_{jj}^{ic}) \cdot \sqrt{\left| T_{jj}^{ic} \right|} \cdot \cos\left(\omega_j \cdot t + \epsilon_j \right) \cdot \sum_{k=1}^{N} \zeta_{a,k} \cdot \sqrt{\left| T_{kk}^{ic} \right|} \cos\left(\omega_k \cdot t + \epsilon_k \right) \\
&+ \sum_{k=1}^{N} \zeta_{a,k} \cdot \text{sgn}(T_{kk}^{ic}) \cdot \sqrt{\left| T_{kk}^{ic} \right|} \cdot \sin\left(\omega_k \cdot t + \epsilon_k \right) \cdot \sum_{j=1}^{N} \zeta_{a,j} \cdot \sqrt{\left| T_{jj}^{ic} \right|} \sin\left(\omega_j \cdot t + \epsilon_j \right)
\end{aligned}
\tag{2.13}
$$

The mean drift component can be calculated using the linear velocity potential as the second order potential do not give contribution to the mean loads (Faltinsen, 1990, p.134). Furthermore, these mean loads can be calculated by two different approaches where the first is based on conservation of momentum and the second uses a direct pressure integration of the pressure in Bernoulli equation, including second-order terms. These will not be discussed further, but it is important to note that the first only gives results for the three load components in the horizontal plane, while the latter produces six load components (Faltinsen, 1990). Another point is that if the velocity potential is calculated by the panel method using direct pressure formulation for the mean load may be sensitive to sharp corners in the panel model. As a result the calculations may be inaccurate in such locations (Faltinsen, 1990, p.142). Moe (2016) noted that it is possible to verify the calculated second-order transfer functions by using an asymptotic formula for high frequencies. For a section similar to Figure 2.1 with vertical sides, these formulas are described by Equation 2.14, 2.15 and 2.16 for the in-plane loads (Faltinsen, 1990, p.145). These can therefor be used to check the calculated second-order transfer functions. In these equations R is the radius of the circular ends of the pontoon, L is half the length between each circular end, β is the wave heading, ρ the water density, g acceleration of gravity and ζ_a is the wave amplitude. $\bar{F}_1$ and $\bar{F}_2$ are the asymptotic mean drift forces in x- and y-axis, respectively, while $\bar{F}_6$ is the mean drift moment about the vertical axis. The coordinate system is defined in Figure 2.1.

$$\frac{\bar{F}_1}{\zeta_a^2} = \frac{2}{3} \cdot \rho \cdot g \cdot R \cdot \cos(\beta) \tag{2.14}$$

$$\frac{\bar{F}_2}{\zeta_a^2} = \rho \cdot g \cdot \left(\frac{2}{3} \cdot R \cdot \sin(\beta) + L \cdot \sin(\beta) \cdot |\sin(\beta)| \right) \tag{2.15}$$

$$\frac{\bar{F}_6}{\zeta_a^2} = -\frac{\rho \cdot g}{3} \cdot L \cdot R \cdot \sin(2 \cdot \beta) \tag{2.16}$$

2.2.4 Wind loading

A wind field will in general consist of a mean and fluctuating part, which are often handled separately and then added together to obtain the total wind speed at a given point in space (Strømmen, 2010). This is illustrated in Figure 2.2 where the stipulated line represents a typical shape of the mean component, while the fluctuating part illustrated by the solid line. These contributions are presented as $V(z)$ and $u(z, t)$ in this figure respectively,
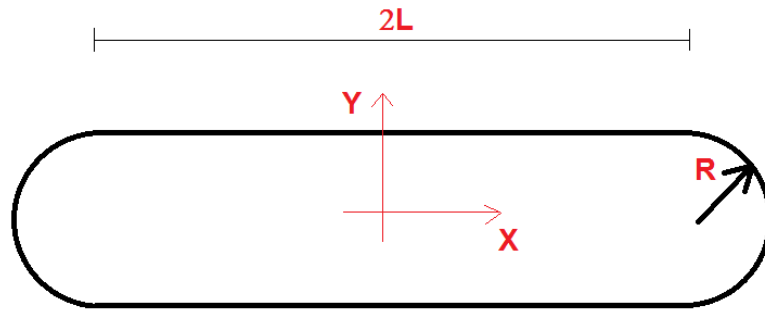
Figure 2.1: Shape of the water plane are for the asymptotic mean drift formulas. The figure is a reproduction of the one presented in Faltinsen (1990, p.145).

and are functions of the vertical position z above the surface. The resulting velocity field will induce forces on an exposed structure, which for a horizontal slender structure often is decomposed into three components. These are drag, lift and torsional moment and may be expressed as a function of the instantaneous wind field velocity in addition to non-dimensional coefficients (Strømmen, 2010, p.92).
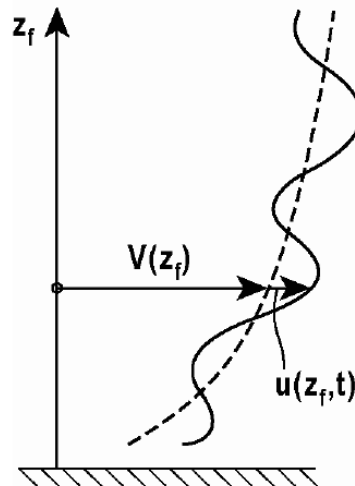
Figure 2.2: Mean and fluctuating wind components (Strømmen, 2010, Fig.3.1,p.54).

There exists different ways of describing the mean wind component, but a common procedure is to express it as a function of the average 10 minutes speed at a reference height of 10 meters U_{10min} (Strømmen, 2010, p.54). For the fluctuating part one could use a similar procedure as described for the surface elevation in connection with waves, i.e. transforming a frequency domain solution back to time domain. This could be exemplified for one single point where the fluctuating wind speed time history is established using an formulation as in Equation 2.17. For this special case the time history is fully described by the point spectrum $S_i(\omega)$, which contains information about the frequency properties of the turbulent component at a single point. Further, $\Delta\omega$ is the frequency increment, ω_n the frequency component number n, t the time instant, ϵ_n is a random phase angle while N

is the number of components in the spectrum (Strømmen, 2010, p.264-265).

$$u(t) = \sum_{n=1}^{N} \sqrt{2 \cdot S_i(\omega_n) \cdot \Delta\omega} \cdot \cos\left(\omega_n \cdot t + \epsilon_n\right) \tag{2.17}$$

A total wind field will not consist of a single point, but multiple points where the time histories at the different locations may have a statistical connection, at a curtain time instant (Strømmen, 2010, p.263). According to Strømmen (2010) this connection is accounted for by introducing a so called cross spectrum $S_{ii}(\omega, \Delta s)$, which can be expressed by Equation 2.18 where the subscript ii refer to the velocity component in x-, y- and z-axis. In general there will be a correlation between these velocity components, but are neglected in this formulation. Further, $S_i(\omega)$ is still the point spectrum, Δs the distance between two points while Coh_{ii} is the coherence spectrum, which defines the correlation of the turbulent component between points for different frequencies (Jia, 2014, p.274). Without going into further detail it should also be noted that ϕ describes the phase spectrum, which may be neglected for straight horizontal structures (Strømmen, 2010, p.67). With this information the time histories of the fluctuating wind speed at a given point can be calculated, accounting for the correlation between points, by introducing these into Equation 2.17. It should be noted that as the cross spectrum will be defined for each point m, it will be represented as a matrix with m rows and columns. This leads to a slightly different equation than for the single point case as the matrix may be decomposition using a method called Cholesky decomposition (K. Aas-Jakobsen & Strømmen, 2001, p.345). Further, since the contributions from all points in the wind filed are accounted for Equation 2.17 must be modified to a double sum. For more information on how to obtain time series of the turbulent wind speed it is referred to litterateur such as Strømmen (2010) and K. Aas-Jakobsen and Strømmen (2001).

$$S_{ii}(\omega, \Delta s) = S_i(\omega) \cdot \sqrt{Coh_{ii}(\omega, \Delta s)} \cdot \exp\left[\sqrt{-1} \cdot \phi_{ii}(\omega)\right] \tag{2.18}$$

2.3 Extreme characteristic response by use of the contour method

In order to estimate an extreme characteristic response it is in general required to establish a long term distribution of the specific response parameter (Baarholm, Haver, & Økland, 2010, p.149). There are different methods for describing the long term distribution, but the most frequent used on the "Norwegian continent shelf" is the so called

"d-hour maximum" with d taken as three hours (Haver, 2013, p. 56). Such a distribution describes how a given response varies during a specific environmental condition in addition to the long term variations of the the environmental characteristics. These two contributions are often referred to as the short term and long term variability, where the long term variability is "the most important" (Haver, 2013, p.97). But one should keep in mind that both contributions should in general be included when establishing a long term distribution, especially if the response problem is non-linear (Haver, 2013, p.97). Mathematically a long term distribution of a given extreme response can be formulated as presented in Equation 2.19, where sea state characteristics are used as the environmental parameters. In this formulation the $F_{X_{3h}|H_s,T_p}(x|h,t)$ is the conditional distribution of the 3-hour response variable X_{3h} given a sea state described by the significant wave height H_s and peak period T_p, and $f_{H_s,T_p}(h,t)$ is the joint probability density distribution (Baarholm et al., 2010, p.149).

$$F_{X_{3h}}(x) = \int_h \int_t F_{X_{3h}|H_s,T_p}(x|h,t) f_{H_s,T_p}(h,t) dt dh \tag{2.19}$$

According to Baarholm et al. (2010, p.149) the problem with Equation 2.19 is that it may be difficult to define the conditional distribution function properly for the response parameter, for all sea states. One way to prevent solving this equation is to use the so called contour line method, which states that a characteristic response can be established contour lines of the environmental parameters in question (Baarholm et al., 2010). An example of a contour line is presented in Figure 2.3 for the significant wave height H_s and peak period T_p. These can be obtained by transforming a marginal and conditional distribution function of the environmental parameters to the Gaussian space (Haver, 2013, Ch.7.2). For more information on how to establish contour lines it is referred to literature such as Baarholm et al. (2010). The contour method states that the characteristic response can be estimated using the worst environmental conditions along the contour lines with similar return period as the characteristic response in question Baarholm et al. (2010). The worst sea state will be the one giving largest response for a specific component, and may be found by running simulations for different combinations of H_s and T_p along the curve in Figure 2.3. This sea state can then be used to establish a distribution function of the maximum response by running multiple simulations with the worst sea state, and picking out the largest response from each simulation. These maximum values can the be fitted to a distribution function.

According to Haver (2013, p.102) could the distribution of a maximum response during a time duration of d hours be modelled by a Gumbel distribution, represented by Equation 2.20. In this expression α is termed the scale parameter while β is the location parameter (Naess & Moan, 2012, p.346). These can be calculated using a method called methods
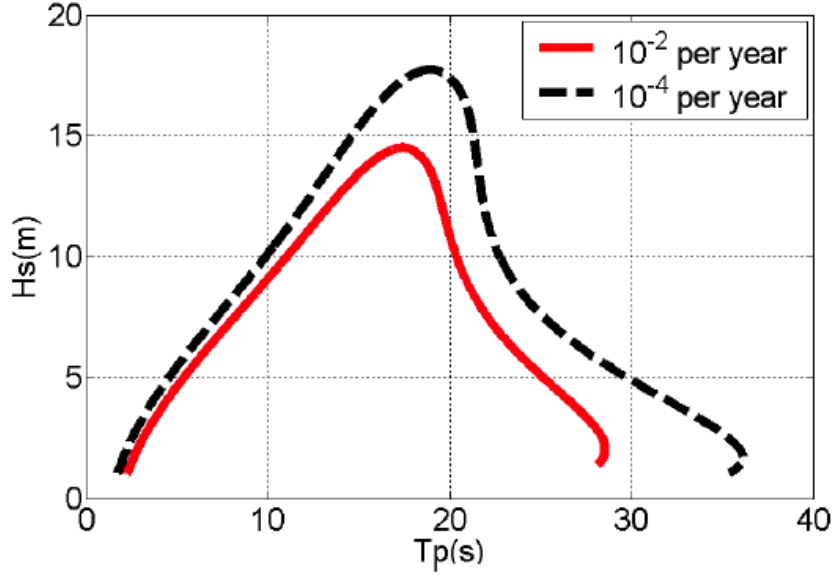
Figure 2.3: Example of a contour line for H$_s$ and T$_p$ (Kleiven & Haver, 2004, Figure 4,p.205)

of moments, where the parameters are established using the estimators for standard deviation s and mean value $\bar{x}$ of the data in the sample (Haver, 2013, p.173). According to Haver (2013, p.173) this is expressed by equation 2.21 and 2.22.

$$F_{X_d}(x) = \exp\left[-\exp\left[-\frac{x - \alpha}{\beta}\right]\right] \tag{2.20}$$

$$\bar{\beta} = 0.7797 \cdot s \tag{2.21}$$

$$\bar{\alpha} = \bar{x} - 0.57722 \cdot \bar{\beta} \tag{2.22}$$

The estimators of the variance and mean value are given by Equation 2.23 and 2.24 respectively (Raymond H. Myers, 2010, p.11,p.15).

$$s^2 = \frac{1}{n - 1} \cdot \sum_{i=1}^{n} (x_i - \bar{x})^2 \tag{2.23}$$

$$\bar{x} = \frac{1}{n} \cdot \sum_{i=1}^{n} x_i \tag{2.24}$$

When the scale and location parameters are known the characteristic 100-year response

can be established using a given fractile level for the extreme response distribution function expressed by Equation 2.20. According to (DNV, 2014b, p.60) common fractiles levels ranges from 75% to 90% for the 100-year response.

2.4 Estimating characteristic largest response during a short term sea state

If a response amplitude can be assumed to be Rayleigh distributed on the form as presented in Equation 2.25, Equation 2.26 can be used to estimate the characteristic largest response x_c during a short term sea state with N occurrences of the response variable x (DNV, 2014b, p.54). σ_x is standard deviation of the response.

$$F(x) = 1 - \exp\left\{-\frac{1}{2}\left(\frac{x}{\sigma}\right)^2\right\} \tag{2.25}$$

$$x_c = \sqrt{2 \cdot \ln(N)\,\sigma_x^2} \tag{2.26}$$

Equation 2.19 is easily solved under the assumption that the load and response is linear, which is satisfied if both the applied load and response are linearly proportional to the wave amplitude and the structure oscillates with the same frequency as the wave process (C. M. Larsen, 2014, p.151). With these assumption satisfied the response is totally described by the response spectrum, which is a function of the transfer function of the response in question and the wave spectrum. This can be used to calculate the characteristic largest wave force during a short term sea state, if the transfer function of the excitation force is known.

2.5 Ship Collision

The global behaviour due to ship collision can be regarded as a special case of Equation 2.1, where the applied force is only acting for a certain period of time t_d, i.e. acting as an impulse (C. M. Larsen, 2014). For impulse loads one may, in a similar manner as for general loading, distinguish between three different cases depending on the relation between t_d and the fundamental period of oscillation T_n. NORSOK (2004, Annex A,p.111) uses the following classification of impulse loads, in the case of explosion:

- Impulsive domain: $\frac{t_d}{T_n} < 0.3$

- Dynamic domain: $0.3 < \frac{t_d}{T_n} < 3$

- Quasi-static domain: $3 < \frac{t_d}{T_n}$

Even though this classification in NORSOK (2004) is used in relation to explosions, it may also illustrate the behaviour of a struck object in the case of collision (C. M. Larsen, 2014, p.34-36). In the impulse domain the response is governed by the impulse of the load, i.e. the area under the force-time history curve (C. M. Larsen, 2014, p.36). In the quasi-static domain, the response is predominantly static and dynamic effects might be included by dynamic amplification factor (DAF), which depends on how fast the collision load reaches its peak value (C. M. Larsen, 2014, p.36). In the dynamic domain one should perform a dynamic analysis to analyse the response of the hit object. NORSOK (2004, Annex A) also uses the terms "compliant" and "fixed" in connection with ship collision. These definitions also refer to the ratio between the impulse duration and the fundamental eigenperiod. A compliant installation indicates that $t_d << T_n$, while a fixed installation can be assumed if $t_d >> T_n$. This will be used in the following to illustrate how one may estimate the damage of both striking and struck object.

2.5.1 Decoupled approach

In the analysis of ship collisions it is usual to distinguish between two types of methods for analysing the impact event, defined as the coupled and decoupled approach (Tabri, 2012, p.47-48). The difference between these methods is that the latter method deals with analysing the collision event by dividing into two separate steps. These steps are regularly referred to as external dynamics and internal mechanics (Yu & Amdahl, 2016). In the case of compliant and fixed structures one may obtain a simple formulations for the decoupled approach (NORSOK, 2004, Annex A, p.88). As it also may give a better insight to what mechanisms that are relevant in connection with collision, the decoupled method will in the following be studied more in detail. The review of the decoupled approach is mainly based upon Annex A in (NORSOK, 2004).

2.5.2 External dynamics

The governing action in connection with collision is the initial kinetic energy (NORSOK, 2004). When two objects collide, the initial kinetic energy will be distributed among the objects involved. This may lead to permanent damage of one or both of the objects,

if the strength is not sufficient to resist the action, which represent a transformation of the kinetic energy into the form of strain energy. It is this strain energy that is aimed for in the external dynamics. The approach for estimating the total strain energy will be illustrated for a compliant structure using a simple one dimensional case where the components are attached after the collision, i.e. absolutely inelastic collision (Pedersen & Zhang, 1998).

The energy that must be absorbed as strain energy can be estimated using two laws of conservation, namely conservation of energy and momentum. As long as there are no external forces acting on a system, the formulations in Equation 2.27 and 2.28 will hold for a collision event (Tipler & Mosca, 2008, p.209,p.260-261).

$$\Delta E_{mech} = E_s \tag{2.27}$$

$$\frac{d}{dt}p = 0 \rightarrow p_1 = p_2 \tag{2.28}$$

In Equation 2.27 and 2.28 where ΔE_{mech} is the change in mechanical energy and p_1 and p_2 is the momentum before and after the collision respectively. E_s in Equation 2.27 is the strain energy, i.e. the amount of the total initial kinetic energy that is lost during deformation of one or both of the colliding objects. By using Equation 2.27 one may obtain the formulation in Equation 2.29, where it is assumed no contribution from additional stiffness such as mooring lines.

$$\frac{1}{2}\left(m_1 \cdot v_1^2 + m_2 \cdot v_2^2\right) - \frac{1}{2}\left(m_1 + m_2\right) \cdot v_c^2 = E_s \tag{2.29}$$

The common velocity v_c of the two objects right after the collision can be established using the conservation of momentum, which gives the expression as presented in Equation 2.30. In this equation m_1 and m_2 are the masses of the two objects, while v_1 and v_2 are the corresponding initial velocities. By introducing Equation 2.30 into Equation 2.29, the expression as presented in Equation 2.31 is established. This is a similar expression as the equation given for a compliant installation in Annex A in NORSOK (NORSOK, 2004, p.88). Further it is evident from equation 2.31 that as long as the masses and initial velocities are known, it is possible to estimate the total strain energy in the one dimensional case. One should note that if the colliding objects are situated in water, they will interact with the fluid. This interaction will result in force and moment contributions which are proportional to the acceleration of the objects, and may be handled as increased translation and angular masses in the dynamic equation of motion. This correction, the

so called added mass, should be added to the masses in Equation 2.31.

$$v_c = \frac{m_1 \cdot v_1 + m_2 \cdot v_2}{m_1 + m_2} \tag{2.30}$$

$$E_s = \frac{1}{2} m_1 v_1^2 \cdot \frac{1}{1 + \frac{m_1}{m_2}} \cdot \left(1 - \frac{v_2}{v_1}\right)^2 \tag{2.31}$$

2.5.3 Internal mechanics

The internal mechanics deals with how the strain energy obtained from the external dynamics is distributed in both striking and struck object. The objective of such an analysis is to estimate the amount of damage taken by the colliding objects. Thus it is essential to know the local behaviour of the objects in contact, i.e. how susceptible both objects are to deform given the shape and strength of the other object. In this connection the relative strength is important. NORSOK (2004, Annex A,p.) distinguishes between three different principles that illustrates how structures behave when exposed to collision. These "design principles" are presented as

- Strength design

- Ductile design

- Shared energy design

In the case of ship colliding with a bridge, strength design indicates that the vessel will dissipate most of the strain energy. Ductile design will in this situation mean that the bridge dissipates most of the strain energy. While shared energy design indicates substantial deformation in both the vessel and bridge.

An object strength against deformation is often described using force-deformation curves. These curves illustrates how the stiffness changes during deformation, and can be used to estimate the strain energy dissipated for a given amount of deformation. An illustration of typical force-deformation curves is presented in Figure 2.4. If the force-deformation curves are known for both the striking and struck object, it possible to estimate the local damage due to collision. The sum of the area under both curves should equal the total strain energy E_s estimated in the external mechanics. Mathematically this may by expressed as in Equation 2.32 (NORSOK, 2004, Annex A, p.89), where R and w designates the force-displacement curve and deformation respectively, while subscripts i and s represent the installation vessel respectively.

$$E_s = \int_0^{w_s} R_s dw_s + \int_0^{w_i} R_i dw_i \qquad (2.32)$$
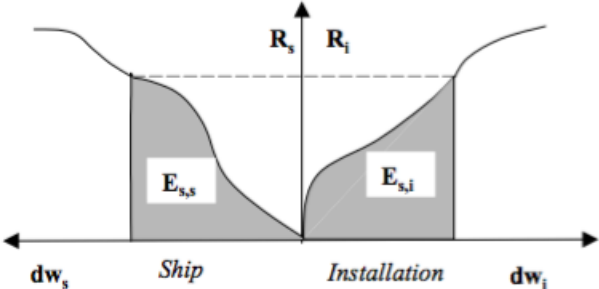
Figure 2.4: Energy dissipation in striking and struck object (NORSOK, 2004, Annex A, Figure A.3-3,p.89).

Chapter 3

Methodology

The methods that are used to analyse the bridge behaviour in this thesis reflects in many ways the design check the bridge must fulfil. It is the Norwegian Public Road Administration (NPRA) that gives rules and regulations connected to the final design of a bridge, which states that a bridge shall be designed according to the partial safety factor method (Statens vegvesen, 2015). This is a method which states that the structure should be designed according to Equation 3.1 for different limit states (Moan, 2016). Equation 3.1 states that the design strength R_d of a component, and the structure as a whole, should balance the load effects from the design load S_d. f_k and Q_k are characteristic values of the strength and applied load respectively, while γ_m and γ_f are partial safety factors and Ψ_i is a correlation factor. The partial safety factors are introduced as a consequence of uncertainties in both material and load behaviour, but do not account for so called gross errors such as human errors (Haver, 2013, p.49). Further S consists of both permanent loading and variable loading, which in general have different safety factors. The various limit states refer to different types of loading where two examples are Ultimate Limit State and Accidental Limit State which often refer to loads with return periods of 100 and 10 000 years (Moan, 2016).

$$R(f_k)/\gamma_m \geq \Sigma_i \gamma_{fi} \Psi_i S(Q_{ik}) \tag{3.1}$$

As noted it is required that the bridge should withstand 100-year loads in an ULS condition (Statens vegvesen, 2015, p.166). This is checked in connection with wave loads by using a similar approach as the contour method presented in Chapter 2.3. Initial analysis are performed using two different wave headings and two approaches for handling the correlations in the wave loads acting on the different pontoons. This is done in order to

find the worst wave condition. Though it should be noted that the significant wave height H_s and peak period T_p are the same in all conditions for the wind generated waves, which may be similar to assuming that the largest response occurs at the peak of the contour line. For the worst wave condition the extreme response is established using 90 1-hour simulations, as will be noted in Chapter 5.5, and fitted to a Gumble distribution. Some of the response components are checked against the requirement using a procedure similar to Equation 3.1 with yielding as the criteria. The response caused by extreme wind is also studied but is not included in the characteristic response analysis.

For the ALS check it is required that the bridge should not only withstand the accidental event it self, but also 100-year environmental loads in damaged condition (Statens vegvesen, 2015, p.168). For ship collision with the a floating bridge this requirement could be formulated as the following two steps presented in Statens vegvesen (2015, p.168):

1. First should the bridge be subjected to the ship impact, where the bridge is allowed to take local damage as long as it "survives" the collision event.

2. To ensure that the bridge is stable and does not collapses due to the damage caused by the impact, it should be able to withstand a 100-year environmental event in damaged condition. This is to be verified in step two.

These steps are analysed in this thesis by first running ship collisions against the pontoon and bridge girder. Secondly a damage is applied to the bridge, where both bridge girder and pontoon damage are studied, and exposed to a 100-year sea state. Though one should note that the energy levels used for the collision analysis in this thesis is not necessarily the design collision scenario. Which means that the collision events studied could be more rare events than the 10 000-year scenario that should be used in an ALS check (Statens vegvesen, 2015, p.168).

Chapter 4

Global bridge model

4.1 Bridge design and global definitions

The bridge design studied is presented in Figure 4.1 together with an illustration of the global coordinate system that will be referred to during the rest of this thesis.
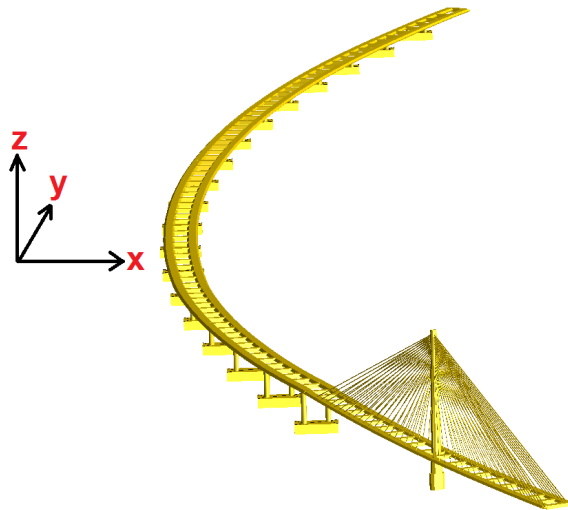
Figure 4.1: Global bridge model and coordinate system.

The bridge girder consists of two parallel box girders, connected by cross beams. This bridge girder is supported by two different parts, namely a floating and cable stayed section, which carries loads in distinct manners. For the floating part permanent loads are carried by buoyancy produced by the 19 pontoons, which also provides with water plane stiffness as the buoyancy changes. Since there are no mooring system for this design the bridge girder is the only contributor to the stiffness in the horizontal xy-plane

of the bridge. According to COWI et al. (2016, p.8) the curved shape of the bridge has a radius of 5 km and enables transverse loading to be taken as membrane action in the bridge girder. Furthermore, the distance between the two ends of the bridge is nearly 5 kilometres. The purpose of the cable stayed part is to accommodate the requirement of a navigation channel (COWI et al., 2016, p. 8). In this region permanent loads are taken as tension in the cables and transferred to both the tower and support at the south end of the bridge.

Figure 4.2 shows the bridge design from two different angles and illustrates important definitions which will be used in this thesis. In Figure 4.2a the bridge is viewed from above with the compass arrow pointing towards the rightmost support. This end will be referred to as the north end support, while the end at the cable stayed part in the leftmost corner is the south end support. Using this definition one may distinguish between the west and east side of the bridge, where east will be on the right and west on the left hand side when travelling from the south end to the north end. This will be used to separate between the two parallel box girders in the bridge girder, which will be referred to as the "west side girder" and "east side girder". In Figure 4.2 the bridge is viewed from the east side with numbers marked with circles located above the bridge. These are the bridge axis and will be used to define which parts of the bridge that are studied. The 19 pontoons are located from axis 3 at the end of the cable stayed part to axis 21 in the north end region. Further, the cable stayed part from the south support at axis 1 to the tower at axis 2 is termed the side span, while the part from axis 2 to 3 is the main span.
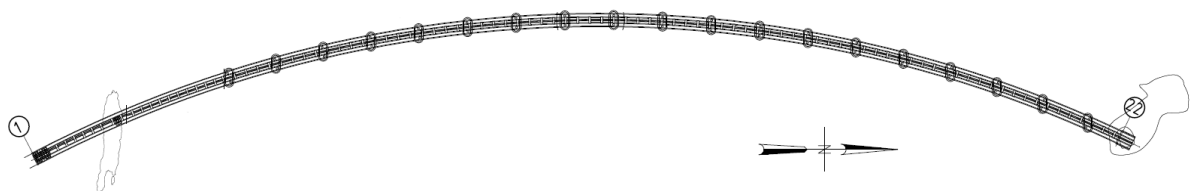
(a) Bridge orientation.
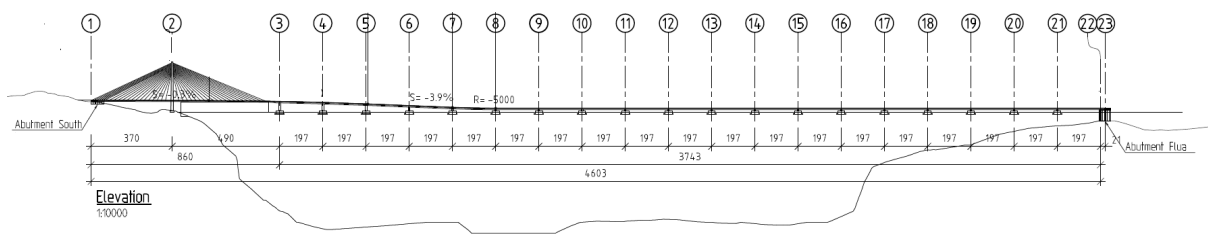
(b) Bridge axes.

Figure 4.2: Definition of the bridge orientation and axes (Aas Jakobsen, COWI, & Johs. Holt, 2016a).

The definition of the pontoon motions is illustrated in Figure 4.3. Sway is the motion

in longitudinal direction of the pontoon, while surge is transverse to the pontoon. Pitch is rotation about the longitudinal pontoon axis and roll is rotation about the transverse axis. Heave and yaw are vertical motion and rotation about the vertical axis, respectively. Though Figure 4.3 is equipped with one column the design used in this thesis has two columns per pontoon. These connects the pontoons to each of the two parallel box girder. Figure 4.3 is on the other hand only included to illustrate the definition of the motions of the pontoons.
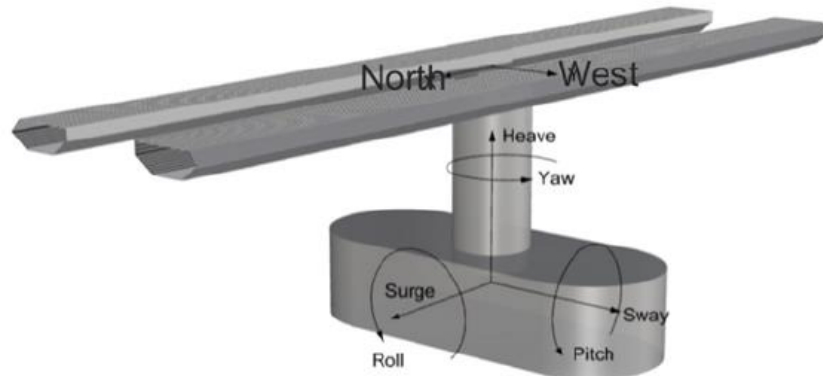
Figure 4.3: Definition of the pontoon motions (COWI, Aas Jakobsen, Global Maritim, & Johs. Holt, 2016, p.7).

4.2 USFOS model

The USFOS model of the bridge design was obtained from Postdoc Yanyan Sha, and after a thorough review it was decided to make updates for some of the parts. This included all cross sectional properties of the bridge girder, tower and stay cables as well as modelling the stay cables pretension in a different manner. The hydrodynamic properties of the pontoons was also studied including a hydrodynamic analysis in Wadam. The resulting added mass is assigned to the pontoons using another approach than in the initial model, and the other hydrodynamic properties was also updated. These updates and a description of the most important parts in the bridge model will be presented in the following sections. Most of the bridge is modelled using the standard USFOS beam element with one beam element per structural part. The exception from this are the pontoons and stay cables where different element types are used, which will be noted in the associated sections.

4.2.1 Bridge girder

In Chapter 4.1 it was noted that the cross section of the bridge girder consists of two parallel box girders. These are placed on each side of a pedestrian lane as illustrated in

Figure 4.4, and connected by cross beams every 50 meter for the floating part, and every 40 meter for the cable stayed part (COWI et al., 2016, p. 10-11). The local coordinate system for each box girder is also indicated in this figure.
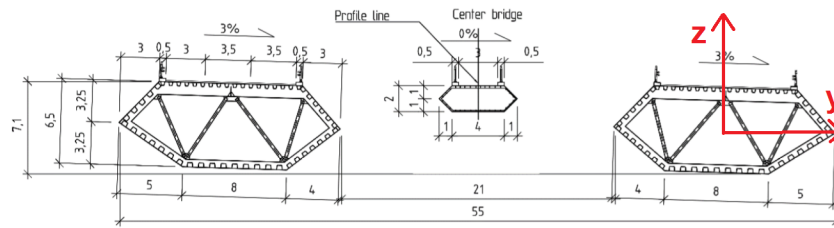
Figure 4.4: One cross section of the bridge girder and definition of local axis. This is a modification of a figure in COWI, Aas Jakobsen, Global Maritim, and Johs. Holt (2016, Figure 5-2,p. 33)

The pedestrian lane is neglected in this modelled as it have minor impact on the bridge behaviour. As an example, the main contribution to the total second moment of area I_{tot} about the vertical axis of the cross section comes from the second part in Equation 4.1. In which the two box girders are the main contributors. This due to the large distance between the neutral axis of the individual components and the neutral axis of the system a_i. A_i and I_i is the cross sectional area and second moment of area for each structural component, respectively. Furthermore, Figure 4.4 reviles the relative large difference in the strength of the box girders and the pedestrian lane, and thus neglecting the pedestrian lane will not affect the result significantly.

$$I_{tot} = \Sigma_i I_i + a_i^2 \cdot A_i \tag{4.1}$$

Since the cross sectional shape of the box girder is not a standard shape in USFOS, these are defined as so called general beams. With this approach the user must manually specify the cross sectional properties including cross sectional area, second moment of area, plastic section modulus and shear area. Further, nine different cross sections are used for the box girders along the bridge, where the floating part in general has more capacity than those used for the cable stayed sections. The elastic and plastic properties for all these nine cross sections are presented in Table 4.1. Sections H1 to H3 are used for the cable stayed part where H3 has the largest capacity and is used at the connection with the tower at axis 2. F1 to S3* are positioned along the floating part where S1 to S3* are mainly used at the connection with the columns at axis 3 to 21. S2* and S3* are equipped with two additional longitudinal stiffeners going from the top to bottom plate, and gives extra capacity at the connection with the columns. The bridge girder is divided into enough elements to properly capture the variation in cross sectional properties along the bridge.

Table 4.1: Cross sectional properties used to describe the different bridge girder sections.

	H1	**H2**	**H3**	**F1**	**F2**	**S1**	**S2***	**S3**	**S3***	**Unit**
A	0.70	1.04	1.29	0.90	1.01	1.20	1.68	1.63	2.06	[m^2]
I_t	8.75	12.60	15.45	20.77	22.58	26.18	28.90	31.33	33.97	[m^4]
I_y	2.98	4.47	5.90	6.47	7.47	8.76	11.38	13.11	14.64	[m^4]
I_z	14.11	19.55	23.56	23.16	24.02	28.21	32.24	32.14	39.67	[m^4]
W_{pt}	1.74	2.51	3.08	3.45	3.75	4.37	4.82	5.21	5.65	[m^3]
W_{py}	1.21	1.85	2.34	2.12	2.43	2.88	4.08	4.23	4.99	[m^3]
W_{pz}	2.11	3.00	3.60	3.18	3.28	4.08	4.44	4.52	5.56	[m^3]
S_{hy}	0.40	0.60	0.77	0.48	0.57	0.67	0.76	1.09	1.09	[m^2]
S_{hz}	0.32	0.45	0.53	0.45	0.45	0.54	1.01	0.54	1.01	[m^2]

The values in Table 4.1 are the updated properties, where the cross sectional area A and second moment of areas about the local y- and z-axis, I_y and I_z, was calculated using AutoCad. The values in this table are generally larger than those that came with the model, as an example I_z for S3* is 66% larger. Therefor the second moment of area was compared against hand calculations by simplifying the diagonal sides in the cross section to vertical lines. As this gave similar results, it was decided to use these properties. The plastic section modulus W_{py} and W_{pz} for S2* and S3* are based on the values for a quadratic thin walled section (Amdahl, 2005, Ch.7,p.12). For the other sections these are established from the plastic bending moment in the cross sections using the approach in (Amdahl, 2005). The torsional moment of areas I_t was calculated according to Equation 4.2 (Amdahl, 2005, p.51), for all sections expect S2* and S3*. These are calculated accounting for the shear current in the longitudinal stiffeners according to Leira, Amdahl, Syvertsen, and Larsen (2014, Appendix IV). In Equation 4.2 F is the enclosed area and t is the thickness, which is integrated inversely along the cross sections. Further, the plastic torsional section modulus is assumed to be the same as the elastic. The shear area in y-axis S_{hy} is assumed to be equal to the area of the top and bottom plate, while the diagonal sides are used for the shear area in z-axis S_{hz}. In all calculations stiffeners are handled as equivalent thickness as given in Aas Jakobsen, COWI, and Johs. Holt (2016a), the only exception is for the additional vertical longitudinal stiffeners for S2* and S3*.

$$I_t = \frac{4 \cdot F^2}{\int \frac{ds}{t}} \qquad (4.2)$$

The the density of the material used for the box girders are increased to account for all permanent loads including the effect from asphalt and railings. The density of steel is taken as 7850 [kg/m^3], while the weight per railing is 0.5 [kN/m] and wight of asphalt is 2.5 [kN/m^2]. The the weight of asphalt and two railings per box girder distributed was converted to distributed mass and added to the steel density. The total material density

ρ is presented in Table 4.2 for only two of the cross sections to illustrate the order of the distributed mass. The yield stress σ_Y and elastic modulus E used for the bridge girder sections are presented in Table 4.3.

Table 4.2: Mass density for two of the box girder sections.

	H1	F1	Unit
ρ	11913.02	10109.94	$[\text{kg/m}^3]$

Table 4.3: Yield stress and elastic modulus for bridge girder.

	Value	Unit
σ_Y	460	[MPa]
E	195	[GPa]

4.2.2   Tower

According to COWI et al. (2016, p.42) the tower at axis 2 is made out of reinforced concrete with a rectangular shape and chamfered corners. As the tower that came with the model was represented by two circular cylinders this was updated to a shape that is more in accordance with the tower presented in COWI et al. (2016). The height was also increased with 34 meters in order to get a more correct representation of the tower design. The resulting geometry is presented in Figure 4.5.

(a) Tower at axis 2.

(b) Cross section, and local z-axis.
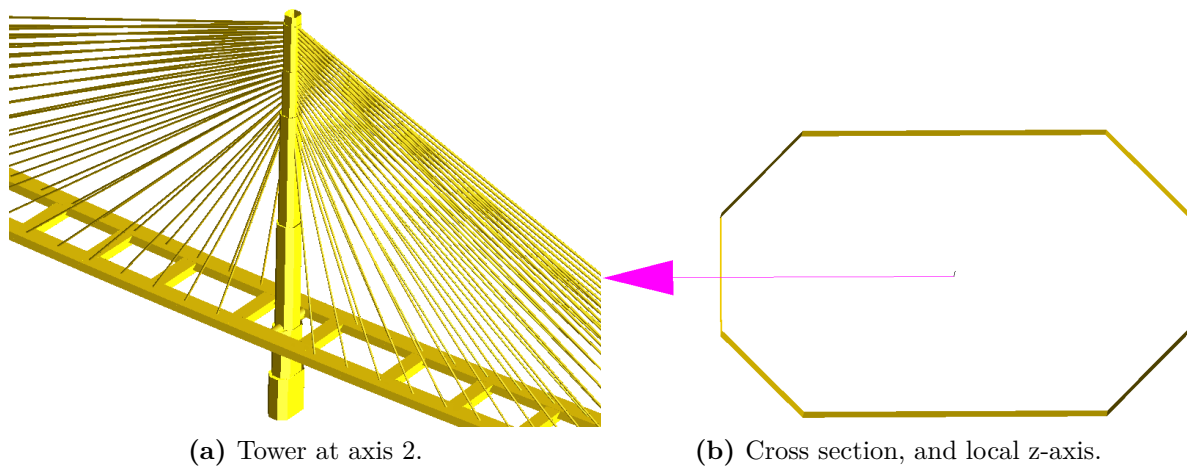
Figure 4.5: Tower at axis 2 together with the cross section at the support of the tower. Arrow is parallel to cross beams and points in local z-axis.

To capture the reduction in dimensions of the cross section towards the top, the tower is divided into seven different sections. As for the bridge girders these are defined using general beam elements, which requires manually input of the cross sectional characteristics. The elastic properties for these sections are presented in Table 4.4 where T1 is the

cross section at the bottom of the tower and T7 the tower tip. The second moment of area refer to the local beam axis, which is defined in Figure 4.5b. It should be noted that the plastic properties of this structure are set to large values to ensure elastic behaviour in all analysis. This because it was chosen to only study possible plastic utilization for the bridge girder, which is made out of steel.

Table 4.4: Elastic cross sectional properties of the tower.

	T1	**T2**	**T3**	**T4**	**T5**	**T6**	**T7**	**Unit**
A	62.19	47.99	35.41	27.73	18.78	18.40	15.53	[m^2]
I_t	657	368.61	181.90	104.44	55.74	41.52	29.97	[m^4]
I_y	2685.58	1342.60	573.05	335.30	165.89	133.84	91.41	[m^4]
I_z	1234.23	824.15	503.75	302.60	155.34	133.05	91.35	[m^4]

The shape of the cross section at the bottom of the tower is illustrated in Figure 4.5b together with the local z-axis, represented by the arrow which is parallel to the cross beams. Further, local y-axis is normal to this arrow in the horizontal plane of this figure. Using these definitions bending about local z-axis will be referred to as bending about the weak axis, while bending about the strong axis is about the local y-axis.

The yield stress, mass density and effective elastic modulus that are used for the concrete tower is presented in Table 4.5. The effective elastic modulus E_{eff} was calculated for two of the cross sections using Equation 4.3 to account for the contribution from the steel reinforcement. A_s in this equation is the total cross sectional area of the steel and is established using the information in COWI et al. (2016), A_c is the area of concrete, while A_{tot} is the total cross sectional area. In this calculation it is assumed that the elastic modulus of concrete E_c is 30 [GPa], while 210 [GPa] is used for the steel reinforcement. $E_{eff,1}$ is used for the sections T1 to T4, while $E_{eff,2}$ is used for the remaining cross sections.

$$E_{eff} = \frac{E_c \cdot A_c + E_s \cdot A_s}{A_{tot}} \tag{4.3}$$

Table 4.5: Yield stress, mass density and elastic modulus for the tower.

	Value	**Unit**
$\boldsymbol{\sigma_Y}$	50	[MPa]
$\boldsymbol{\rho}$	2400	[kg/m^3]
$\boldsymbol{E_{eff,1}}$	33.23	[GPa]
$\boldsymbol{E_{eff,2}}$	32.77	[GPa]

4.2.3 Cross beams and columns

The cross sectional properties of the columns and cross beams are the same as presented in COWI et al. (2016). The cross beams are modelled as general beam elements with the elastic properties as defined in Table 4.6. There are two types of cross beams where those used for the floating part has a larger capacity than at the cable stayed section. In Figure 4.6 the two different types are presented. Only the elastic properties of the cross beams are given in Table 4.6, which is a consequence of the discussion in Chapter 9.1.

(a) Cable stayed part.   **(b)** Floating part.
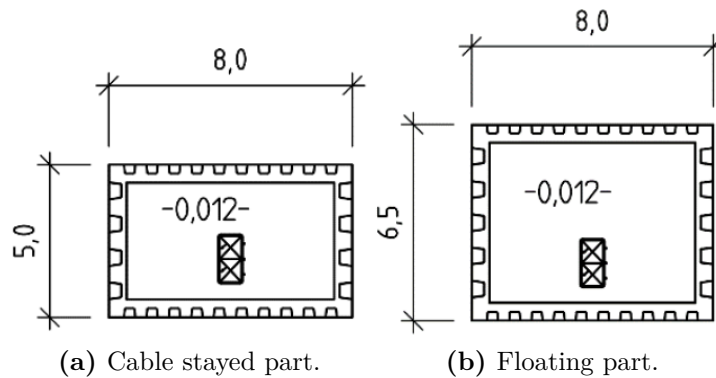
Figure 4.6: The two different types of cross beams (COWI, Aas Jakobsen, Global Maritim, & Johs. Holt, 2016, Figure 5-7,p.38).

Table 4.6: Cross sectional properties for the cross beams.

	Cable stayed part	Floating part	Unit
A	0.62	0.71	$[m^2]$
I_t	5.58	8.68	$[m^4]$
I_y	2.58	4.70	$[m^4]$
I_z	6.43	7.85	$[m^4]$
ρ	7850	7850	$[kg/m^3]$

All columns are defined as circular pipes with an equivalent thickness t_{eq}, accounting for the vertical stiffeners, a diameter D and mass density ρ as presented in Table 4.7. The mass density is increased from a steel density of 7850 $[kg/m^3]$ to account for the weight ring stiffeners which is not included in the bending properties of the columns (COWI et al., 2016, p.46).

Table 4.7: Equivalent thickness and diameter of columns.

	Axis 3 to 6	Axis 7 to 21	Unit
t_{eq}	0.055	0.035	$[m]$
D	8	8	$[m]$
ρ	8559	8961	$[kg/m^3]$

According to COWI et al. (2016) should the column height at axis 3 be nearly 40 meters, measured from pontoon deck to the bottom plate of each box girder, with a diminishing value at each bridge axis until axis 9. From this point to bridge axis 21 the height is 7.5 meters. In the USFOS model the bridge girder is positioned too high in the cable stayed region giving a column height at axis 3 of 45.80 meters, measured to the bottom of the box girders. As a result the slope towards bridge axis 9 is approximately 16% larger than the correct value. This may lead to some differences in the global stiffness properties in this region, another point is that loads on the pontoon will act with a larger moment arm than in the correct design. As a result the induced moments in the bridge girder and columns will be affected by this discrepancy. It was on the other hand decided not to update this as a 16% difference in slope may not give a significant error. As another point an update could prove to be more time consuming than the positive effect of it, and therefore it was decided to rather focus on other parts of the master thesis than update this. Though one should note that a too large column height may have some effect on the stability of the combined pontoon-column section. An increased vertical position of the bridge girder could reduce the pitch stiffness as the centre of gravity is shifted upwards.

The yield stress for both cross beams and columns is the same as for the box girders, i.e. 460 [MPa]. The elastic modulus used for the cross beams is 195 [GPa], while the columns are assigned with a value of 210 [GPa].

4.2.4 Pontoons

The pontoon design and how this is modelled in USFOS is presented in Figure 4.7, where Figure 4.7a is taken from COWI et al. (2016, Figure 5-25,p.52). These pontoons are modelled using buoyancy elements, which are a special kind of element with the only task of representing hydrodynamic properties. The columns are attached to the pontoons four corner nodes through rigid beams, highlighted in red in Figure 4.7c, such that all forces are transferred directly to the columns. As will be noted, the pontoons appears to only give stiffness in heave and therefor additional roll and pitch stiffness is applied at the centre of these elements. This location is illustrated with an arrow in Figure 4.7c. The dimensions of the pontoon is presented in Table 4.8 where L is length in longitudinal direction, B is the transverse width and D the vertical depth, and subscripts p and f refer to the pontoon and flange respectively.

The buoyancy elements do not have any material properties and the pontoon self weight and ballast is therefor handled as nodal mass. These are applied at the intersection with the columns at the deck of the pontoon, which may worsen the pontoon stability. It should also be noted that the pontoon length varies somewhat along the bridge, giving

(a) Pontoon design.

(b) Pontoon in USFOS.

(c) Connecting columns to pontoon.
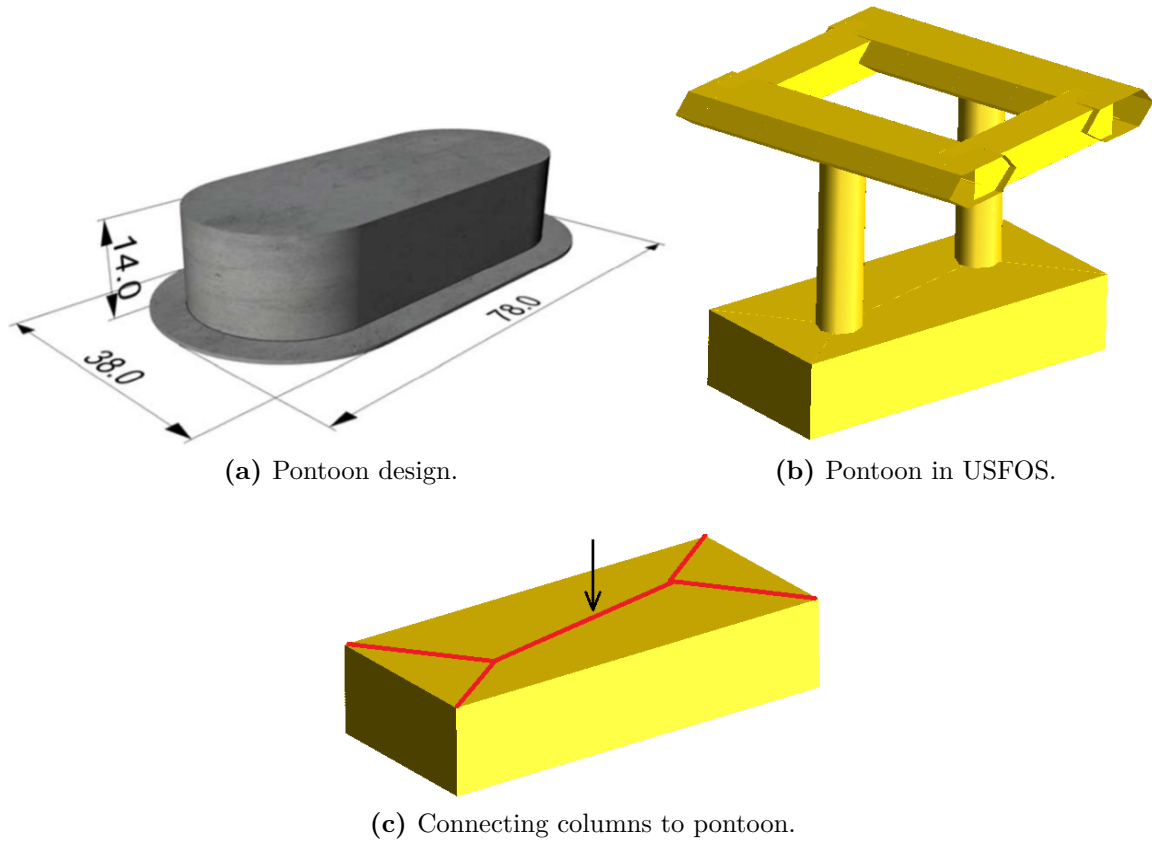
Figure 4.7: Pontoon design and how it is modelled in USFOS.

Table 4.8: Pontoon dimensions according to Aas Jakobsen, COWI, and Johs. Holt (2016a, p.10).

	Value, [m]
L_p	68
B_p	28
D_p	13.40
D_f	0.6
L_f	78
B_f	38

approximately 10% larger heave stiffness at the middle of the bridge. In general both the position of nodal mass and the pontoon lengths should have been updated to get a more correct model, but this was not prioritised.

Water plane stiffness

The stiffness properties of the pontoons are as presented in Table 4.9 for heave, roll and pitch motion, according to COWI et al. (2016, p.53). The buoyancy elements calculates

the heave stiffness correctly, but some extra attention was put on the pitch and roll motion. One single pontoon was studied and exposed to an increasing pitch and roll moment individually. The applied moment and resulting pontoon rotation for this study is plotted in Figure 4.8 for both individual cases. The model setup for this study is presented in Appendix A.

Table 4.9: Pontoon water plane stiffness in heave, roll and pitch.

	Stiffness	**Unit**
Heave	17.5	[MN/m]
Roll	5700	[MNm/rad]
Pitch	1000	[MNm/rad]

(a) Pitch.   **(b)** Roll.
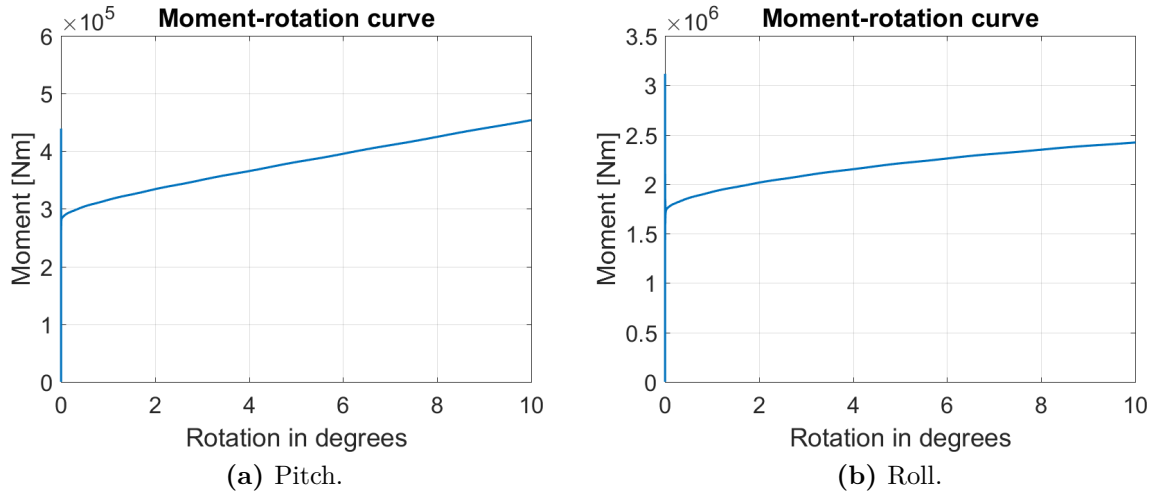
Figure 4.8: Moment-rotation curves for pontoon pitch and roll motion.

By using the stiffness in Table 4.9 a corresponding 10 ° rotation requires pitch and roll moments of $1.75E + 08$ [Nm] and $9.95E + 08$ [Nm], respectively. The contribution to the rotational stiffness from the buoyancy elements is approximately 0.25% at this angle in both cases, which is negligible. It was therefor decided to introduce additional stiffness using one node spring to ground elements with the same water pane stiffness in pitch and roll as in Table 4.9. These springs are applied at the centre of each pontoon illustrated by an arrow in Figure 4.7c. It should be noted that the pitch and roll stiffness in Table 4.9 are the contribution from the second moment of area of the water plane. According to COWI et al. (2016, p.55) is the vertical centre of gravity located above the buoyancy centre, and these properties is therefor too large. But using this approach may compensate somewhat for applying the mass at deck level.

Added mass and damping

Added mass, potential damping and drag damping are calculated according to Equation 4.4, 4.5 and 4.6, respectively, for the buoyancy elements. In Equation 4.4 $F_{m,i}$ is the added mass force, $C_{m,ii}$ the added mass coefficient, ∇ displaced volume, ρ water density and a_i acceleration. The additional parameters in Equation 4.5 are potential damping force $F_{r,i}$, potential damping coefficient $C_{r,ii}$, draft T, acceleration of gravity g and velocity v_i. In Equation 4.6 $F_{d,i}$ is the drag force, $C_{d,ii}$ is the drag coefficient and W the width of the projected area. The other parameters in the latter equation are the same as in the previous ones. Further, subscript i designate the direction referring to x-, y- and z-axis.

$$F_{m,i} = C_{m,ii} \cdot \nabla \cdot \rho \cdot a_i \tag{4.4}$$

$$F_{r,i} = C_{r,ii} \cdot \nabla \cdot \rho \cdot \sqrt{\frac{2 \cdot g}{T}} \cdot v_i \tag{4.5}$$

$$F_{d,i} = C_{d,ii} \cdot W \cdot T \cdot \rho \cdot v_i \cdot \sqrt{v_x^2 + v_y^2 + v_z^2} \tag{4.6}$$

To verify the added mass and damping formulas an analysis with one pontoon was studied applying a single force of 2000 [MN] in sway direction. For the two damping components the load was applied gradually over 1000 seconds, while studying the added mass equation it was applied as an impulse load with a duration of 1 seconds. The latter will produce a response initially predominated by acceleration (C. M. Larsen, 2014, p.37). A pontoon with similar properties as in the USFOS bridge model was studied with main dimensions as presented in Table 4.10. Further, only the coefficient in the studied equation was set to a non-zero value of 12, for all three individual cases. When assigning these coefficients it is important to be aware of the orientation of the local axis of the pontoon. This because the hydrodynamic coefficients are referring to these. The orientation is defined by the sequence of the four corner nodes that is used when defining the pontoon element, which could either be clockwise or counter clockwise. The local x-axis will be pointing in a direction parallel to a line going through the first and second node, and the local y- will be directed transversely to the same line. A figure illustrating the set up of this study together with an illustration of the orientation is presented in Appendix B.

Table 4.11 compares the result from the three USFOS analysis, with the values obtained using Equation 4.4, 4.5 and 4.6. The largest difference occurs for the acceleration which is approximately 0.6% lower in the USFOS simulations, which gives confidence to the

Table 4.10: Pontoon properties used for analysing pitch and roll stiffness.

	Value	Unit
L	64	[m]
B	28	[m]
T	10	[m]
Mass	$18.35E+06$	[kg]

applied the formulas. It should be noted that the pontoons self weight must be included to obtain the acceleration values in this table.

Table 4.11: Acceleration and velocities in sway using Equation 4.4, 4.5 and 4.6.

	From equations	From USFOS	Unit
Acceleration	8.37	8.32	$[m/s^2]$
Velocity, potential damping	6.47	6.45	$[m/s]$
Velocity, drag damping	24.11	23.97	$[m/s]$

Figure 4.7 illustrates that the buoyancy elements deviates from the shape of the pontoon design. But using the equations for added mass and damping one may obtain the correct hydrodynamic properties as long as the correct two dimensional coefficients are known. Therefor a hydrodynamic analysis was performed to obtain added mass and potential damping from potential theory. For this purpose the SESAM package with GeniE, HydroD and Wadam was used. The pontoon was modelled and meshed in GeniE, and imported into HydroD which used Wadam to calculated the hydrodynamic forces. Only one quarter of the pontoon was modelled in order to utilizing the symmetry properties about the transverse and longitudinal axis as this could reduce the computational time (DNV GL, 2015, p.2-5). The pontoon properties used in the Wadam analysis is presented in Table 4.12 and are based on those found in COWI et al. (2016, p.53, Table 5-10). COG_z is the centre of gravity with reference to the bottom of the pontoon, T the draft, while r_x, r_y and r_z represents the radius of gyration. These are calculated using Equation 4.7, where r_i is the radius of gyration about axis i, I_{ii} is the moment of inertia and M the total pontoon mass (DNV, 2014b, p.101-102). The pontoon geometry used in the hydrodynamic calculations is presented in Figure 4.9 after defining the symmetry planes. In this figure the mesh size is 0.5 [m] as used in the hydrodynamic analysis. The arguments for choosing this mesh size is discussed in Chapter 5.2.

$$r_i = \sqrt{\frac{I_{ii}}{M}} \tag{4.7}$$

The resulting frequency dependent added mass and potential damping is presented in Figure 4.10, 4.11 and 4.12 in sway, surge and heave motion, respectively. The buoyancy

Table 4.12: Pontoon properties used in the hydrodynamic calculations.

	Value	Unit
COG_z	5.76	[m]
T	10	[m]
r_x	8.62	[m]
r_y	16.35	[m]
r_z	17.65	[m]
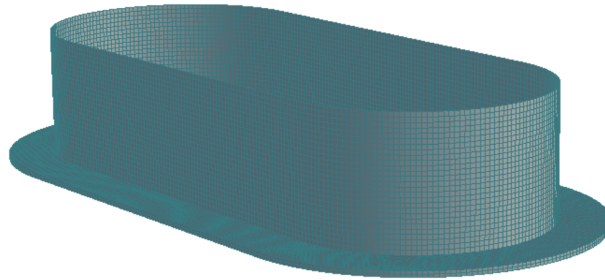
Figure 4.9: Pontoon model used in hydrodynamic calculations.

elements can on the other hand only be assigned with one coefficient for each motion. For sway and surge the added mass appears to approach an asymptotic value for large periods. It should be noted that the largest eigenmodes oscillates with a component in both sway and surge and the added mass for large periods is therefor used for these components. The potential damping is set to zero for sway and surge due to the behaviour in Figure 4.10b and 4.11b for large periods. In heave motion the coefficients are selected at a period of 11 seconds in order to get correct values in the region with vertical eigenmodes. The peak at approximately 5 seconds in Figure 4.12b could be caused by irregular frequencies, but these should not affect the potential damping at the period of 11 seconds. The coefficients is obtained by dividing these results by the additional parameters in Equation 4.4 and 4.5. The resulting coefficients are presented in Table 4.13, where the average pontoon length is used.

Table 4.13: Hydrodynamic coefficients assigned to the buoyancy elements.

Motion	Added mass, C_m	Wave damping, C_r	Drag, C_d
Sway	0.25	0	0.10
Surge	0.95	0	0.35
Heave	1.94	0.09	1.40

The drag coefficients in Table 4.13 for surge and sway are chosen based on studying common values for large tank ships, see for example Norrbin (1971) and van Berlekom and Goddard (1972). The drag coefficient in pontoon sway direction is increased to account for a less stream lined shape than a tank ship. In heave direction the drag was assumed to be predominated by the pontoon flange. The value presented in Table 4.13 is

(a) Added mass in sway.

(b) Potential damping in sway.
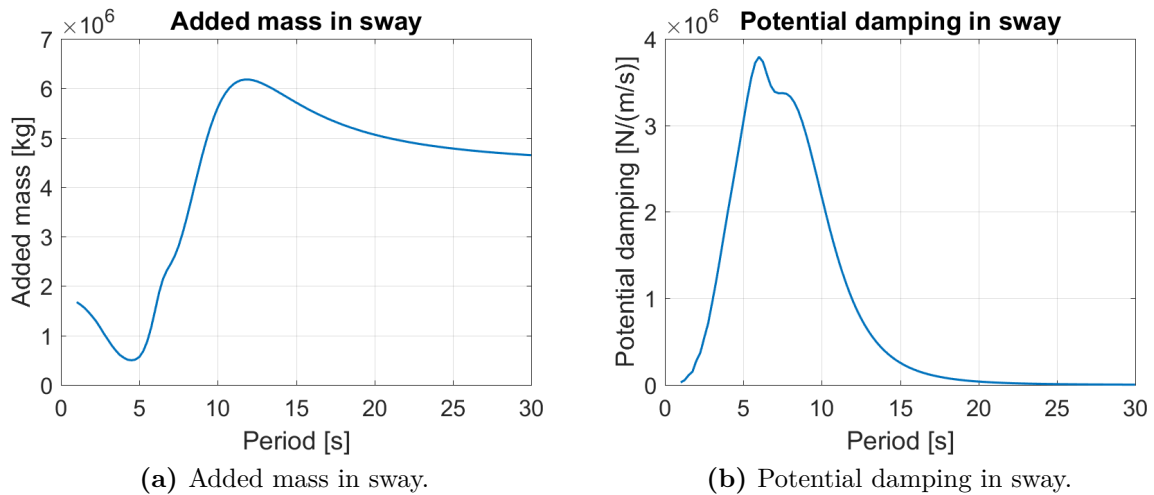
Figure 4.10: Added mass and damping in sway motion.

(a) Added mass in surge.

(b) Potential damping in surge.
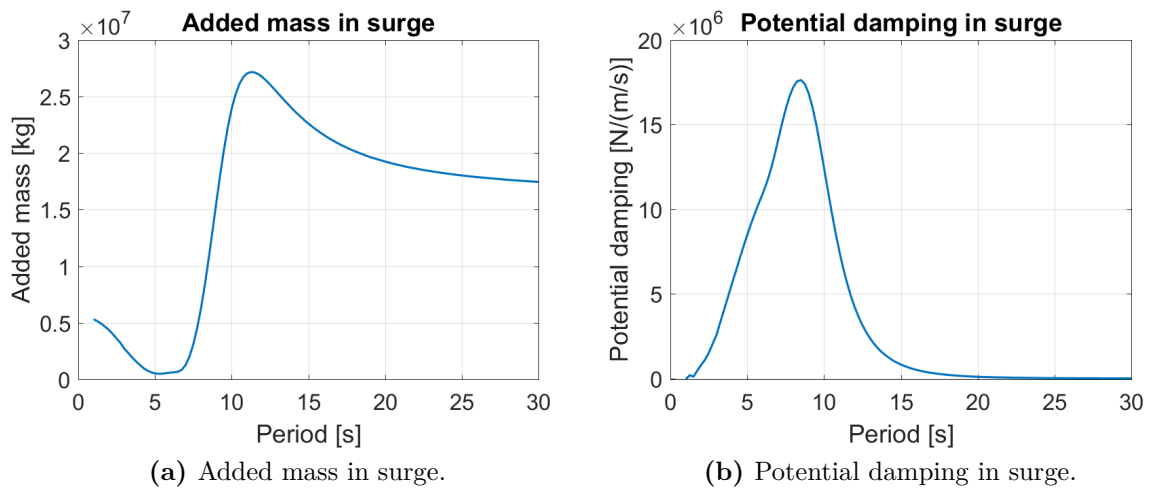
Figure 4.11: Added mass and damping in surge motion.

based on a rectangular thin plate as presented in Cengel and Cimbala (2009, p.595, Table 11-1).

Special considerations for eigenvalue analysis

The heave stiffness provided by the buoyancy elements is obtained by integrating the hydrostatic pressure over the element, which is handled as an applied force component in USFOS. Since forces are not considered in an eigenvalue analysis, only the mass and stiffness properties are considered as illustrated in Chapter 2.1, it will not contribute to the total stiffness. Therefor the heave stiffness is modelled as one node spring element, applied in the same way as for the pitch and roll stiffness.

(a) Added mass in heave.

(b) Potential damping in heave.
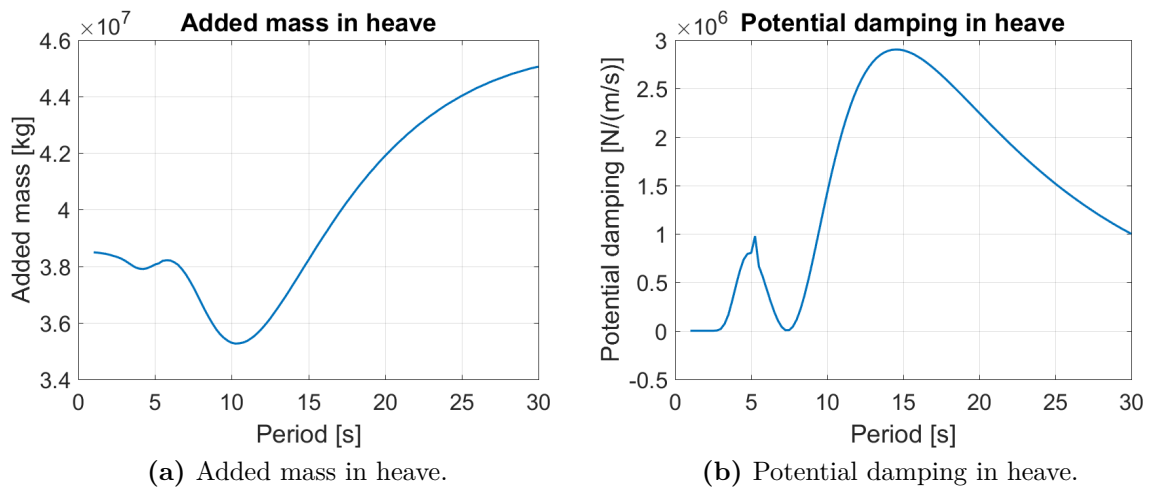
Figure 4.12: Added mass and damping in heave motion.

The added mass is also handled differently in this analysis and applied as constant values per unit length in local x-, y- and z-direction to one beam element per pontoon. This beam is introduced only in the eigenvalue analysis and is located at the middle of the pontoons and connected to the four corner nodes, as illustrated in Figure 4.13. In the initial model added mass was assigned to three of the rigid beam elements in Figure 4.7c. This middle beam element is an update and introduced such that pure motion in one of the local x-, y- and z-axis only produce added mass forces in this direction. The added mass per unit length adds up to the same total added mass as used for the buoyancy element.
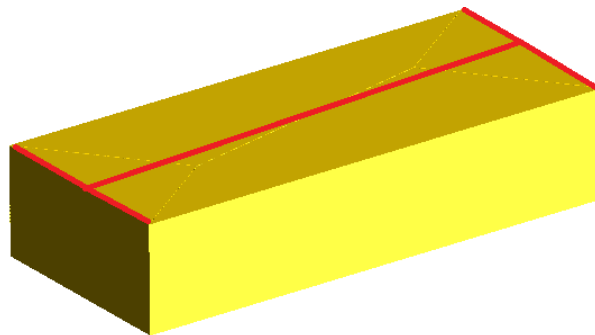
Figure 4.13: Beam element assigned with added mass properties in the eigenvalue analysis.

4.2.5 Stay cables

The cable stayed part of the bridge consists of 84 stay cables with 42 cables on each side of the tower. These cables are modelled using slender beam elements, so called riser elements, to prevent elastic buckling (USFOS, 2016, p.6.3-44). The geometry is defined as

hollow pipes though the cables in the bridge design in COWI et al. (2016) are solid. Using a hollow pipe to represent these structural parts could introduce some errors regarding the bending capacity, but by tuning the diameter and thickness it is possible to obtain the correct cross sectional area. As cables carries loading mainly by axial elongation, the cross sectional area is the most important property. The diameter and thickness values that came with the model gave too large cross sectional areas and was therefor updated according to the areas in COWI et al. (2016, p.118). It should be noted that these are in general different for the main and side span, but for simplicity the same cross sectional properties are used for both spans. The exceptions are for those where the difference in the two spans are largest. Using this approach the largest deviation from the values given in COWI et al. (2016, p.118) is approximately two percent. The cross sectional properties used in the model is presented in Table 4.14, where geometry number 201 designates the properties of longest cables, while 221 is used for the shortest. In a similar manner is geometry number 420 used for the second largest cables in the main span.

A cable hanging between two points will in general not be straight, which is an effect referred to as catenary effect (Norsk Standard, 2006b, p.17). This behaviour will reduce the stiffness of the cable and is accounted for by introducing an effective elastic modulus. According to Norsk Standard (2006b, p.17) should the effective modulus E_t be calculated using Equation 4.8, where E is the elastic modulus of the cable material, w is the unit weight of the material, l the horizontal length of the cable span and σ the cable stress due to self weight and pretensioning.

$$E_t = \frac{E}{1 + \frac{w^2 \cdot l^2 \cdot E}{12 \cdot \sigma^3}} \tag{4.8}$$

The effective modulus in the model are the same as the side span in COWI et al. (2016), which calculated these using 28% of the yield stress σ_y as the cable stress σ. In this thesis the main span is assumed to have the same effective modulus as the side span, which is not correct as the cable length in general is larger in the main span. This results in an effective modulus which is approximately three percent too large for the longest cables in the main span. Table 4.16 presents the effective elastic modulus for the longest and shortest cable to give an impression of how this property is affected by the cable length. A complete table for the 21 cables is presented in Appendix C.

The initial version of the model the elastic modulus was multiplied with a factor of 1000. By reducing these values to the correct order revealed the lack of pretension in the stay cables. According to Norsk Standard (2006b, p.10) is cable pretension used to obtain the intended bridge shape and forces when all permanent loads is applied. The pretension in the stay cables is obtained utilizing the properties of steel exposed to

Table 4.14: Cross sectional properties of the stay cables.

Geometry number	Diameter [mm]	Thickness [mm]	Area [mm²]	Cross sectional property is used for the following spans
201	133.56	58.61	13800	Main and side span
202	130.63	57.24	13200	Main and side span
203	128.40	56.21	12750	Main and side span
204	126.13	55.15	12300	Main and side span
205	123.04	53.70	11700	Main and side span
206	120.67	52.59	11250	Main and side span
207	117.45	51.08	10650	Main and side span
208	114.95	49.92	10200	Main and side span
209	112.42	48.73	9750	Main and side span
210	109.82	47.52	9300	Main and side span
211	107.14	46.26	8850	Main and side span
212	104.42	45.00	8400	Main and side span
213	100.66	43.24	7800	Main and side span
214	97.74	41.90	7350	Side span
215	94.72	40.49	6900	Side span
216	100.66	43.24	7800	Main and side span
217	97.74	41.90	7350	Side span
218	95.73	40.96	7050	Side span
219	97.74	41.90	7350	Side span
220	100.66	43.24	7800	Side span
221	106.25	45.84	8700	Main and side span
415	99.68	42.79	7650	Main span
417	101.61	43.70	7950	Main span
418	102.54	44.12	8100	Main span
419	100.66	43.24	7800	Main span
420	105.34	45.43	8550	Main span

Table 4.15: Material properties of the stay cables.

Property	Value	Unit
E	195	[GPa]
σ_Y	1860	[MPa]
σ	520.8	[MPa]
w	7850	[kg/m³]

Table 4.16: Effective modulus. Material number 201 is used for the longest cables, while 221 is used for the shortest cables.

Material number	E_t	Unit
201	178.35	[GPa]
221	194.87	[GPa]

temperature variation. A structural component which is made out of steel will shrink when exposed to temperature below a curtain level. If the ends of this component is fixed during the temperature variation, an axial force will be induced in the structural part. Mathematically this can be expressed by Equation 4.9 (Bell, 2011, p.289) where σ is the axial stress, E the elastic modulus, λ the thermal expansion coefficient and ΔT is the temperature variation. If this temperature is applied only to the cables it will force parts of the permanent loads to be transferred from the bridge girder to the cables, as the cable tries to shrink. The size of this component will depend on the temperature variation. Thus it is possible to play around with the temperature in each cable such that the shortening produces a force that is similar to the permanent loads the individual cables is supposed to carry.

$$\sigma = E \cdot \lambda \cdot \Delta T \tag{4.9}$$

The thermal expansion coefficient λ used to pretension the stay cables is presented in Table 4.17. A first approximation of the temperature was estimated using Equation 4.9, and then adjusted for each cable by comparing with the cable forces from permanent loads in COWI et al. (2016, p.114-115), in addition to the observed displacements. An illustration of the final temperatures applied to the different cables is presented in Figure 4.14, and ranges from $-114°C$ to $-194°C$. The temperature tends to be smallest in absolute value for the longest cables. Using the temperature distribution as presented in this figure the largest deviation between the cable forces compared with COWI et al. (2016, p.114-115) is approximately 10%. The forces in all cables are given in Appendix 4.14 together with the corresponding values from COWI et al. (2016, p.114-115). It is important to note that using this temperature distribution results in vertical displacement of the bridge girder towards the cables at the middle of the side span with a peak value of approximately 0.12 meters in addition to large axial stress at the support in the north end. Also the tower is displaced 0.15 metres towards the main span, which indicates that there is some potential for further improvement of the pretension. The presented temperature distribution is used, as such improvements will be very time consuming as the force in one cable is highly depended on the forces in the other cables, both in the side and main span.

Table 4.17: Thermal expansion coefficient

Thermal expansion coefficient, λ	Unit
1.40E-05	[1/° C]
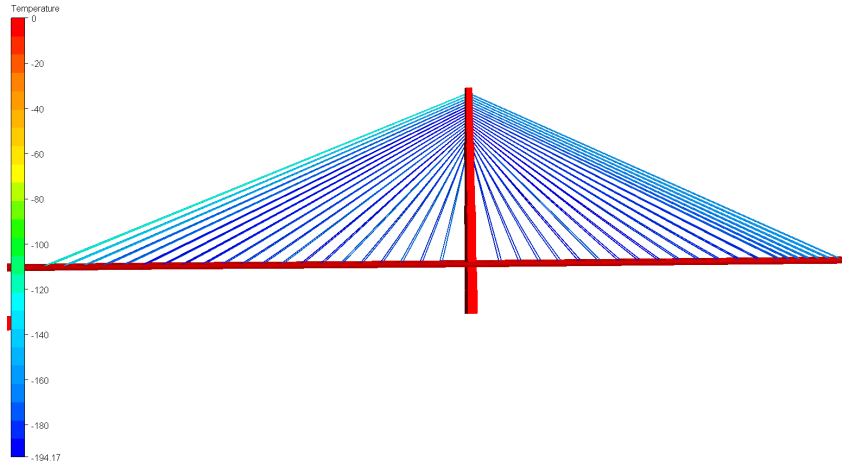
Figure 4.14: Temperature used to apply pretension in the stay cables.

4.2.6 Structural damping

The structural damping is modelled as Rayleigh damping, i.e. the damping matrix $\boldsymbol{C}$ is assumed to be proportional to the stiffness and mass matrix expressed by $\boldsymbol{K}$ and $\boldsymbol{M}$ in Equation 4.10 (Langen & Sigbjörnsson, 1979, p.9.24), respectively. The coefficients α_1 and α_2 determines the contribution from each matrix and are defined by Equation 4.11 and 4.12. From these equations one may establish the total damping matrix as long as the damping ratio ξ is known at two different frequency components (Langen & Sigbjörnsson, 1979, p.9.24). USFOS calculates these coefficients based on two frequency components and corresponding damping ratios specified as input to the program (USFOS, 2016, p.6.3-20). It should be noted that the angular frequency ω is used in Equation 4.11 and 4.12, but the input frequencies to USFOS should be given in hertz [1/s] (USFOS, 2016). It was chosen to specify the damping to periods of 30 and 2 seconds and the corresponding input frequencies and associated damping ratios as presented in Table 4.18. According to Langen and Sigbjörnsson (1979, p.9.13) are common values of damping ratios for steel structure between 0.5% and 0.8%. The values in Table 4.18 gives the distribution as illustrated in Figure 4.15 where the damping ratio is presented in percentage and the frequency in hertz. The damping ratio is within 0.5% and 0.8% between periods of 2.63 and 23.8 seconds, 0.38 and 0.04 in this figure, which is in the region with linear waves. The damping ratio for the largest eigenperiod is 2.06% using this approach.

$$\boldsymbol{C} = \alpha_1 \cdot \boldsymbol{M} + \alpha_2 \cdot \boldsymbol{K} \tag{4.10}$$

$$\alpha_1 = \frac{2 \cdot \omega_1 \cdot \omega_2}{\omega_2^2 - \omega_1^2} \cdot (\xi_1 \cdot \omega_2 - \xi_2 \cdot \omega_1) \tag{4.11}$$

$$\alpha_1 = 2 \cdot \frac{\xi_2 \cdot \omega_2 - \xi_1 \cdot \omega_1}{\omega_2^2 - \omega_1^2} \tag{4.12}$$

Table 4.18: Frequencies and corresponding damping ratios.

Frequency, [1/s]	Damping ratio
$1/30 = 0.033$	0.01
$1/2 = 0.5$	0.01
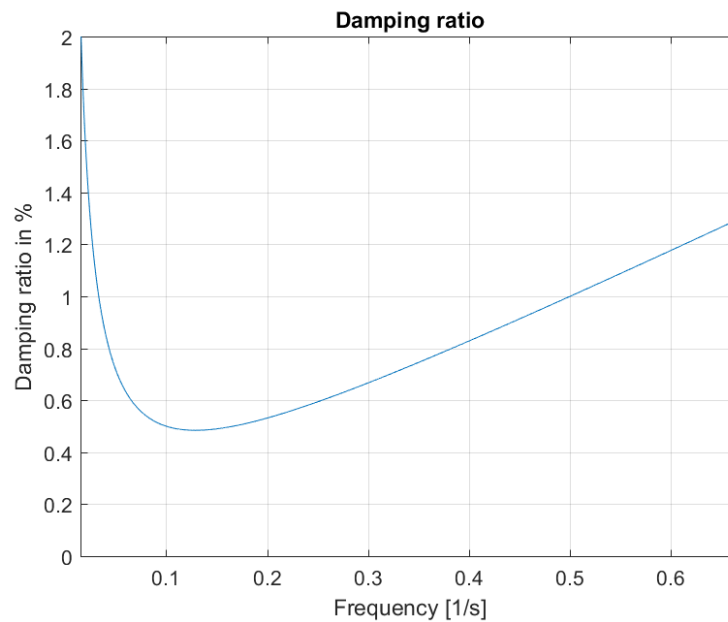
Figure 4.15: Damping ratio in percentage as a function of frequency.

4.3 Modelling of a damaged bridge girder

Figure 4.16 illustrates how the damage of the west side bridge girder is modelled, which is used in one of the damaged conditions. As seen from this figure the middle beam element in the west side girder between bridge axis 10 and 11 is totally removed.
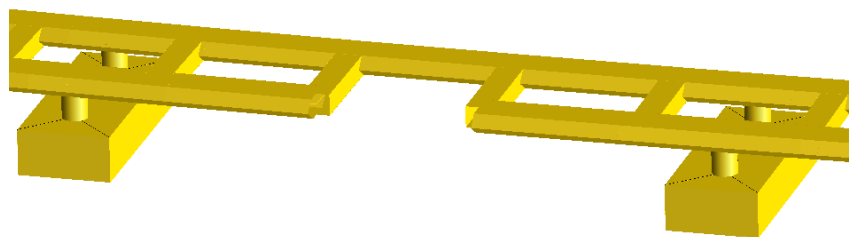
Figure 4.16: Modelled damage to the bridge girder between axis 10 and 11.

Chapter 5

Environmental conditions and loads

5.1 Environmental conditions at Bjørnafjorden

Some of the relevant environmental conditions at Bjørnafjorden includes waves, wind, current and tide. In the following some attention will be put on these environmental loads and their importance at this location. Further, it was focused on the 100-year values, as this should be used for the dominating load component in ULS condition according to Statens vegvesen (2015, p.166). It is important to noted that one should in general assume that the extreme loads from waves, wind, current and tide occurs at the same time (Statens vegvesen, 2015, p.77-78). But for a floating bridge Statens vegvesen (2015, p.166) states that the mentioned environmental loads should still be treated as one single characteristic load, while the total characteristic environmental 100-year load itself is obtained by using a 100-year return period for the dominating load and "relevant returnperiods" for the remaining loads. Aas-Jakobsen et al. (2016, p.19) solved this by checking different combinations of return periods for the environmental load, e.g. where one such combination could be to use 100-year values for wind and waves and 10-year value for the other environmental loads. One explanation for such a procedure could be to account for that a 100-year load effect in the structure do not necessarily correspond to a 100-year condition of all environmental load components, as described by DNV (2014a, p.33-34,p.93).

COWI et al. (2016, Table 3-7,p.19) presents a description of various 100-year sea states for different wave headings at Bjørnafjorden described by the significant wave height H_s and peak period T_p. According to these values the largest H_s and T_p occurs for wave directions west and north-west. It is assumed that this means the waves are propagating from west to east and north-west to south-west respectively, see Figure 4.2 in Chapter 4
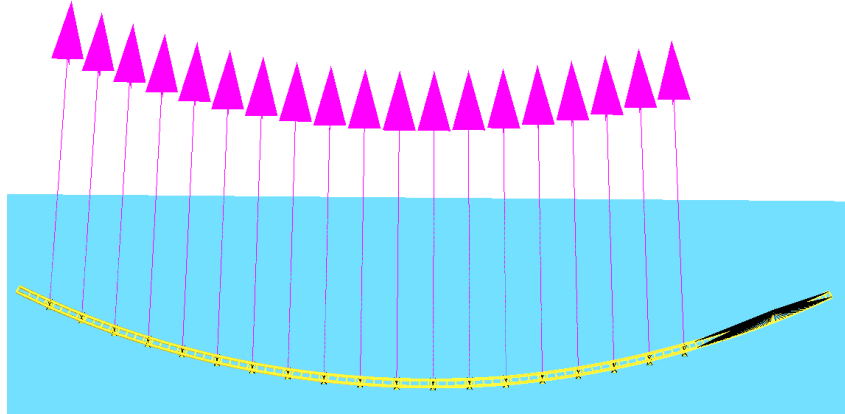
Figure 5.1: Definition of the direction of waves coming from west, giving positive wave force in sway direction. Bridge is viewed from above.

for the orientation of the bridge. This is based on the definition of the most severe wave headings in (COWI et al., 2016, p.58,Table 7-1,p.72) and that the largest wind comes from the region between north and west directions Aas-Jakobsen et al. (2016, p.A.3). Waves from west will therefor give a positive wave force in sway direction as illustrated in Figure 5.1. This is important as it will affect the direction of the mean drift force.

The combination of H_s and T_s that applies for waves from west and north-west are presented in Table 5.1 for the 100-year sea states for both wind generated waves and swells. It should be noted that these values are based on simulations and measured data at the bridge location (Aas Jakobsen, COWI, & Johs. Holt, 2016b, p.64-65).

Table 5.1: 100-year sea states for wind generated waves and swells.

	H_s [m]	T_p [s]
Wind generated waves	3	6
Swell waves	0.4	12
	0.4	14
	0.4	16

As noted the largest wind speed at Bjørnafjorden comes from the region between north and west, according to Aas-Jakobsen et al. (2016, p.A.3). This report presents a value of the so called basic wind speed v_b, which can be used to calculate the 10-minute mean wind speed at a reference height of 10 meter $U_m(10)$, in accordance with Norsk Standard (2005). The relation between these values will be described in Chapter 5.3 together with a more through review of how the wind loads are modelled. The 100-year v_b as defined in Aas-Jakobsen et al. (2016, p.A.3) is presented in Table 5.2 together with the corresponding 10-minutes mean wind speed at 10 meters. The standard deviations σ that can be used to describe the fluctuating wind at this location is also presented in Table 5.2 and are almost the same values as used by (Moe, 2016, p.80). These can be established using the

wind description for Bjørnafjorden found in Aas-Jakobsen et al. (2016, p.A2-A3). The subscript x, y and z refers to the wind component in the axes corresponding to the global coordinate system of the USFOS model, see Chapter 4.1.

Table 5.2: Basic wind speed and mean wind speed together wind the standard deviation of the fluctuating wind component.

	Value [m/s]
v_b	27
$U_m(10)$	31.7
σ_x	4.59
σ_y	3.67
σ_z	2.75

The 100-year current speed down to a depth corresponding to the pontoon draft of 10 meters is given in Table 5.3, as defined by Aas-Jakobsen et al. (2016, Table 11-3,p.B.6). Current is not accounted for in the analysis but could easily be included in USFOS by defining a profile using the command "Current". One should note that COWI et al. (2016) come to the conclusion that loads from current is small for this bridge design compared to the wave loads, and neglected therefor this load in their analysis.

Table 5.3: Current profile down to a depth of 10 meters according to Aas-Jakobsen et al. (2016).

Depth [m]	Current speed [m/s]
$0 - 5$	0.70
10	0.40

Table 5.4 presents the variation in water level with a 100-year return period as found in Aas-Jakobsen et al. (2016, Table 11-5,p.B.8). One way of including this water level variation in USFOS could be to apply it as nodal forces corresponding to an additional increase or decrease in pontoon displaced volume, where the change in draft is determined by either the highest or lowest water level. Alternatively one may specify the tidal level directly in USFOS using the command "Switches" (USFOS, 2016, p.6.3-113 - 6.3-114). Tidal variation may be relevant for the weak axis moment in the bridge girder, but will only give a static contribution to the bridge response. Therefor it was decided to rather focus on the response from wave and wind loads, as these have frequency components in the same range as the eigenperiods of the bridge and may be critical with regard to dynamic amplification. As an example, the wind generated sea in Table 5.1 has a peak period of 6 seconds, which is well below the largest eigenperiod for the bridge is 65 seconds. Consequently the bridge may have lower eigenperiods in the range of the wave frequency as will be shown in Chapter 8.1. The next sections will describe how environmental loads from wind and waves are established and handled in the USFOS bridge model.

Table 5.4: Highest and lowest water level accoding to Aas-Jakobsen et al. (2016).

Highest water level [m]	Lowest water level [m]
1.88	-0.26

5.2 Modelling wave loads

USFOS has the possibility of calculating wave loads from an irregular sea state directly in the program by means of either a user defined or standard wave spectrum (USFOS, 2016, p.6.3-119). With this option specified USFOS uses the resulting wave kinematics to calculate the wave loads acting on a body for each time increment (USFOS, 2010, p.27). Since linear wave theory is used to generate the irregular waves in USFOS (USFOS, 2010, p.27) it will not be able to capture slowly-varying drift forces as this in general requires a second order velocity potential, i.e second order wave theory (Faltinsen, 1990, p.155). Therefor these slowly-varying wave loads are introduced as precalculated time-varying load histories, using Newman's approximation together with second order transfer functions established in Wadam. A similar approach is also used for the linear wave forces with the argument that the buoyancy elements deviates from the actual pontoon design, as the bottom flange and the curved ends is not modelled. According to USFOS (2010, p.31) the wave forces in USFOS can be calculated by Morrison equation or "Mac-Camy and Fuchs" theory, which are valid for circular cylinders (Faltinsen, 1990, p.61). Thus it was decided to use Wadam since wave loads depends on the pontoon shape, such as the curved ends in addition to contribution from the bottom flange. These effects are easily accounted for using this approach and could therefor give accurate results. As a consequence the irregular wave option in USFOS is not used in this thesis.

Wave loads are introduced as individual time varying nodal loads applied to each of the 19 pontoons including effects from both linear and slowly varying wave loads. All wave forces are applied in the centre of the water plane area at the free surface of each pontoon, assuming a draft of 10 meters. This is done as the transfer functions refer to the global coordinate system of the model used in the hydrodynamic calculations (DNV GL, 2015, p.2-3), which is located at this position. It is also important to note that the transfer functions in general are dependent on the wave heading, which is defined according to Figure 5.2 in Wadam (DNV GL, 2015, p.2-31). The x-axis in Figure 5.2 coincides with the longitudinal direction of the pontoon model, see Figure 4.7 in Chapter 4.2.4, with the origin at the centre of the water plane area. Furthermore, all wave forces are calculated assuming long crested waves, though some analysis includes the phase difference caused by the different pontoon locations, see Chapter 5.2.4. These phase angles are introduced to study the effect of correlation between the wave loads action on the various pontoons. Since the axes in the local coordinate system in Figure 5.2 is parallel to those in the global

USFOS model a wave heading of 0° corresponds to waves from west while 315° means waves from north-west. These wave headings are used as the significant wave height is largest from west and north-west, as noted in Chapter 5.1. Therefor the main focus was put on these wave headings, which implies the assumption that the 100-year bridge response occurring at the largest H_s value.
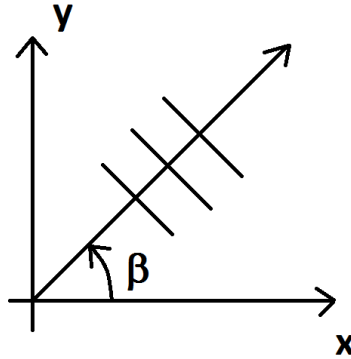
Figure 5.2: Definition of wave heading in Wadam (DNV GL, 2015, p.2-31). This figure is a reproduction of the original figure in (DNV GL, 2015, Figure 2.25,p.2-31).

5.2.1 Linear wave forces

The linear wave forces are calculated for all six load components using the transfer functions calculated in Wadam, and summed over all wave frequencies according to Equation 2.5 in Chapter 2.2.2. Figures 5.3 to 5.5 presents the transfer functions for the linear wave excitation forces and moments for a wave heading of 315°. The largest difference between these results and the graphs presented COWI et al. (2016, p.55) occurs for the peak value in roll, for a period of seven seconds. The value reported in COWI et al. (2016, p.55) is approximately 23% lower. The non-zero transfer functions for a wave heading of 0° are presented in Appendix D.

5.2.2 Second order drift forces

The time histories for the slowly varying drift forces are established using second order transfer functions together with Newman's approximation. In sway direction the force is calculated according to Equation 2.11 in Chapter 2.2.3. In this chapter it was noted that non-physical high frequency components produced by this equation should not have impact on the response from slowly-varying drift. But to ensure that these frequencies do not affect the linear frequency components it was decided to use the same band-pass as Moe (2016, p.74-75) used on the slow-drift force time history to remove these high

(a) Transfer function in sway.

(b) Transfer function in surge.
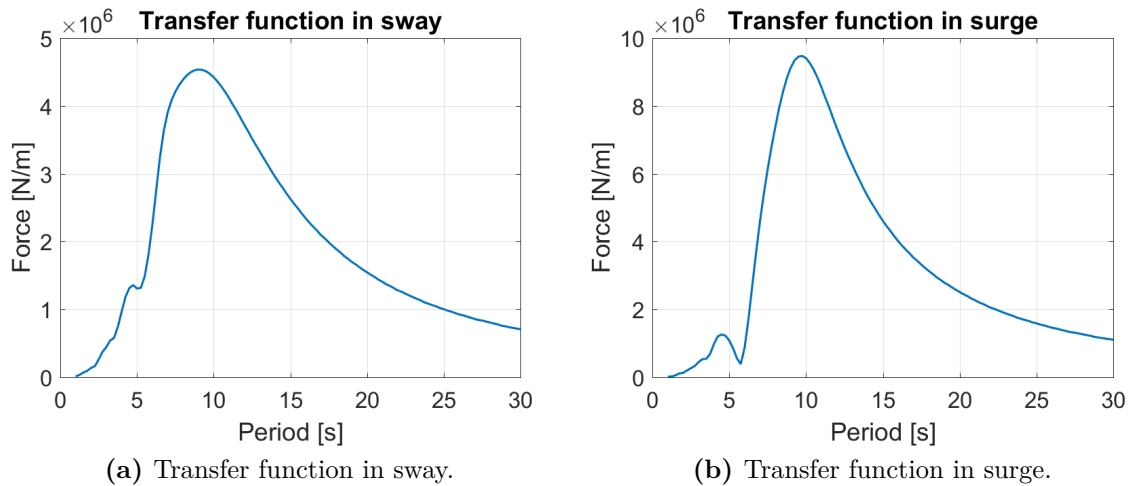
Figure 5.3: Transfer function for the excitation force in sway and surge, in the case of 315°heading.

(a) Transfer function in heave.

(b) Transfer function in pitch.
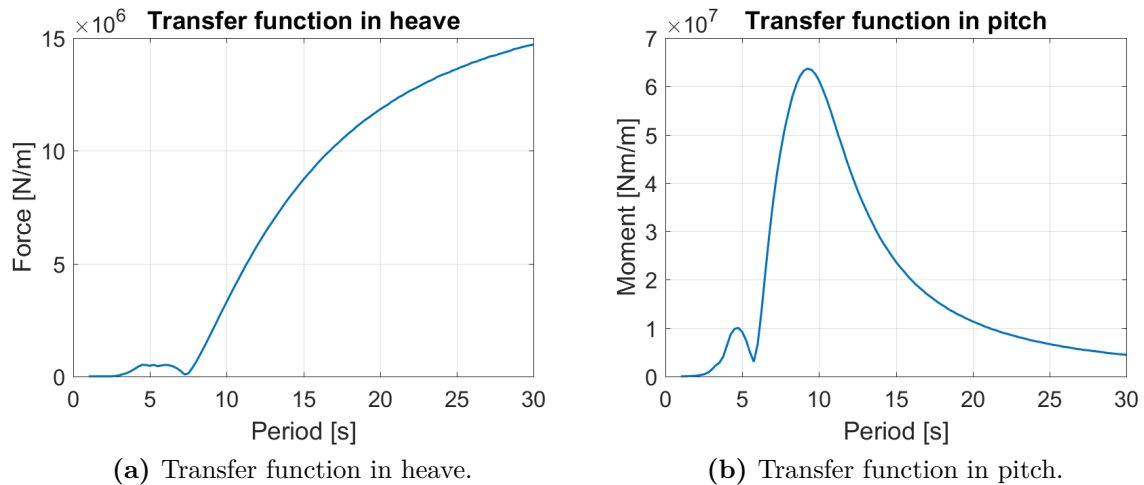
Figure 5.4: Transfer function for the excitation force in heave and excitation moment in pitch, in the case of 315°heading.

frequencies. In Chapter 2.2.3 it was noted that slow drift forces may excite eigenperiods in the range of $1-2$ minutes, therefor all periods below 50 seconds are filtered out from the slow-drift force time histories. This is well below the largest eigenperiod of 65 seconds for this bridge. In surge and yaw motion the formulation which accounts for the sign of the second order transfer function was used, see Equation 2.13 in Chapter 2.2.3, as it allows for negative values. It is not stated in Standing et al. (1987) that this formulation should result in similar non-physical high frequency components as in the expression used for the drift force in sway direction. Nevertheless it was decided to use the same band-pass for the time histories calculated by this approach. This to be consistent in which frequency components that are included in the slowly-varying forces. As it is the difference-frequency for the largest eigenperiod that are expected to be most relevant for this second order

(a) Transfer function in roll.

(b) Transfer function in yaw.
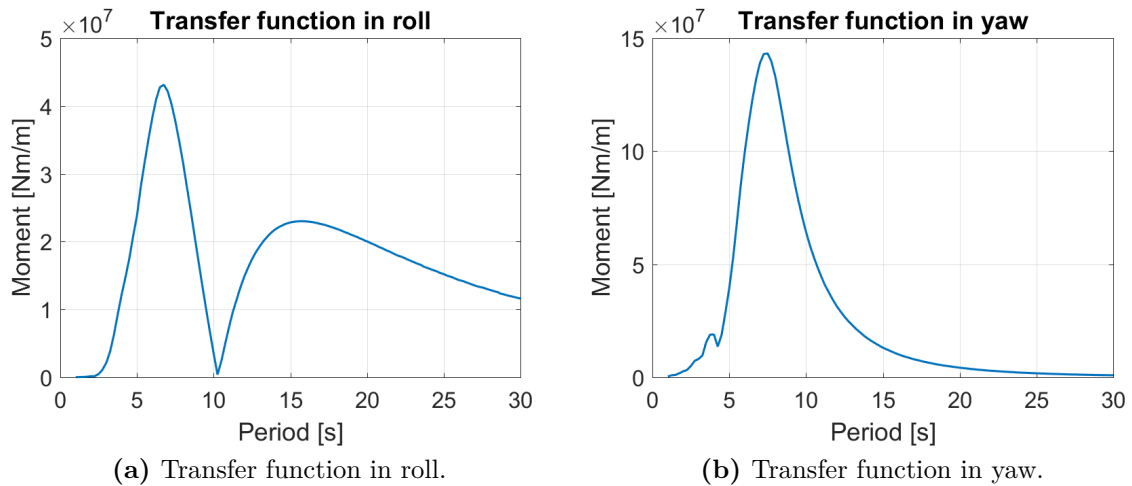
Figure 5.5: Transfer function for the excitation moment in roll and yaw, in the case of 315° heading.

effect, the error by using the band-pass in the latter formulation is expected to be low.

According to DNV (2014b, p. 103) it is important to perform a convergence study to verify that the result from the hydrodynamic calculations are accurate. This was done by running four analysis with decreasing mesh size. As noted in Chapter 2.2.3 there exists two different methods that could be used to calculate the second order transfer functions, i.e. direct pressure integration and conservation of momentum. The latter is also termed far field integration. Both these methods where used and compared to each other as they should give similar results for the converged solution (DNV, 2014b, p. 103). The results from the convergence study is presented in Figure 5.6 for both direct pressure integration and far field integration in the case of 0° wave heading.

(a) Direct pressure integration.

(b) Far field integration.
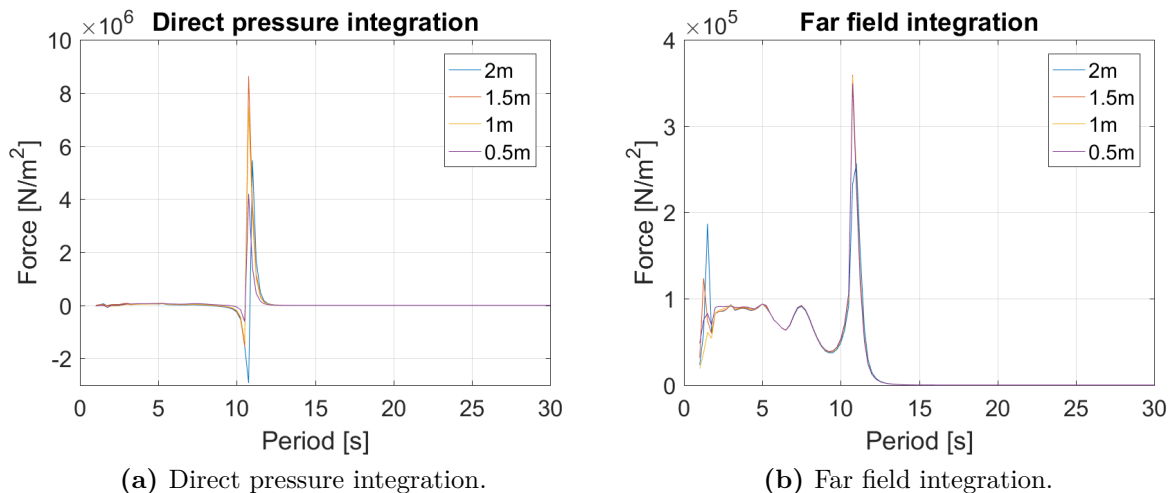
Figure 5.6: Convergence study using both direct pressure integration and far field integration in the case of 0° heading.

From Figure 5.6 it is evident that the second order transfer functions calculated by the far field integration have only minor changes in the region above a period of five seconds. By using direct pressure integration on the other hand the difference in the results from 1 meter to 0.5 meter mesh is large. As both methods should give similar results (DNV, 2014b, p. 103), one should in general run with even lower mesh size to verify that the two approaches converges towards the same solution. But due to the computational effort that is required calculating the second-order transfer functions for very fine mesh, in addition to the restriction in the amount of panels (DNV GL, 2015, p.4-6), another approach was chosen. After discussing these issues with supervisor Professor Jørgen Amdahl it was decided to run an analysis excluding the flange, and then compare these with the results obtained with the flange. This because the direct pressure integration could be more sensitive to the sharp changes in geometry caused by the flange, see Chapter 2.2.3, resulting in a very slow convergence for this method. One could argue that the results with and without the flange should be in the same range and have similar shape, and could therefor be used to decide whether the far field integration represents the converged solution. The second order transfer function when disregarding the bottom flange is presented in Figure 5.7.
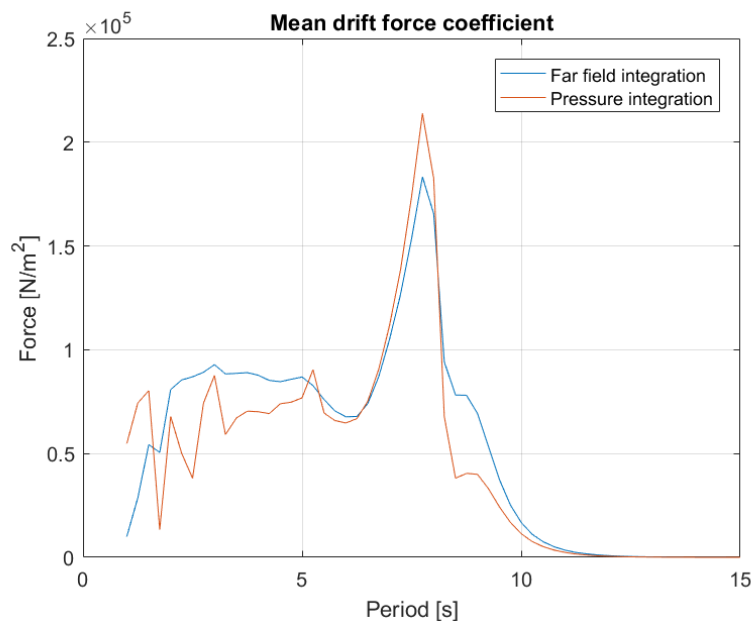
Figure 5.7: Second order transfer function for a pontoon without the bottom flange for a mesh size of 1 meter.

Figure 5.7 illustrates that the two methods gives similar results for a mesh size of 1 meter when the bottom flange is removed. Also the behaviour of the second order transfer functions are more similar to the far field integration curve in Figure 5.6b than the direct pressure integration curve in Figure 5.6a. It was therefor decided to use the far field integration method for calculation of the second order transfer functions, and a mesh size

of 0.5 meters. This mesh size is also used for all the other hydrodynamic calculations. It should be noted that the result in Figure 5.6b is similar in shape as the result presented in COWI et al. (2016, p.78), though the peak value in the mentioned report is approximately 40% lower. If the result in Figure 5.6b is not fully converged it could explain this difference. On the other hand it was also noted that this peak value is sensitive to the radius of gyration values defined in the hydrodynamic model, see Chapter 4.2.4. If these are defined differently it could be a possible cause of the observed differences.

The second order transfer functions for a wave heading of 315° is presented in Figure 5.8 and 5.9. According to Faltinsen (1990, p.139) these transfer functions may exhibit peaks in regions around eigenperiods. Such peaks is seen in for all three load components at a period of approximately 11 seconds, which is in the range of the eigenperiod in heave for a single pontoon.

(a) Sway direction.
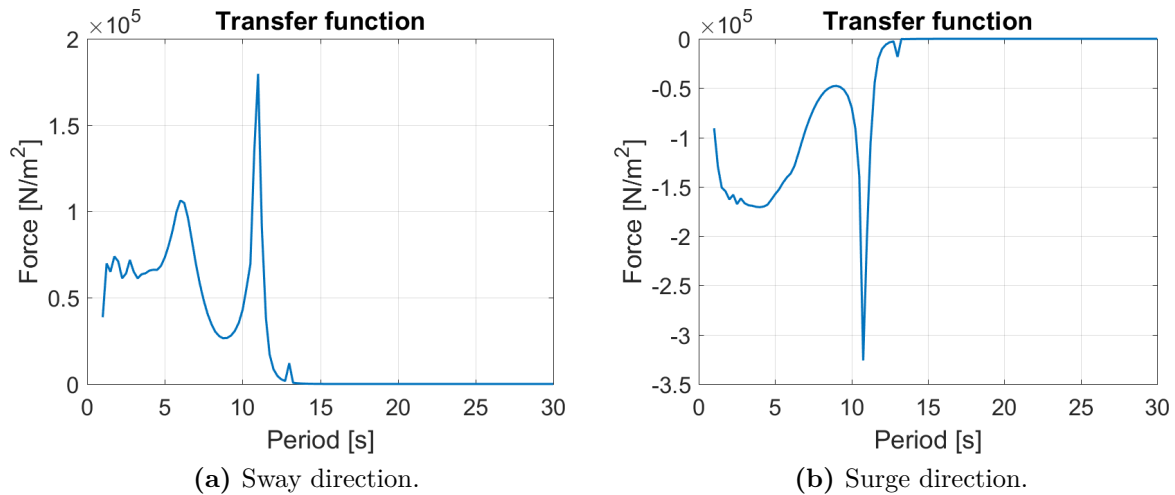
(b) Surge direction.

Figure 5.8: Second order transfer in sway and surge direction, 315° wave heading.

The second order transfer functions was compared against values obtained using the asymptotic equations for high frequencies in Chapter 2.2.3. These are valid for a shape similar to the pontoon, and the result is presented in Table 5.5. It is seen that all of the three second order transfer functions have a sudden drop at a period of approximately 1 seconds. One explanation for this behaviour could be presence of irregular frequencies, which is studied by Pan, Vada, and Hanssen (2013). Moe (2016) solved a similar problem by forcing the transfer functions to be constant below a curtain period. This is not done in this work, but it is noted that the wave spectrum used for the wind generated waves has little energy for a period below 2.5 seconds, see Figure 5.10 in Chapter 5.2.3. A drop in the transfer functions in this region is therefor expected to have low impact on the final result. Except from this the results in Figure 5.8 and 5.9 are close to the corresponding asymptotic value in Table 5.5 for periods between $1-5$ seconds. A similar tendency is also seen for the 0° wave heading results in this table and in Figure 5.6b. For definition
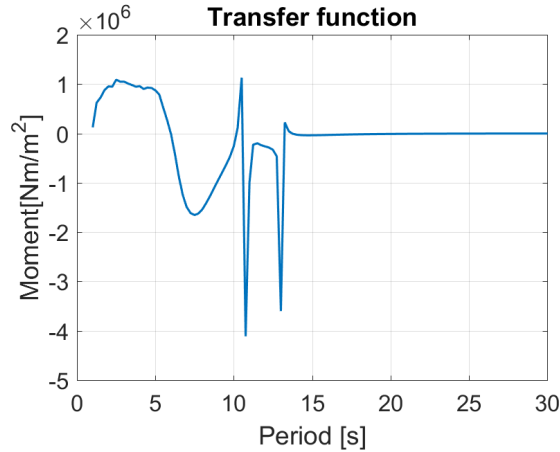
Figure 5.9: Second order transfer function for yaw moment, 315° wave heading.

of sway, surge and yaw see Chapter 4.1.

Table 5.5: Second order transfer function for small wave length using Equation 2.14, 2.15 and 2.16 in Chapter 2.2.3.

	0° wave heading	315° wave heading	Unit
Sway	0.94E+05	0.66E+05	[N/m^2]
Surge	0	-1.67E+05	[N/m^2]
Yaw	0	0.94E+06	[Nm/m^2]

5.2.3 Sea spectrum

The wind generated sea is described by a JONSWAP spectrum using the formulation as expressed by Equation 5.1 (DNV, 2014b, p.49). In this equation γ is a parameter defining the shape of the spectrum peak, H_s is the significant wave height, ω_p is the peak frequency, σ_w describes the width of the peak and $S_{wind}(\omega)$ is the spectrum value for wave frequency ω. The values used for γ and σ_w are presented in Table 5.6 (DNV, 2014b, p.49).

$$S_{wind\,sea}(\omega) = (1 - 0.287\ln(\gamma)) \cdot \frac{5}{16} \cdot H_s^2 \omega_p^4 \cdot \omega^{-5} \cdot \exp\left[-\frac{5}{4}\left(\frac{\omega}{\omega_p}\right)^{-4}\right] \cdot \gamma^{\exp\left[-0.5\left(\frac{\omega-\omega_p}{\sigma_p \cdot \omega_p}\right)^2\right]} \quad (5.1)$$

Figure 5.10 illustrates the resulting JONSWAP spectrum that is used for the wind generated waves in the analysis. This is established using the formulation of the JONSWAP spectrum in Equation 5.1 together the information in Table 5.1. The significant wave height and peak period is the ones presented in Table 5.6, see Chapter 5.1.

Table 5.6: Parameters used to describe the JONSWAP spectrum for wind generated sea.

Parameter	Value
γ	3.3
σ_w, for $\omega \leq \omega_p$	0.07
σ_w, for $\omega > \omega_p$	0.09
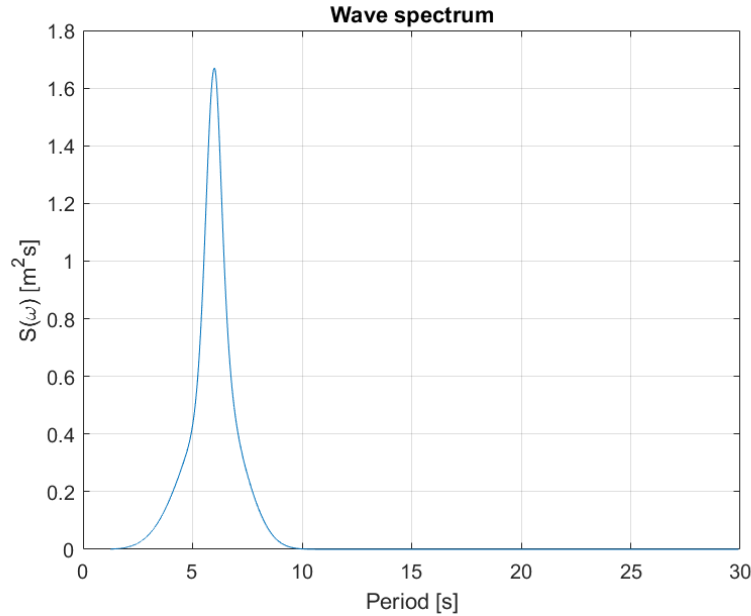
Figure 5.10: JONSWAP spectrum used to describe the wind generated sea.

The effect from swells was included by defining a separate JONSWAP spectrum from swell sea $S_{swell}(\omega)$, and adding this contribution to the wind generated wave spectrum according to Equation 5.2 (DNV, 2014b, p.50-51). The values used for σ_w is the same as for wind generated sea in Table 5.6, while the γ value was chosen to 7 as proposed in Aas Jakobsen, COWI, and Johs. Holt (2016b, p.). The goodness of this value was not studied further. The approach for selecting the worst swell sea state for the characteristic response analysis will be discussed in Chapter 5.4.1.

$$S(\omega) = S_{wind\,sea}(\omega) + S_{swell}(\omega) \tag{5.2}$$

Both the linear and slowly-varying wave forces are calculated by integrating transfer functions over all components in the wave spectrum. As the integration is simplified to a finite sum, the resulting time history will repeat itself after a time duration expressed by Equation 5.3 (Faltinsen, 1990, p.148). In this expression t is the time duration, N is the number of frequency components, ω_{max} and ω_{min} is the largest and smallest wave frequency in the wave spectrum, while $\Delta\omega$ is the frequency increment. The number of frequency components must therefor be large enough such that the time series is unique

during the whole simulation time. It is also essential to use a large number of frequency components to ensure that the frequency increment is a "small fraction" of the important eigenperiods (Faltinsen, 1990, p.159). Both the linear and slowly-varying drift time histories are calculated choosing N such that the time histories do not repeat itself during three hour, which is within the time period where the environmental parameters for a short term sea state is assumed to be constant (Myrhaug, 2007, p.2).

$$t = \frac{2 \cdot \pi}{\Delta \omega} = \frac{2 \cdot \pi \cdot N}{\omega_{max} - \omega_{min}} \tag{5.3}$$

5.2.4 Phase difference used for wave load correlation study

The bridge studied in thesis is a relatively large structure consisting of several pontoons exposed to waves. The wave forces acting on these individual parts will in general have different phase angles. This could be an important aspect to account for, as it may result in reduction or amplification of the response (Naess & Moan, 2012, p.183). The phase difference is accounted for in some of the wave conditions using the expression in Equation 5.4, which is similar to the expression in Naess and Moan (2012, p.181) for a regular wave. In Equation 5.4 θ_i is the phase angle, k_i is the wave number, β is the wave heading and x and y are the x- and y-coordinates of the pontoon respectively. The subscript i designates the wave component.

$$\theta_i = k_i \cdot x \cdot \cos(\beta) + k_i \cdot y \cdot \sin(\beta) \tag{5.4}$$

The phase angle in Equation 5.4 is calculated for each pontoon and subtracted from the random phase angle and $\omega \cdot t$ in the expressions for the linear and second order wave forces. This is similar to how short crested sea may be modelled (Faltinsen, 1990, p.29) except that only one wave heading is included per analysis. Using this approach Equation 5.4 will in general produce different wave force time histories for all the pontoons, which makes it difficult to verify that the effect of using the phase angles is correct. Therefor the method was investigated by calculating the excitation force in sway direction at two pontoons caused by regular waves with the properties given in Table 5.7. In this table T is the wave period, λ the wave length and β the wave heading. The wave heading refer to the definition in Figure 5.2.

The two pontoons was positioned such when the wave reaches pontoon 18 in Figure 5.11 the distance to pontoon 16 is $\frac{\lambda}{2}$, where λ is the wave length. With this approach the wave forces at pontoon 16 should be shifted 180° relative to pontoon 18, which is confirmed by

Table 5.7: Definition of the regular waves used to check the effect of phase angle.

Parameter	Value
T	6[s]
λ	56.21 [m]
β	315°

the result in Figure 5.11. An illustration of this analysis is presented in Appendix J.
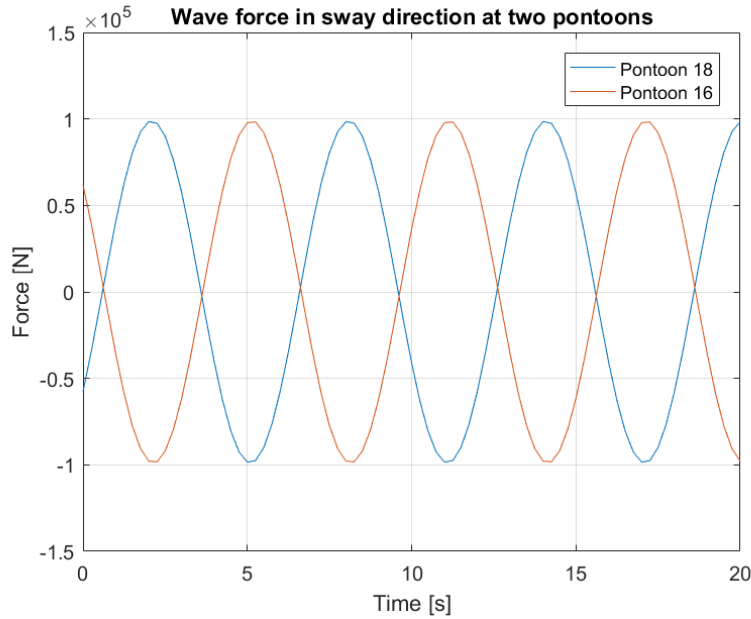
Figure 5.11: Illustration of the resulting wave force in sway direction at two pontoons caused by regular waves. The waves will hit pontoon 18 before pontoon 16.

5.3 Modelling wind loads

Wind loads is calculated in USFOS by means of the instantaneous wind speed. As an example is the drag force component F_d established from Equation 5.5 where C_D is the drag coefficient, v_r the relative velocity between the structure and wind field and d is the projected diameter of the component (Jia, 2014, p.13). A simple check of this formula, in addition to the definition of the projected diameter d relative to the incoming wind, is presented in Appendix D for a horizontally aligned beam element. The mean wind field can be specified directly in USFOS, while fluctuating wind can be given as input when the USFOS command 'WindField'" is used (USFOS, 2016, p.6.3-144). In this thesis both the mean and fluctuating part is established using the program WindSim, which generates mean and stochastic wind velocities at user defined points (Aas-Jakobsen, 2015, p.11).

$$F_d = \frac{1}{2} \cdot \rho \cdot C_D \cdot v_r \cdot |v_r| \cdot d \tag{5.5}$$

Table 5.8 presents the coordinates and number of nodes which defines the wind grid used in the simulations, i.e. the location of the points where the wind velocity is calculated. These coordinates refer to the global axis and the space corresponding to these values is illustrated in Figure 5.12. Outside this space the wind velocity will be fully correlated with the nearest point in the grid (Moe, 2016, p.77). This means that the north part will experience the same wind history as at the middle of the bridge. Alternatively one could have used points along the whole bridge, but this approach may require a large amount of points in the wind grid. But due to memory restrictions of the computer it was not able run with more than 240 nodes in the grid. It was therefor focused on getting a good representation of the south part as this region has a larger wind exposed area.

Table 5.8: Definition of the grid where the stochastic wind speed is calculated, referring to the global axis.

Coordinate	Maximum	Minimum	Number of nodes
x	-5000	-5000	1
y	-2222	0	80
z	30	227	3
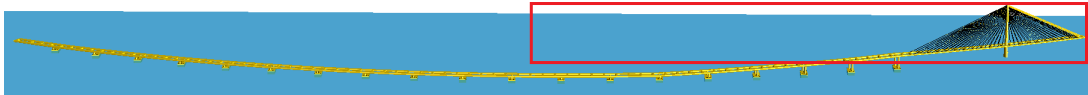
Figure 5.12: Region used to calculate the where the stochastic wind. A similar figure is found in Moe (2016).

According to Norsk Standard (2005, National Annex, p.12) should the mean wind velocity component $U_m(z)$ be modelled by Equation 5.6. In this expression $c_r(z)$ and $c_o(z)$ describes the variation of the mean wind speed due to the terrain, while v_b is the basic wind speed.

$$U_m(z) = c_r(z) \cdot c_o(z) \cdot v_b \tag{5.6}$$

Since Equation 5.6 is not an option in WindSim (Aas-Jakobsen, 2015, p.13) the mean wind speed was assumed to follow a shape defined by Equation 5.7. In this formulation α is a shape parameter and U_{ref} is a reference value for the wind speed at a reference height of z_{ref} (Aas-Jakobsen, 2015, p.13). The parameters used for this equation is presented in the rightmost column in Table 5.9 and are the same as used by Moe (2016). The reference velocity is taken as the 10-minutes mean wind speed and calculated using Equation 5.6

with $c_r(z)$ and $c_o(z)$ as described in Norsk Standard (2005, Ch. 4.3) and a 100-year basic wind speed of 27 [m/s], as proposed in Aas-Jakobsen et al. (2016, p. A3).

$$U_m(z) = U_{ref} \cdot \left(\frac{z}{z_{ref}} \right)^\alpha \tag{5.7}$$

Figure 5.13 illustrates the difference in mean wind speed using the equation proposed by Norsk Standard (2005) and the one used in this thesis. This figure shows that the two approaches are almost the same below a vertical position of 100 meters, while the WindSim profile gives somewhat larger values above this position. From this it seems to be safe to use Equation 5.7 in the wind analysis. The values used for the parameters in the two approaches are as presented in Table 5.9.

Table 5.9: Parameters used in Figure 5.13

Norsk Standard (2005), Equation 5.6	This thesis, Equation 5.7
$c_r(z) = 0.17 \cdot \ln \frac{z}{0.01}$	$U_{ref} = 31.7$ [m/s]
$c_o(z) = 1$	$z_{ref} = 10$ [m]
$v_b = 27$ [m/s]	$\alpha = 0.128$
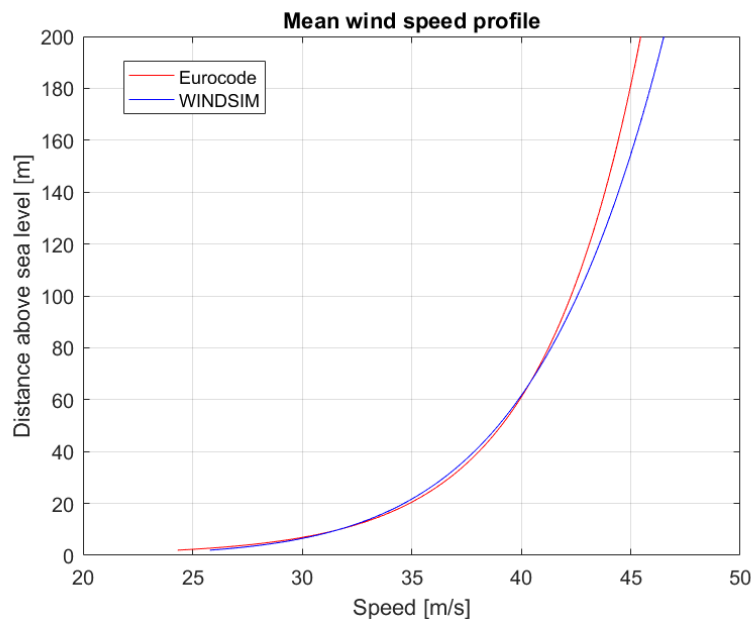
Figure 5.13: Mean wind speed profile

The fluctuating part of the wind speed is defined by the power spectrum expressed by Equation 5.8 on non-dimensional form (Statens vegvesen, 2015, p.63). In this expression $\bar{f}_i$ is a function of the so called turbulence length scale, mean wind speed and the frequency component f of the turbulent wind (Strømmen, 2010, p.61-62). For definition of the turbulence length scale, see e.g. Strømmen (2010, p.61-62) and Statens vegvesen (2015,

p.62). Further, S_i is the point spectrum, σ_i the standard deviation and A_i are parameters defined in Table 5.10. The subscript i designates the direction of the wind speed in x-, y- and z-axis.

$$\frac{f \cdot S_i}{\sigma_i^2} = \frac{A_i \cdot \bar{f}_i}{(1 + 1.5 \cdot A_i \cdot \bar{f}_i)^{5/3}} \tag{5.8}$$

The coherence $Coh(f, \Delta s)$ is defined by Equation 5.9 where f is still the turbulent wind frequency, $U_m(z)$ is the mean wind component and Δs the distance between two points. c_i are decay factors chosen based on the information in (Statens vegvesen, 2015, p.63) and presented in Table 5.10. Further, the length of the wind simulation in WindSim was specified to 4300 seconds, and with this information the program divides the point spectrum into frequency segments with maximum and minimum frequency components of 5.00010 and 0.00010 respectively. This means that the wind field should be unique during this length. It should be noted that 4300 is chosen as the first 700 seconds in the analysis is disregarded due to the initialisation phase, see Chapter 7, and transient effects. When these are subtracted the resulting length of the wind simulation is 3600 seconds, i.e. one hour. Another point is that the 10-minute mean wind speed is used to generate these one hour simulations as this is the mean wind which is specified in Norsk Standard (2005). In general one should probably use a 1-hour mean wind speed for simulations with this length.

$$\sqrt{Coh(f, \Delta s)} = \exp\left[\frac{c_i \cdot f \cdot \Delta s}{U_m(z)}\right] \tag{5.9}$$

Table 5.10: A_i values used in the point spectrum and decay factors c_i.

	Value
A_u	6.8
A_v	9.4
A_w	9.4
c_u	0
c_v	6.5
c_w	3

The wind load coefficients that are used when studying the global bridge response caused by wind are presented in Table 5.11. The drag coefficients for the bridge girder is established using information presented in A. Larsen (1998) for different bridge girder cross sections and modified to account for the effect of having two box girders in parallel. When two box girders are placed in parallel the resulting drag force is affected by the gap between these girders Chen, Li, and Hu (2014). In this thesis the effect is accounted for by

assuming that the windward box girder will experience a larger resulting drag force than the leeward one. But in order to use the same drag coefficient for both box girders the total drag coefficient is taken as the mean value leeward and windward side. For the other structural parts in Table 5.11 the drag coefficients are based on the information in Norsk Standard (2005, p.72). The lift and moment coefficients are chosen based on A. Larsen (1998, Table 1,p. 75). Only the coefficients for the main components are presented in Table 5.11, but it should be noted that the cross beams connecting the two box girders is assumed to be sheltered and therefor assigned with a small drag coefficient in the bridge model.

Table 5.11: Wind load coefficients.

Structural parts	Coefficients
Bridge girder	$C_D = 0.55$
	$C_L = 0.122$
	$C_M = 0.051$
Cables	$C_D = 0.84$
Columns	$C_D = 0.77$
Tower	$C_D = 0.80$

5.4 Environmental conditions that are studied

5.4.1 Wave loading

The following four environmental conditions was studied in connection with wave loading:

1. Wave condition 1: Fully correlated wave loads due to wind generated waves from west.

2. Wave condition 2: Fully uncorrelated wave force in heave direction due to wind generated waves from west.

3. Wave condition 3: Fully correlated wave loads due to wind generated waves from north-west.

4. Wave condition 4: Wind generated waves from north-west with different phase angles for the wave load acting on all pontoons, accounting for the relative position in space.

As presented in Chapter 5.2 the two wave directions describing waves coming from west and north-west was chosen since these has the largest significant wave heights, which may

result in the largest wave forces. It should also be noted that COWI et al. (2016, Ch.7) concluded that these directions gave the worst conditions with regard to design of the bridge girder. According the contour method one should in principle run analysis with different combinations of the environmental parameters near the peak of the contour line. As an example Baarholm et al. (2010) did run model tests for five points along the contour line in order to estimate the worst sea state. In addition to checking different combinations of the significant wave height H_s and peak period T_p it could also be important to study different wave headings. But after consulting with supervisor Professor Jørgen Amdahl it was decided to only run analysis for the two mentioned wave directions, with the corresponding H_s and T_p values in Table 5.1 in Chapter 5.1. Another point is that the peak at 6 seconds in the wave spectrum is in a region with motions dominated by roll and horizontal displacement of the bridge girder. By comparing the spectrum in Figure 5.10 with the eigenmodes of the bridge it is also evident that the spectrum fall in a region with motions dominated by vertical motion, rotation about the bridge axis and sway motion. These can be exited by waves and it was therefor decided to focus on the combination as presented in Table 5.1.

The length of the analysis used during the four condition is 1000 seconds, or approximately 17 minutes. This was used to limit the simulation time, as the conditions are mainly used to find the worst condition due to wave loading. The worst out of the mentioned wave conditions is chosen as the condition that is used to establish the characteristic wave response. The effect from swell is also included in the characteristic response calculations. Therefor, a separate study was conducted in order to determine the significant wave height and peak period that should be used to describe the effect from swells. The reason why such a study was performed for swell and not for wind generated waves, is due to the range of the peak period for the swell sea. The peak period with the largest H_s value ranges from 12 to 16 seconds, for swell sea. Since these periods could excite eigenmodes with relatively large eigenperiods it is not easy to know in forehand which combination that is the worst. With this in mind it was decided to investigate which of the combinations that gave the most significant response. It should also be noted that the same set of random phase angles are used in all of the four wave conditions, and the effect from slowly-varying drift forces are also included in these analysis.

The second and fourth wave condition are chosen in order to study the effect of correlation between the wave loads acting of the different pontoons. In general the wave loads act the pontoons with different phases in the wave force components. As noted in Chapter 5.2.4 it could be important to account for the phase difference as it may result in amplification or cancellation effects (Naess & Moan, 2012, p.181). The second condition is one approach to study the phase difference where all non zero wave forces are fully correlated, except from the heave force. This condition was chosen based on the hypothesis that it could

give rise to large weak axis moments in the bridge girder. In the fourth wave condition the phase difference is dealt with by adding a separate phase angle described in Chapter 5.2. Using this formulation one may obtain a more realistic phase difference than in the second condition.

5.4.2   Wind loading

Wind is mainly studied together with waves and compared against pure wave simulations using a 100-year condition for both of these environmental loads. This is done in order to analyse the relative importance of these environmental loads and how the response of the bridge is affected by including both wind and waves. The investigation is performed by running two sets of 10 1-hour simulations, where the first set includes waves only, while in the second both wind and waves are accounted for. The same set of random phase angles is used for the wave loads in the two sets of 10 1-hour simulations. In these analysis the wind loads include both the mean and fluctuating components and are assumed coming from west. The same direction is used for the wave loads, which includes both wind generated was and swell together with the slowly-varying drift loads and are applied as fully correlated. An additional 1000 seconds analysis was run in order to get a sense of the bridge behaviour caused by pure wind loads, and to study the effect of the mean and fluctuating component.

5.5   Establishing characteristic response

The characteristic response due to wave loading are established based on 90 one hour simulations for the worst wave condition of the ones presented in Chapter 5.4.1. In general the length of each analysis should be three hours in order to make sure that the largest wave force which can occur with the given set of random phase angles is captured in the simulation. But due to problems with opening the result files for an analysis with this duration it was decided to use another approach. Thus the largest response during a three hour simulation is approximated by the largest response out of three one hour simulations, i.e. 30 3-hour simulations are approximated by 90 1-hour simulations. Furthermore, the resulting 30 maximums for each response component are fitted to a Gumbel distribution using the approach described in Chapter 2.3. The characteristic wave response is established using the 90% fractile in these distributions, see Chapter 2.3.

5.6 Modelling filling of pontoon compartments

As noted in Chapter 3 should a floating bridge be able to service a 100-year environmental event in damaged condition. A relevant damage in connection with ship collision is flooded pontoons compartments, which may inflict with the stiffness properties of the pontoon due to the reduction in water plane area (COWI et al., 2016, p.80). As the bridge is equipped with a navigational channel between axis 2 and 3, see Chapter 4.1, a situation where a ship collides with the pontoon at axis 3 is possible. According to Sha and Amdahl (2016b, p.5) may an impact against a pontoon result in large local damage. As a result of this it may be relevant to study this damaged condition.

The effect of pontoon flooding is modelled as an applied force which is equal to the weight of sea water in three of the compartments as illustrated in Figure 5.14. The compartments with a red cross are assumed flooded. The inertia effects of the water mass captured in the compartments will not be including using this approach, but as the mass of the pontoon it self is approximately 88% larger than this water mass the simplification is expected to give only minor errors. It is assumed that the compartments are filled up to the free surface level in intact condition. The total force applied in this damaged condition is 1.69E+07 [N].
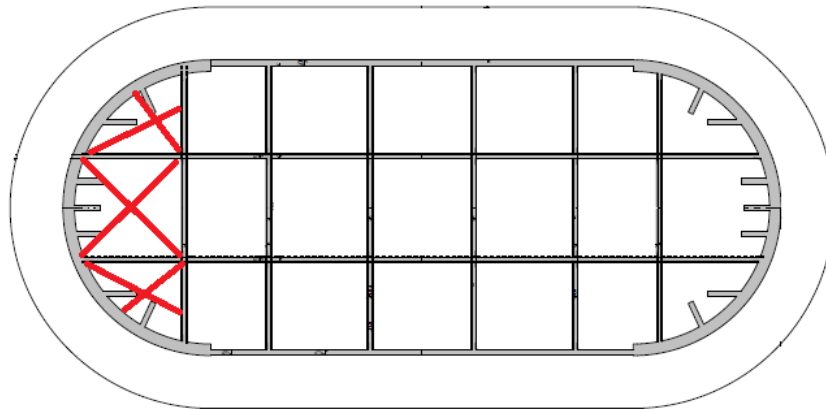
Figure 5.14: Illustration of the compartments that are assumed filled with water due to ship impact. This figure is a modification of the pontoons as presented in Aas Jakobsen, COWI, and Johs. Holt (2016a).

Chapter 6

Ship collision modelling and collision scenarios

6.1 How ship impact is applied in USFOS

The loads from the ship impact in the global analysis is applied to the structure using a methodology similar to the simple single degree of freedom system in Section 2.5. The applied impact is represented by the initial kinetic energy of the vessel $E_{k,i}$, defined as a point mass with an initial speed in the USFOS model. This mass is connected to the bridge through two springs where the first spring is a non-linear spring element assigned with the same stiffness properties as the crushing strength, i.e. the force-deformation curve, of the vessel. This is represented in Figure 6.1 for bridge girder impact, where the mass is applied at the leftmost end of the first spring. When the ship mass pushes against the force-deformation spring this element will deform, which produces a time varying impact load that is transferred to the bridge girder. In this way the initial kinetic energy is converted into deformation of the vessel and bridge motions, i.e. deformation energy in the ship E_s and kinetic energy of the bridge $E_{k,b}$. Mathematically one could express the amount of energy transferred to bridge girder motions by Equation 6.1 right after the impact. It should be noted that this description assumes strength design of the bridge, i.e. assuming all deformations are taken by the vessel. If sheared energy design is aimed for the damage of the bridge should also be modelled correctly. Another point is that the local behaviour at the impacted area might not be correct with this approach, since the load is applied at a single node. In a real collision this will be distributed over a larger area. The global behaviour should on the other hand be correctly represented using this approach.
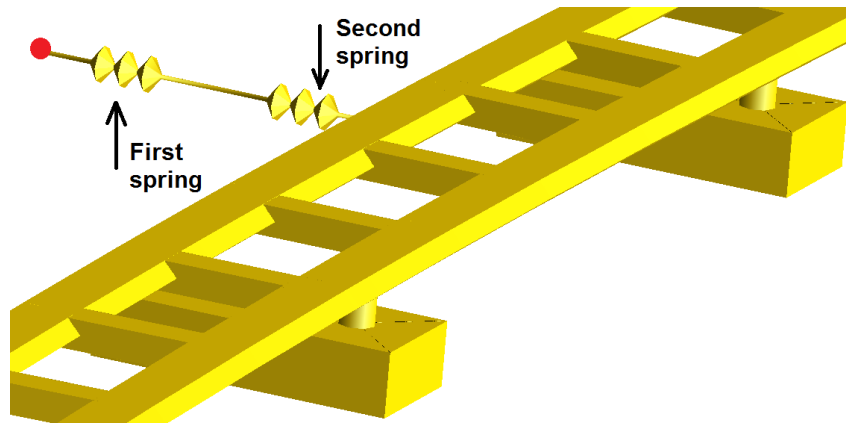
Figure 6.1: Illustration of how collision is applied in the bridge model.

$$E_{k,b} = E_{k,i} - E_{k,s} - E_s \tag{6.1}$$

The second spring in Figure 6.1 is used to transfer collision forces from the ship to the bridge as long as the relative speed of the vessel is larger that the bridge's speed. It is important to include this second spring to obtain a correct unloading behaviour of the force-deformation curve. At the moment when the bridge has a larger speed relative to the ship mass the second spring detaches the colliding objects, and the first spring is unloaded. This behaviour is obtained using a spring element with large stiffness in compression and almost no stiffness in tension. It was experienced unnaturally large peaks in the axial force for spring, if the stiffness in compression was chosen too large. Therefor the stiffness had to be adjusted to prevent this behaviour.

6.2 Characteristics of the colliding vessel

The vessel used in the collision analysis is the cruise ship "Color Magic" shown in Figure 6.2 with the main properties as presented in Table 6.1 (Shipping Publications, 2017).

Table 6.1: Main properties of the cruise ship.

	Value	Unit
Length between perpendiculars	202.66	[m]
Breadth moulded	35	[m]
Depth moulded	15.20	[m]
Draught	6.80	[m]
Dead weight	6.13E+06	[kg]
Speed	22	[kn]

Figure 6.2: The cruise vessel "Color Magic" (Marine Traffic, 2017).

The force-deformation curves for this vessel was received from Postdoc Yanyan Sha and are plotted in Figure 6.3. These are established by crushing the ship against a rigid vertical wall with constant speed. This is important to note as using these curves will imply a strength design of the bridge, i.e. one assumes that the bridge components are strong enough to resist and crush the bulb and forecastle. Further, it is evident from this figure that the forecastle deforms approximately 6 meters before the bulb comes in contact with the vertical wall. This illustrates the distance between the tip of the forecastle and the bulb. One should also note that the ship is ice strengthened, which affects the deformation resistance of this vessel. With this in mind it could represent a worst case collision scenario.
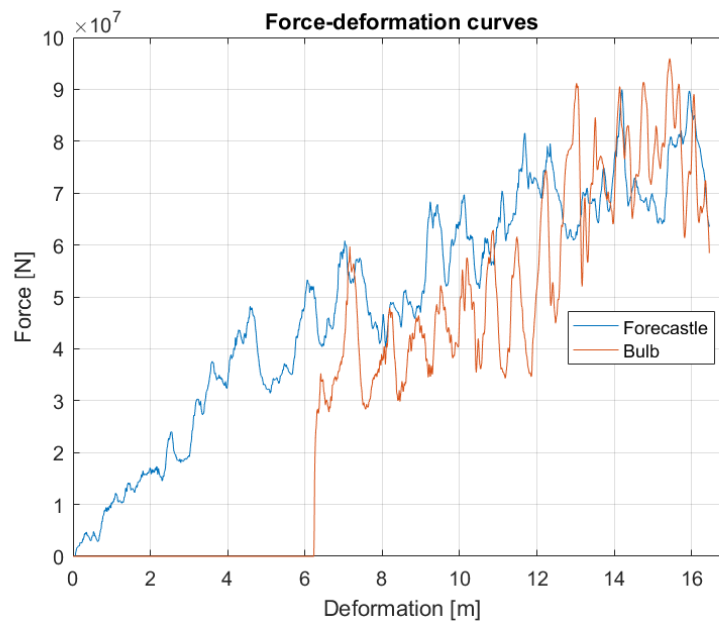
Figure 6.3: Force-deformation curves for "Color Magic".

The total ship mass is estimated assuming a block coefficient C_B of 0.64, based on data as presented by Levander (2012). For head on collision Norsk Standard (2006a, Appendix C,p.51) recommends using an added mass of 10% of the total mass of the ship, which is also within the range proposed by Faltinsen (1990, p.160) for a tank ship. Using these properties together with the main dimensions in Table 6.1 the total ship mass becomes 34.80E+06 [kg], including added mass.

6.3 Collision scenarios studied

Two different collision scenarios is studied in this thesis. The first is collision with the pontoon and column at west side of axis 3, while the second is impact with the west side bridge girder between axis 10 and 11. For definition of the different bridge axis see Figure 4.2b in Chapter 4.1. For both collision scenarios an initial impact energy of 1000 [MJ] is used as base case, which is larger than the design impact energy defined in COWI et al. (2016). This is on the other hand used since the main interest in this thesis is to investigate how the bridge responds to large impact loads. As a consequence this will be a more rare event than the 10 000-year event the bridge should be able to resist (Statens vegvesen, 2015, p.168).

6.3.1 Collision scenario 1: Pontoon-column impact at axis 3

In this collision scenario the ship impact is applied at axis 3 and acts both on the pontoon and column. Since the bridge is equipped with a navigation channel at this location, an impact at this axis is possible. An illustration of how this is modelled is presented in Figure 6.4. It is assumed that the collision force from the bulb will act at the still water level. Further, the forecastle is located 16 meters above the bulb and will hit the column at this level. As illustrated in this figure, the two non-linear springs are connected by vertical elements with a red circle in the middle. The red circle illustrates where the ship mass is positioned, which are connected to the two springs through vertical rigid beams. This is done in order to make the two spring act as a single body and move with the same speed.

For this scenario the bulb should deform 5.34 meters, after hitting the end of the pontoon, before the forecastle comes in contact with the column. This as a result of the position difference of the pontoon and column, in addition to the relative distance between the tip of the forecastle and bulb. The two non-linear springs are connected by vertical rigid beams and will therefor have a synchronised deformation. This is solved by keeping the
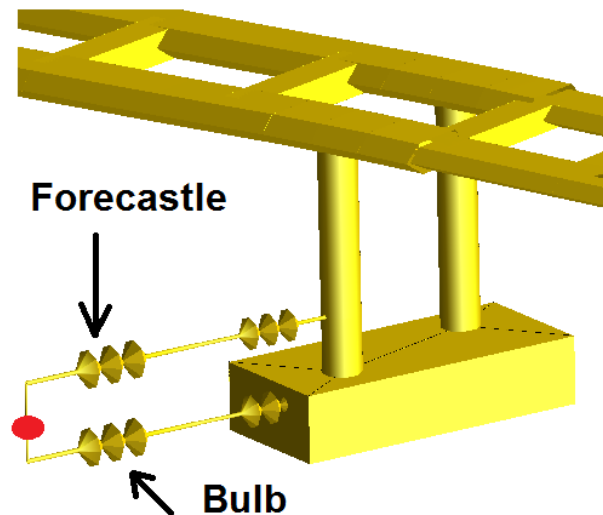
Figure 6.4: Arrangement of non-linear force-deformation springs for collision scenario 1.

force-deformation curve for the forecastle constant at a low force level the first 5.34 meters, illustrated in Figure 6.5a. In this way the bulb will take all the damage until the desired deformation. The force-deformation curves for the forecastle and bulb used in the collision scenario are presented in Figure 6.5. The curves are simplified somewhat compared to those in Figure 6.3, due to restrictions on the total numbers of points that can be used to define these curves in USFOS. These are also extrapolated for large indentations to ensure that the springs' deformations stay within the region with defined curve.

(a) Forecastle.

(b) Bulb.
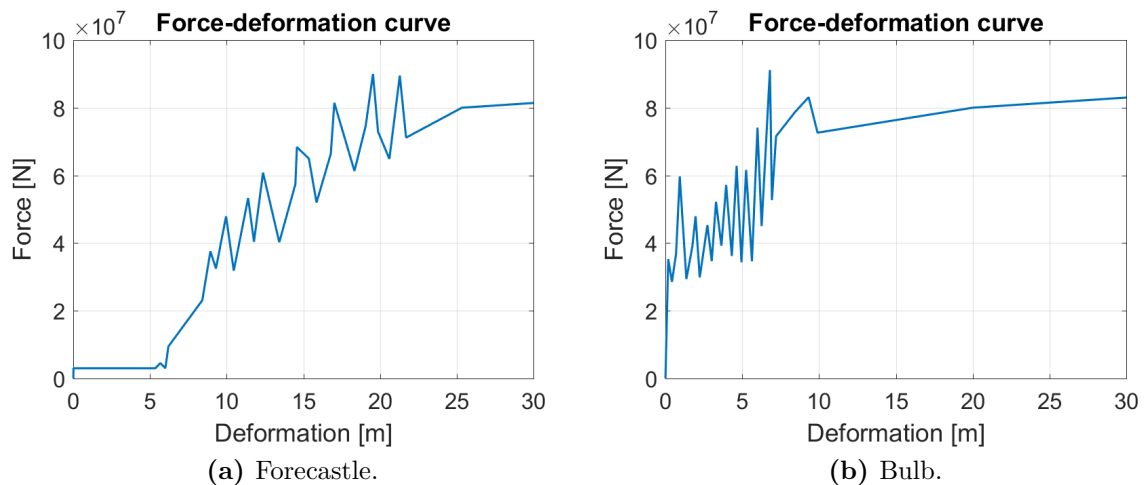
Figure 6.5: Simplified force-deformation curves for bulb and forecastle.

The additional impact energies that are studied for this collision scenario is presented in Table 6.2. It should be noted that the largest impact energy is 1000 [MJ], while for collision scenario 2 1500 [MJ] is the highest energy. The reason for the difference in the largest impact levels will be discussed in Chapter 9.6.

Table 6.2: Impact energies for collision scenario 1.

Impact energy, [MJ]	Vessel speed, [m/s]
300	4.15
600	6.11
1000	7.58

6.3.2   Collision scenario 2: Bridge girder impact

In this collision scenario the forecastle hits the west side box girder between axis 10 and 11. The forecastle is located 16 meters above the sea level, while the bottom and top of the box girder at this location is about 11 and 18 meters above the sea level. The collision scenario is therefor a possible event. Since it is only the forecastle that will deform in this case, the collision is modelled in the same way as in Figure 6.1 in Chapter 6.1. The impact levels that are studied for this collision event is presented in Table 6.3.

Table 6.3: Impact energies for collision scenario 2.

Impact energy, [MJ]	Vessel speed, [m/s]
300	4.15
1000	7.58
1500	9.28

Execution of time domain analysis

The total time domain analysis consists of three different parts, namely a static part for applying permanent loads and pretension, one initialization phase and a third part where the external loads are applied. These steps are used in all analysis for both environmental and ship collision loads, and the first two steps will be explained shortly in the following.

All permanent loads, together with the temperature for pretension of the stay cables, are applied gradually in the static where equilibrium is obtained for each time increment. In this phase additional heave stiffness was introduced as the analysis failed using only the buoyancy elements. This additional stiffness is assigned using one node spring elements, and removed when the dynamic analysis starts. The static analysis is run together with the USFOS command "HJHANSEN" such that the bridge coordinates are not updated when applying permanent loads, while the loads in the bridge are calculated correctly. This is done due to the fact that the bridge model is constructed using the drawings of the bridge design, which shows the structure with self weight applied. The bridge model is on the other hand modelled as if the self weight is not acting, but by using "HJHANSEN" one will get the correct initial configuration of the bridge. It should be noted that the whole bridge deflects downwards when the additional spring stiffness are removed in the beginning of the dynamic analysis. The deflection of the bridge girder at the pontoons varies between approximately 1 to 2.5 meters and could be an indication that the applied pontoon ballast is too large. To totally prevent deflection it was found that nodal mass of the pontoon at axis 3 had to be reduced below the self weight, which is not physical. It was therefor decided not to update this.

As noted, the additional heave stiffness is cut right after the permanent loads are applied. This causes large vertical oscillations of the bridge which is illustrated in Figure 7.1 at the middle of the bridge. Since these motions will affect the frequency domain solution

the first 350 seconds of the dynamic analysis are totally removed from the result files. This is done using the USFOS command "Ini_Time" which sets all displacements to zero at the moment specified time, and the shape of the bridge at this time is used as reference position for the rest of the analysis (USFOS, 2016, p.6.3-18). Another benefit with using this approach is that the vertical displacements caused by the permanent loads are removed from the analysis, such that the displacements only includes those induced by the environmental and ship collision loads. For all analysis with environmental loads these are applied at 350 seconds into the analysis, i.e. right after the initialization phase is finished. For the ship collision analysis a slightly different approach is used, where the initialization phase is reduced by using a time varying structural damping. For the first 50 seconds the structural damping is increased to a large value and then reduced to the correct value before the ship collision is applied at 53 seconds. The "Ini_Time" is still used, but the total simulation time is reduced.
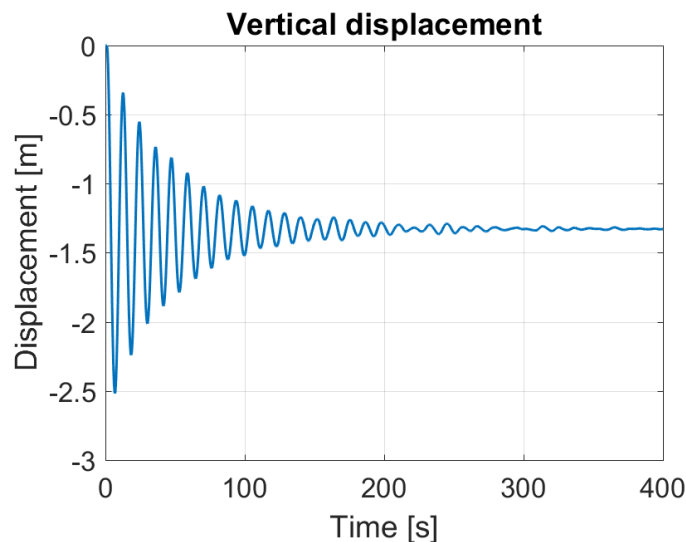
Figure 7.1: Vertical displacement at the middle of the bridge.

The time step used in the analysis is 0.01 seconds, this was decided after initial study of the bridge behaviour. These where run with fully correlated waves from west, and it was noted some drifting behaviour of the bridge girder where the whole girder displaces towards the west side. The effects appeared to reduce when lowering the time increment, but since the computational time increases by for low time increments it was decided not to lower it further. It should be noted that larger drifting was experienced for waves from north-west when accounting for the phase difference in the wave loads caused by the pontoon locations, which will be noted in Chapter 8.8.4. The same time increment is used in the ship collision analysis except for the first seconds of the simulation where a lower increment is used in order to reproduce the force-deformation curve properly.

Chapter 8

Results

The results from the time domain analysis of the bridge response due to environmental and ship collision loads will be presented in this chapter. Some of the results will refer to the different bridge axes as defined in Figure 4.2 in Chapter 4.1. Terms like "west side girder", "east side girder" and "box girders" will be used frequently, and are also defined in Chapter 4.1. Furthermore, the induced loads in the bridge refers to the local coordinate system of the individual components. With reference to the Figure 4.4 in Chapter 4.2.1 for the box girders, the term "weak axis moment" will be used for bending about the local y-axis, while "strong axis moment" is bending about the local z-axis. For the tower "weak axis moment" is bending about the local z-axis and "strong axis moment" about local y-axis, with the local reference system defined in Figure 4.5 in Chapter 4.2.2. The motions of the bridge girder refers on the other hand to the global coordinate system where horizontal displacement will be used for motions in global x-axis, while vertical displacement is in global z-axis. For definition of the global reference system see Figure 4.1 in Chapter 4.1. The term roll will be used for the bridge girder to describe twisting motion, and is defined similarly as the local motions of the pontoon, see Figure 4.3 in Chapter 4.1.

The stress components from bending moment about the strong and weak axis in the bridge girder are calculated at the points where the individual values are largest. These points are illustrated in Figure 8.1 for the east side girder where the strong axis bending stress is calculated at "Bottom plate" and the weak axis bending stress at "Right side" in this figure. For the west side the position of the weak axis stress component will be the same, while the strong axis stress is calculated on the left side. Further, many of the results will be presented in terms of the absolute maximum and minimum values. This means the largest positive and most negative response that occurs at a given point in the bridge during the simulations. It will also be presented figures which shows the distribution of

the absolute maximum and minimum values of a response component along the bridge girder. This is done in order to compare with results in COWI et al. (2016), but also as they may give an impression of how the bridge girder responds at different locations. These plots will be explained in Chapter 8.3.4.
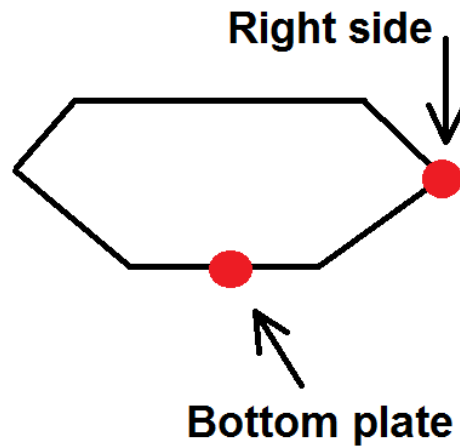
Figure 8.1: Locations where the individual stress components from weak and strong axis moment is calculated for the east side box girder.

8.1 Eigenvalue analysis

An eigenvalue analysis was performed in order to get an indication of how the bridge may respond to different types of loading. Table 8.1 presents 20 different eigenperiods together with a description of the dominating motions for the different mode shapes. These motions refers to the definition in the introduction to this chapter, and if the eigenmode is described by more than one motion the first of these are the most dominating. It should also be noted that the eigenmodes in this table are chosen as they are in the region of the applied loads studied in this thesis. The first 15 is expected to be most important for drift loads, wind, swell and collision, while mode 34 to 38 is in the region of wind generated waves with a peak period of 6 seconds. The largest difference in eigenperiod for the results in Table 8.1 compared with the initial version of the model received from Postdoc Yanyan Sha, occurs for the first mode. This period is nearly 5 seconds lower than for the initial version of the model. The term pendulum motion is used for mode 34, which means that the pontoons has a large component in surge making the pontoon and column behave as a pendulum. This behaviour was also noted by COWI et al. (2016), and an illustration will be given in Chapter 8.5.1.

The result in Table 8.1 shows that the horizontal motion, directed in global x-axis, domi-

Table 8.1: 20 eigenperiods calculated using USFOS

Mode	Motion	Eigenperiod [s]
Mode 1	Horizontal	65.07
Mode 2	Horizontal	37.02
Mode 3	Horizontal and roll	22.65
Mode 4	Horizontal and roll	20.87
Mode 5	Horizontal and roll	15.65
Mode 6	Roll	13.52
Mode 7	Roll	13.13
Mode 8	Horizontal and roll	11.59
Mode 9	Vertical and roll	11.38
Mode 10	Vertical	11.31
Mode 11	Vertical	11.27
Mode 12	Vertical	11.26
Mode 13	Vertical	11.25
Mode 14	Vertical	11.18
Mode 15	Vertical	11.11
Mode 34	Roll and horizontal	6.67
Mode 35	Pendulum and roll	6.33
Mode 36	Roll and horizontal	6.04
Mode 37	Roll and horizontal	5.88
Mode 38	Roll and horizontal	5.82

nates the largest eigenperiods. This is natural as the only stiffness comes from the bending of the bridge girder. The first four eigenmodes dominated by horizontal motion is presented in Figure 8.2 to 8.5, and are similar to the first modes in Aas Jakobsen, COWI, Global Maritim, and Johs. Holt (2016), but the corresponding periods are larger in this thesis. As an example has mode 1 a period of 56.72 seconds in Aas Jakobsen, COWI, Global Maritim, and Johs. Holt (2016) which is about 14.7% lower than in Table 8.1. Further, mode 10 to 15 are all vertical modes where the pontoons have more or less pure heave motion. The main difference between these vertical modes is the number of half waves in the vertical plane, where increasing number of half waves means larger stiffness contribution from the bridge girder. Thus the eigenperiod should be lower for the modes with more half waves, which is also observed. Mode 15 is illustrated in Figure 8.6. It is evident from Table 8.1 that many of the modes includes roll motion, which is also dominating the eigenmodes for periods in the range of 6 seconds as illustrated by mode 34 in Figure 8.7. This is important to note as the peak period of the wind generated waves is in this region.
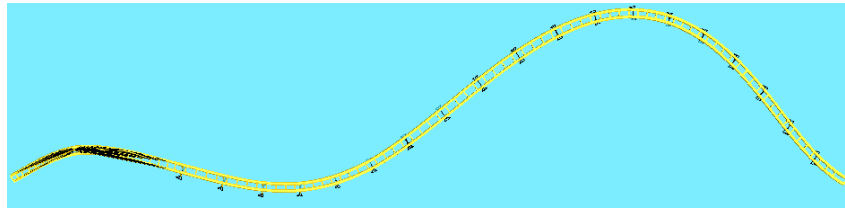
Figure 8.2: Mode 1, two half waves in the horizontal plane.
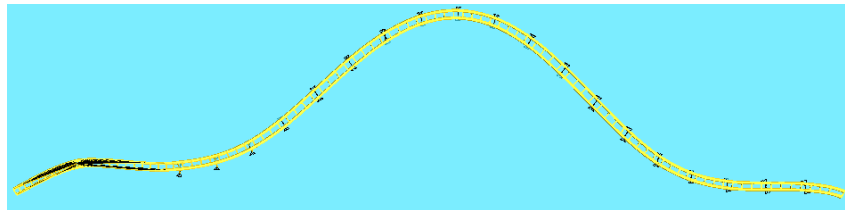
Figure 8.3: Mode 2, three half waves in the horizontal plane.
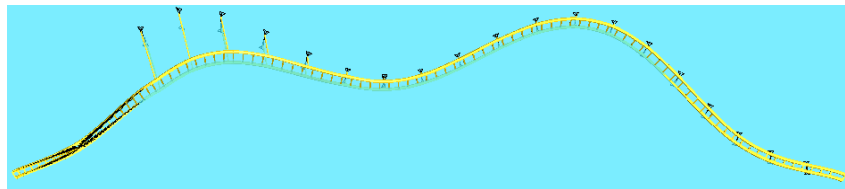
Figure 8.4: Mode 3, two half waves in the horizontal plane with node at the middle.
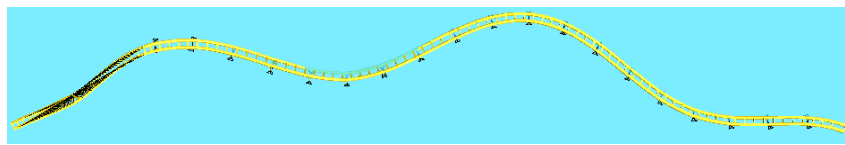
Figure 8.5: Mode 4, four half waves in the horizontal plane.

Figure 8.6: Mode 15, seven half waves in the vertical plane.
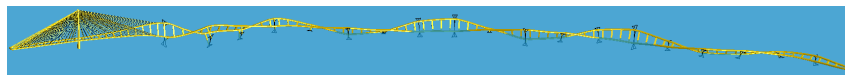
(a) From east side.
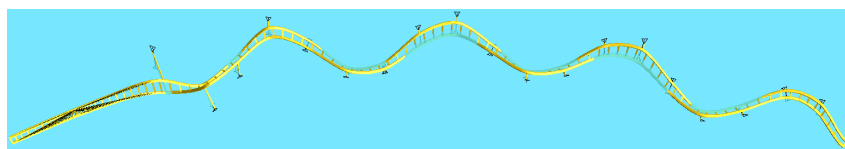
(b) From above.

Figure 8.7: Mode 34, viewed from the east side and above.

8.2 Check of the force time histories used in the wave analysis

To verify the time series of the linear wave loads Equation 2.26 in Chapter 2.3 was used to calculate the characteristic largest wave force component during a short term sea state. The standard deviation used in this expression is the integral over the response spectrum of the wave force, which is a function of the transfer function of the wave force and the sea spectrum (C. M. Larsen, 2014, p.173). The characteristic values calcultated in this Chapter are compared with results in COWI et al. (2016, p.76). COWI et al. (2016) presents their result graphically and the values given in Table 8.2 and 8.3 are therefor not exact, but are included to give an indication of the differences.

The characteristic largest response describes the value that is exceeded once out of N occurrences (Myrhaug, 2007, p.32), and could therefor be used to compare with the wave force time histories that are used as input to the analysis in USFOS. These quantities are calculated using a three hour sea state, and for a time series of similar length one would expect to see one value in each series that are close to the characteristic largest wave force components.

8.2.1 Wind generated waves from west

The characteristic largest wave forces are presented in Table 8.2, for the force components that are present for wind generated waves comes from west.

Table 8.2: Characteristic largest wave force during a short term sea state in the case of wind generated waves from north-west.

Force component	Characteristic wave force	Characteristic wave force from COWI et al. (2016,p.76)	Unit
Sway force	7.94	8	[MN]
Heave force	1.54	1.25	[MN]
Roll moment	86	75	[MNm]

The results presented in Table 8.2 shows that there are some differences in the characteristic largest wave loads in heave and roll motion obtained in this thesis and those presented in COWI et al. (2016). Where the values calculated in this thesis are 23% and 15% larger than those of COWI et al. (2016) for heave and roll respectively. This might indicate that there are some differences in the wave force transfer functions, which could have some impact on the result.

The time histories for the non-zero wave force components when waves comes from west are presented in Figure 8.8, 8.9 and 8.10. By comparing the largest value for each load component with those presented in Table 8.2, it is seen that the largest peaks are close to the characteristic wave forces for a short term sea state. From this the time series of the wave loads appears to behave as they are expected to, and the similarities with the results from COWI et al. (2016) gives further confidence to these wave loads.
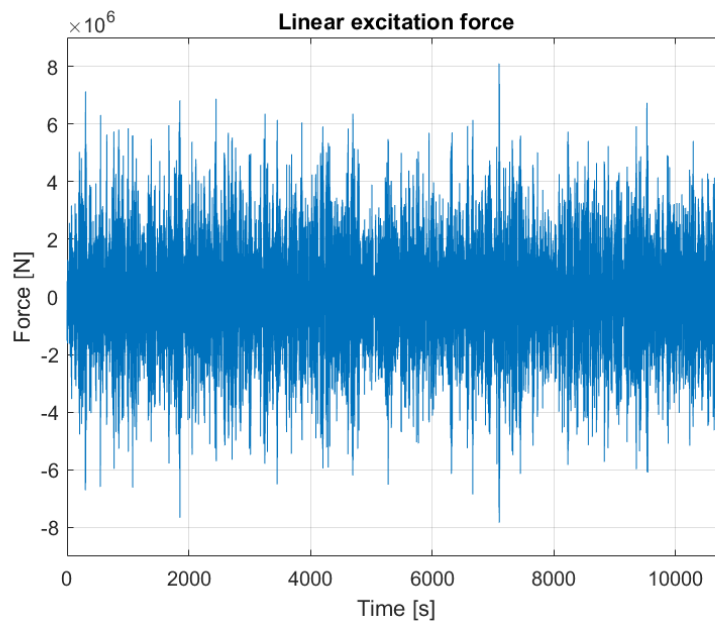
Figure 8.8: One time series of the linear excitation force in sway direction.
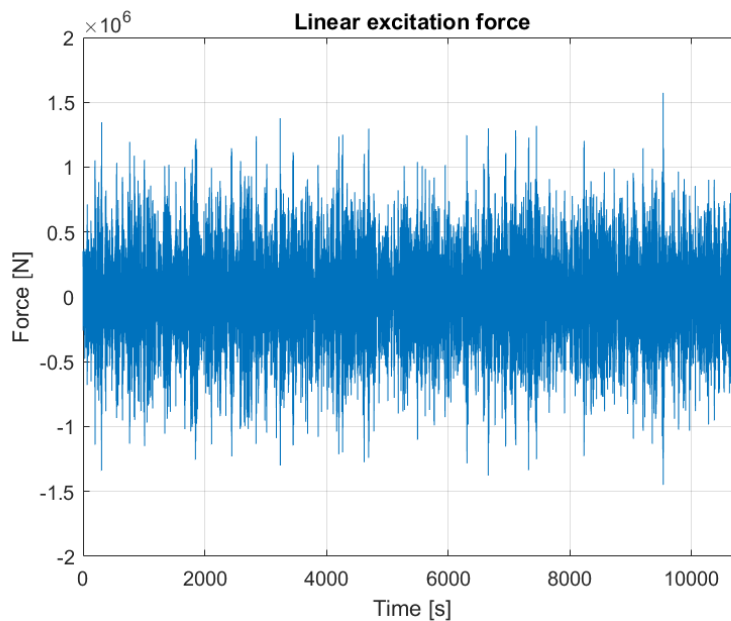
Figure 8.9: One time series of the linear excitation force in heave direction.

The effect of removing the high frequency components from the slowly-varying drift force
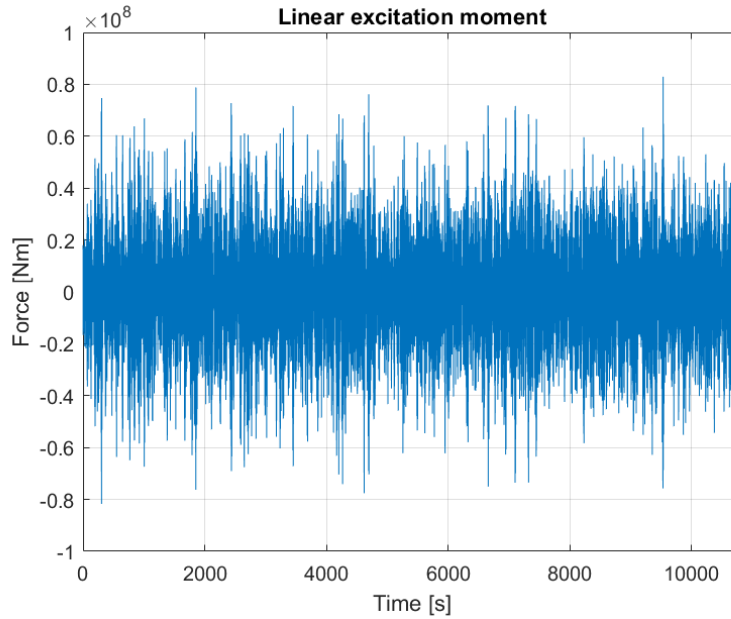
Figure 8.10: One time series of the linear excitation roll moment.

is illustrated in Figure 8.11. This figure presents only the 1000 seconds of the total slowly-varying time history, as the effect of using the filter is more easily seen within a shorter time range. This is also the time history that is used in wave condition 1. Figure 8.11 illustrates that the filtered time history of the slowly-varying drift force in sway direction includes periods above 50 seconds as expected, as the band pass is used for periods below this value. It could also be noted that the mean drift component is more evident in Figure 8.11b than in the original signal presented in Figure 8.11a. Another point is that largest peak for the slowly-varying drift force is approximately 5% of the largest value for the first 1000 seconds of the linear wave force in sway direction, which illustrates that these second order loads are relatively small.

8.2.2 Wind generated waves from north-west

Table 8.3 presents the characteristic largest wave force components with wind generated waves from north-west. Similarly as for waves from west the largest difference occurs for the excitation roll moment and and heave force, where the characteristic roll moment is approximately 26% larger than in COWI et al. (2016). This deviation is probably a result of the differences in the roll moment transfer function, as noted in Chapter. Consequently one may expect the time histories of the excitation roll moments used in these analysis are larger those of COWI et al. (2016).

The result in Table 8.3 corresponds well with the observed maximum peak values in time

(a) Original time history.

(b) Time history with band pass.
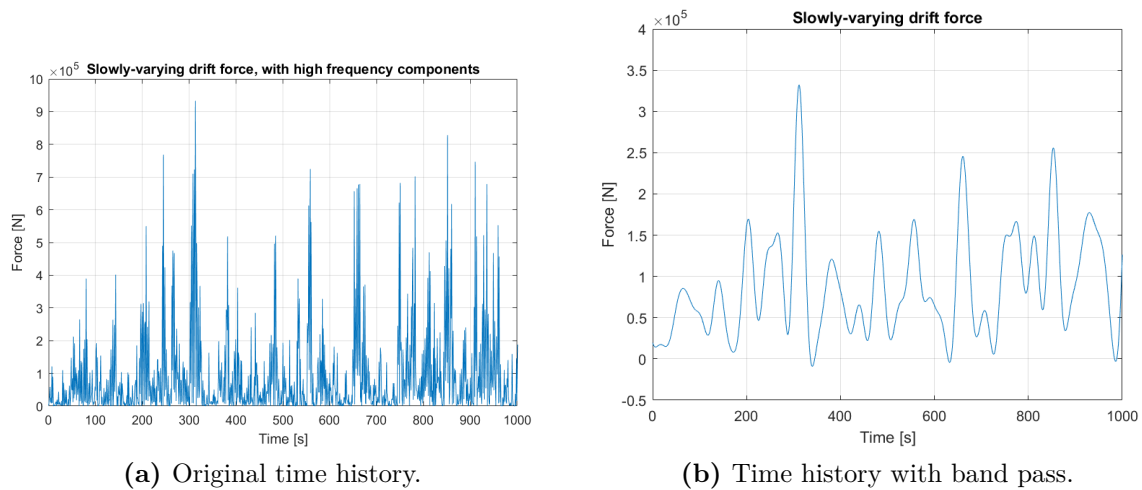
Figure 8.11: The effect of using a band pass on the slowly-varying drift signal.

Table 8.3: Characteristic largest wave loads during a short term sea state for wind generated waves from north-west.

Force component	Characteristic wave force	Characteristic wave force from COWI et al. (2016,p.76)	Unit
Sway force	6.62	7	[MN]
Surge force	6.45	7	[MN]
Heave force	1.35	1.10	[MN]
Roll moment	94.33	75	[MNm]
Pitch moment	49.25	47	[MNm]
Yaw moment	251.81	250	[MNm]

histories for these force components. This is illustrated both in Figure 8.12 and 8.13 which presents the three hour time histories for heave force and roll moment respectively. In Figure 8.12 the largest heave force is close to 1.25 [MN], while the largest peak roll moment in Figure 8.13 is approximately to 90 [MNm] which are close to the characteristic values. The time histories for the other force components has a similar tendency and are presented in Appendix F. As for waves from west one may therefor conclude that the linear wave loads appears to be calculated correctly.

The filtered time histories for the three slowly-varying drift components for waves coming from north-west are presented in Figure 8.14a, 8.14b and 8.15. In a similar manner as the case of waves from west, these figures illustrates that the force varies between a mean value. For the drift force in sway direction this mean force is positive, while the slowly-varying force in sway direction is negative. This is in accordance with the mean drift coefficients presented in Chapter 5.2. The corresponding three hour time series in surge and sway without using band pass is presented in Appendix F.
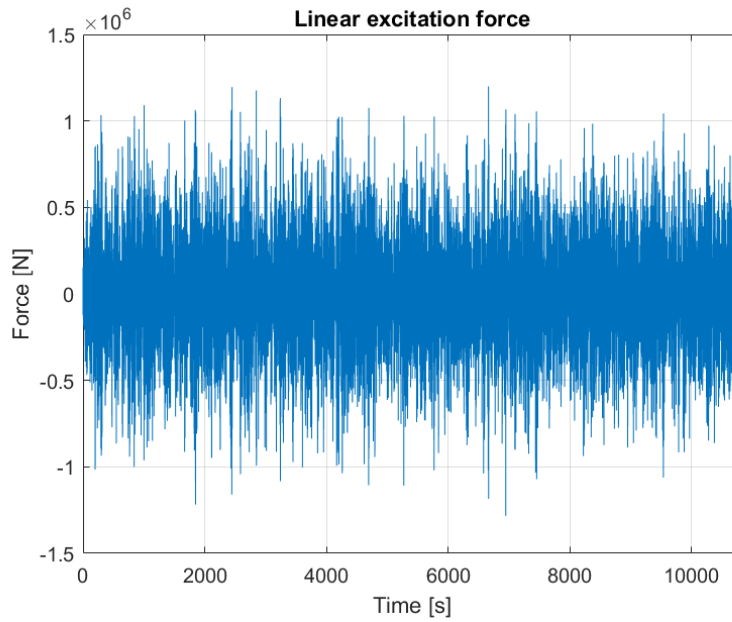
Figure 8.12: Linear excitation force in heave direction due to wind generated waves from north-west.
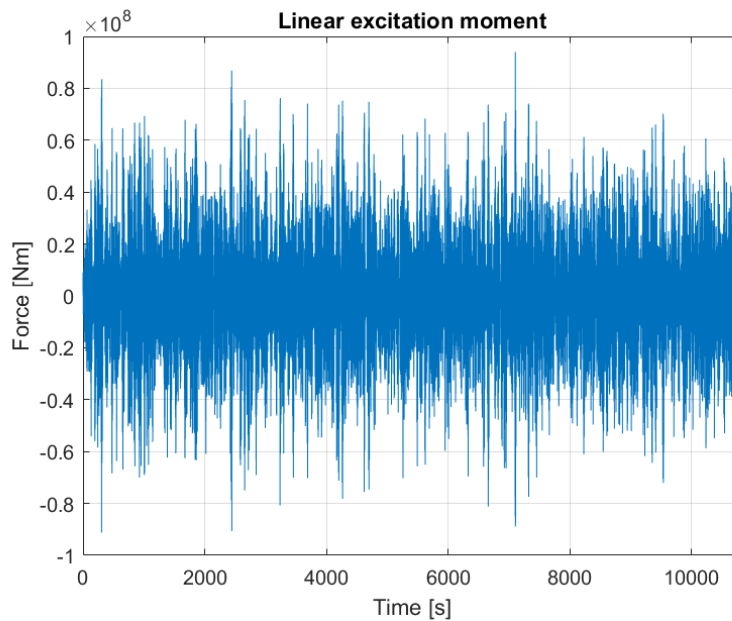
Figure 8.13: Linear excitation roll moment due to wind generated waves from north-west.

(a) Force in sway direction.

(b) Force in surge direction.
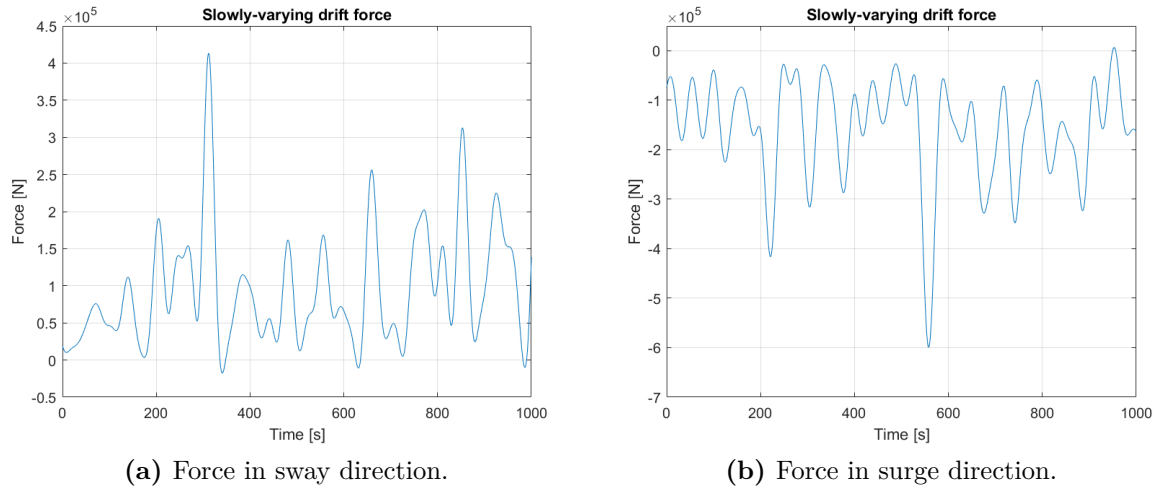
Figure 8.14: Slowly-varying drift forces in sway and surge direction for waves from north-west.
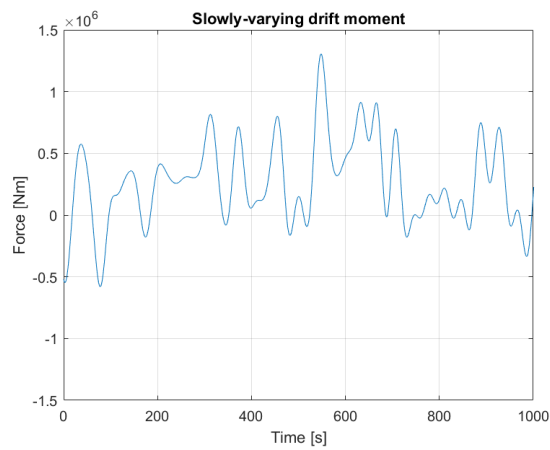
Figure 8.15: Slowly-varying drift yaw moment for waves from north-west.

8.3   Wave Condition 1

Most of the results presented for this wave condition is run with an early version of the bridge model, where the second moment of area for bending about weak and strong axis are lower than in the updated model used in the other analysis. Another point is that the torsional second moment of areas are different in the model used for this wave condition, and the pretension in the stay cables are also modelled more correctly in the updated version of the bridge model. This might introduce some uncertainty into whether the results are representative for the updated model. Therefor some of the most important results are rerun with the updated model and compared against those from the early version. This to investigate how the updates affects the behaviour of the bridge in curtain areas, as the over all behaviour is expected to be similar. It should be noted that wave condition 1 will be studied more in depth than the others, as this condition also was used to verify that the bridge model behaved similarly as previous work in (COWI et al., 2016) and (Aas Jakobsen, COWI, Global Maritim, & Johs. Holt, 2016).

When the waves comes from west they will only give rise to three force components acting on one singe pontoon due to the alignment in west-east direction (COWI et al., 2016, p.45). The only force components are therefor an excitation force in heave and sway direction in addition to an excitation roll moment, as presented in Chapter 8.2. It should be noted that the wave force time histories used in the present condition is the first 1000 seconds of the three hour history presented in the mentioned Chapter. This is important to be aware of as the largest peaks in these time histories do not occur during the first 1000 seconds. Furthermore, the wave forces are applied fully correlated, which is illustrated in Figure 8.16. It is also evident from this figure that the resulting wave forces consists of one component in sway direction and another one in heave direction. The excitation roll moment is not illustrated in this figure, but the effect of this component is included in the analysis.
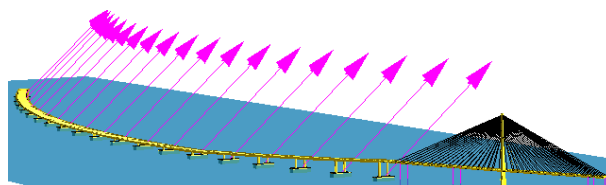
Figure 8.16: Applied wave forces acting on the pontoons at a given time instant.

8.3.1   Initial analysis of the bridge motions

In order to get a first impression of how the bridge responds due to extreme wave loads an animation of the bridge behaviour was studied. This was also done in order to decide which parts of the bridge, in addition to which response types, that should be studied more closely. A short review of the main findings of this investigation will be presented to give an idea of the bridge behaviour.

Even though the wave forces acting on each pontoon are applied as fully correlated, the resulting bridge motions do not reflecting this in a pronounced manner. Except for some tendencies of correlated motions in sway direction, the over all behaviour appears to be irregular with roll motions of the bridge girder being the dominating motion in the floating part of the bridge. A possible cause of this irregular behaviour could be that the geometry is different in the north and south side of the bridge. At the north part of the bridge the column height is relatively low and constant for all pontoons, while for the south part the column height increases towards the cable stayed part. This difference in geometry, in addition to the contribution from the stay cables, will result in different stiffness properties for the two parts. As a result this may force the into an irregular displacement pattern. The fact that the wave loads are only acting on the floating part, and not the whole bridge, could also be a source of the observed behaviour.

The vertical displacement at two points in the west and east girder is illustrated in Figure 8.17. According to this figure the vertical motions in the two box girders changes from being out of phase in some regions to being in phase at other points in time, which shows the rotating tendencies of the bridge girder. Another point is that both of the two largest peaks in Figure 8.17 occurs when the vertical motions in the two box girders appears to be in phase. These peaks are located at approximately 325 and 390 seconds, where the latter peak is the maximum vertical displacement that occurs for this wave condition. This might indicate that the largest displacements are more likely to occur when the vertical motions in the two girders are in phase.

In addition to the roll motion the floating part also shows some tendencies of slowly-varying motion in sway direction. Especially at the middle of the bridge. While at the transition between the cable stayed part and the floating bridge, from axis 3 to 7, the pontoons seems to have a displacement component also in surge direction. At first sight this was unexpected as for this condition no wave force is acting in this direction. This could though be an effect of the curvature of the bridge, and the position of the columns which are not located at the centre line of the pontoon at this part of the bridge. This could force the pontoon into a displacement pattern which deviates from the direction of the applied loads. The result of this is bending about weak axis caused by a combined
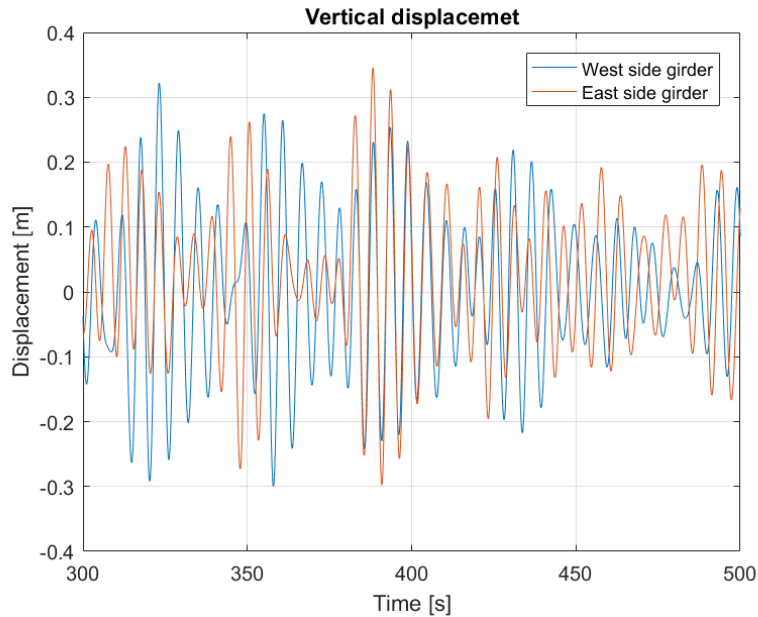
Figure 8.17: The vertical displacement in the east and west side girder between axis 5 and 6.

surge and sway motion, referred to as pendulum motion in COWI et al. (2016). In the cable stayed part the wave induced motions are relatively small, especially in the side span. The largest motion in this part of the bridge occurs in the main span, where the resulting displacement consist of a vertical component and a component that is transverse to the bridge girder.

8.3.2 Dominating motions and largest displacements and accelerations

The frequency domain solution of the vertical and horizontal displacement at two points on the bridge is presented in Figure 8.18. Axis 3 is located at the first pontoon from the navigation channel, while axis 11 is at the middle of the bridge. These are studied to get a better understanding of the bridge girder motions at different parts of the bridge and which eigenmodes that are impotent in connection with wave loads. It should be noted that the motions at axis 3 is affected by the cable stiffness, and should therefor be compared against the eigenvalues established for the early version of the USFOS model. These are presented in Appendix H for some of the relevant eigenmodes, together with a description of the motions at axis 3.

Figure 8.18a illustrates that the horizontal motion consist of a very wide range of frequencies. Nevertheless it appears that there are some frequencies that are more dominant than the others illustrated by the peaks in this figure. The largest peaks for the horizontal

(a) Horizontal displacement.　　　**(b)** Vertical displacement.
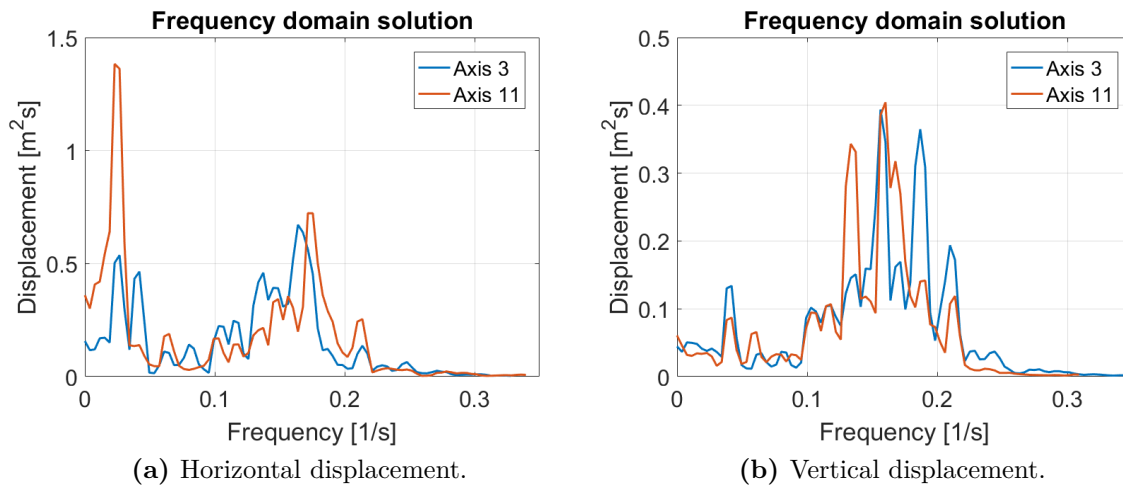
Figure 8.18: Frequency domain solution of the horizontal and vertical displacements at axis 3 and 11.

displacement are given in Table 8.4. The motions at axis 3 is dominated by frequencies in the range of $0.13 - 0.18$ [1/s] which corresponds to periods in the interval $5.6 - 7.7$ [s] with a peak at 6.10 seconds. The eigenmodes in this range consist mainly by a combined roll motion and horizontal displacement of the bridge girder in addition to pendulum motion due to a displacement component for the pontoon in surge direction. At middle of the bridge at axis 11 the largest peak according to Table 8.4 occurs for a period of 43 seconds. This is close to the second largest eigenperiod of this bridge and consist of three half waves in the horizontal plane with a peak at the middle of the bridge. The result could illustrate the contribution from slowly-varying drift loads.

Table 8.4: Frequencies with the largest peak value for the horizontal motion together with corresponding periods.

Location	Peak frequencies [1/s]	Periods [s]
Axis 3	0.164	6.10
Axis 11	0.0229	43.69

The largest peaks in the frequency domain solution of the vertical motion in Figure 8.18b are given in Table 8.5 together with the corresponding period. The single largest peak for both axis 3 and 11 is close to eigenmode 34, presented in Appendix H for the early version of the bridge model. This mode has an eigenperiod of 6.33 seconds and is mainly a pure roll motion. The second largest peak at axis 11 has a period of 7.49 seconds, which is close to eigenmode 30 in Appendix H having an eigenperiod of 7.70 seconds. This mode has both vertical and horizontal motions at the middle of the brigde. The second largest peak at axis 3 occurs for a frequency of 0.1869 [1/s], or a period of 5.35 seconds. Eigenmode 38 with a period of 5.37 seconds is the eigenmode in Appendix H that is nearest to this frequency consisting of roll motion at axis 3.

Table 8.5: Frequencies with the largest peak value for the vertical motion together with corresponding periods.

Location	Peak frequencies [1/s]	Periods [s]
Axis 3	0.1564	6.38
Axis 11	0.1602	6.24

The largest displacements and accelerations for the bridge girder is presented in Table 8.6 at the location with the most extreme absolute maximum and minimum values. Absolute maximum and minimum was defined at the introduction to Chapter 8. These results illustrates that the motions are relatively small for this wave condition, which may indicated that no eigenmode have large amplification. This appears to be in accordance with the frequency domain solution for these motions, as these showed a relatively large range of frequencies with significant contribution. Though some frequencies was more dominant than others.

Table 8.6: Largest displacements and accelerations for fully correlated waves from west.

	Maximum values Minimum values	Unit	Location
Vertical displacement	0.35 -0.30	[m] [m]	Between axis 5 and 6
Horizontal displacement	0.69 -0.52	[m] [m]	Between axis 12 and 13
Vertical acceleration	0.48 -0.45	[m/s^2] [m/s^2]	Between axis 6 and 7
Horizontal acceleration	0.45 -0.49	[m/s^2] [m/s^2]	At axis 13

By comparing the result in Table 8.6 with those reported in COWI et al. (2016, Ch.7.4) it is evident that the maximum horizontal and vertical displacement are nearly half of the 100 year values. This is as expected since the values in Table 8.5 is obtained from one single 1000 seconds analysis, while the 100-year values are established from 10 3-hour simulations (COWI et al., 2016, p.24). The largest vertical accelerations in Table 8.6 is on the other hand approximately 50% larger than the peak characteristic 100-year value in COWI et al. (2016, Ch.7.4). Another point is that all the maximum values for the displacements and accelerations occurs at different locations than in the mentioned report. As an example is the largest horizontal displacement in Table 8.6 located between axis 12 and 13, compared to axis 6 in COWI et al. (2016, Ch.7.4). It should be noted that the results in COWI et al. (2016, Ch.7.4) includes the effect of swell which are not included for the results in Table 8.6. One should also keep in mind that COWI et al. (2016) used a bridge girder consisting of a large single box girders, while the model used in this thesis has two parallel box girders. As a consequence the displacements and accelerations may

refer to different locations. The results in Table 8.6 is measured for one of the box girders, while COWI et al. (2016) may refer to the centre line of the bridge girder, i.e. at the neutral axis between the two box girders used in this thesis.

8.3.3   Largest wave induced loads in the bridge girder

The largest wave induced load effects in the bridge girder is presented in Table 8.7 at the location with the most extreme absolute maximum and minimum values for each of the six load components. The corresponding stresses are also included to give an impression of the severity of each component. In this connection a positive value for the axial and bending stresses means tension, while a negative value is compression. Furthermore, the definition of positive and negative moments follows the right hand rule (USFOS, 1999) such that a positive weak axis bending moment results in compression at the top and tension at the bottom of one box girder. Similarly will a positive strong axis moment give compression at the right edge of the box girder, and tension at the left edge, see Figure 8.1. The stresses from weak axis bending are calculated at the bottom of the box girder, while the strong axis bending stress at the right edge of the box girder as the stresses are largest at these points. For definition of the two locations it is referred to Figure 8.1, while weak and strong axis was also defined in the introduction to Chapter 8.

Table 8.7: Absolute maximum and minimum values at the position with the most extreme response for each force component occur.

Force component	Maximum value Minimum value	Stress	Location
Axial	33.43 [MN] −38.88 [MN]	20.26 [MPa] −23.58 [MPa]	Axis 4, west side girder
Transverse shear	4.04 [MN] −5.16 [MN]	6.08 [MPa] −7.76 [MPa]	Axis 21, east side girder
Vertical shear	8.70 [MN] −8.64 [MN]	15.70 [MPa] −15.60 [MPa]	Axis 5, east side girder
Weak axis bending	343.38 [MNm] −368.26 [MNm]	91.28 [MPa] −97.09 [MPa]	Axis 3, west side girder.
Strong axis bending	247.04 [MNm] −221.34 [MNm]	93 [MPa] −83.34 [MPa]	Support in north end, east side girder.
Torsion	237.42 [MNm] −246.49 [MNm]	63.09 [MPa] 65.50 [MPa]	Between axis 4 and 5, east side girder.

The result in Table 8.7 shows that the largest stresses are caused by the bending moments and torsion. By using the von Mieses yield criterion for the shear stresses (Irgens,

1999, p.21) it is evident that axial and shear stresses only utilize up to 6% of the yield capacity, when the three components are evaluated separately. The torsional stress gives approximately 25% utilization with regard to yielding, while both bending stresses gives utilizations in the range of 20% of the yield stress when the components are analysed individually. This shows that the three moment components appears to be the most important for yielding, and it was therefor decided to put the main focus on these for the rest of the thesis. In the next section some extra attention will be put on comparing the bending moments in addition to the torsional moment with the results presented by COWI et al. (2016).

8.3.4 Torsional and bending moments in the bridge girder

The absolute maximum and minimum values for the weak axis bending moment in the whole bridge girder is presented in Figure 8.19, where only the wave induced response is included. In these figures the south end is located at a position of 0 meters and the north end at 4500 meters. Furthermore, only results for one of the two box girder are presented in this figure as they have the same behaviour. Though one should note that the weak axis bending moment in the low bridge part are slightly larger for the east side girder, while at the transition region between axis 3 to 7 the response is larger in the the west side girder. Since the most extreme peak occurs in the west side girder the result for this box girder is presented. For the east side girder it is referred to Appendix I, for the weak axis moment. One should note that the absolute maximum and minimum plots only presents the largest and smallest response that occur at selected locations along the bridge, i.e. they do not in general show the actual distribution at a given point in time. Figure 8.20 is included to illustrate this. This figure shows the actual distribution of the wave induced weak axis moments in the two box girders at the time instant when the most extreme value occurs in the west side girder. Except for the large values between a bridge position of 500 to 1000 meters, the moment is relatively low in the rest of the bridge girder. This shows that the peaks are relatively local.

Figure 8.19 illustrates that there are differences in the maximum and minimum weak axis moments at different locations. At the region between axis 3 to 7, from 750 to 1500 meters in this figure, the values are up to 4 times larger than in the lower part of the floating bridge, from 1500 to 4500 meters. As noted by COWI et al. (2016, p.58) this could be explained by the difference in the observed motions at these locations. In the transition region from axis 3 to 7 there are some pendulum motion due to the displacement component in surge direction, in addition to roll motion. This motion is not observed in the rest of the floating part, where roll motion of the bridge girder is the dominating
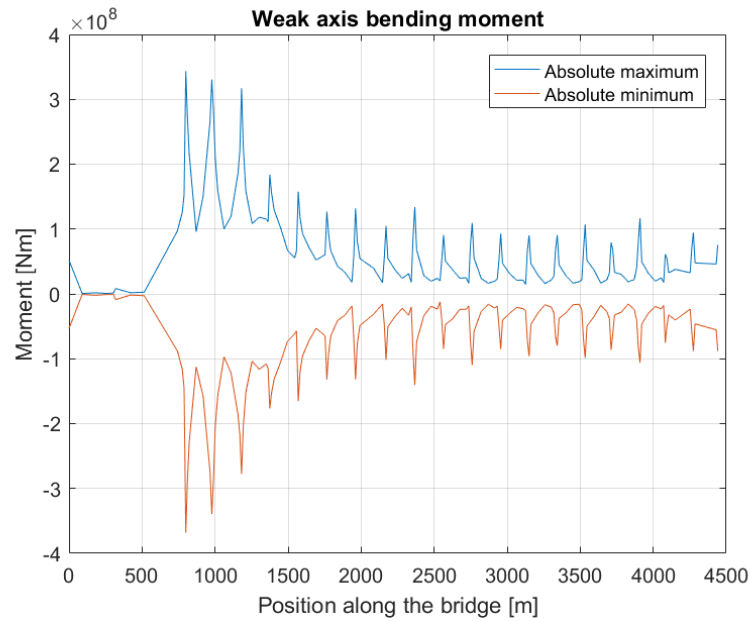
Figure 8.19: Absolute maximum and minimum weak axis bending moment at selected points along the west side girder.
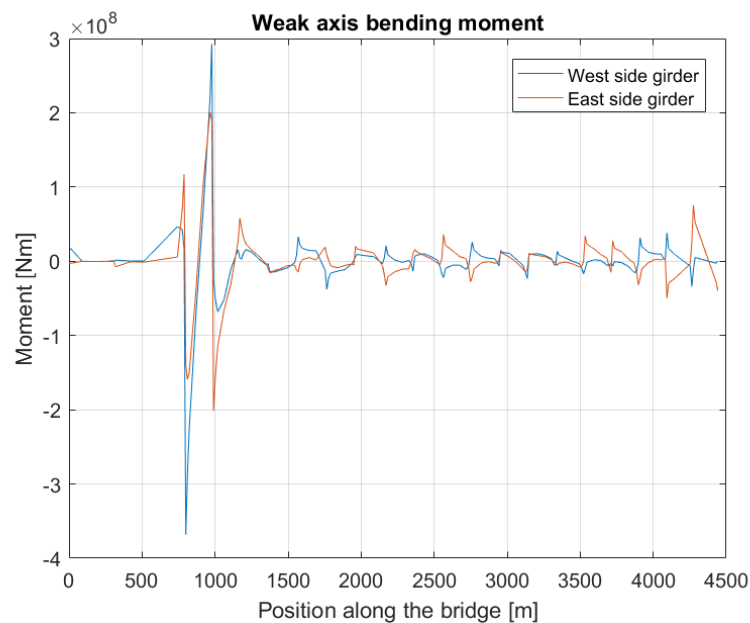
Figure 8.20: The wave induces weak axis bending moment in west and east side girder at the time instant when the most extreme peak in the west side girder.

behaviour. Since the bridge consist of two parallel box girder this rolling behaviour could induce weak axis moments in the east and west side girders.

To check the validity of the results, these where compared with those reported by COWI et al. (2016). As noted COWI et al. (2016) used a model with one single box girder compared to the double box girder model used in this thesis. Therefor one could expect

that the weak axis bending in each of the two girders should be half the value of a single girder model. By comparing the weak axis bending moment in Figure 8.19 with the corresponding 30 minutes simulation in COWI et al. (2016, Ch.7.2.1) it is evident that the two results have peak values of similar magnitude in the low part of the bridge. And in the region between axis 3 to 5 the results obtained in this thesis are larger. The largest difference occurs for the absolute maximum value at axis 5, where the difference is approximately 50%. At first sight this may seem unreasonable but a similar tendency is also illustrated in (Aas Jakobsen, COWI, Global Maritim, & Johs. Holt, 2016, p.23-40) for waves from west. In the mentioned report the weak axis bending moment for a single box girder model is compared with a double box girder model and shows that the largest peaks are close to those for a single girder case. These result seems to give some confidence to the ones presented in this thesis.

The absolute maximum and minimum strong axis moment along the east side girder is presented in Figure 8.21. This figure shows that the largest strong axis moments are low in most part of the bridge except at the support in the north end of the bridge. One should note that the results in this figure has large deviations compared to those in COWI et al. (2016, Ch.7.2.1). In the results from the 30 minutes simulation COWI et al. (2016, Ch.7.2.1) obtains a strong axis bending moment which is almost 10 times larger than the values in Figure 8.21. One explanation for this could be the difference in modelling. If the bridge is modelled with two parallel box girders the total bending action about the strong axis will be taken as bending moment in each girder in addition to axial compression and tension. While in the single box girder case the total bending is taken as pure strong axis bending moment. This is also confirmed by studying the Appendix of COWI et al. (2016), where the effects of using two box girders compared to one single is indicated also for strong axis moment (Aas Jakobsen, COWI, Global Maritim, & Johs. Holt, 2016, p.23-40). In Aas Jakobsen, COWI, Global Maritim, and Johs. Holt (2016, p.23-40) the strong axis bending moment in each box girder is in the order of magnitude as the results presented in this thesis.

The absolute maximum and minimum torsional moment along the east side girder is presented in Figure 8.22. The peak values occurs in general at the midpoint between two axis, while the values at the bridge axes are lower. This is almost contrary to the behaviour of the weak axis global bending moments where the largest peaks are concentrated around the various axis. It may suggest that the dominating roll motions are supported as weak axis moments at the bridge axes and torsion between the axes. One should keep in mind that the bridge girder consists of two parallel box girders, such that a pontoon roll motion may be decoupled into a vertical force couple with opposite sign acting through the columns. This may induce bending about the weak axis for each of the box girders, and if the roll motions at two neighbouring pontoons have opposite phase this could result
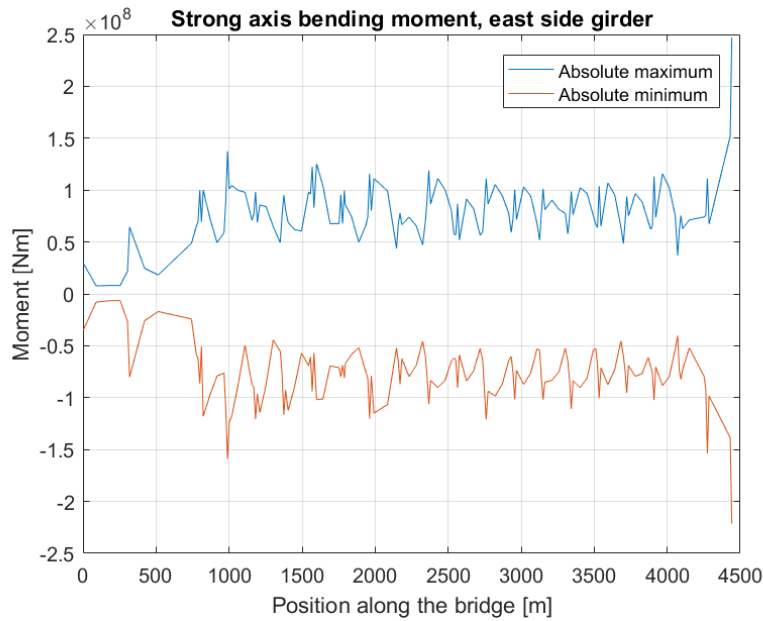
Figure 8.21: Absolute maximum and minimum strong axis bending moment at selected points along east side girder.

in large torsional moments at the middle of the bridge span between these pontoons. For a model with one single box girder this roll motion of the pontoons may induce pure torsion of the bridge girder, causing different response than for two parallel box girders. It should be noted that COWI et al. (2016) found that a ULS check with dominating torsional moment was not the most critical for these requirements. But on the other hand, for the model used in this thesis the results from Chapter 8.3.3 shows that this is the moment component that separately gives the largest utilization.

8.3.5 Stay cables

The largest wave induce axial cable forces occurs in the longest stay cables. To illustrate the magnitude of these forces the largest increase and decrease in tension force is presented in Table 8.8 for the longest cable on the west side of the side span.

Table 8.8: Largest wave induced axial force in the stay cable force.

	Force [MN]	**Stress** [MPa]
Compression	-35.01	-2551.46
Tension	32.23	2409.63

The result in Table 8.8 indicates that the wave induced forces alone exceeds the yield stress of 1860 [MPa], which is unreasonable. Such large values occur in all of the 4 longest cables in each span, while for the other cables the wave induces loads are only exploiting
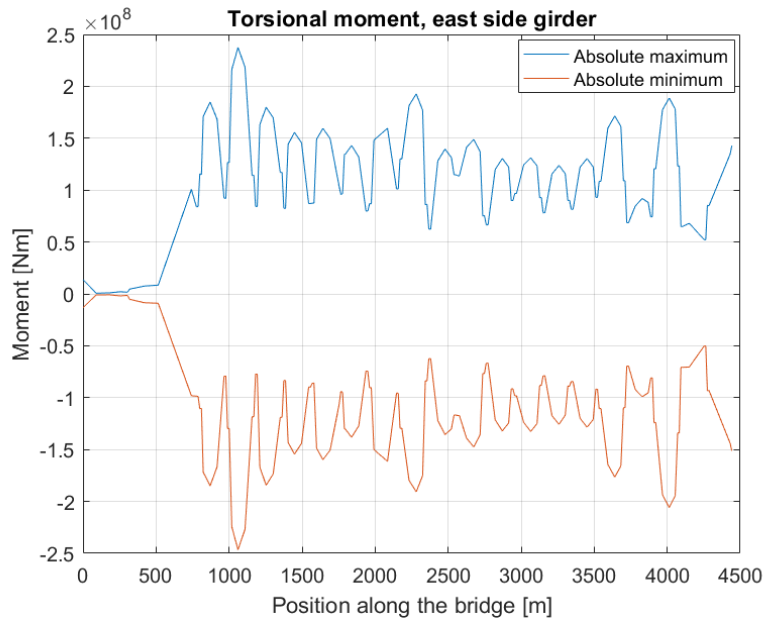
Figure 8.22: Global maximum and minimum torsional moment at selected points along the east side girder.

up to 10% of the total yield capacity. This is a consequence of the cable stiffness in the early version of the bridge model which was too large. As a result the longest stay cables will extract large forces, which results in the observed behaviour. In the updated model such large forces are not present, as will be shown in Chapter 8.3.9.

8.3.6 Tower

The largest wave induced load effects in the tower occurs at the foundation and varies more or less gradually to zero at the top. The exception is for the axial force where the whole tower experience approximately the same value of the largest force. Table 8.9 presents the largest wave induced load effects and compared against the effects from permanent loads the support of the tower. These results illustrates that the axial force is the largest out of the three wave induces force components, while weak and strong axis moment are the largest wave induced moments. It is also evident from this table that the permanent loads are larger than the wave induced ones, except for torsion. For definition of weak and strong axis it is referred to the introduction to Chapter 8.

Table 8.9: The absolute maximum and minimum values at the support of the tower.

Force component	Maximum values Minimum values	Effects from permanent load
Axial	19.17 [MN] -19.08 [MN]	428.45 [MN]
Shear force, directed towards global y-axis	8.37 [MN] -6.56 [MN]	26.39 [MN]
Shear force, directed towards global x-axis	4.44 [MN] -5.26 [MN]	-2.50 [MN]
Weak axis bending	296.67 [MNm] 238.34 [MNm]	721.12 [MNm]
Strong axis bending	236.81 [MNm] -204.89 [MNm]	-1065.61 [MNm]
Torsion	38.95 [MNm] -44.40 [MNm]	16.40 [MNm]

8.3.7 Columns

The wave induced bending moment is presented in Table 8.10 for one column in the transition area between axis 3 and 7, and one column in the low bridge part. In addition the torsional moment is included at the location with the largest value. From this table it is evident that it is the bending component at axis 3 that gives the largest utilization with regard to yielding. The columns have the largest height at axis 3 and it is therefor expected that the bending component is largest at this region.

Table 8.10: Wave induced force components that gives the largest stresses in columns.

	Moment	Stress
Bending moment, axis 3	487.12 [MNm]	177.53 [MPa]
Bending moment, axis 19	132.98 [MNm]	76.43 [MPa]
Bending moment, axis 6	69.44 [MNm]	12.81 [MPa]
Torsional moment, axis 15	113.9 [MNm]	32.82 [MPa]

8.3.8 Effects from slowly-varying drift forces

The effect of the slowly-varying drift force was studied using the absolute maximum and minimum plots of the horizontal displacement and strong axis bending moment along the bridge girder. These are established for a simulation with only second order effects and compared against results including both first and second order loads. This is done as it may give an indication of the importance of the slowly-varying drift loads compared to the total displacement and moment. Though it should be noted that the largest peak from the first and second order loads may not necessarily occurs simultaneously.

Figure 8.23 presents the absolute maximum and minimum horizontal displacement of the bridge girder, where the south and north end of the bridge is located at 0 and 4500 meters respectively. These figures illustrates that the contribution from the slowly-varying drift force to this response type is relatively large and in the same order as the total displacement including linear wave loads. The single largest contribution to the horizontal displacement along the bridge is found at approximately 2200 meters. At this location the drift loads causes a response which is almost 60% of the total displacement from the linear and second order analysis. It should be noted that this location is close to the middle of the bridge where the second eigenmode has its peak value. This eigenmode appeared to be present in the frequency domain solution presented in Chapter 8.3.2 for the middle of the bridge. Another point is that the maximum horizontal displacement for the analysis with linear and second order loads seems to occur when the effect from second order loads are largest. This is illustrated in Figure 8.24 which shows the time-varying horizontal displacement at the location with the largest total response, i.e. at about 2500 meters in Figure 8.23. At the largest peak at 310 seconds the second order loads contributes with approximately 40% of the total displacement.

The contribution to the strong axis bending moment from slowly-varying drift forces is illustrated in Figure 8.25. The largest effects are observed in the bridge girder at the tower at 370 meters and the support at the north end. At the tower the the contribution from the second order wave load is approximately 28%, while at the north end the effects causes a moment which is about 16% of the maximum strong axis moment including linear effects. The contribution to the torsional moment is approximately 10% along the whole bridge girder compared to the analysis with linear wave forces, while the largest effect for the weak axis moment is about 5% of these results. This seems to indicate that the horizontal displacement is highly affected by the second order contribution, while linear wave loads forces dominates the wave induced moments in the bridge girder.

8.3.9 The effect of using the updated model

Since wave condition 1 gave larger response than those reported by COWI et al. (2016) the USFOS bridge model was reconsidered. This resulted in updates of the model file for some of bridge girder properties such as second moment of area, second torsional moment of area and plastic section modulus. The axial stiffness of the stay cables was also updated to the correct value and pretension was introduced by applying temperature loads to the cables. Some of the main effects of these updates will be presented in the following.

The effect on the weak axis bending and torsional moments along the bridge girder are illustrated in Figure 8.26. The two components are presented as these appears to have

(a) Absolute maximum.
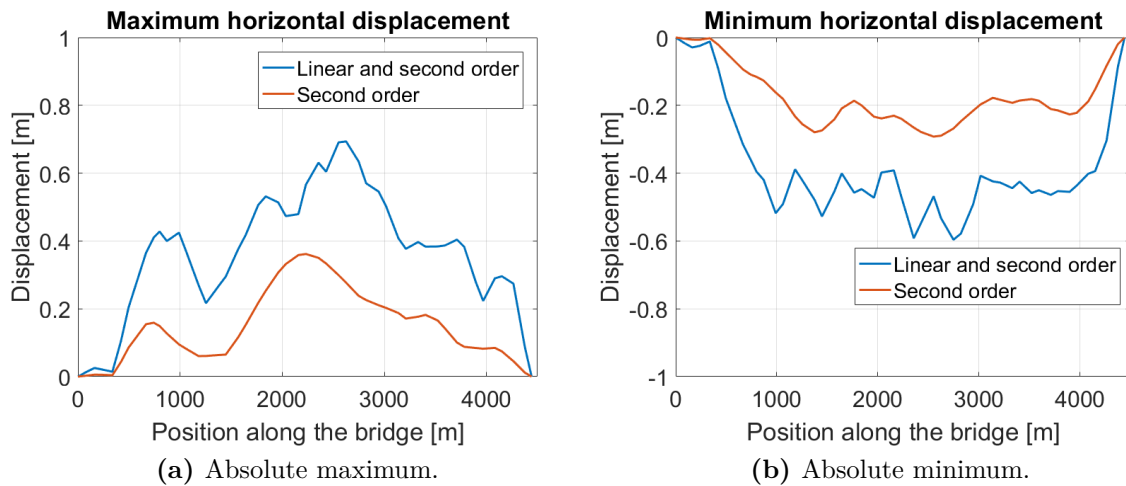
(b) Absolute minimum.

Figure 8.23: Absolute maximum and minimum horizontal displacement along the whole bridge.
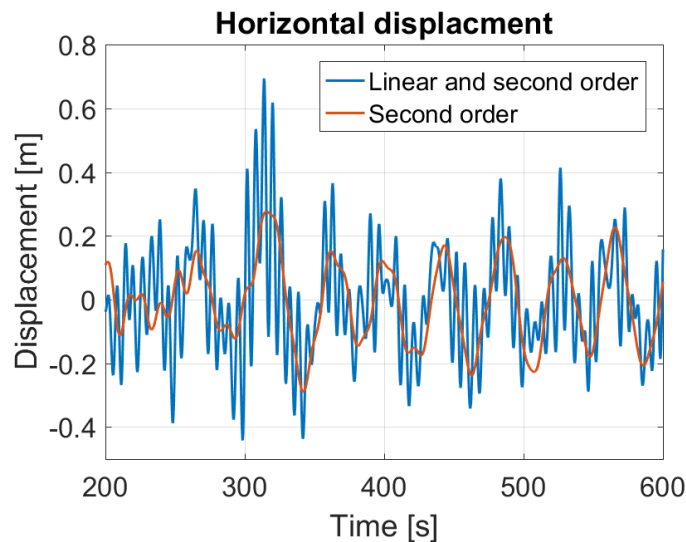
Figure 8.24: Contribution from second order slowly-varying loads at maximum displacement.

the largest changes compared to the old version of the model, out of the three moment components. Only the absolute maximum values are presented as the absolute minimum shows a similar tendency. The largest difference is observed in the region between 500 to 1200 meters for the maximum weak axis moments, which is also the location with the single largest change for the torsional moments. In the old version of the model the stiffness of the stay cables was too large, as a consequence the region close to these was probably affected and forced to attract larger load effects than in the updated model. As an example the torsional moment between axis 3 and 4, i.e. the peak between 1000 and 1200 meters, is reduced with almost 67% compared to the old model. For the weak axis moment the largest change is observed at axis 5, i.e. at nearly 1200 meters, where the value for the updated model is about 60% lower. It should also be noted that since the torsional moment has considerably lower values at many locations along the bridge, which

(a) Absolute maximum.
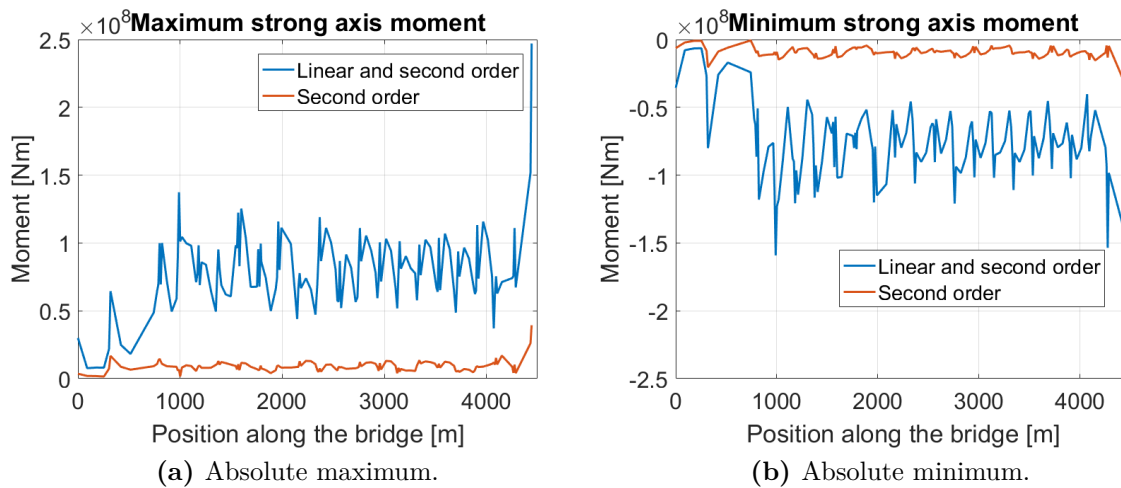
(b) Absolute minimum.

Figure 8.25: Absolute maximum and minimum strong axis bending moment along the whole bridge.

could indicate that the update in torsional moment of area had a large impact.

(a) Weak axis moment.
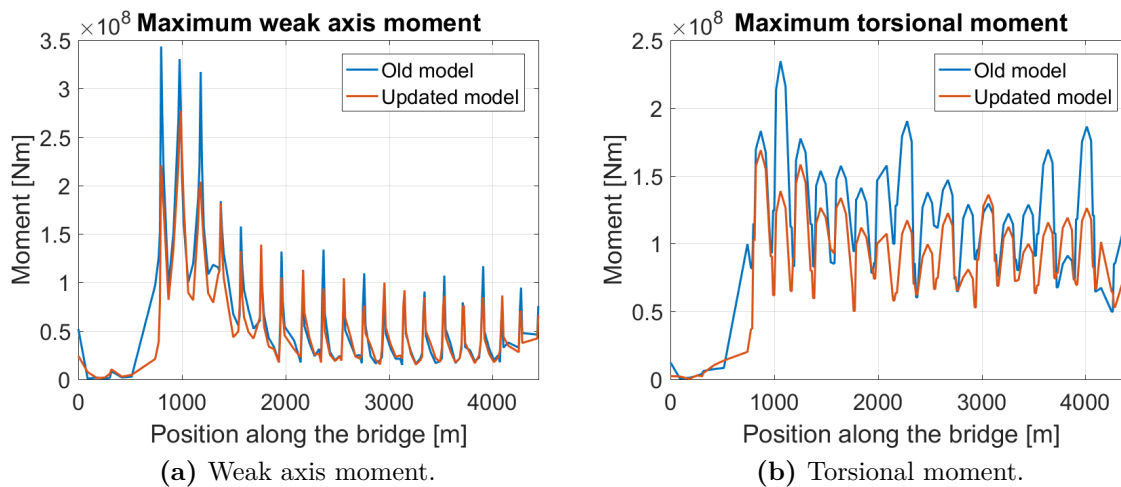
(b) Torsional moment.

Figure 8.26: Absolute maximum weak axis bending and torsional moment for the old and updated model.

The largest wave induced axial force that occurs in the same stay cable as presented in Chapter 8.3.5 are given in Table 8.11 for the updated model. By comparing these it is clear that the updated model has a lower wave induced forces. As can be seen from this table, the corresponding stresses are utilizing a small amount of the yield stress of 1860 [MPa]. The largest contribution to the axial stresses in this condition comes therefor from permanent loads, giving an utilization of approximately 28% in all cables.

Table 8.11: Largest wave induced axial cable force in the longest stay cable in the west side of the side span, for the updated model.

	Force [N]	**Stress** [MPa]
Compression	-3.25E+05	-23.53
Tension	2.68E+05	19.40

8.4 Wave condition 2

In wave condition 2 the heave component of the wave excitation loads are applied as fully uncorrelated to the 19 pontoons, which is illustrated in Figure 8.27. It is evident from this figure that the heave forces are directed oppositely for every second pontoon, as intended for this wave condition.
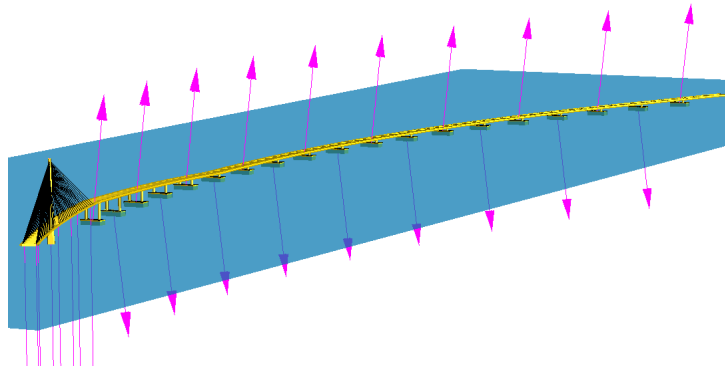
Figure 8.27: Applied wave forces in wave condition 2 at a given point in time.

As for the first condition, wave condition 2 is run with an early version of the bridge model. Since the effects of this condition appeared to be small it was decide to rather put the attention on the remanding conditions then rerun condition 2. Therefor only some few notes will be made for this wave condition. The minor differences between wave condition 1 and 2 is illustrated in Figure 8.28, which compares the absolute maximum weak axis moment at selected points along the bridge girder. This figure includes only the wave induced part and except for small changes in some areas, the response appears to be nearly the same. Further, the south support is located at a bridge position of 0 meters and the north support at 4500 meters.

Wave condition 2 is mainly relevant for eigenmodes dominated by pure vertical motion, especially mode 32 consisting of nearly one half wave in the vertical plane per pontoon. This mode has an eigenperiod of 7.52 seconds, which is within the region where the wave spectrum has energy, though it is small compared to the peak at 6 seconds, see Figure 5.10. Since roll motions appears to dominate the bridge behaviour these could prevent the pure vertical modes of being triggered. This may explain the minor differences compared to wave condition 1. Another point is that the eigenmodes in the range of the peak period
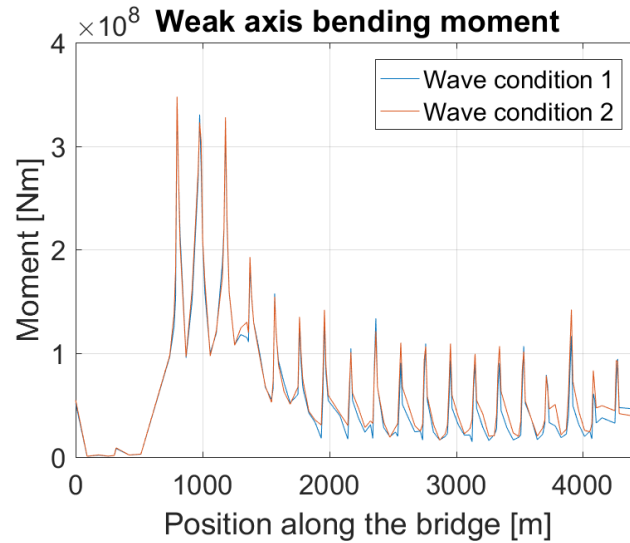
Figure 8.28: Absolute maximum weak axis moment along the bridge for wave condition 1 and 2.

of 6 seconds are mainly roll motions. Thus a more relevant wave condition could therefor be to apply all the wave load components as fully uncorrelated, i.e. oppositely directed for every second pontoon. Eigenmode 32 is presented in Appendix G.

8.5 Wave condition 3

In wave condition 3 the waves comes from north-west and will therefor include wave force component in sway, surge and heave in addition to pitch, roll and yaw moment. Since the first wave conditions showed that moments gave the largest stresses in the bridge girder, the main focus was put on analysing these for the remaining wave conditions, i.e. wave condition 3 and 4. An illustration of the applied wave loads at a given point in time is illustrated in Figure 8.29. As the figure shows the resulting wave force at this specific point in time includes components in global y- and z-axis. It is also evident that the forces are applied fully correlated as they should.

Figure 8.29: Applied wave forces acting on the pontoons at a given point in time during wave condition 3.

The response in this condition appeared to be much larger than in condition 1 and 2. Therefor some extra attention was put on verifying that the wave forces where applied correctly to the pontoons. Figure 8.30 illustrates the time history for the wave force in

sway direction, comparing the input history with the resulting time history in the USFOS analysis. This figure illustrates that the time histories are similar, and the differences is some regions are expected as the resulting wave force in USFOS includes the effect of second order drift loads. There may also be effects from the hydrodynamic properties of the pontoon elements included in Figure 8.30b.

(a) Input to USFOS.

(b) Extracted from USFOS.
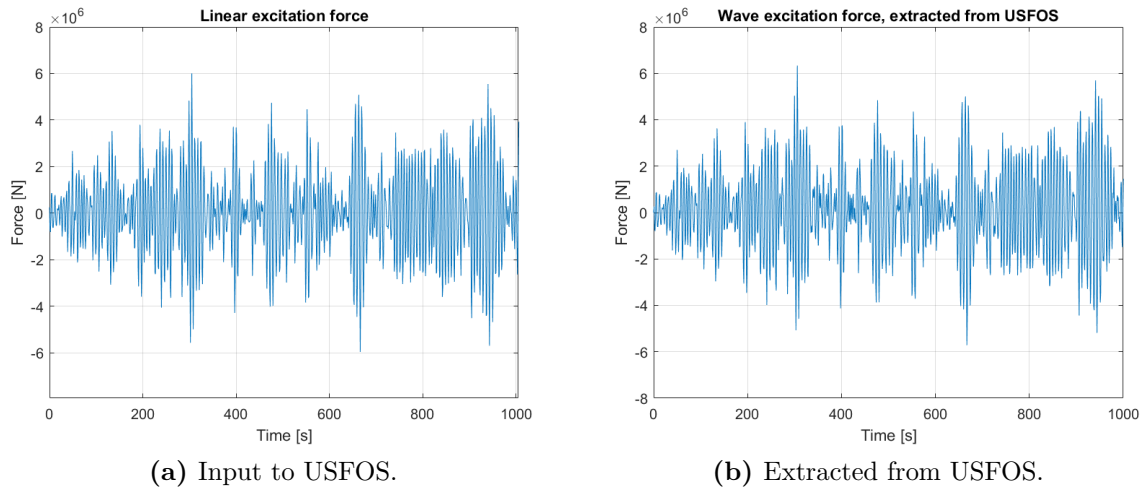
Figure 8.30: The linear wave force in sway direction given as input to USFOS in addition to the total wave sway force extracted from USFOS.

8.5.1 Dominating motions

In a similar way as for wave condition 1 are roll motions of the bridge girder one of the dominating response patters, which reflects the behaviour of the pontoons. In addition it is also observed horizontal motions where Figure 8.31 shows one displacement pattern that occurs regularly during the 1000 seconds analysis. This is a combined roll and horizontal motion which has similarities with eigenmode 34 presented in Figure 8.7 in Chapter 8.1, especially in the north part of the bridge. The bridge is viewed from above with the north support in the rightmost corner of this figure.
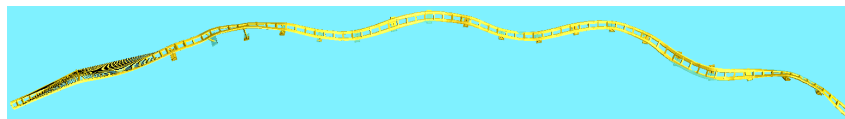
Figure 8.31: Dominating motion at the north part of the floating bridge. Displacements scaled by a factor of 100.

Figure 8.32 illustrates a motion that occurs frequently at the transition region between the cable stayed and floating part of the bridge, where the rightmost pontoon is axis 3 and leftmost is axis 4. The pontoons at axis 3 and 4 exhibits significant motions in surge

direction which induces vertical displacement of the end of the main span. This behaviour dominates the motions when the largest vertical displacements occurs at this region. It should be noted that this is the motion that have been referred to as pendulum motion earlier in this chapter and is observed both for eigenmode 35 and 36. These modes are presented in Appendix G.
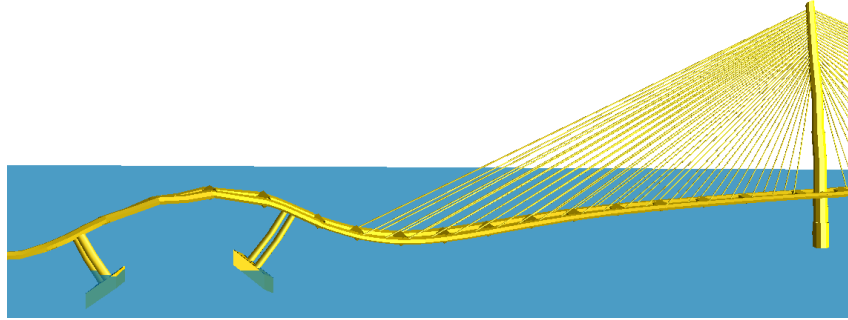
Figure 8.32: Dominating motion at axis 3 and 4. Displacement scaled by a factor of 50.

Figure 8.32 presents the frequency domain solutions of the horizontal and vertical displacement at the same two points as for wave condition 1. Horizontal displacement still refer to the component in global x-axis. The frequencies with the largest peak in these figures are presented in Table 8.12 and 8.13 with the corresponding periods, for the horizontal and vertical displacement respectively. At axis 11 the largest peak in the horizontal displacement is located at a period of 65.53 seconds, which is close to the largest eigenperiod. This is caused by the slowly varying drift force and illustrates the importance of the second order wave loads for these motions. A similar period is also seen for the largest peak at axis 3, while the single largest point is 87.41 seconds at this location. One explanation for this could be that the analysis is only 1000 seconds, and by running a longer simulation one may get a more converged solution. Another point could be that the motions at this location reflects the applied loads, since the second order forces may have periods larger than the fundamental eigenperiod. In the linear frequency range the largest peak in Figure 8.33a occurs for a period of about 7.09 seconds, i.e. 0.1411 [1/s], for both positions. Eigenmode 33 in Appendix G is the closest period, which is mainly a roll motion but has a horizontal component at axis 3. The shape of this mode is also presented in Appendix G. One could note that there exist other eigenmodes consisting of horizontal motions with eigenperiods close to the largest peak in the frequency domain solution of the horizontal displacement.

Table 8.12: Largest peak in the frequency domain plot of the horizontal displacement.

	Peak frequencies, [1/s]	Periods, [s]
Axis 3	0.01144 to 0.01526	87.41 to 65.53
Axis 11	0.01526	65.53

(a) Horizontal displacement.

(b) Vertical displacement.
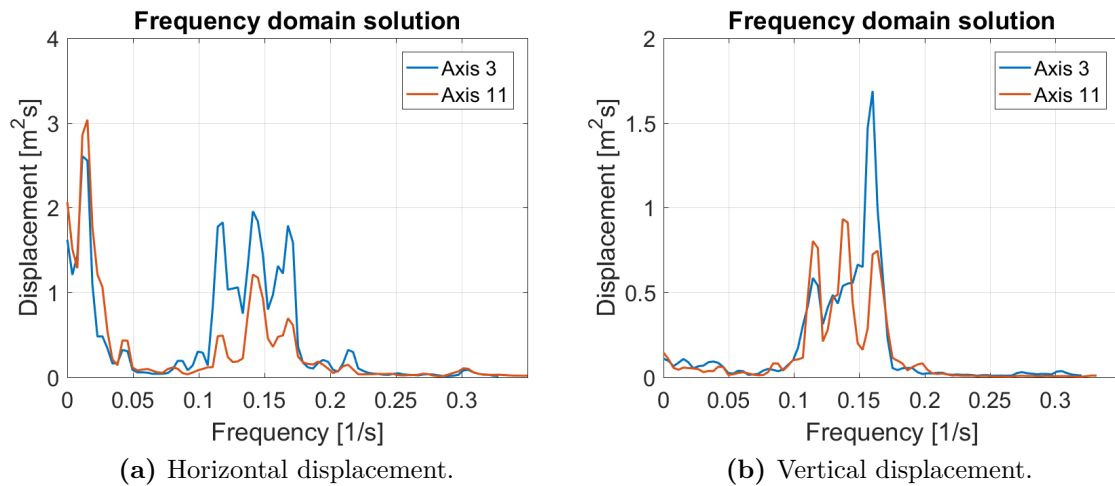
Figure 8.33: Frequency domain solution of the horizontal and vertical displacement at two locations.

The largest peak in the frequency domain solution of the vertical displacement at axis 3 is close to eigenmode 35 with a period 6.33 seconds, see Figure 8.33b and Table 8.13. This corresponds well with the observed pendulum motion in this region, as presented in Figure 8.32. At axis 11 a peak at 7.27 seconds is seen, which is between mode 32 and 33 where the first is a pure vertical mode while the latter is a roll motion. Both of these modes are illustrated in Appendix G.

Table 8.13: Largest peak in the frequency domain plot of the vertical displacement.

	Peak frequencies, [1/s]	Periods, [s]
Axis 3	0.16020	6.23
Axis 11	0.13730	7.27

8.5.2 Largest displacements and accelerations

The largest displacements and accelerations of the bridge girder is presented in Table 8.14 for wave condition 3. This table shows the absolute maximum and minimum at the point with the largest response. It is evident from this figure that the largest values occurs at other locations than in wave condition 1, which may illustrate differences in wave induced motions. Further, the result in this table shows that large vertical motions occurs at the end of the main span. This point is illustrated by a red circle in Figure 8.34. One should also note that the response reported in Table 8.14 is measured at the box girders with the largest values, though the differences in response for the west and east side girder are minor. For definition of box girder, west side girder and east side girder see Chapter 4.1.

Some of the results presented in Table 8.14 was compared with the those presented by

Table 8.14: Largest displacements and accelerations in wave condition 3.

	Maximum value Minimum value	Unit	Location
Vertical displacement	1.32 −1.35	[m] [m]	End of the main span
Horizontal displacement	1.53 −2.35	[m] [m]	Between axis 4 and 5
Vertical acceleration	1.38 −1.60	[m/s²] [m/s²]	Between axis 4 and 5
Horizontal acceleration	1.69 −1.54	[m/s²] [m/s²]	Axis 5
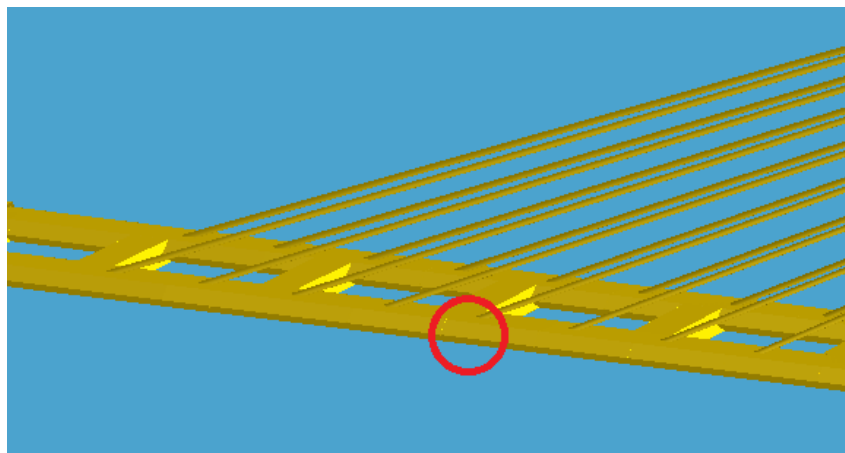
Figure 8.34: Position at the end of the main span where large vertical displacements occurs.

COWI et al. (2016, p.84) using the absolute maximum and minimum plots of vertical acceleration and displacement in Figure 8.35. In these figures the south support is located in the leftmost corner and north support at the rightmost corner. It should be noted that the absolute maximum and minimum values along the bridge for vertical displacement in Figure 8.35a follows the same pattern as in COWI et al. (2016). The largest values occurs at the end of the main span and then decreases towards the low part of the bridge. Except for large vertical accelerations between axis 4 and 5 in Figure 8.35b, these also have similar distribution as in the mentioned report. There is on the other hand differences when it comes to the size of the vertical accelerations and displacements. COWI et al. (2016, p.84) presents the characteristic 1-year values, and multiplying these with a factor of 2 one obtains the characteristic 100-year values (COWI et al., 2016, p.24). As and example the largest absolute maximum and minimum vertical displacement in COWI et al. (2016) for waves from north-west are 0.64 [m] and −0.64 [m] respectively in the main span compared to 1.32 [m] and −1.35 [m] in Table 8.34. Thus the largest vertical displacement obtained for the 1000 seconds analysis is 2.11 times larger than the characteristic 1000-year value in (COWI et al., 2016, p.24). One should also keep in mind that the values

in Table 8.14 assumes fully correlated waves, while it is not found any clear statement in COWI et al. (2016) how the phase difference is taken care of in their analysis. Further, as explained for wave condition 1 could the displacements and accelerations in COWI et al. (2016) may refer to a different location on the bridge girder than those in Table 8.35. This is important to note as a roll motion of the bridge girder will give significant contribution to the vertical displacements and accelerations for the parallel box girders. While for a single box girder such motions will have less contribution for displacements and accelerations if they are measured at the neutral axis of the bridge girder.

(a) Vertical displacement.   (b) Vertical acceleration.
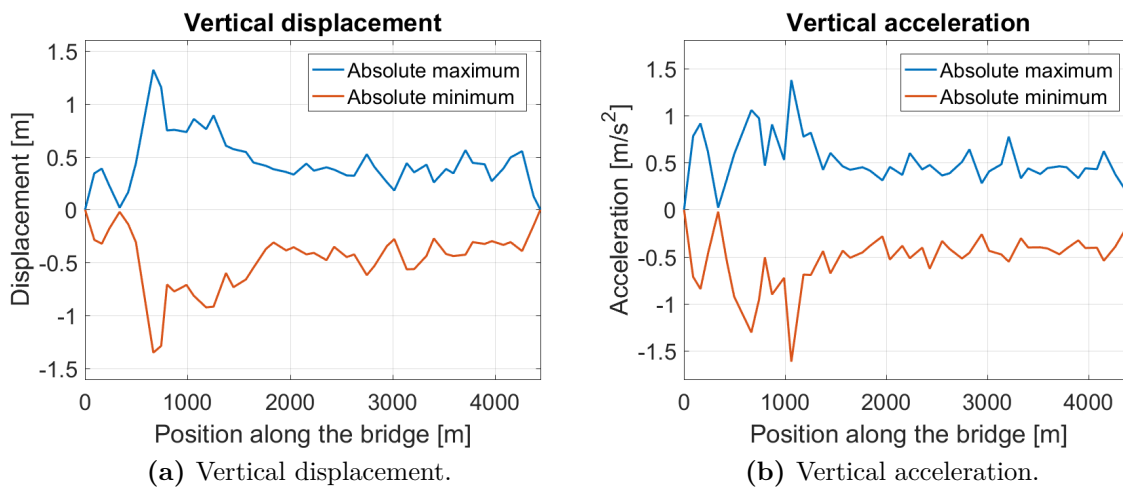
Figure 8.35: Absolute maximum and minimum plots of the vertical acceleration and displacement. Displacements are for the west side girder and accelerations for the east side girder.

8.5.3 Largest wave induced loads in the bridge

As noted, the three moment components was the main focus in this condition. Table 8.15 presents the absolute maximum and minimum of these components together with the corresponding stresses at selected locations. These locations are chosen as the largest wave induced response of the individual components occurs at the respective points. Further, the results in this table presents only the wave induced part of the moments, i.e. effects from permanent loads are subtracted. For definition of the weak and strong axis in addition to where these stresses are calculated see the introduction to Chapter 8.

The result in Table 8.15 shows that a wave heading from north-west gives much larger moments in the bridge girder compared to waves from west, see Table 8.7 in Chapter 8.3.3. As an example is the largest bending moment about the weak axis approximately 2.96 times larger for north-west heading than for west. Though the wave heading from west is run with somewhat different bridge girder properties, it gives a quite clear indication than waves from north-west is more critical with respect to these response types. A similar

Table 8.15: The absolute maximum and minimum values for the three moment components along the bridge girder.

	Maximum value Minimum value	Stress	Location
Weak axis moment	1018.11 [MNm] −889.11 [MNm]	236.44 [MPa] −206.47 [MPa]	At axis 4, east side girder
Strong axis moment	987.45 [MNm] −921.95 [MNm]	−270.98 [MPa] 253 [MPa]	North support, east side girder
Torsional moment	541.45 [MNm] −531.62 [MNm]	156.31 [MPa] 153.47 [MPa]	Between axis 5 and 6, east side girder

behaviour is also evident for the tower support forces in Table 8.16, where the largest increase is seen for the weak axis moment compared to the results in Chapter 8.3.6. See introduction to Chapter 8 for definition of weak axis moment. The set of random phase angles used in these analysis gives approximately 15 times larger weak axis moment when waves comes from north-west. An almost equal increase is seen for the shear force in global y-axis which is expected, as it follows the weak axis moment. Another observation is that most of the wave induced components in Table 8.17 is larger than the effect from permanent loads, which is different from wave condition 1. One explanation for the increase in loads at the tower support could be the relatively larger vertical displacement of the main span. These motions must be transferred to the tower through the stay cables, which will give contribution to weak axis bending of the tower.

Table 8.16: The absolute maximum and minimum values at the support of the tower.

Force component	Maximum values Minimum values	Effects from permanent load
Axial	14.80 [MN] −12.20 [MN]	405.20 [MN]
Shear force, directed towards global y-axis	105.89 [MN] −101.11 [MN]	47.11 [MN]
Shear force, directed towards global x-axis	25.40 [MN] −30.80 [MN]	1.30 [MN]
Weak axis bending	4547.59 [MNm] −4282.41 [MNm]	1802.41 [MNm]
Strong axis bending	2150.46 [MNm] −1796.54 [MNm]	−1393.46 [MNm]
Torsion	138.53 [MNm] −207.47 [MNm]	11.47 [MNm]

The stay cable forces for the longest cable in the west side of side span is presented in Table 8.17. These must be compared with the updated model in Chapter 8.3.9, as the old model has unnaturally large cable forces. The stay cables are has pretension, and the result in Table 8.17 shows the absolute maximum increase and decrease in this axial force.

In this connection compression means a decrease in the axial tension force. It should also be noted that only the wave induces part of the axial cable forces are presented in this table. The largest increase in tensile cable force for waves from north-west are 4.18 times larger than those obtained with the updated model in wave condition 1. Though the resulting wave induces stress is still well below the yielding, as it utilizes only 4.45% of the yield stress. This means that permanent loads which utilizes 23.26% of the yield stress has the largest contribution also for this wave condition.

Table 8.17: Largest wave induced axial force in the longest stay cable in the side span on the west side of the bridge girder.

	Force [MN]	**Stress** [MPa]
Compression	-1.50	-111.11
Tension	1.12	82.95

8.5.4   Effects from slowly-varying drift forces

Some notes on the importance of the second order forces versus the linear, which are both included in the wave analysis, will be presented in the following. As for wave condition 1 the horizontal displacement of the bridge girder in addition to the strong axis bending moment for the east side box girder are studied. These was expected to show the largest contribution from second order loads, and the absolute maximum and minimum values of these responses was studied. This means the largest positive and most negative displacements and moments that occurs at each point along the bridge, during the 1000 second analysis. As a consequence these plots do not in general show the response at a given time instant, and the largest contribution from the second order loads may occur at a different time than those from the linear. On the other hand these results may give an understanding of the relative importance of the linear and second order loads, as noted for wave condition 1.

Figure 8.36 presents the absolute maximum and minimum horizontal displacement along the bridge. In these figures the south support is at the leftmost corner and north support at the rightmost corner. What is interesting is that the second order contribution in these figures have two half waves, which is different from wave condition 1. The largest contribution to the horizontal displacement from these loads occurs approximately at a location of 1500 and 3100 meters on the x-axis in these figures. These locations corresponds well with the position of the amplitudes of the first eigenmode, which is in accordance with the dominating frequencies of the horizontal displacements for this wave condition, see Chapter 8.5.1. Though the largest displacement from a combined linear and second order analysis in general occurs at a different time, these figures illustrates that the contribu-

tion from pure second order loads are significant. As an example, at a bridge position of 3100 meters in Figure 8.36a the largest displacement from pure slowly-varying loads is approximately 58% of the maximum from the results including both linear and second order effects. A similar contribution was also seen for wave condition 1. The importance of the linear loads is also illustrated in this figure since the blue curves are larger than the pure second order induced response. This may be used to argue that both linear and second order slowly-varying drift effects gives significant contribution the horizontal displacement.

(a) Absolute maximum.
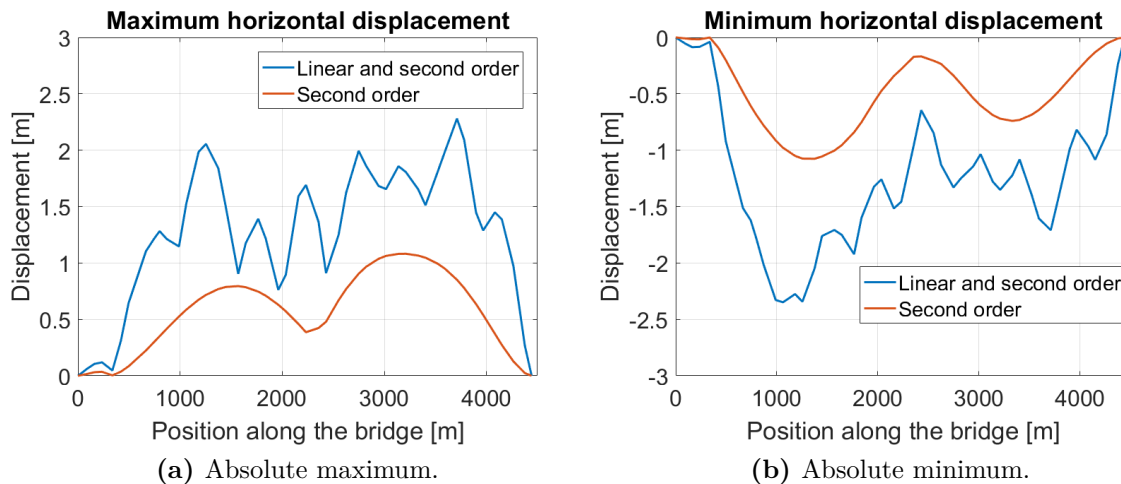
(b) Absolute minimum.

Figure 8.36: Absolute maximum and minimum horizontal displacement along the whole bridge.

Figure 8.37 presents the absolute maximum and minimum strong axis bending moment for the same two analysis as for the horizontal displacement. It is quite clear from this figure that the linear wave forces gives much larger moments in the east side box girder than the second order slowly-varying loads. The largest moment induced by the second order loads is found for the minimum strong axis moment at the tower, i.e. about a bridge position of 370 meters in Figure 8.37b. At this location the effect is 9.86% of the total moment including first and second order loads, while at the north end the largest effect is 7.25% for the maximum moment. This is somewhat lower than observed for wave condition 1, but one should note that the total strong axis moment in Figure 8.37 is much larger than the corresponding values for the first wave condition, see Figure 8.25 in Chapter 8.24. This indicates that the effects from linear wave loads to the strong axis bending moment is much larger for waves from north-west. One should also keep in mind that the first wave condition was run with the early version of the model. From this one may conclude that the main effect from slowly-varying loads are contribution to the horizontal displacements, while linear wave forces predominates the strong axis moments, as for waves from west.

(a) Absolute maximum. **(b)** Absolute minimum.
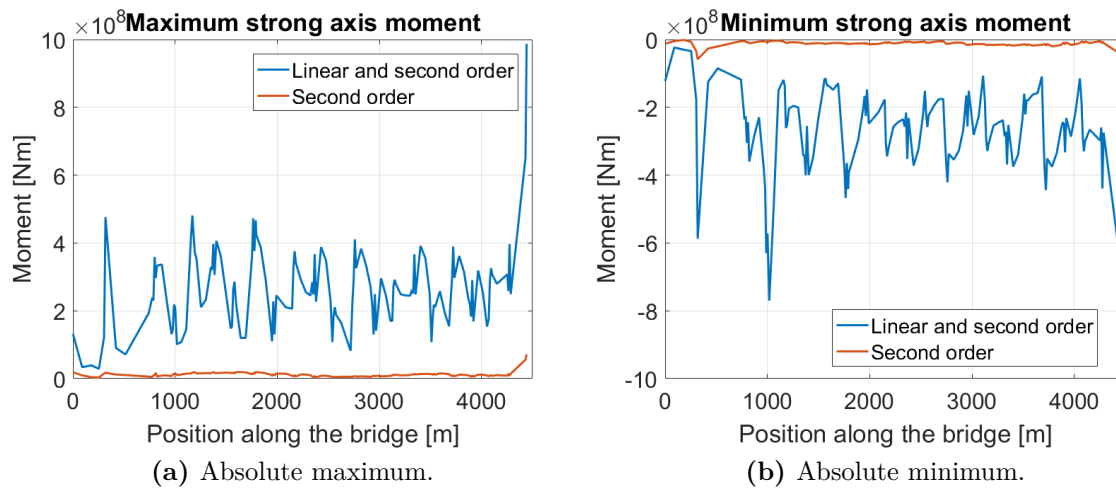
Figure 8.37: Absolute maximum and minimum strong axis moment along the whole bridge.

8.6 Wave condition 4

This wave condition is similar to wave condition 3 except that these analysis accounts for the correlation in wave loads, using the phase differences caused by the locations of the pontoons. Therefor the main focus was put on illustrating how this affects the response of the bridge compared to condition 3. The phase difference is calculated using the coordinates of pontoon centres, which gives 171 different wave load-time histories with six linear and three slowly-varying drift loads per pontoon. Figure 8.38 illustrates the applied loads for a given point in time for this wave condition, where components below a value of 1.5 [MN] are filtered to remove effects from permanent loads and buoyancy. Therefor some of the pontoons on this figure is illustrated without arrows. At least Figure 8.38 shows that the wave forces on the various pontoons in general are different.
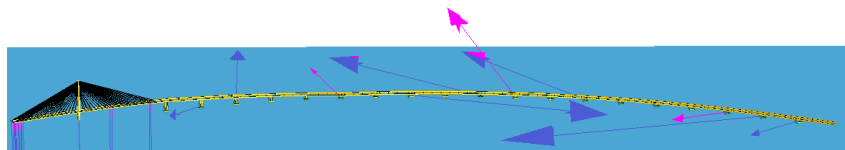
Figure 8.38: Applied forces at a given point in time for wave condition 4.

The wave force time history at two of the pontoons was studied in order to check the effect of using phase angles calculated using the pontoon positions. The first 500 seconds of the time history in sway direction is presented in Figure 8.39. This figure shows that the time series are in general different which is expected, as the sea state is irregular and consists of different frequency components. Since different frequencies travels with different speed the resulting sea surface will change as the wave propagates, which in turn gives different wave forces. Though it seems like there are some similarities that are repeated at pontoon

16, but on a later point in time than for pontoon 18. One of these groups are circled in Figure 8.39. Pontoon 16 is located at bridge axis 18 which is approximately 400 meters south relative to pontoon 18, while pontoon 18 is the second pontoon from the north end. Thus the distance between pontoon 16 and 18 is relatively small, and one could expect to find some of the largest components also at pontoon 16.
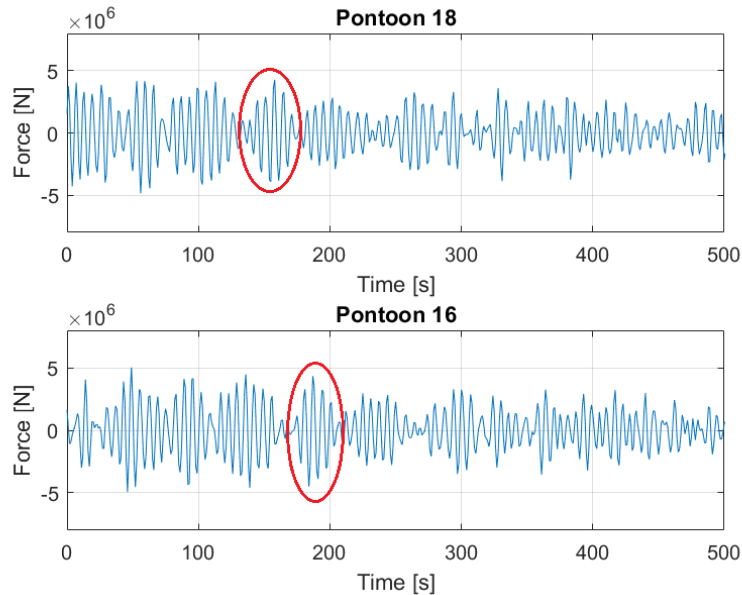
Figure 8.39: Excitation wave force in sway direction acting on two pontoons.

Figure 8.40 takes a closer look at the region between the two circles in Figure 8.39, i.e. the interval from 130 to 210 seconds. This figure shows that the wave force component at the two pontoons in general are not in phase. Another point is that the force at pontoon 16 seems to be quite similar to the one at pontoon 18, but with a shift in time. By using the difference between the peaks at approximately 158 and 179 seconds, the history seems to be shifted with 30 seconds from pontoon 18 to pontoon 16.

8.6.1 Dominating motions and largest displacements and accelerations

The frequency domain solutions of the vertical and horizontal displacements was studied to give an impression if there are difference in these response, caused by the phase difference. One of the largest differences is found for the horizontal displacement where the peak at both locations is largest at a frequency corresponding to a period of 5.81 seconds, see Table 8.18. While for the fully correlated condition the largest single contribution came for a period of 65.53. This may indicate that the response from second order loads are less important for the present wave condition, which could be a natural consequence of
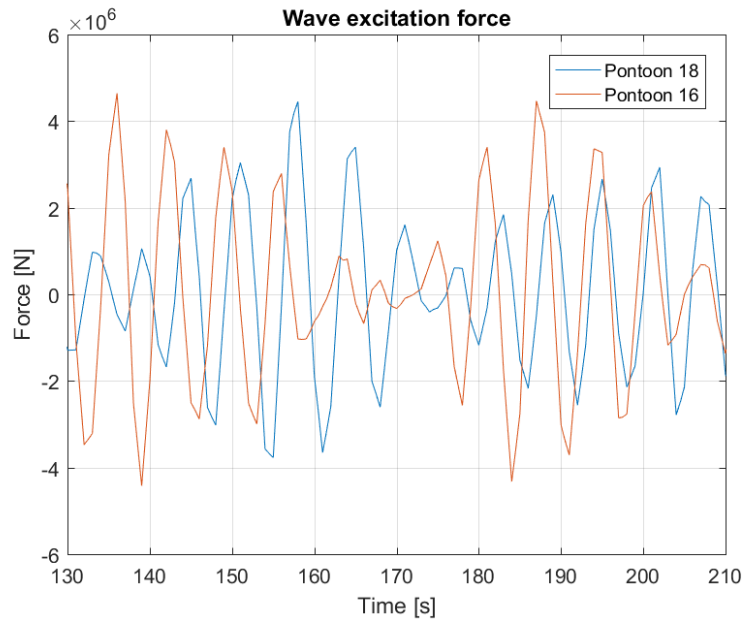
Figure 8.40: Wave excitation force in sway direction acting on pontoon 18 and 16.

accounting for the phase angle in the wave loads. From Figure 8.38 it is seen that the wave forces in this condition in general have different directions at a given point in time. This could make it more difficult to trigger the first eigenmode. Further, it should be noted that a period of 5.81 seconds coincides with mode 38 and is a combined roll and horizontal motion, see Appendix G. It is also interesting to see that the vertical displacement at axis 3 has a peak at a period of 6.38 seconds, which is close to mode 35 with pendulum behaviour at this region. This is similar to the result for wave condition 3. One should note that the horizontal displacement appears to have large contribution for a frequency tending to zero. This could be due to drifting in the horizontal plane observed for this condition, which will be discussed in Chapter 8.8.4.

Table 8.18: Largest peak in the frequency domain plot of the horizontal displacement.

	Peak frequencies, [1/s]	Periods, [s]
Axis 3	0.1717	5.81
Axis 11	0.1717	5.81

Table 8.19: Largest peak in the frequency domain plot of the vertical displacement.

	Peak frequencies, [1/s]	Periods, [s]
Axis 3	0.1564	6.38
Axis 11	0.1526	6.54

The largest displacements and accelerations that occurs along the bridge girder for this wave condition is presented in Table 8.20. As for the other wave conditions the values in this table are the absolute maximum and minimum response, using the same approach for

(a) Horizontal displacement.   **(b)** Vertical displacement.
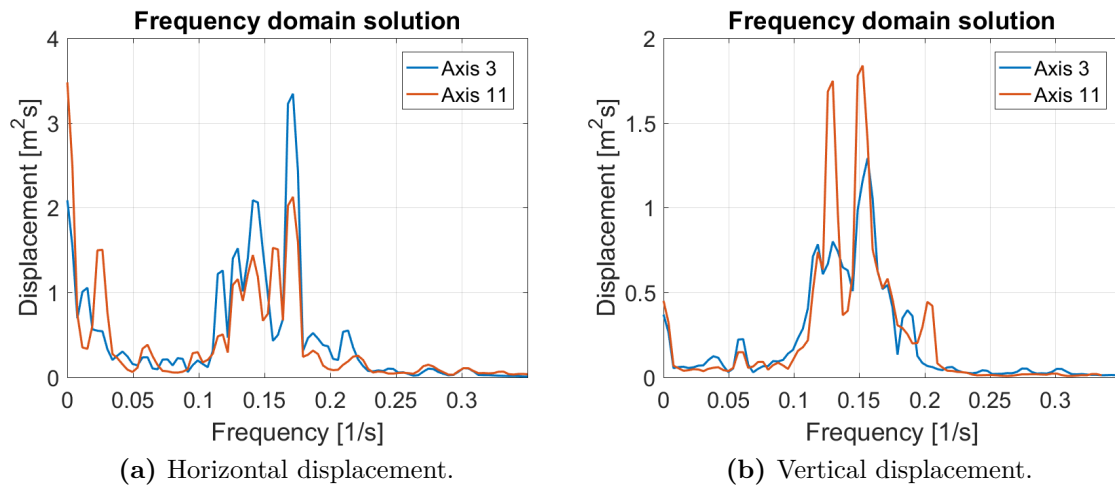
Figure 8.41: Frequency domain solution of the horizontal and vertical displacement at two locations.

choosing the locations as noted in Chapter 8.5.2. These results shows that except for the horizontal displacement, all of the the largest values occurs in the region at "the end of main span". This region was illustrated in Figure 8.34 and the result may indicate some changes in the bridge motions caused by using a different correlation in the wave forces, compared to wave condition 3.

Table 8.20: Largest displacements and accelerations.

	Maximum values Minimum values	Unit	Location
Vertical displacement	1.34 −1.39	[m] [m]	End of the main span,
Horizontal displacement	1.22 −2.05	[m] [m]	At axis 4
Vertical acceleration	1.33 −1.60	[m/s²] [m/s²]	End of the main span,
Horizontal acceleration	1.62 −1.75	[m/s²] [m/s²]	End of the main span

8.6.2 Largest wave induced loads in the bridge

Some of the wave induced loads in the bridge girder and tower support is presented in Table 8.21 and 8.22. These components are chosen just to illustrate some of the tendencies for this condition compared to wave condition 3. The result in Table 8.21 are presented for the point where the largest absolute maximum and minimum values occurs.

The results in Table 8.21 appears to be larger than those reported for wave condition 3 in

Chapter 8.5.3. The largest difference occurs for the absolute minimum weak axis moment, where the response for wave condition 4 is nearly 53% larger. For the torsional moment the maximum value in Table 8.21 is about 43% larger, while less differences is on the other hand observed for the strong axis moment. It is also observed that the largest weak axis and torsional moment has shifted towards the main span, with the extreme values occurs at axis 3 and between axis 3 and 4 respectively. For definition of the bridge axes see Chapter 4.1. For the moments at the tower support the behaviour is slightly reversed, i.e. the condition with fully correlated waves gives in general larger values. As an example is the strong axis moment about 34.06% larger for wave condition 3 than in Table 8.21. The exception is for the absolute maximum torsional moment where the result in Table 8.22 is approximately 55% larger than the corresponding value for the fully correlated condition. Thus it appears that wave condition 4 is the worst condition with regard to moments in the bridge girder, but not necessarily the worst condition for other types of response. This is evident for the horizontal displacement and tower moments, which is more severe for wave condition 3. One should also note that only one set of random phase angles are used in this investigation in addition to a simulation length of 1000 seconds. In general one should run with more sets of random seeds in addition to a longer simulation to have a better basis for choosing the most severe condition correctly.

Table 8.21: The absolute maximum and minimum values for the three moment components along the bridge girder.

	Maximum value Minimum value	Stress	Location
Weak axis moment	1389.60 [MNm] −1358.60 [MNm]	322.71 [MPa] −315.51 [MPa]	At axis 3, east side girder
Strong axis moment	1114.70 [MNm] −1108.00 [MNm]	−305.90 [MPa] 306.05 [MPa]	North end support, east side girder
Torsional moment	775 [MNm] −737.08 [MNm]	160.79 [MPa] 152.91 [MPa]	Between axis 3 and 4, east side girder

Table 8.22: The absolute maximum and minimum values of the moment components at the tower support.

	Maximum values Minimum values	Effects from permanent load
Weak axis moment	3482.62 [MNm] −3582.95 [MNm]	1802.41 [MNm]
Strong axis moment	1604.10 [MNm] −1460.74 [MNm]	−1393.46 [MNm]
Torsional moment	215.66 [MNm] −179.31 [MNm]	11.47 [MNm]

8.6.3 Closer look on the weak axis moment at bridge axis 3

The wave induced weak axis moment for the present condition reviled to be larger compared with fully correlated waves from north-west. Therefor some attention was put on checking whether this could be explained by handling the correlation in the wave excitation forces differently, i.e. by using different phase angles caused by the pontoon locations. Figure 8.42 shows how the weak axis moment in the east side girder varies with time at axis 3, for wave condition 3 and 4. One should note that the effect from permanent loads is included in these figures.

(a) Whole time series.

(b) Part of time series.
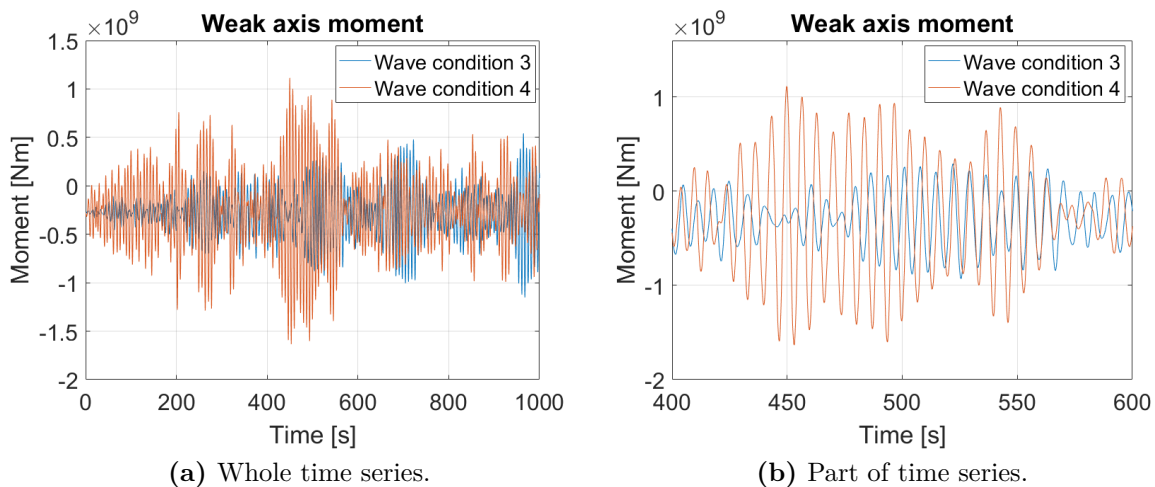
Figure 8.42: Comparing weak axis moment at axis 3 in the east side girder for wave condition 3 and 4.

Figure 8.42b presents the region with the largest response for wave condition 4, and shows that these are considerably larger than for wave condition 3. Between 400 and 600 seconds the dominating motions is pendulum motion at axis 3 and 4 which is part of eigenmode 35. Axis 3 is at the rightmost pontoon in Figure 8.43b and axis 4 at the leftmost pontoon in the same figure. In Chapter 8.6.1 it was also noted that the vertical motions at axis 3 appears to have a large contribution from a period close to this eigenmode and as a consequence this large response could be a cause of dynamic amplification. A similar period was also seen for condition 3, but if the wave forces at the two pontoons pushes towards each other as in Figure 8.43b it could trigger the eigenmode to become more dominant. Figure 8.43a shows that the wave excitation force in surge at the two pontoons in Figure 8.43b appears to be out of phase in the same region as the largest moments occurs in wave condition 3 in Figure 8.42b. In addition the amplitudes of the wave forces are relatively large, where some of the negative components are up to about 77% of the characteristic largest value for a short term sea state as presented in Chapter 8.2.2. One explanation could therefor be that the phase difference in the surge force causes a situation similar to Figure 8.43b, which gives amplification to eigenmode 35.
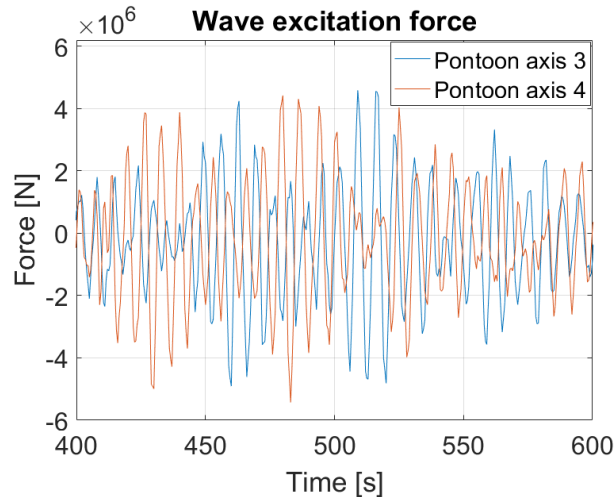
(a) Wave force at two pontoons.
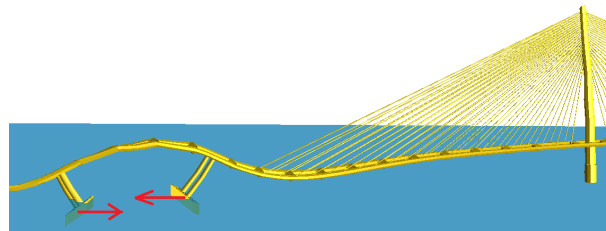
(b) Illustrated out of phase surge force.

Figure 8.43: Wave excitation force in surge at two pontoons and illustrated out of phase surge force at the same pontoons.

8.6.4 Most utilized components

The component with the largest utilization during the 1000 second analysis is illustrated in Figure 8.44 as the "Critical location". At this point the largest plastic utilization is 0.93, which means that the component actually experience yielding in some locations. Further, one may get a value closer to 1 for simulations with longer duration. Since the structure should have a stress level well below the yield stress in a ULS condition the yield capacity was artificially increased for all components to ensure elastic behaviour in the characteristic response calculations. When the large value occurs at this point the contribution from weak axis moment is the largest giving a stress of about 410 [MPa], while strong axis and torsional stress are 150 and 35 [MPa] respectively. The wave induced part of the weak axis moment is approximately 300 [MPa], i.e. 73% of the total weak axis stress. It is also evident from this figure that the columns at the leftmost pontoon has large utilization. A similar utilization is seen for all columns in this figure during the analysis.
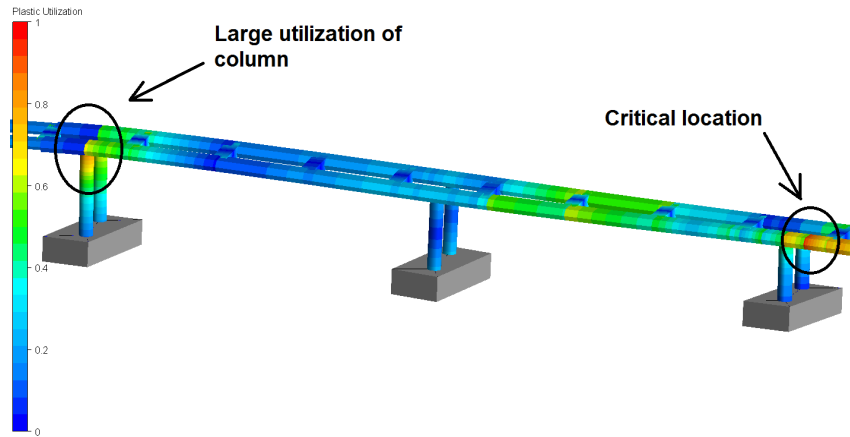
Figure 8.44: Most utilized component caused by wave loads between axis 3 and 5.

8.7 Effects from swell sea

The effect of including swells in the wave simulations was mainly analysed for wave condition 4. This because the condition was chosen to be used for the characteristic wave response calculations, see Chapter 8.8. Some comments will also be made for wave condition 1 as this is used when studying the effect of applying wind and wave loads in the same analysis, as will be discussed in Chapter 8.10. All results in this section is obtained using force components caused by swell sea, i.e. wind generated wave components are not present, while drift loads are included to be consistent with the previous results.

8.7.1 Effect of swell: Wave condition 4

The criterion used to select the design swell sea state was induced moments in the bridge girder. Figure 8.45 presents the absolute maximum weak axis bending moment along the east side girder for three 1000 seconds simulations with different peak period. The same significant wave height is used in all three analysis and the random seeds are the same as used in the four wind generated wave conditions. It is evident from Figure 8.45 that a peak period of 12 seconds yields the largest weak axis moments of the three cases studied. The weak axis moment caused by this peak period is approximately 12% of the moments induced by wind generated wave at axis 3. A similar effect is also seen for both torsional moments and strong axis moments. A swell sea state described by a peak period of 12 seconds is therefor used in the characteristic response calculations.

When the bridge is exposed to pure swell sea the motions of the bridge girder are experiencing more pure vertical motions than for wind generated waves. This is confirmed by studying the frequency domain solution for the vertical displacement at two points in
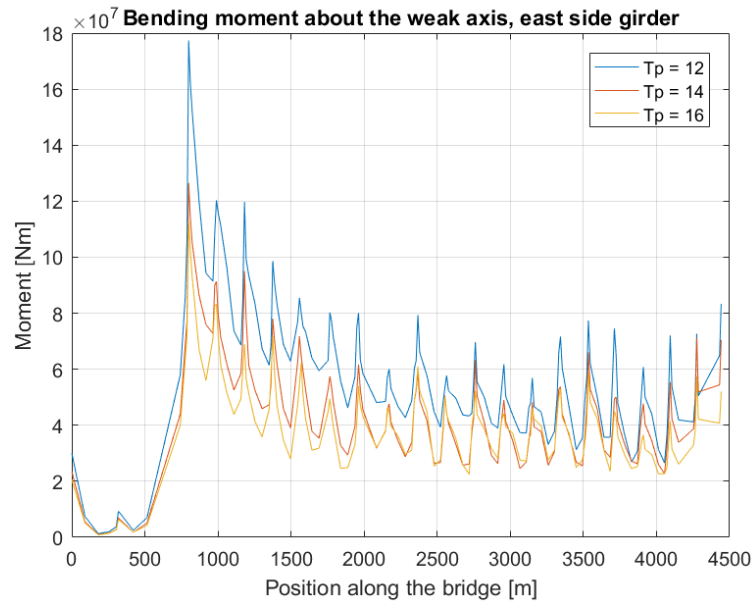
Figure 8.45: Absolute maximum weak axis moment in the east side bridge girder due to swell sea with three different peak periods.

Figure 8.46. The dominating frequencies are located between approximately 0.08 and 0.1 [1/s], with the largest peak close to 0.08 [1/s] for axis 3 and 0.09 [1/s] for axis 11. These corresponds to periods of 12.5 and 11.11 seconds, respectively. The latter is the same period as eigenmode 15 which is a pure heave mode consisting of seven half waves in the vertical plane, while a period of 12.5 seconds corresponds to the peak frequency of 0.08 [1/s] in the applied heave force in Figure 8.46b. Thus, the largest peak at axis 3 appears to reflect the applied load. The second largest peak at axis 3 is close to eigenmode 20 and 21 with 11 and 12 half waves in the vertical plane, respectively. By comparing these findings with the frequency domain solution for pure wind generated waves in Chapter 8.6.1 it is evident that the swell causes more energy in the range of the vertical modes than wind generated waves. The largest vertical displacement is approximately 0.80 meters, which is 58% of the largest value for wind generated waves. This value occurs between axis 4 and 5, while 0.3 meter is the maximum displacement that occurs at the point with the largest values for wind generated waves. This illustrates some of the tendencies observed, namely that the vertical displacements caused by swell is in the same range as the wind generated waves for the floating part. While for the end of the main span swell cases lower displacement.

(a) Vertical displacement.

(b) Heave excitation force.
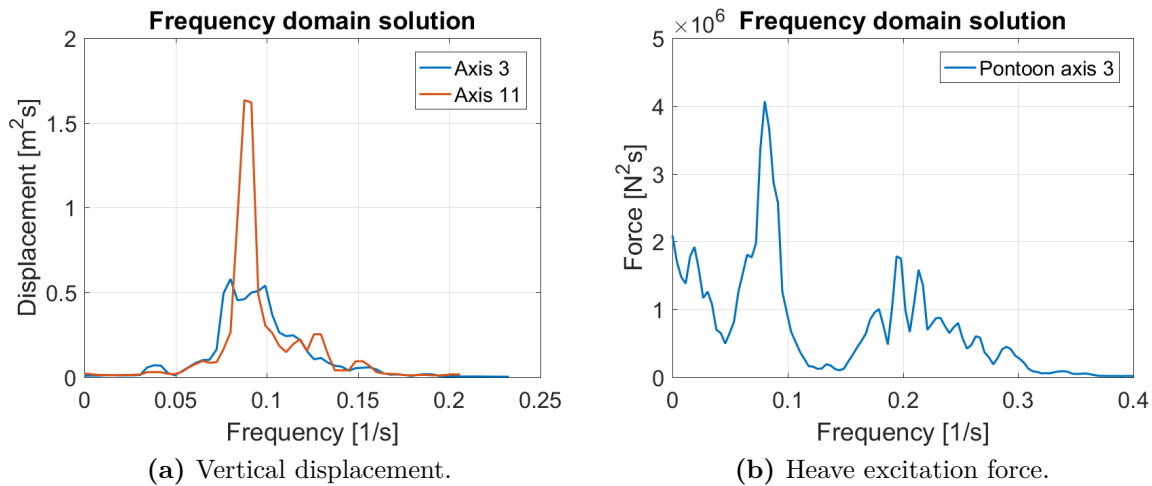
Figure 8.46: Frequency domain solution of the vertical displacement at two points and the applied heave excitation force at axis 3.

8.7.2 Effect of swell: Wave condition 1

For wave condition 1 the largest vertical displacement induced by swell sea with a peak period of 12 seconds is approximately 0.6 meters, compared to 0.35 meters for wind generated waves only. It should be noted that the displacements for the latter case are mainly cased by roll motion of the pontoons, while in the former case the heave wave force appears to be the main source of these vertical displacements. This observation may imply that swells with this peak period induces considerable vertical motions of the bridge girder, for wave condition 1. Therefor some extra attention was put on this behaviour by running a simulation with only the heave component of the wave forces from swells. It should be noted that the wave forces are applied fully correlated in this wave condition.

Figure 8.47 and 8.48 shows the response of the bridge girder when applying the heave force from swells. The whole bridge girder oscillates with a period of approximately 11.75 seconds, with the shape illustrated by these figures. This shape is not an eigenmode but could be a consequence of applying the wave forces as fully correlated. Due to the length of the bridge the main contribution to the heave stiffness comes from the pontoons, when the bridge oscillates with this shape. With this in mind and the fact that the heave wave force is acting simultaneously on each pontoon, one may get a situation where the response is governed by the pontoon properties. To check this the vertical displacement at the bridge girder right above the pontoon at bridge axis 11 was compared against the heave motions of a single pontoon exposed to the same sea state. The time-varying heave motions of a single pontoon can be established using the transfer function obtained from the Wadam analysis. Figure 8.49 presents the heave motions measured right above the pontoon from the USFOS analysis together with the response calculated using the transfer functions of

the heave motion. It is seen from this figure that the response follows the same pattern for both approaches and the motions also appears to be in phase. This seems to confirm that the vertical bridge motions in USFOS are predominated by the pontoon properties in this condition, which could explain the relatively large motions that are observed. A single pontoon has an eigenperiod around 11 seconds, and by applying swell loads with a peak period of 12 seconds one gets dynamic amplification of the vertical motion with displacements up to 0.60 meters. In comparison if the characteristic largest heave force from swell had been applied statically to one single pontoon, the vertical displacement should have been 0.11 meters.

Figure 8.47: Bridge shape at maximum vertical displacement for fully correlated swell from west. Displacements scaled with a factor of 100.

Figure 8.48: Bridge shape at minimum vertical displacement for fully correlated swell from west. Displacements scaled with a factor of 100.

8.8   Characteristic wave response

It was chosen to use wave condition 4 in the characteristic response calculations, since these gave the largest moments in the bridge girder. This is important to note a different wave condition may prove to be more critical for other response types, as noted for tower support moments in Chapter 8.6.2. The characteristic response due to wave loading are established at selected locations based on the maximum response at these points from each simulation. Furthermore, each of the 90 one hour simulations are performed running a wave history with a duration of 1 hour and 350 seconds. This is done in order to erase the first 350 seconds from the analysis to remove possible transient effects in the characteristic wave response calculations. Both the effect from wind generated waves and swells are included in these calculations in addition to slowly-varying drift loads.

8.8.1   Bridge girder displacements and accelerations

The characteristic values for displacements and acceleration are presented in Table 8.23 for two locations on the bridge girder. At each location the characteristic response was calculated at three points and the largest out of these is presented in Table 8.23 for each response type. It is evident from this table that the accelerations and displacements are
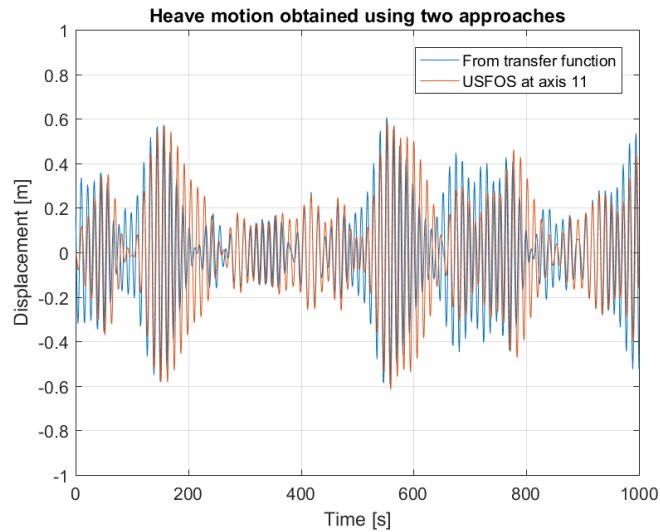
(a) Whole time series.
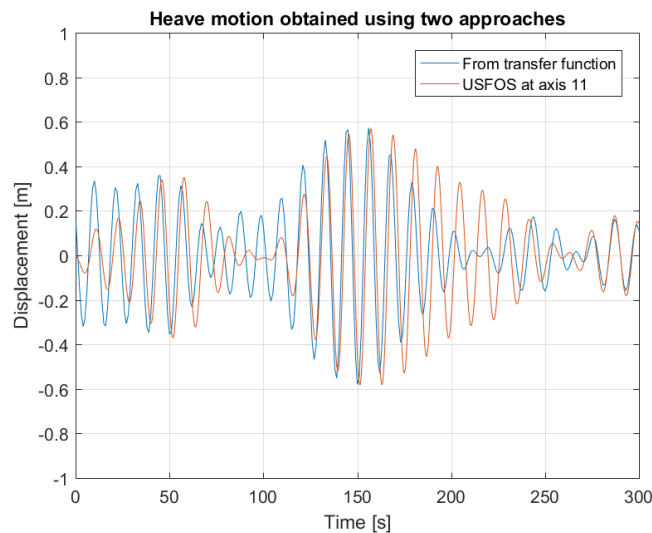
(b) First 300 seconds.

Figure 8.49: The vertical displacements of the bridge girder at at axis 11 together with the time series of the heave motion for one single pontoon exposed to the same sea state as in USFOS.

in general largest in the end of the main span which is located in the region with the longest cables towards axis 3. The exception is for the horizontal displacement which has a large negative value at the middle of the bridge. Such large negative values are also observed along most of the bridge and will be discussed further in Chapter 8.8.4.

Table 8.23: Characteristic wave induced displacement and acceleration for two selected locations on the west side girder.

Response component	Maximum value Minimum value	Unit	Location
Horizontal displacement	1.78 -2.55	[m]	End of the main span
Horizontal displacement	1.63 -4.20	[m]	Middle of the bridge
Vertical displacement	1.84 -1.78	[m]	End of the main span
Vertical displacement	1.55 -1.28	[m]	Middle of the bridge
Horizontal acceleration	1.84 1.80	[m/s^2]	End of the main span
Horizontal acceleration	1.36 1.38	[m/s^2]	Middle of the bridge
Vertical acceleration	1.71 -1.81	[m/s^2]	End of the main span
Vertical acceleration	1.20 -1.15	[m/s^2]	Middle of the bridge

8.8.2 Characteristic forces in the bridge girder, columns and tower foundation

The initial analysis showed that the weak and strong axis bending moments in addition to torsional moment gave the largest stresses. Therefor the main focus was put on establishing characteristic values for these components at the regions with the largest response in the initial 1000 seconds analysis. In Table 8.24 the characteristic values of the three moment components is presented at the locations where the larges individual values occurs in the bridge girder. Though wave condition 4 in Chapter 8.6.2 gave largest weak axis moment at bridge axis 3, the characteristic response is found to be larger at bridge axis 4. Other characteristic values in this table are the moments that must be resisted by the support of the tower in addition to the largest bending moment observed in the columns between axis 3 and 5. Only values for the east side girder is presented in Table 8.24 as the resulting moments are largest in this box girder at the points studied. Though it should be noted that the west side girder experiences wave induced forces of the same order.

The stress components induced in the bridge girder and column due to the maximum characteristic loads in Table 8.24 are presented in Table 8.25. Both the bridge girder and columns has an yield stress of 460 [MPa], and from Table 8.25 it is evident that the wave induced bending moment in the column at axis 4 exceeds the yield stress by a

Table 8.24: Characteristic wave induced response for some of the force components in the bridge girder, tower foundation and one of the columns.

Response component	Maximum value Minimum value	Unit	Location
Weak axis moment, bridge girder	1656.11 -1594.59	[MNm]	Axis 4, east side girder
Strong axis moment, bridge girder	1365.76 -1442.81	[MNm]	Support at north end, east side girder
Torsional moment, bridge girder	1204.52 -1221.03	[MNm]	Between axis 3 and 4, east side girder
Weak axis moment, tower foundation	4671.62 -4629.04	[MNm]	Tower foundation
Strong axis moment, tower foundation	2124.21 -1971.65	[MNm]	Tower foundation
Torsional moment, tower foundation	211.97 -290.63	[MNm]	Tower foundation
Bending moment, column	1683.97 -1583.55	[MNm]	Column at axis 4, east side

factor of 1.35. As components are not allowed to exceed the yield stress during a 100-year storm such large values would indicate that the column is dimensioned with a too low capacity. For the bridge girder the characteristic wave induced bending moments at the two locations causes stresses that are below the yield stress. Though in a design situation one has to add material and load factors to the steel resistance and characteristic loads, respectively. By using a material factor of 1.15 the design yield stress capacity is 400 [MPa]. Furthermore, by adding the stresses from permanent loads to those of the wave induced weak axis moments the total characteristic stress at axis 4 is 454.61 [MPa], i.e. without any load factors. The calculated characteristic values therefor implies that the design resistance at axis 4 must be increased against weak axis moment. At the north end support the maximum characteristic strong axis moment utilizes approximately 27% of the design resistance.

Table 8.25: Stress resultants caused by the characteristic wave induced forces in the bridge girder and one of the columns.

Response component	Stress	Unit	Location
Weak axis moment, bridge girder	384.61	[MPa]	Axis 4, east side girder
Strong axis moment, bridge girder	291.36	[MPa]	Support at north end, east side girder
Bending moment, column	621.39	[MPa]	Column at axis 4, east side

By comparing the largest torsional moment at the tower support with the results obtained

for the 1000 seconds analysis in Chapter 8.6.2 it is evident that the characteristic value is somewhat lower than the maximum response in the mentioned chapter. Figure 8.50 shows that most of the 30 largest torsional moments from the characteristic analysis are below a value of 200 [MNm]. In this region the fitted Gumble distribution appears to follow the empirical curve, while the deviations are larger at the upper tail. This is probably caused by the limited amount of data for the largest response and illustrates some of the uncertainty when establishing the characteristic response. Using Figure 8.50 implies that the response in Chapter 8.6.2 is a more rare event than the 0.90 fractile used in this thesis. A value of 2.25 on the vertical axis in this figure corresponds to a cumulative probability of 0.90.
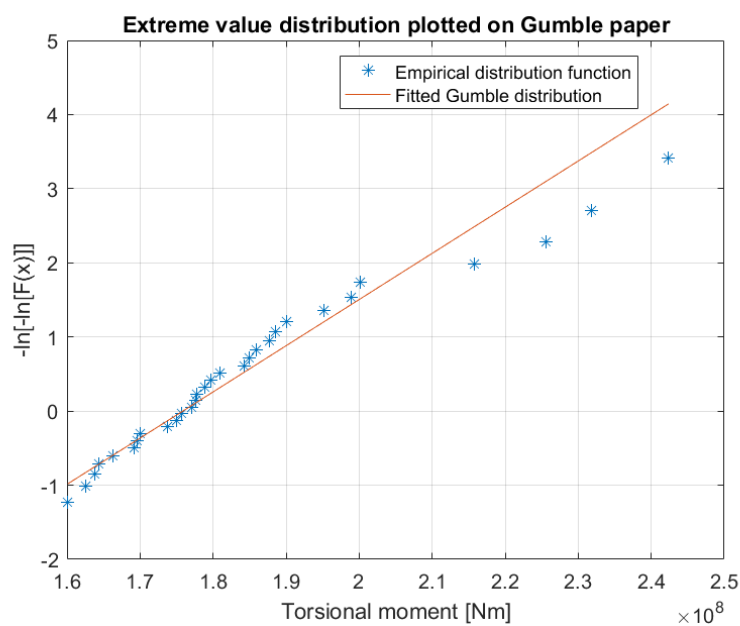
Figure 8.50: Illustration of the empirical distribution function and fitted Gumble distribution plotted on Gumble paper for the simulated data of torsional moment at tower foundation.

8.8.3 Characteristic axial cable force

The characteristic cable force was calculated individually for eight of the longest stay cables in each span, where the cable with the largest increase in tensile force is presented in Table 8.26 for both spans. It should be noted that a positive and negative value in this table refer to an increase and decrease in tensile force respectively, i.e. the stay cables do not go into compression. Another point is that all of the eight cables in each span experience forces in the same order. As an example, the smallest increase in tensile cable force in the main span is 87% of the value in Table 8.26.

From Table 8.26 it can be shown that the characteristic wave response for the cable in

Table 8.26: Characteristic wave induced cable forces.

Response component	Maximum value [N] Minimum value [N]	Stress [MPa]	Location
Cable force	2.15E+06 -2.51E+06	175.80 -204.88	Forth longest, west side of main span
Cable force	2.34E+06 -2.31E+06	169.57 -167.39	Longest, west side of side span

the main span gives a stress contribution which is approximately 9.45% of the cable yield stress. As a comparison the stress caused by the pretension in this cable is 490.24 [MPa] utilizing 26.36% of the yield capacity, and the sum of pretensioning and wave induced forces is thus 666.04 [MPa] which amounts to 35.80% of the yield stress. From this it could be concluded that the cables appears to have a sufficient resistance against the 100-year wave loads.

8.8.4 Drifting of the bridge towards the west side

One problem that arose when simulating wave condition 4 for a duration of one hour was drifting of the whole bridge towards the west side. This is illustrated in Figure 8.51 which shows that the horizontal displacement in global x-axis at the middle of the bridge diverges in negative direction. At the end of this simulation the point has drifted almost 2.5 meters. This behaviour is largest at the middle part of the bridge and will highly affect the displacements at this region. Another point is that such drifting may induce forces in the bridge girder and influence the strong axis moment at the support. There was not found a proper way to account for this behaviour, and this effect will therefor introduce uncertinity to the characteristic horizontal displacement and strong axis bending moments.

8.9 Wind analysis

In order to get information on how the bridge responds to mean and fluctating wind initial analysis was performed using the same length of the simulations as for the four wave conditions. Some of the main results from these 1000 seconds analysis will be presented in this chapter with focus on the motions of the bridge girder.
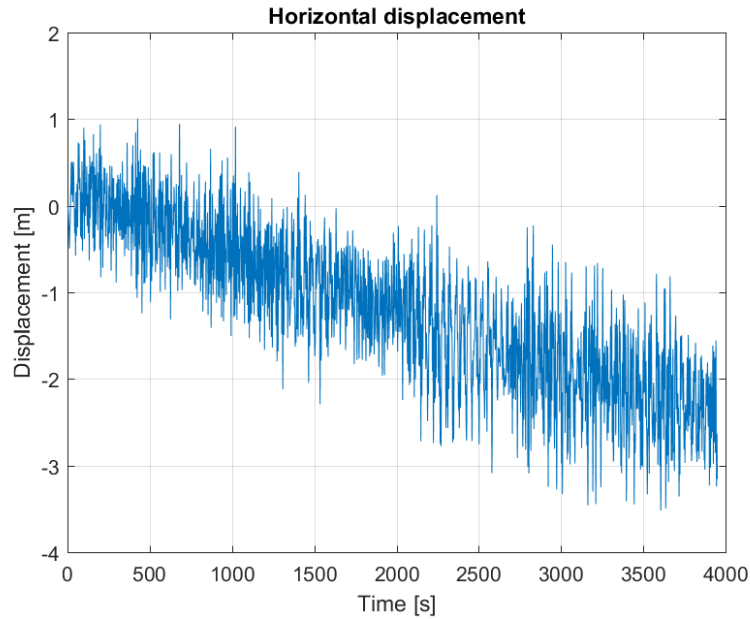
Figure 8.51: Drifting of the bridge girder towards the west side of the bridge.

8.9.1 Effect from the mean wind component

The effect from the mean wind component on the bridge girder horizontal displacement is illustrated in Figure 8.52, where the curve represents the shape of the bridge viewed from above. Further, the navigation channel is located in the leftmost corner and north support at the rightmost corner of this figure. This figure shows that most of the bridge is pushed from west to east, which is also expected as the wind is applied in this direction. For definition of west and east see Chapter 4. Furthermore, the effect from mean wind is largest arround bridge axis 8, i.e. 1750 [m] in Figure 8.52, where the displacement is approximately one meter. It is also interesting to note that the displacement pattern is not symmetric about the midpoint of the bridge. One source for this observation could be that the bridge has different supports at the north and south end. At the north end the bridge girder is fixed, simulating the connection to the land. While in the south part the cable stayed bridge and connection to the tower at axis 2 may cause different stiffness properties than in the north support. Another point is that the bridge is curved, which may force the bridge girder into a pattern which is more complex than one single half wave which is expected for a straight bridge. These effects may explain the displacement pattern in the north end, where the bridge is pushed into an opposite manner than the rest of the bridge. The resulting mean bending moment about the strong axis for the east side girder is presented in Figure 8.53. It should be noted that the west side girder has a similar distribution except at the tower, i.e. at about 370 meters in Figure 8.53, where the west side girder has a peak of about 4.5E+07 [Nm].
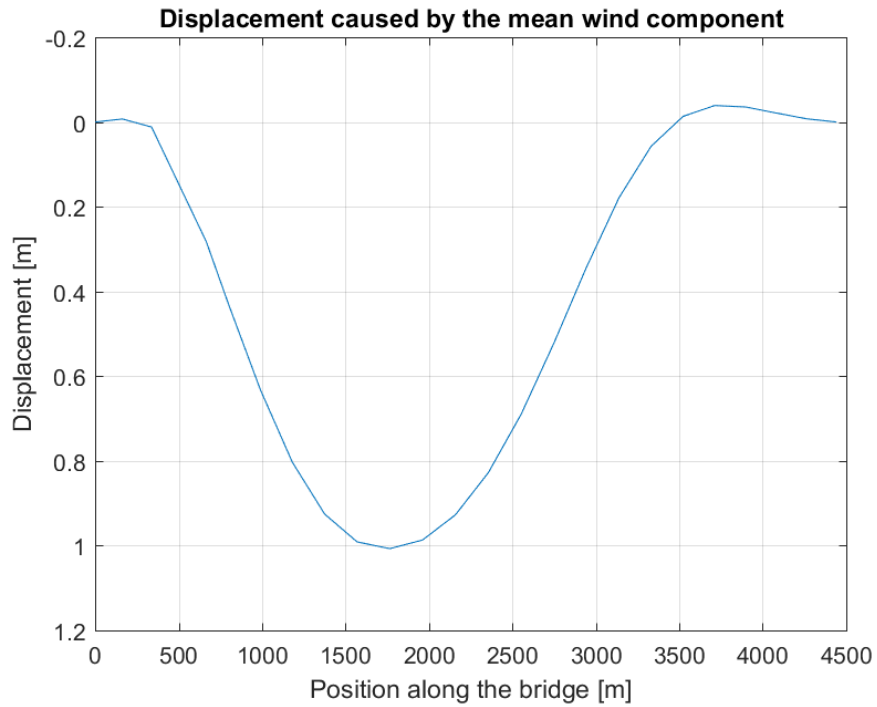
Figure 8.52: The displacement pattern of the bridge girder caused by the mean wind component. Positive displacement is directed towards the east side of the bridge girder.
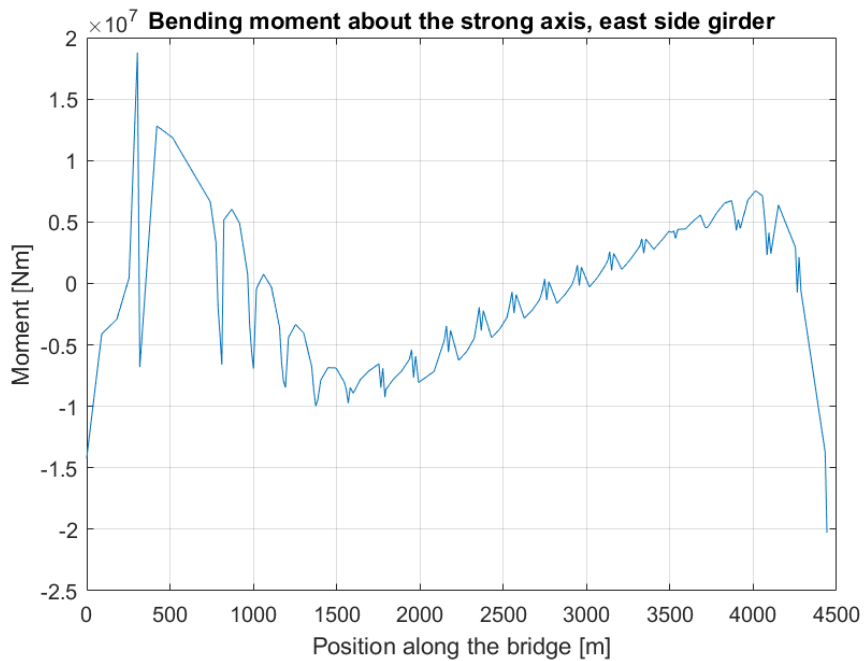
Figure 8.53: Strong axis bending moment caused by the mean wind component.

8.9.2 Combined mean and fluctuating wind

The frequency domain solution of the horizontal displacement is presented in Figure 8.54. The largest peak at axis 11, i.e. the middle of the bridge, is found at 0.025 [1/s] or a period of 40 seconds. This period is close to the second eigenmode consisting of three half waves in the horizontal plane. The largest peak at axis 3 is located at approximately 0.013 [1/s], corresponding to a period of 74.9 seconds when using all digits in the frequency component. This is a oscillation period which is 10 seconds larger than the first eigenmode, and may be explained by the fluctuating wind having a component with this period. In that case it means the bridge follows the wind at axis 3.
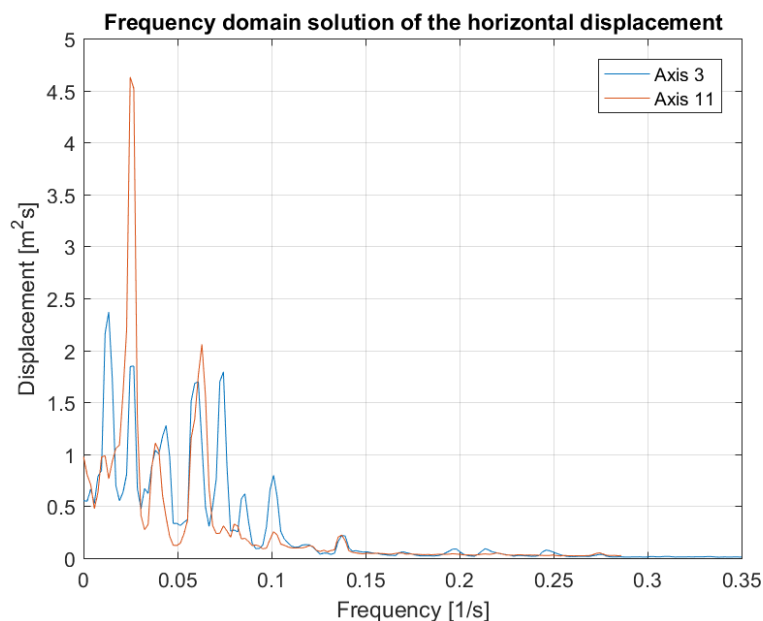
Figure 8.54: Frequency domain solution of the bridge girder motions at two locations.

Compared to the result from the wave analysis Figure 8.54 illustrates that the bridge girder response due to wind is to a larger degree dominated by low frequency components, i.e. larger periods. As an example the largest peaks in this figure are positioned below 0.1 [1/s], i.e. above 10 seconds, while in the case of fully correlated waves from west the horizontal motions had significant contribution between 10 and 5 seconds in addition to some large peaks at 44 seconds. This difference is also reflected in the bridge girder forces, where the strong axis moments are similar in magnitude to the wave induced forces. The strong axis moment obtained during the 1000 seconds analysis is presented in Figure 8.55. The weak axis and torsional moment caused by wind was on the other hand much lower than those due to waves, for the set of random seeds used in this wind analysis. The difference between wind and wave induced response will be studied more in detail in Chapter 8.10.
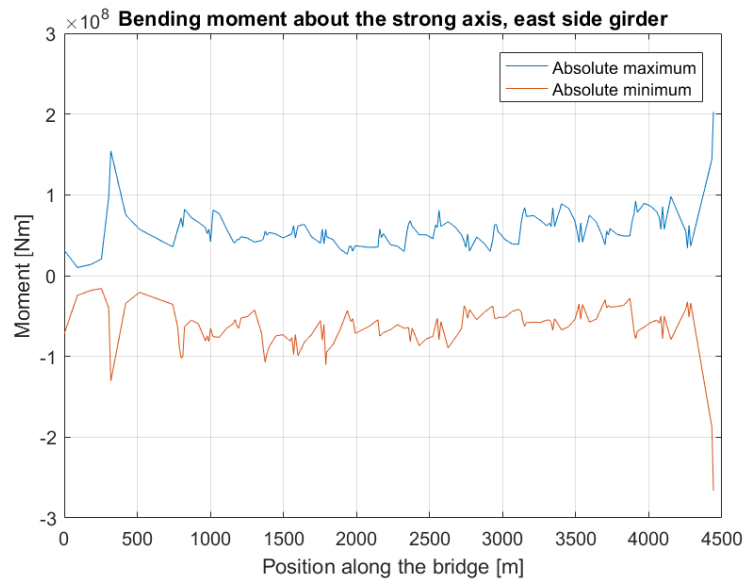
Figure 8.55: Absolute maximum strong axis moment at selected points along the east side box girder. The result is for one single 1000 seconds analysis.

By comparing the strong axis moment in Figure 8.55 with the response from pure mean wind component in Figure 8.53 it is evident that the fluctuating wind amplifies the strong axis moments. A similar effect is also seen for the horizontal displacement which is illustrated in Figure 8.56. According to this figure the mean wind explains only 37% of the total displacement for the node with largest horizontal motions in this analysis, which indicates that the fluctuating wind contributes with a large part of the largest displacement at this point.

8.10 Time domain analysis with wind and waves

The relative importance of wave and wind loads was analysed by running two sets of 10 one hour simulations. First 10 simulations was run including only the effect of waves. Secondly these was compared against results obtained by accounting for both wind and waves, using the same set of random phase angles for the wave loads. Some of the results from this investigation is presented in Table 8.27 where the results are averaged over the total of 10 simulations for both set. To get a good prediction of how the bridge responds to a combined wind and wave loading one should probably run more than 10 one hour simulation. The approach is on the other hand used as it will give some information about the tendencies, which is of main interest in this thesis. As for the characteristic response calculations the first 350 seconds of the analysis with environmental loads are disregarded to remove transient effects. The goodness of this will be discussed later in this section.
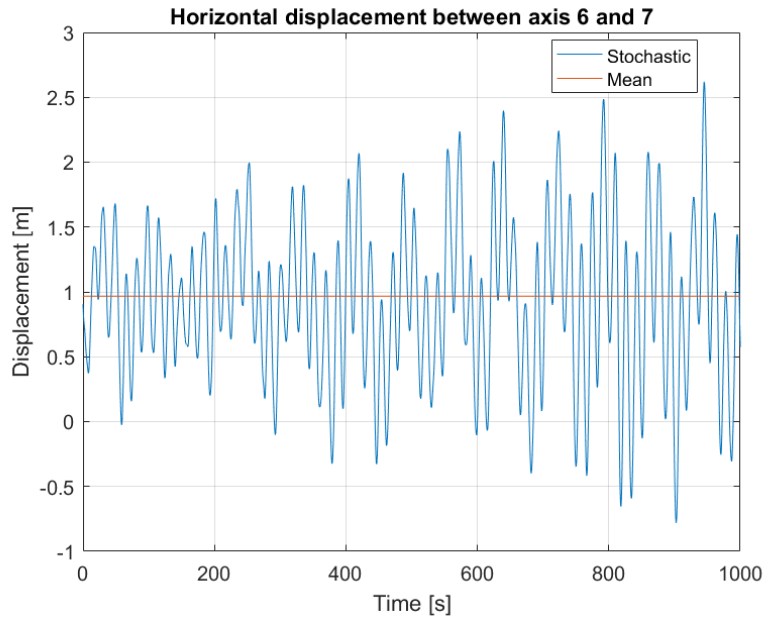
Figure 8.56: The contribution to the total displacement at a node in between axis 6 and 7 is illustrated in this figure.

Furthermore, both wind and waves are assumed to come from west with fully correlated waves including the effect from swells. These swells are described by the same sea state as used in the characteristic response analysis.

From Table 8.27 it is clear that the horizontal displacements increases when including the effect from wind. It is also seen that the positive displacement is larger in absolute value than the negative, which may be explained by the mean wind component giving a positive displacement contribution. Another point is that the negative displacements are in the same range for the results with and without wind. By keeping in mind the mean horizontal displacement caused by wind, this observation may illustrate that the fluctuating part also gives significant contribution to the negative values. The horizontal displacement at the middle of the bridge is presented in Figure 8.57a for one of the simulations and compared against the corresponding pure wave analysis, i.e. using the same set of random phase angles for the wave loads. This figure shows that the largest peak occurs at a point where the pure wave induced motions are small, indicating large displacement caused by the fluctuating wind.

The largest vertical displacements of the bridge girder is also presented in Table 8.27. For this response including wind gives minor differences and could indicate that waves are the main contributor to this motion. This is confirmed by Figure 8.57b which illustrates that the vertical displacement at the point "between axis 4 and 5" in Table 8.27 are almost the same as the pure wave induced response. Even though the difference between the average vertical displacements for the two sets of simulations are relatively small, the vertical

Table 8.27: Averaged results from two sets of 10 one hour simulations where the effect of including both waves and wind in the same simulation is studied. The bridge girder displacements in this table are measured on the west side girder as the east side exhibits similar behaviour.

Response component and unit	Waves only: *Maximum values* *Minimum values*	Wind and waves: *Maximum values* *Minimum values*	Location
Horizontal displacement, [m]	0.97 −1.01	1.77 −1.09	End of main span
Horizontal displacement, [m]	1.00 −0.88	2.41 −0.62	Middle of the bridge
Vertical displacement, [m]	1.00 −0.95	1.10 −1.00	Between axis 4 and 5
Vertical acceleration, [m/s^2]	0.16 −0.17	0.58 −0.60	Middle of the side span
Horizontal tower tip displacement, [m]	0.23 −0.27	0.70 −0.30	Tip of tower
Strong axis moment, bridge girder, [MNm]	395.14 −421.46	437.07 −498.71	North end, east side girder
Weak axis moment, bridge girder, [MNm]	342.85 −320.47	340.38 −341.32	Axis 3, east side girder
Strong axis moment, tower foundation, [MNm]	657.91 −546.91	774.11 −1629.41	Tower foundation

accelerations in the cable stayed part are larger when including wind. From Table 8.27 it is clear that the positive acceleration increases with a factor of nearly 3.6, while the vertical displacements in this region are less affected. This observation could be a result of the observed high frequent oscillations for simulations with fluctuating wind. These high frequent motions could be caused by a combination of the tower motions, which has significant displacement due to wind, and the large stiffness of the stay cables. The large stiffness may result in oscillations with large frequency giving low amplitudes for the displacement, but large accelerations, when the tower oscillates.

The results in Table 8.27 shows that while the horizontal displacement of the bridge girder has notably differences, the largest strong axis moments at the north support is only slightly affected when including wind. This does not necessarily mean that the wind has insignificant contribution, especially as the initial analysis with wind for one set of random seeds gave strong axis moments in the same order as waves. Though it may actually illustrate that the largest peaks caused by wind and waves do not occur simultaneously, in general. This behaviour is accounted for by using combination factors in limit state design (Naess & Moan, 2012, Ch. 13.12.1). Further, it should be noted that the largest increase in average positive strong axis moment occurs in the bridge girder at
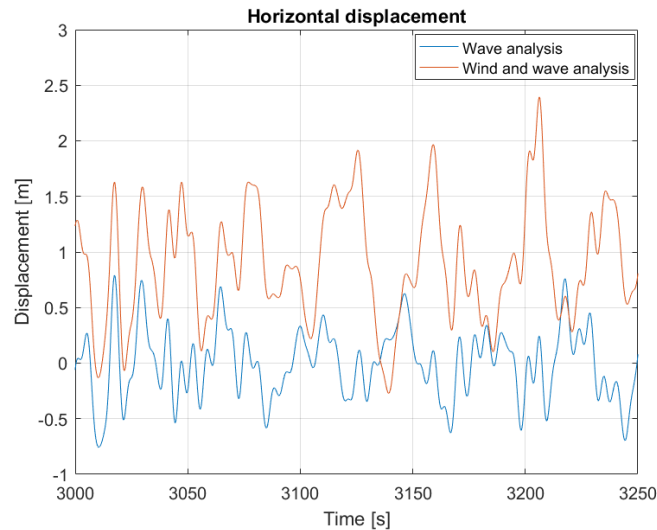
(a) Horizontal displacement.
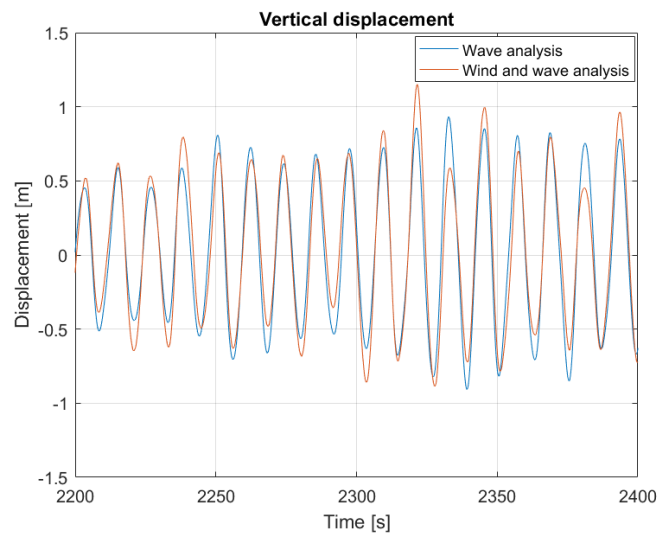
(b) Vertical displacement.

Figure 8.57: The difference in horizontal and vertical displacement is presented in this figure for two simulations, where one contains only wave forces and the other includes waves and wind. The same random seeds are used for the wave forces in these simulations. Figure 8.57a shows the horizontal displacement at the middle of the bridge, while the vertical displacement between axis 4 and 5 is presented in Figure 8.57b.

the connection with the tower at axis 2. At this location the average strong axis moment is increased with a factor of 1.88 in the west side girder, compared with the simulations with only waves forces. Consequently the wind loads gives a large contribution at this location.

The weak axis moment in Table 8.27 is the largest average weak axis moment out of the locations studied. There are only slightly differences between the averaged maximum

and minimums for the two simulation sets, which was expected as the initial pure wind analysis gave small contributions to this response compared to waves. Except for some increased value at the north support most parts of the bridge seems to exhibit the same tendencies, i.e. that including wind have minor effect on this response component. A similar behaviour is also observed for the torsional moment.

The tower experience a large increase in absolute value of the negative strong axis moment, which must be supported at the foundation. By comparing the two results in Table 8.27, this difference corresponds to a factor of nearly 3. The absolute value of the negative strong axis moment will increase when the tower tip is deflected in positive x-axis, which could be illustrated as a cantilever beam. Due to the mean wind it is therefor expected that the absolute value of the negative moment should be larger than the maximum weak axis moment, which is in accordance with the result in Table 8.27. The fluctuating wind gives also large motions of the tower, consequently it is natural that the it will be exposed to larger forces.

Transient effects due to wind

The horizontal displacement is presented in Figure 8.58 for a simulation including only the mean wind component and combined against an analysis with both mean and stochastic wind. The point at axis 8 was studied as the displacement caused by the mean wind is largest at this location and therefor gives the largest contribution to the total displacement. This figure illustrates that in the initial 200 seconds, the oscillations caused by transient effects from applying the mean wind appears to give a large contribution to the total displacement. While from 200 seconds and above, the oscillations are primary dominated by the fluctuating part of the stochastic wind field. As the oscillations caused by the mean wind seems to give some contribution up to 800 seconds one could argue that the first 800 seconds of the analysis should be disregarded. This to make sure that transient effects are not affecting the result. Nevertheless only the first 350 seconds are disregarded in the final wind and wave analysis, this to be consistent with the approach used for establishing the characteristic response from waves. Figure 8.58 also illustrates that even though there are some oscillations caused by the mean wind after 350 seconds, the predominating part for this particular set of random seeds comes from the fluctuating wind. This may change for other random sets, but as the transient oscillations above 350 seconds are relatively small it was decided to use this approach.
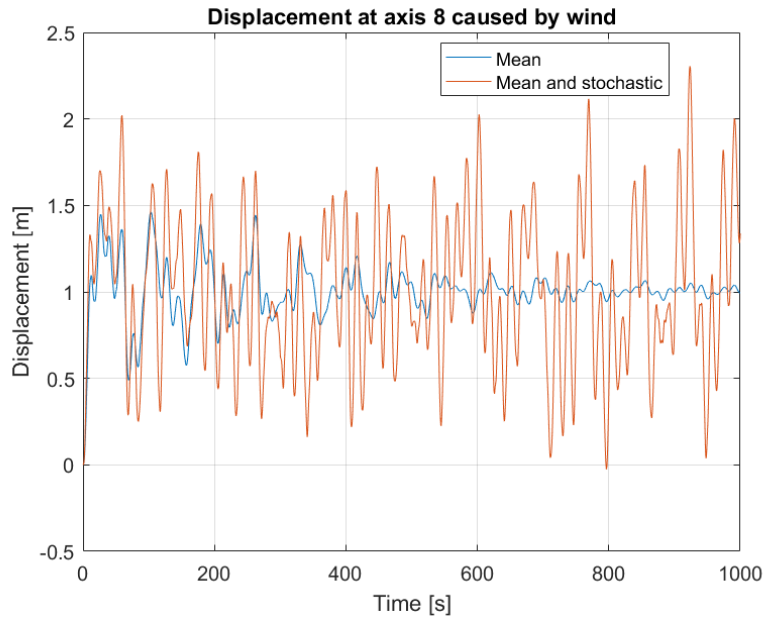
Figure 8.58: Displacement at axis 8 during the first 1000 seconds of two one hour analysis. The effects from the mean wind component is compared against a simulation including mean and stochastic wind.

8.11 Collision scenario 1: Impact with the pontoon at navigational channel

In collision scenario 1 the ship collides with the pontoon and column at axis 3. Initially the impact is taken locally as a twisting of the bridge girder at this location, which is illustrated in Figure 8.59 for an impact energy of 1000 [MJ]. The impact energy is further distributed to the rest of the bridge through a large transverse deflection going to the north side in addition to twisting, causing a global oscillating behaviour. These motions illustrate the kinetic energy transferred to the bridge from the initial impact energy and is damped out by structural and hydrodynamic damping as well as plastic deformations. In the following the global behaviour of the bridge will be addressed together with some of the main results using different impact energy for collision scenario 1.

8.11.1 Impact energy of 1000 [MJ]

Collision force

The force-deformation curves for the forecastle and bulb is presented in Figure 8.60a and 8.60b respectively. Both of these figures shows the force-deformation curves that are
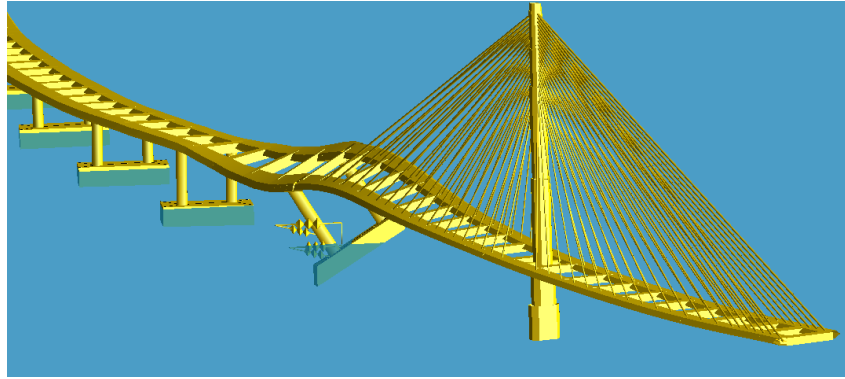
Figure 8.59: Initial deformations at axis 3 caused by a ship impact of 1000 [MJ]. The displacements are scaled with a factor of 10.

produced when the ship mass is decelerated against the non-linear springs representing the ship's stiffness. These are plotted against the curves given as input to the simulations, illustrated by the stipulated lines. As the time varying collision force is constructed using the resistance curves of the vessel it is importaint that these are correctly reproduced in the analysis. The two figures shows that the curves appears to be similar to those given as input. It is also evident from Figure 8.60a that the non-linear spring of the forecastle unloads at two locations between 8 and 9 meters of indentation. At a deformation of nearly 8.5 meters the column deflects away from the ship causing the first unloading. When the forecastle comes in contact with the column at a later stage the spring "remembers" the previous damage and continues on the deformation curve. This illustrates that the non-linear spring behaves as they should.

By taking the integral under the force-deformation curves up to the final damage one may estimate the total energy dissipated in the vessel. This information is given in Table 8.28 for both the bulb and forecastle together with the remaining of the initial impact energy. From these results it is evident that the bulb dissipates most of the deformation energy, which is natural as it must take all damage until an indentation of 5.34 meters, see Chapter 6.3.1. The remaining energy is somewhat larger than half the impact energy and illustrates the size of the total kinetic energy of the colliding objects right after the impact. It should be noted that the forecastle includes the fictitious deformation energy caused by the first 5.34 meters, but this is included as it will dissipate energy in the analysis.
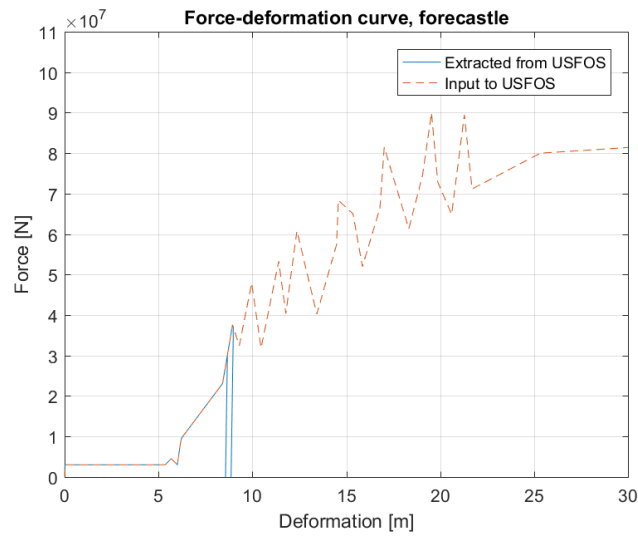
(a) Forecastle
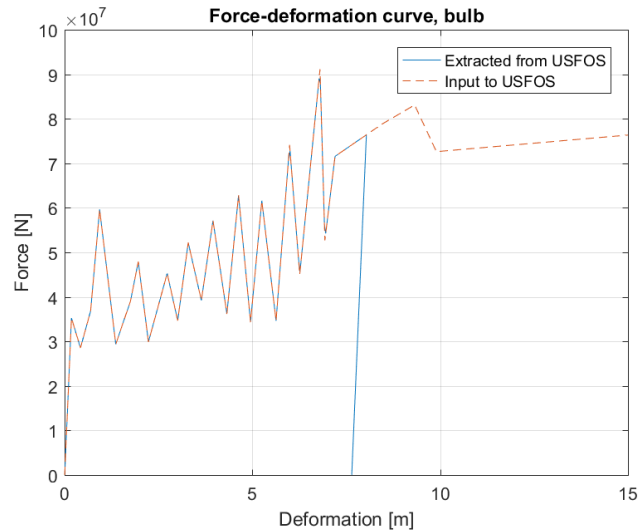
(b) Bulb

Figure 8.60: Force-deformation curves for the forecastle and bulb of the cruise ship.

Table 8.28: Deformation energy dissipated by the forecastle and bulb together with the remaining energy.

Energy component	Value [MJ]	Percentage of the initial impact energy
Deformation energy, forecastle	71.14	7.10%
Deformation energy, bulb	382.60	38.26%
Remaining energy	546.00	54.60%

Global motions

The global transverse motions of the bridge girder is illustrated in Figure 8.61 for three different points in time during the first 32 seconds of the collision analysis. In this figure the bridge is viewed from above with the north end in the rightmost corner and the cable stayed part in the leftmost corner. These figures shows that the initial motions at 4.71 seconds are very localised arround the impacted location which spreads out as a transverse wave to the north end. It is also interesting to see that it takes approximately 27 seconds from the shock wave starts to propagate from axis 3 at Figure 8.61a until it reaches the north end in Figure 8.61c. As this distance is about 3700 meters, this shock wave has to travel with a speed of 137 [m/s]. The time in these figures is relative to the instant when the collision is applied.

(a) 4.71 seconds.

(b) 17.91 seconds.

(c) 31.49 seconds.
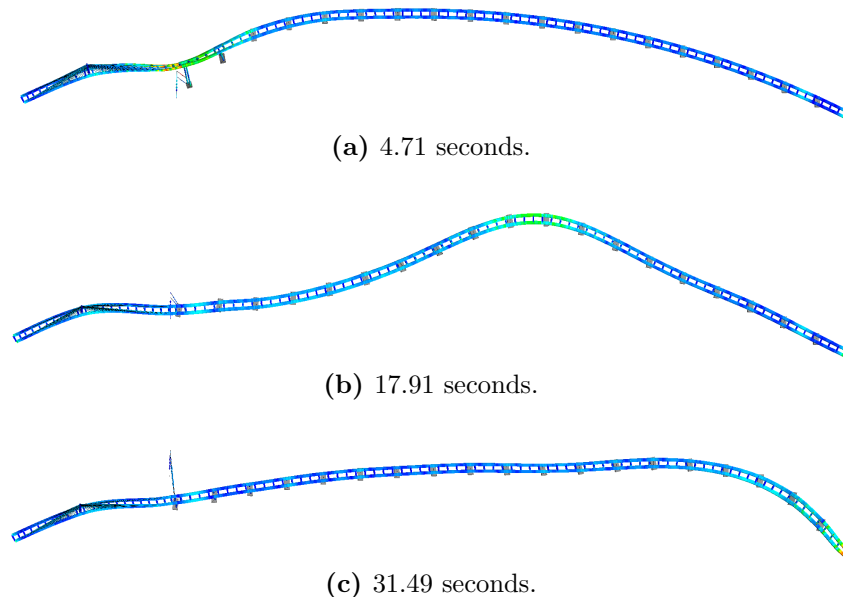
Figure 8.61: Horizontal displacement of the bridge girder at three different points in time after applying the impact. The displacements scaled with a factor of 20.

The frequency domain solution of the horizontal displacement in global x-axis is presented at two locations in Figure 8.62. These two points are located on the bridge girder where axis 3 is right above the impacted pontoon, while axis 11 is positioned at the middle of the bridge. At axis 3 the two largest points of the peak with the most significant contribution has frequencies of 0.01221 and 0.01526 [1/s]. These corresponds to periods of 81.90 and 65.53 seconds respectively. The second period is close to the first eigenperiod of 65 seconds and may indicate that the motions at this location are dominated by the fundamental mode in the free oscillation phase after the impact. At the middle of the bridge the two largest point on the highest peak has frequencies of 0.02441 and 0.02747 [1/s], i.e. periods of 40.96 and 36.40 seconds respectively. The second eigenmode has a natural period of 37.02 seconds which is in between these dominating frequencies at this

location. From this one may conclude that the two largest eigenmodes are important for the bridge behaviour, for this collision scenario. It should also be noted that the first mode has zero displacement at the middle of the bridge as it rotates about this point, while the second mode has a peak at this region. This could explain why the horizontal displacements are predominated by mode 2 at bridge axis 11.
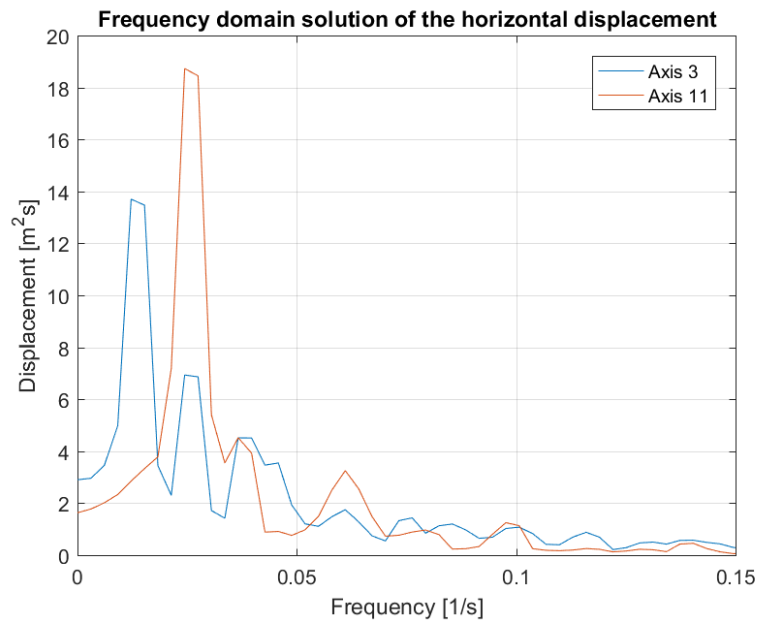
Figure 8.62: Frequency domain solution of the horizontal displacement at axis 3 and 11.

Figure 8.63 shows the resulting collision force-time histories that will act on the impact locations at the pontoon and column. It is seen from this figure that the initial crushing of the bulb causes a impact duration of 2.34 seconds. This is small compared to the relevant eigenmodes addressed above and confirms that the situation could be regarded as an impulse loading. From the same figure it could also be argued that the pontoon must resist large forces locally in the initial phase. As an example, during the first second the crushing force has reached a peak of 7.27E+07 [N], while the impacted point on the pontoon has displaced only 0.8 meters. In comparison the largest deflection of this point is about 11.5 meters after 8 seconds, which means that the pontoon has to carry large local forces. As a result of the assumed strength design the ship is forced to dissipate all deformation energy, but in a real situation the relative strength may change during deformation (Storheim & Amdahl, 2014, p.137), and the pontoon could start to deform. This may affect the global behaviour if the damage is considerable, but is not accounted for in these analysis. It could also be interesting to note that Figure 8.63a shows the unloading of the forecastle as mentioned previously, where the second crushing starts when there are no force from the bulb. This may be a cause of the pendulum behaviour of the pontoon and column illustrated in the figure at the introduction to this chapter, see Figure 8.59. Thus the resulting deflection of the pontoon will be larger than at the

column, such that the forecastle may come in contact with the column while the bulb is unloaded. At 10 seconds the bridge pushes the ship away and the free oscillation of the bridge starts.
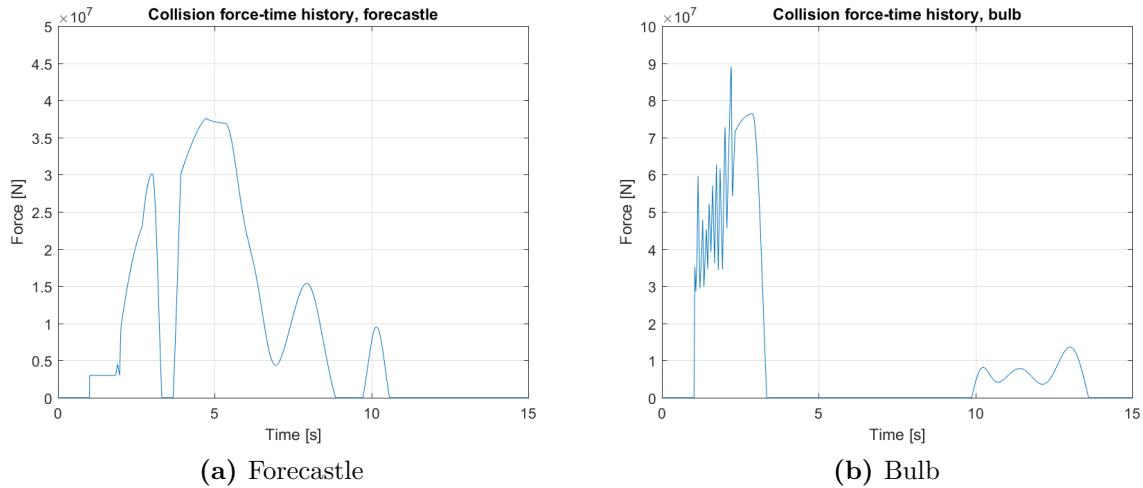
(a) Forecastle
(b) Bulb

Figure 8.63: Collision force-time histories for the forecastle and bulb of the cruise ship.

It was noted that collision scenario 1 gave a permanent displacement of the whole bridge girder and therefor some attention was put on finding the cause of this. The behaviour appears to be caused by plastic deformation of the cross beams, which is illustrated by Figure 8.64. This figure shows the horizontal displacement of the bridge girder at axis 3, where the blue curve is for the correct yield stress while the red curve is obtained by increasing the yield stress for the cross beams. It is seen from this figure that by increasing the yield stress of the cross beams the motion oscillates arround a value of zero displacement, while the in the case of normal yield stress it oscillates about a value of nearly 3 meters. This seems to confirm that the cross beams are the cause of the permanent displacement. The horizontal motions of the bridge girder induces large bending moments in the cross beams about the vertical axis. As an example experiences the "critical cross beam" in Figure 8.65 a bending moment of 469.40 [MNm], which is approximately 98% of the plastic bending moment. If these large moments causes plastic rotations of the cross beams it could explain the permanent displacements. The plastic rotation in the "critical cross beam" is about -0.009 [rad] and a similar value is seen for many of the other cross beams both in the main span and towards the north end. This may not be a very large rotation, but bearing in mind the large length of the bridge it could cause permanent displacements. It should be noted that these rotations could be a cause of switching the bending properties of the local y- and z-axis for these structural parts, which will be discussed in Chapter 9.

In addition to the cross beams it is also observed large utilizations in the bridge girder in the main span and north end. This is illustrated in Figure 8.65 and 8.66, where the
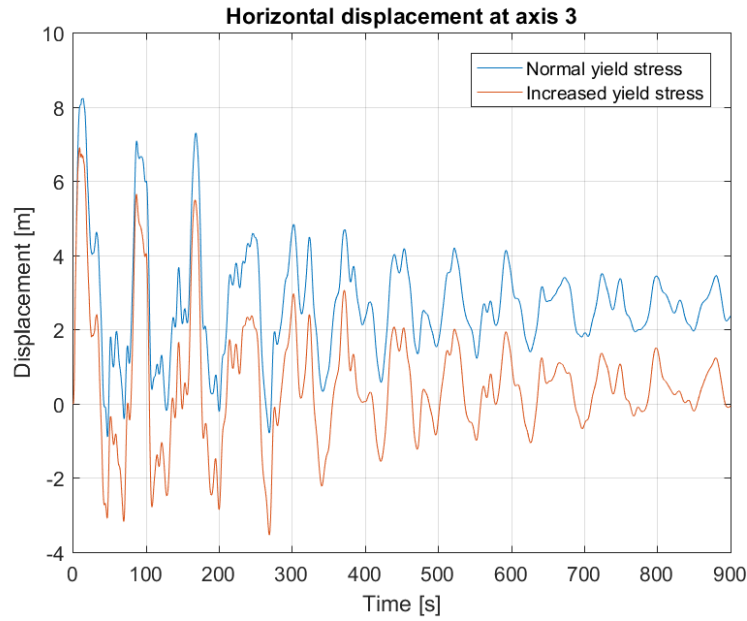
Figure 8.64: Horizontal displacement at axis 3 with normal and increased yield stress of the cross beams.

three locations marked with an arrow in Figure 8.65 was used to study the effect of having different impact energies of the colliding vessel. The column at axis 3 do also experience large loads from the ship impact where bending is the most important. For an impact energy of 1000 [MJ] this gave an utilization of approximately 0.84, but it was decided to focus on the mentioned parts as these had a larger utilization for this energy level.
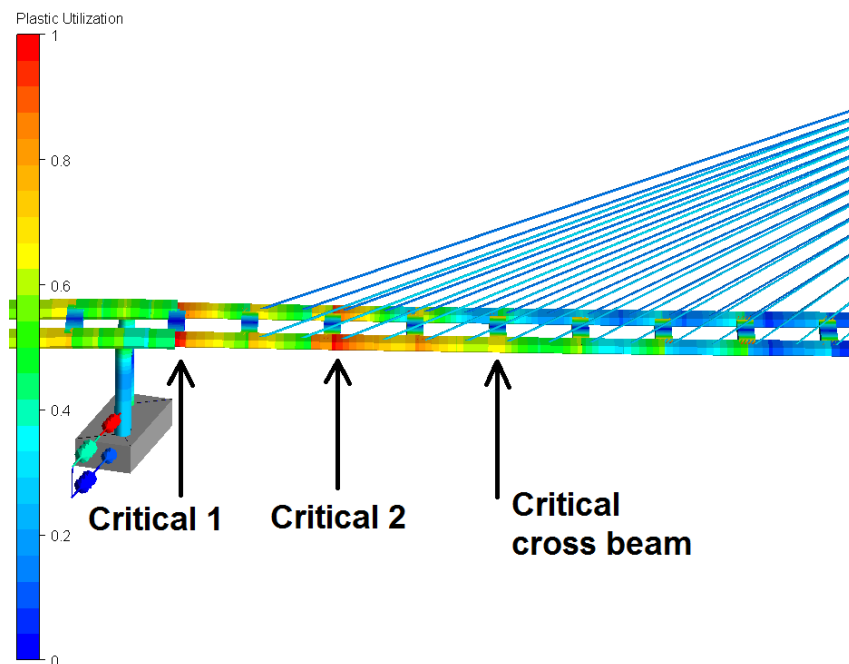
Figure 8.65: Most utilized components in the main span for collision scenario 1.
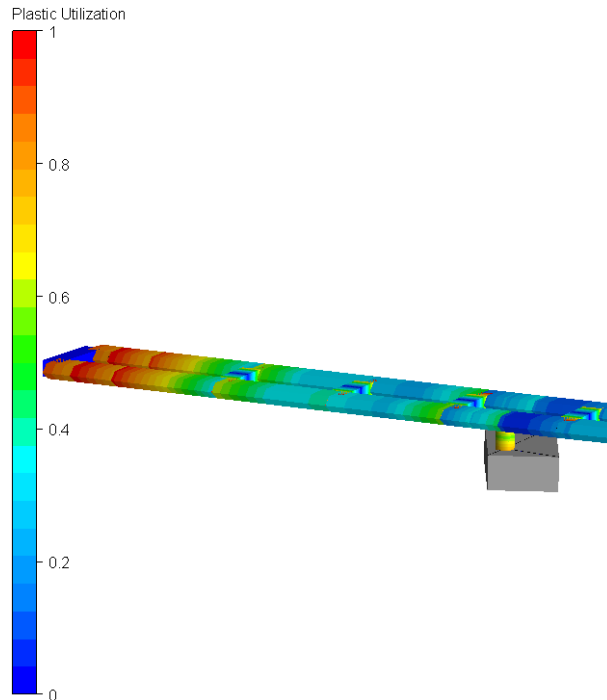
Figure 8.66: Most utilized components in the north end for collision scenario 1.

8.11.2 Effect of using different impact energies

Three different impact energies was used to study how the bridge behaviour is affected by the speed of the colliding ship, as defined in Chapter 6.3.1. Some of the main results from this investigation is presented in Table 8.29, where "Critical 1" and "Critical 2" refer to the location in the west side girder in Figure 8.65, while "Critical cross beam" is the indicated cross beam in the same figure. In this table the total horizontal displacement is the maximum value that occurs, while the mean displacement is included as it may give information about the permanent displacement caused by the impact. The peak bulb force is also studied since this may give an indication of the load than must be resisted locally by the pontoon.

From Table 8.29 it is seen that the horizontal displacement at the middle of the bridge and the end of the cable stayed part increases gradually with the impact energy. It is also noted that the displacement at the two locations are in the same range, which may illustrate that a large amount of energy is transferred from the impact location to the north end. The mean displacement results shows that this value is in general largest at the end of the main span, where 1000 [MJ] gives the most significant value. Thus it may indicate that such permanent displacement only occurs at the end of main span and for relatively large impact energies. The horizontal acceleration is larger at the tip of the main span than at the middle of the bridge for both cases, which is expected as this location is closer to the point of impact. It is also noted that the horizontal acceleration at the main

Table 8.29: Results illustrating the effect of using two different impact energies for collision scenario 1.

Response component and unit	1000 [MJ]	600 [MJ]	300 [MJ]	Location
Total horizontal displacement, [m]	7.61	5.44	3.55	End of main span
Mean horizontal displacement, [m]	2.50	0.78	0.07	End of main span
Total horizontal displacement, [m]	6.39	5.60	3.93	Middle of the bridge
Mean horizontal displacement, [m]	0.23	0.28	0.09	Middle of the bridge
Horizontal acceleration, [m/s^2]	11.25	1.51	1.64	End of main span
Horizontal acceleration, [m/s^2]	0.70	0.53	0.46	Middle of the bridge
Peak bulb force, [MN]	89.08	73.64	59.64	Bulb force
Plastic utilization, [-]	0.9995	0.6397	0.4455	"Critical 1"
Plastic utilization, [-]	0.9966	0.8308	0.5220	"Critical 2"
Plastic utilization, [-]	0.9883	0.9382	0.7875	"Critical cross beam"

span for 1000 [MJ] takes a large value. This value occurs between $4.1 - 4.2$ seconds after the collision is applied and is very localized in time and shifts from a positive to negative value within 0.2 seconds. At the time range when this takes place the forecastle unloads for the second time, but there was not found any good explanation for why this large value occurs at this location and point in time. Though one explanation could be numerical problems, which may be solved using a smaller time step. A similar behaviour was also found for nodes in the region around axis 3, but the acceleration appears to be largest at the end of the main span. At "critical 1" and "critical 2" the utilization is well below fully utilized for 300 [MJ] and below 0.90 for 1000 [MJ]. This means that the locations have remaining capacity compared to a fully utilized cross section, while the values are close to 1 for 1000 [MJ]. The permanent loads at these points are 0.14 and 0.028, which means that most of the stresses are due to the collision. Though the utilizations for the largest impact energy is close to 1 it does not necessarily mean that the global integrity is impaired, as long as the components are able to maintain the stresses.

According to Sha and Amdahl (2016b) a concrete pontoon may experience local damage if the capacity against punching shear is reached, see e.g. (King & Delatte, 2004) for

definition of this failure mechanism. Further, Sha and Amdahl (2016b) noted that a collision force with a peak at 14 [MN] caused this local failure mechanism of a similar pontoon as for the design in this thesis. This force is smaller than the peak bulb force registered in Table 8.29 for all impact energies. Though it should be noted that the pontoons are designed for a collision force of 80 [MN] (Vejrum, 2016, p. 141), which is exceeded by 9.08 [MN] for the impact energy of 1000 [MJ].

8.12 Collision scenario 2: Impact with the bridge girder at the middle of the bridge

In this collision event the impact is applied to the west side girder between bridge axis 10 and 11 where only the forecastle is in contact with the bridge. These differences affects the response of the bridge in addition to how the impact energy is distributed between kinetic and deformation energy compared to collision scenario 1. As for the first collision scenario an impact energy of 1000 [MJ] was used as a base case, while other energy levels was used to study how this affects some of the response components.

8.12.1 Impact energy of 1000 [MJ]

Collision force

The force-deformation curve extracted from the simulation is compared against the input curve in Figure 8.67 which also presents the resulting force-time history. From this figure it is seen that the forecastle deforms almost 14 meters before it unloads, which is a much larger indentation than experienced for both bulb and forecastle in collision scenario 1. This is natural as the forecastle has a lower stiffness for the initial deformations, and must therefor take more damage to absorb the same amount of energy as the bulb. It is on the other hand important to note that the total deformation energy in the ship is larger for collision with the bridge girder, as the result in Table 8.30 implies. It was noted in scenario 1 that the pontoon and column act as a pendulum which deflects away from the applied load, while in collision scenario 2 the bridge deflects mainly in the transverse direction in the initial collision phase. This could force the bridge to withstand the ship for a longer period in the latter case, and more of the energy is transformed into deformations. Another point is that the initial impact has a duration of 4.28 seconds which is almost twice the value of the first impulse for the bulb in scenario 1. This may be a natural consequence of the noted behaviour of the bridge girder compared to collision with the

pontoon.

Force-deformation curve, forecastle

(a) Force-deformation curve.
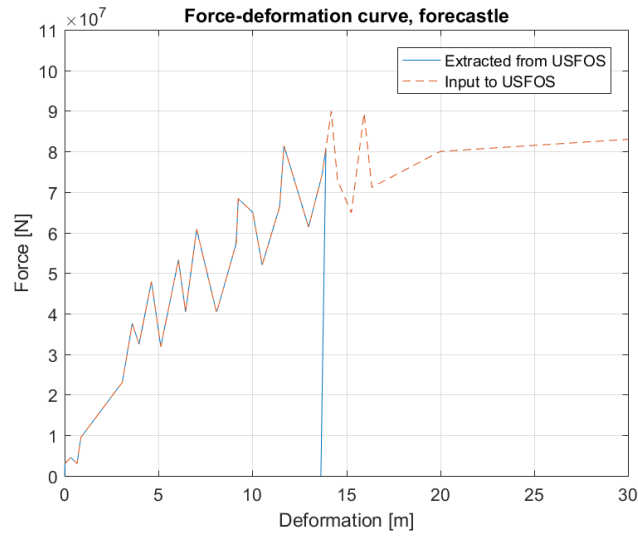
Collision force-time history
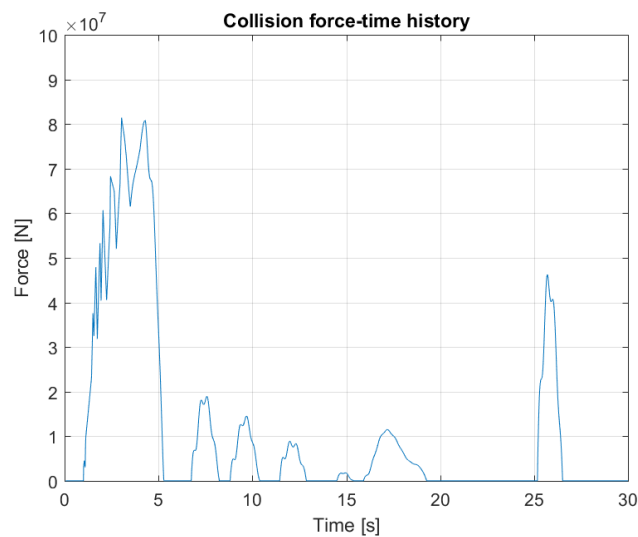
(b) Force-time history.

Figure 8.67: Force-deformation curve and resulting force-time history of the collision force for impact with the bridge girder.

Table 8.30: Deformation energy dissipated by the forecastle together with the remaining impact energy.

Energy component	Value [MJ]	Percentage of the initial impact energy
Deformation energy, forecastle	614.22	61.41%
Remaining energy	385.53	38.54%

Global motions

In Figure 8.68 the global horizontal motions of the bridge girder is illustrated for the first 32 seconds after applying the impact. In this figure the bridge is viewed from above with the north end at the right and tower at the leftmost side of each subfigure. The initial horizontal displacements is spread to the tower and north support as two nearly symmetric waves, which has reached the main span in the left side of Figure 8.68b. The rightmost half wave in Figure 8.68b reaches the north support 13 seconds after the impact. In Figure 8.68c the ship is pushed away and the bridge takes a shape that is similar to the second mode. As will be illustrated this is the mode that dominates the free oscillating phase of the analysis. There are also noted some motions with higher frequencies which includes some roll motion of the bridge girder. This illustrates that the kinetic energy is transformed into different motions, both large global displacements and high frequent behaviour.

(a) 3.33 seconds.

(b) 10.17 seconds.

(c) 31.99 seconds.
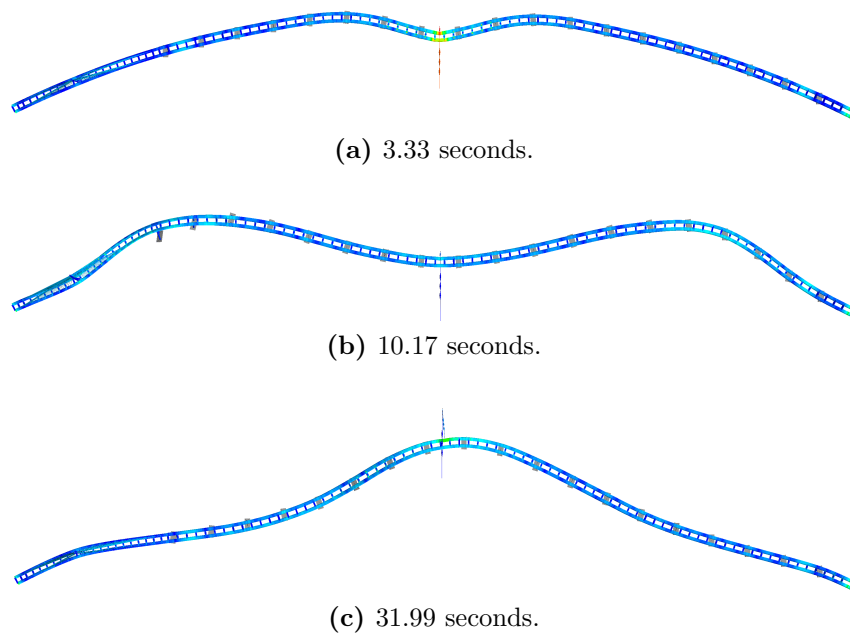
Figure 8.68: Horizontal displacement of the bridge girder at three different points in time for collision with the bridge girder. Displacements scaled with a factor of 30.

From the frequency domain solution of the horizontal displacement in Figure 8.69 it is seen that the two locations are dominated by the same frequencies. The largest peaks occurs on the exact same place as for bridge axis 11 in collision scenario 1, i.e. between frequencies of 0.02441 [1/s] and 0.02747 [1/s] corresponding periods of 40.97 and 36.40 seconds respectively. Consequently it may illustrates that the second eigenmode dominates the motions at both locations. This is slightly different than for collision scenario 1 where the first eigenmode appeared to give large contribution at bridge axis 3.
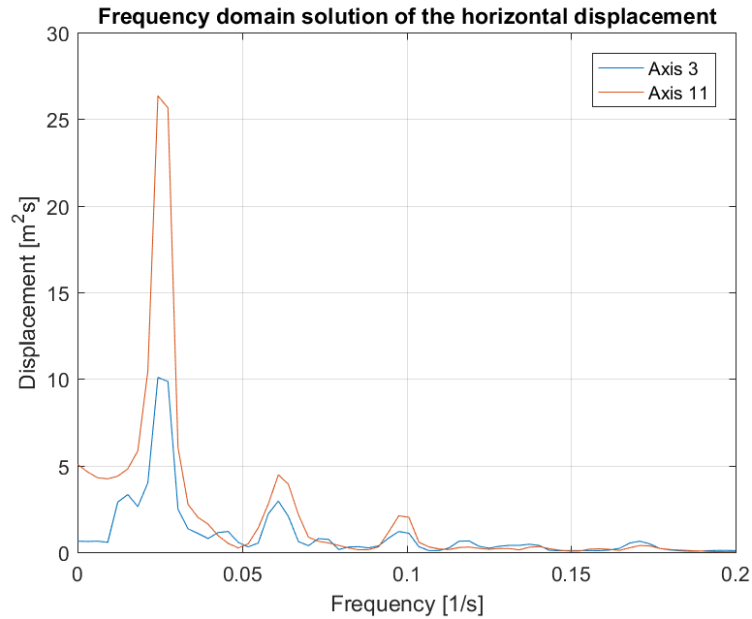
Figure 8.69: Frequency domain solution of the horizontal displacement at axis 3 and 11 for collision scenario 2.

The components with the largest utilization is found in the region close to the impact location illustrated in Figure 8.70 in addition to the north end. The single structural part with the largest value is obtained in the cross beam termed as "Critical cross beam" in Figure 8.71 with an utilization of approximately 0.96. As for collision scenario 1 the cross beams experience large bending about the vertical axis, which for this particular beam results in a stress component of about 440 [MPa]. With a yield stress of 460 [MPa] it is clear that this stress is the main contributor to the utilization. There are on the other hand not experienced any large permanent deflection as for collision scenario 1. The plastic rotation about the vertical axis is approximately 2.5E-05 for the most utilized cross beam, which is much lower than in the collision with the pontoon at axis 3. The second most utilized components are the beams where the collision load is applied, see "critical 1" in Figure 8.70, with an utilization of about 0.95. Since the impact force will act as a point load at this location it may not give a correct distribution locally. Therefor it may be connected some uncertainty to whether this utilization is representative to a real case collision. The location termed as "Critical 2" on the east side girder in Figure 8.70 gets a maximum utilization of 0.83.

8.12.2 Effect of using different impact energies

Table 8.31 presents results for selected response components using three different impact energies. For the plastic utilization the focus was put on the three locations presented
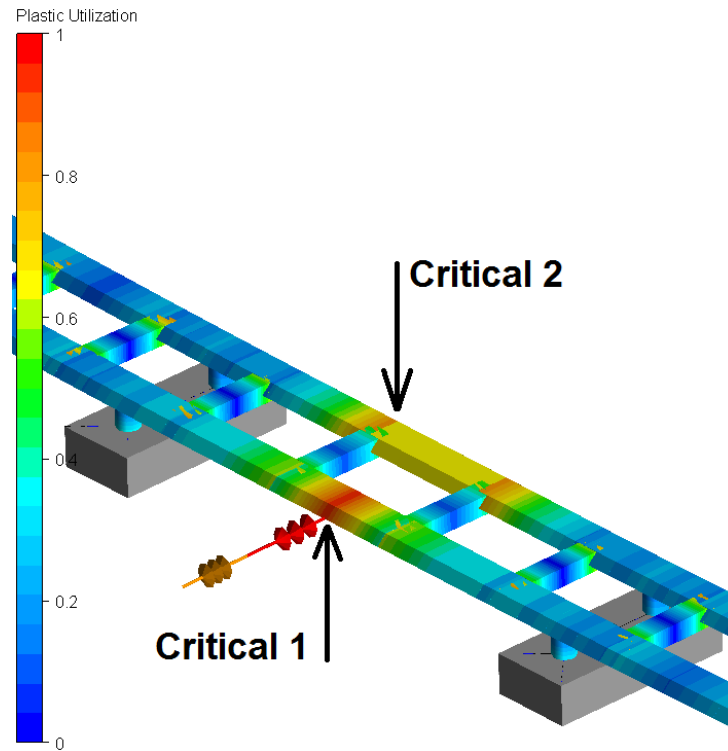
Figure 8.70: The bridge components with the largest plastic utilization at the impacted region in collision scenario 2.
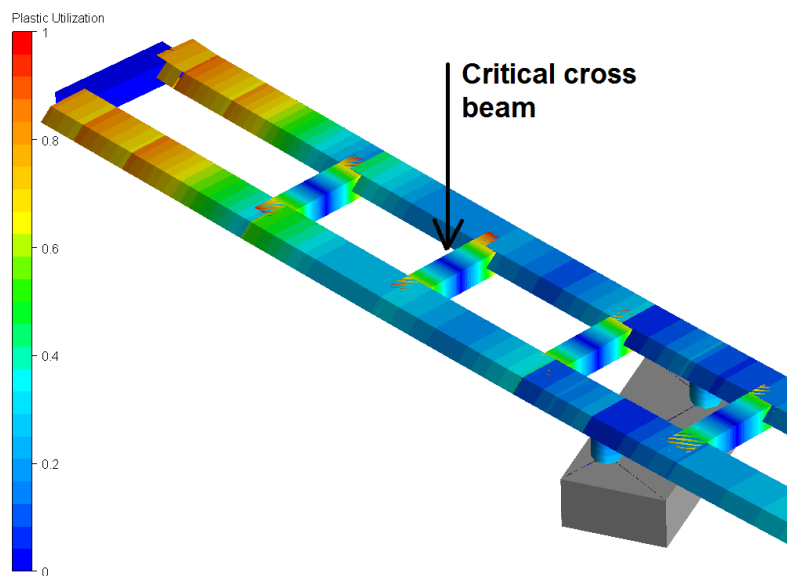
Figure 8.71: The bridge components with the largest plastic utilization at the north end in collision scenario 2.

in Figure 8.70 8.71, where "Critical 1" is the impacted beam. The strong axis bending moment for the impacted beam is included as it may give an indication of the loads this component must resist in order to maintain a strength design.

The main difference in the horizontal displacement compared to collision scenario 1 is

Table 8.31: Results illustrating the effect of using different impact energies for collision scenario 2.

Response component and unit	1500 [MJ]	1000 [MJ]	300 [MJ]	Location
Horizontal displacement, [m]	4.27	3.63	2.08	End of main span
Horizontal displacement, [m]	10.56	8.52	4.54	Middle of the bridge
Horizontal acceleration, [m/s^2]	0.86	1.05	0.87	End of main span
Horizontal acceleration, [m/s^2]	2.79	1.90	1.01	Middle of the bridge
Bending moment, [MNm]	1160.60	1185.05	817.43	"Critical 1"
Plastic utilization, [-]	0.9754	0.9549	0.6279	"Critical 1"
Plastic utilization, [-]	0.8893	0.8392	0.4571	"Critical 2"
Plastic utilization, [-]	0.9753	0.9635	0.8149	"Critical cross beam"

that the displacement at the end of main span is nearly half the value at the middle of the bridge. This could illustrate that half of the kinetic energy of the bridge is transferred to each end of the bridge, as illustrated by the two waves in Figure 8.68. It is also noted that the accelerations is largest closest to the impacted region, as for the pontoon impact. Both the "critical cross beam" and impacted beam element "critical 1" experience large utilizations for 1000 and 1500 [MJ], though these are lower than the maximum value for 1000 [MJ] in scenario 1. Another point is that the cross beam obtains a quite large utilization even for the lowest impact energy. As the effect from permanent loads is relatively low in all three locations this shows that the impact causes large stresses at these points.

8.13 Damaged condition 1: Flooded pontoon compartments

The method used to model flooded pontoon compartments is presented in Figure 8.72, where the box girder closes to the applied load is the west side girder. For definition of these terms, see Chapter 4. Figure 8.72 illustrates that the bridge girder is twisted about the bridge's own axis inducing weak axis bending moments in both box girders. The

largest effect is seen at west side girder which is expected, as the bridge girder appears to rotate about the east side girder. This can be seen from the vertical displacements, which is nearly one meter larger at the west side girder. The damage causes a positive weak axis bending moment of approximately 2.40E+08 [Nm], due to permanent loads. In comparison the permanent loads in intact condition causes a negative moment of nearly −3E+08 [Nm], i.e. a difference of 5.5E+08 [MN]. The forces are transferred to the bridge girder mainly through a force couple in the two columns with tension in the west side column and compression in the east most column. As both columns are in compression due to permanent load, the tension will reduce the magnitude of the compression in the west side column. By using the reduction in compression of approximately 9.50E+06 [N] for the west column and increase of 5.40E+06 [N] in the compressive force for east side column, this force couple supports a moment of 2.60E+08 [Nm]. This moment is calculated about the centre of the pontoon, using an moment arm of 17.47 [m] for both components. By using this moment in a moment equilibrium analysis about the pontoon centre, there is an unbalance of approximately 0.52 E+08 [Nm] when the moment in the spring to ground element is accounted for. The spring to ground element simulates the roll stiffness, see Chapter 4.2.4. One explanation for this unbalance could be the heave stiffness properties of the buoyancy elements. In addition to the induced weak axis moments in the bridge girder, forces are also transferred to the stay cables on the west side. As an example the longest cable in the west side of the main span gets an increased axial force of approximately 1.45E+06 [N].
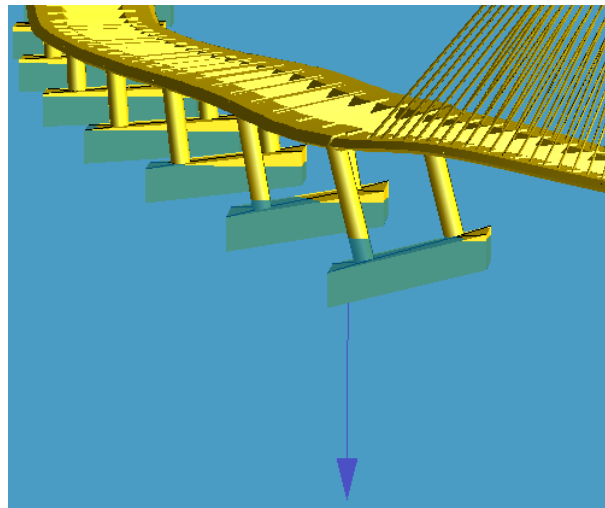
Figure 8.72: Applied weight of water in three of the pontoon compartments at axis 3. Displacements scaled with a factor of 10.

Another effect of this pontoon damage is illustrated in Figure 8.73, which shows the new equilibrium position of the bridge viewed from above. From Figure 8.72 it appears that the bridge rotates about the east side girder due to the damage. As the bridge is stiffer in vertical motion than in horizontal motion this may force the bridge into the observed

displacement pattern. The largest horizontal displacement of the bridge girder in the new equilibrium position is 1.4 meters, found between axis 5 and 6. In comparison, the effect from mean wind caused a maximum of 1 meter displacement.
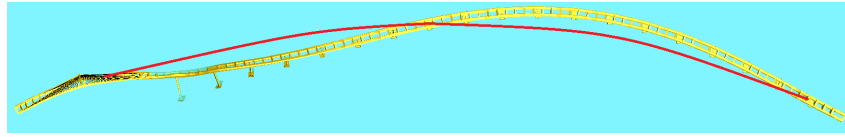
Figure 8.73: New equilibrium position after applying the filling of pontoon compartments at axis 3 where the red line illustrates the intact position. Displacements scaled with a factor of 100.

The residual capacity of the bridge with a damaged pontoon was assessed by exposing it to the same wave loads as for wave condition 4. Further, the analysis was run for 1000 seconds in order to compare with results from the intact condition. It was focused on studying the behaviour in the area close to the damage as this region was expected to experience the largest effect. The analysis showed that the difference in how the bridge responds to wave loads compared to the intact condition is relatively low. To illustrate this the plastic utilization at the same point in time as the largest utilization occurs for the intact condition, see Figure 8.44 in Chapter 8.6.4, is presented in Figure 8.74. At this point in time the intact and damaged condition has similar plastic utilization between axis 3 and 5, where the largest value occurs at the "critical location" in these figures. There are some differences such as the utilization between the first and second pontoon from right in Figure 8.74 is slightly lower than in intact condition. This is probably a cause of the new equilibrium position of the bridge. The largest plastic utilization for the damaged bridge occurs also at another point in time than for the intact condition, though the intact bridge do have a large utilization at the same time.
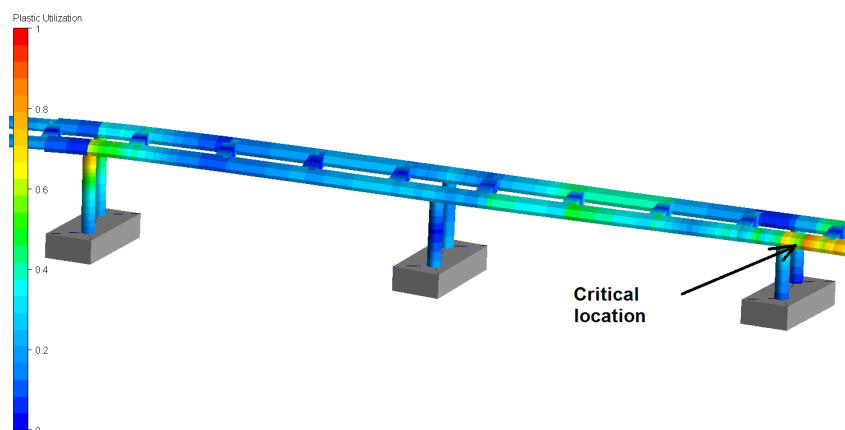
Figure 8.74: Plastic utilization in damaged condition at the instant with largest utilization in intact condition.

Some results from the intact and damaged condition is presented in Table 8.32 to illustrate the effect of flooded pontoon compartments. Both the effect of permanent loads and waves

are included in these values, and the weak axis and torsional moment are measured at the same location as presented for wave condition 4. It is seen that the effect of damage is relatively low for all response components, except for the minimum tensile cable force. This is expected as it is the closest cable to the damaged pontoon, and will therefor carry more load. Only the maximum plastic utilization is included in this table, which occurs at the "'critical location" in Figure 8.74.

Table 8.32: Selected results from damaged condition 1 compared with intact condition.

	Intact condition: *Maximum value* *Minimum value*	**Damaged condition 1:** *Maximum value* *Minimum value*	**Location**
Weak axis moment	1095 [MNm] −1632 [MNm]	1129 [MNm] −1583 [MNm]	At axis 3, east side girder
Torsional moment	774 [MNm] −735 [MNm]	717 [MNm] −874 [MNm]	Between axis 3 and 4, east side girder
Cable force	7.50 [MN] 3.64 [MN]	8.91 [MN] 5.07 [MN]	Longest cable, west side of main span
Plastic utilization	0.93 [-]	0.94 [-]	"Critical location"

8.14 Damaged condition 2: Damaged bridge girder

In this condition the effect of applying a damage to the west side box girder between axis 10 and 11 was analysed by means of totally removing the middle beam element. Before applying wave loads some attention was put on studying how the damage affects the way permanent loads are carried compared to the intact condition. This was done by introducing a fracture to the middle beam element after the bridge had reached an equilibrium position. The gray element between axis 10 and 11 in Figure 8.75 illustrates the fractured element. It should be noted that even though the pontoons in this figure also are gray, these are not fractured. Furthermore, the method using element fracture is only used to study the effect on permanent loads, while when exposed to environmental loads the element is totally removed from the model. This to make sure it has no contribution to the dynamic bridge behaviour.

The largest effect from removing the middle element appears to be an increased torsion moment in addition to a reduction in the vertical shear force at the pontoons at these axes. This behaviour is observed both for the remaining two parts of the west side box girder and in the east side box girder in this span. As an example, the torsional moment in the west side girder at axis 10 changes from approximately −2 [MNm] to −17.5 [MNm]. On
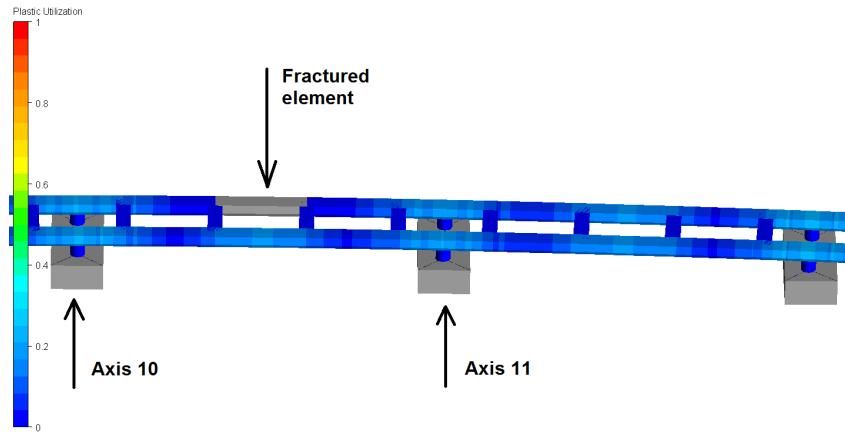
Figure 8.75: Illustration of the fractured element between axis 10 and 11.

the one hand this is a large increase in moment caused by permanent loads, but compared to the wave induced torsional moment of -324.53 [MNm] at this location in the intact wave condition, i.e. wave condition 4, the increase is relatively low. This shows that it is the resistance against wave induced components that is expected to predominate the behaviour in this damaged condition rather than increased loads at curtain location due to redistribution of permanent loads.

Similarly as for damaged condition 1 the residual strength of the bridge with damaged bridge girder was studied using the same wave loads and duration of the analysis as in wave condition 4, i.e. simulation length of 1000 seconds. Further, the focus was put on the region closest to the applied damage since the largest effects was expected to occur in this area. Figure 8.76 shows the location of the most utilized component in the bridge girder when exposed to waves, while Figure 8.77 is the plastic utilization in intact condition at the same point in time. In the latter figure the arrow points at the same location as in Figure 8.76. It is evident from these figures that the whole region has a larger stress level in the damaged condition, where the largest component at the "critical location" is the torsional stress which is about 232 [MPa]. In comparison this stress component is 47 [MPa] for the intact condition at the same point in time and shows that the "critical location" must resist a much larger torsional moment due to the damage. A large contribution to the total stress comes also from bending about the strong axis which is 159 [MPa], while the weak axis stress component is approximately 75 [MPa]. A similar tendency is also seen for the other locations with large utilization in this region, i.e. that a large contribution comes from torsion. It should be noted that the mentioned stresses are the total stress, including permanent loads. Though for both the torsional and strong axis components the effect from permanent loads have minor contribution such that most of these stresses are purely wave induced.

Table 8.33 presents some results for this damage condition together with the corresponding
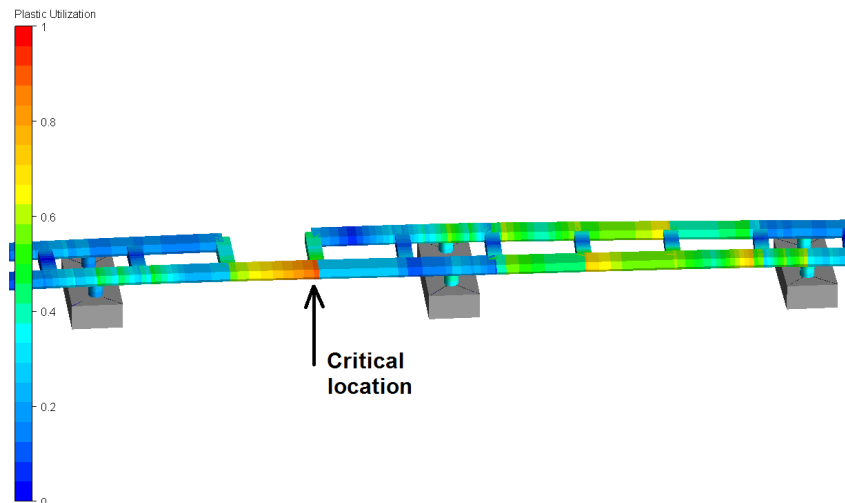
Figure 8.76: Largest plastic utilization between axis 10 and 11 in damaged condition 2.
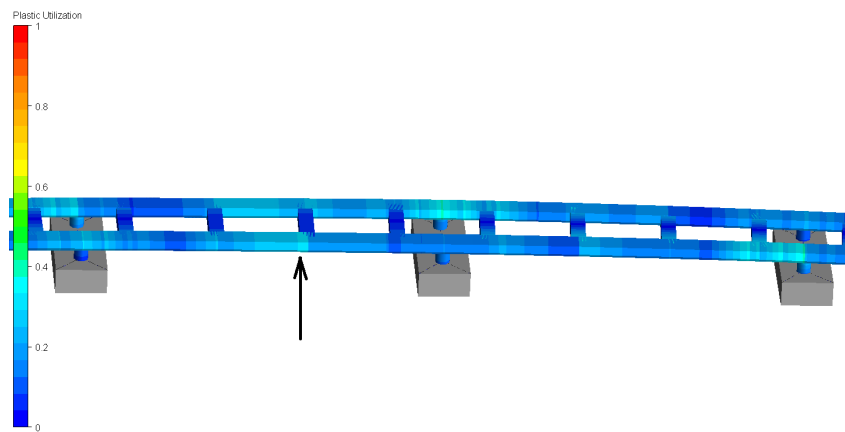
Figure 8.77: Plastic utilization between axis 10 and 11 in intact condition.

intact response. The stresses from torsional and strong axis moments appeared to be the most critical at the "critical location". Therefor the corresponding moments are used to illustrate the differences compared to the intact condition, to be consistent with the approach used for damage condition 1. The maximum and minimum moments at axis 10 are also presented to give an indication how the connection with the column is affected. Further, it should be note that the moments in this table includes both the permanent and wave induces component. These results shows that the main difference occurs at the "critical location" which has to carry moments that are more than twice the intact value. At this location largest change is for the negative strong axis moment where the value in the damaged condition is about 3.13 times larger. While the moments at axis 10 are less affected compared to the intact condition. The maximum plastic utilization is presented for the "critical location" and shows that this point experience a relatively large utilization. According to Statens vegvesen (2015, p.168) shall the residual strength in a damaged condition be large enough to prevent global failure of the structure. If the

simulations are run for three hours, which is a common duration for a sea state (Myrhaug, 2007), the cross section may reach a fully plastic utilization. The effect of this will be discussed further in Chapter 9.

Table 8.33: Selected results from damaged condition 2 compared with intact condition.

	Intact condition: *Maximum value* *Minimum value*	Damaged condition 2: *Maximum value* *Minimum value*	Location
Strong axis moment	333 [MNm] −410 [MNm]	272 [MNm] −289 [MNm]	At axis 10, east side girder
Strong axis moment	285 [MNm] −262 [MNm]	637 [MNm] −806 [MNm]	"Critical location"
Torsional moment	315 [MNm] −735 [MNm]	267 [MNm] −292 [MNm]	Axis 10 east side girder
Torsional moment	285 [MNm] −263 [MNm]	717 [MNm] −874 [MNm]	"Critical location"
Plastic utilization	0.48 [-]	0.90 [-]	"Critical location"

Chapter 9

Discussion

9.1 Global bridge model

In Chapter 4.2.3 it was noted that the bridge girder is positioned too high at the cable stayed part, which will influence the column height and affect the moment arm for the applied wave forces. The largest deviation is found at bridge axis 3 where the difference is approximately 5.8 meters. To get an impression of the error in the end moment caused by this deviation one may use simple hand calculations. If the same force is applied in sway direction for the correct column height and the one with a too large height, the difference in end moment will be the ratio between the moment arms. Using this it is found that the column height used in this thesis gives approximately 14.5% larger moment. Since the characteristic bending stress of the columns exceeds the yield limit by factor of 1.35 this deviation alone will probably not explain the large bending moments.

When updating the bridge model file the main focus was put on the properties of the pontoons, box girders and stay cable, including pretension. Less attention was put on the cross beam properties as these appeared to be the same as in COWI et al. (2016). While working with ship collision scenario 1 it was on the other hand noted that the cross sectional properties for the local y- and z-axis appears to be switched in the model file for the cross beams. For the floating part this gives a second moment of area that is 67% too large for bending about local y-axis, where local z-axis is parallel to the global z-axis. This could affect the stiffness properties of the bridge girder including the roll motion behaviour, which may have some impact on the result for the response caused by linear wave loads. But it is difficult to assess how the response due to environmental loads is affected by this without rerunning some of the analysis. Another point is that the plastic section modulus for bending about the weak and strong axis seems to be defined

as the elastic properties, in addition to being switched. As a result the plastic capacity for bending about the vertical axis used in the analysis is about 38% too low, when it is assumed that both have the same shape factor, see e.g. Amdahl (2005, Ch.7). This may have impact on the permanent displacements that are observed for the first collision scenario. As for the environmental loads one should in general rerun some of the collision analysis in order to study the effect of these discrepancies. Due to time limitations at the end of the thesis no simulations have been rerun for neither environmental loads nor ship collision.

As noted in Chapter 7 the whole bridge girder gets a permanent displacement in negative z-axis, which varies between $1 - 2.5$ meters along the bridge. This may affect the hydrodynamic properties such as added mass and damping since these are established in USFOS using the displaced volume of the pontoons. If the instantaneous volume displacement is used for these calculations it will give a too large contribution to these properties. As a result the bridge could have somewhat different eigenvalues than those obtained in the eigenvalue analysis, since a larger permanent volume displacement means a larger added mass. One should note that the eigenvalues are established using a different approach for handling the added mass which is not dependent on the volume displacement, as described in Chapter 4.2.4. On the other hand the eigenperiod is proportional to the square root of the total mass, and it should therefore give only minor changes in the eigenvalues for these extra pontoon draft. The effect could have a larger impact on both the potential and drag damping as these are proportional to the pontoon draft. But since the damping coefficients are relatively low, except for drag damping in heave, these effects are also expected to be of minor degree.

9.2 The importance of the different environmental loads

The contribution from linear wave forces is the environmental load that give the largest load effects in the bridge girder out of those studied. In relation to this the weak and strong axis moment in addition to torsional moment appears to be the components that gives the largest contribution to the stress level. The wind generated waves are established for a sea state with a peak period of 6 seconds, which is in the region with many relevant eigenmodes for the applied load components. For waves from west and north-west it is found that the linear wave loads gives a bridge response which is close to some of the eigenperiods of the bridge. Since eigenmodes around a period of 6 seconds have large stiffness it may result in large load effects in the bridge when they are excited, though one should note that wave

condition 1 did not appear to have any large motions. While for waves from north-west some eigenperiods appeared to be more dominating. It is also interesting to note that the wave heading causes somewhat different response of the bridge girder where waves from north-west is more critical, both with regard to motions and induced moments. This could be a consequence of that waves from north-west have six load components while waves from west only have three, due to the pontoon heading. Another point is that the response appears to be highly affected by the phase difference in wave loads, as illustrated by wave condition 4. When the phase angle caused by the pontoon position is accounted for some of the response components increase, such as moments in the bridge girder, while the weak and strong axis moments at the tower support decreases. This illustrates that it may be important to account for phase difference for a large structure like this bridge. Thus it could also be relevant to check the effect of using short crested sea, since this could be a more correct 100-year sea state at this location.

The largest contribution from the second order slowly-varying drift loads is to the horizontal displacement, while the bending moments about the strong axis for the bridge girder are less affected. The relatively small contribution to this moments may illustrate that there are little dynamic amplification of the largest eigenmodes, which could indicate that the eigenperiods of the bridge girder is too low for the second order effects to be important. Though it should be noted that the horizontal displacement caused by these slowly-varying loads are in the same range as the linear contribution. Consequently it may be important to include these second order loads if the horizontal displacement should be calculated exactly, while for the bridge girder moments they appears to be almost negligible. Thus the bridge appears to have large resistance against these loads. One should on the other hand note that the effect of slowly-varying loads was only studied in depth for two of the wave conditions, which was only run for 1000 seconds. Since these loads has a relatively large period of oscillation one should probably use a longer simulation in order to include larger slowly-varying drift components. A similar statement was noted by COWI et al. (2016, p.77) which came to the conclusion that a 3-hour simulation is needed in order to capture the slowly-varying drift effects properly. Another point is that COWI found that the largest contribution to the strong axis moment from these loads was 20% compared to a simulation including linear wave loads. This is close to the maximum contribution of 28% found for fully correlated waves from west in this thesis. It should be noted that COWI et al. (2016) used a 3-hour simulation compared to the 1000 seconds for wave condition 1. It is also interesting to note that the second order effects are most significant for the two fully correlated conditions. While for wave condition 4 the contribution appears to be lower. The effect of these second order loads was not studied in depth for wave condition 4, but it was noted that there was a lower contribution from the two largest eigenperiods than for the fully correlated conditions.

This behaviour could reflect that the slowly-varying loads are smaller in magnitude than linear, and must act fully correlated in order to triggers the largest modes.

As for the slowly-varying loads wind appears to be relevant for the largest eigenperiods, especially at the middle part of the bridge where periods close to the second eigenmode dominates. Similarly as the second order loads the wind components gives large horizontal displacement, but they also contribute with bending moment about the strong axis in the same order as the wave loads. This could imply that these loads causes amplification of the second eigenmode though there are observed frequency components corresponding to lower periods, which also could give large contribution to this moment component. By running simulations including both wind and waves it was found that the wind caused a large increase in the bending moment about the strong axis of the tower foundation. The average value of this response component from the 10 simulations appeared to be 83% of the value established for the characteristic wave response. Since such a large value only occurred for the analysis including wind, it indicates that the tower will be exposed to large contribution from wind. This is also expected due to the large height of this structural part. Except for this, and a large contribution to the bending moment about the strong axis in the box girder at axis 2, the main contribution from wind was to the horizontal displacement compared to pure wave analysis.

9.3   Characteristic response

The characteristic response was among others established for the bending moment about weak axis in the east side girder at axis 4 and the east side column at axis 4. Both of these results showed that the design resistance of the components was exceeded, when using yielding as the criteria. As a result these components must be strengthened in order to satisfy the design criteria, which may be accomplished by increasing the second moment of area for both components. For the box girder this can be done by increasing the height of the cross section or by introducing additional longitudinal stiffeners going from the top to bottom plate. While for the columns this can be achieved by for instance increasing the diameter.

It should be noted that for both the column and box girder only one moment component was used to evaluate the resistance against the characteristic wave loads. The problem with this approach is that it will not in general give the correct resulting stresses at these locations. This because the total stress level will be affect by all stress components at the location, and if the total characteristic stress is of interest one have to account for all of these components. It should on the other hand be noted that the stress from weak axis

moment appears to be the dominating component when the largest values occurs at axis 4 for the "bottom plate", see Figure 8 in Chapter 8.1. This is illustrated in Table 9.1 for the non-zero stress components that are present when the maximum weak axis moment occurs at axis 4, in wave condition 4. "Bottom plate" is located at the neutral axis such that the strong axis moment should not give contribution, and the vertical shear force is assumed to be carried by the diagonal sides of the box girder. It is evident from this table that the contribution from the weak axis moment is much larger than the other stress components. Consequently using the characteristic stress from bending moment about the weak axis could give a good indication of the stress level at this location. But in a design situation one also has to verify the capacity at different locations in the cross section, where the contribution from the other stress components may be significant. Therefore a better approach may be to calculating the maximum von Mieses stress and use this to establish the characteristic stress at the location of interest. This will on the other hand be more time consuming as the equivalent stress must be calculated at the points studied for all simulations. Another approach could be to take out the maximum values as used in this thesis, but including all six load components at each location and then introduce some corrections to account for the fact that the largest values do not occur simultaneously. This approach was used by COWI et al. (2016) and is also proposed by Statens vegvesen (2015, p.79). The characteristic values was not calculated for the location with the largest utilization for wave condition 4, in a design situation this must also be done in order to establish a proper design at this location.

Table 9.1: Non-zero stress components at axis 4 when the maximum weak axis moment occurs in wave condition 4.

Stress component	Stress [MPa]
Weak axis	335.16
Axial	18.85
Transverse shear	16.11
Torsional	60.09

9.4 Effect of using a band-pass on the slowly-varying drift loads

It was decided to use use a band-pass filter on the slowly-varying drift loads for periods below 50 seconds in order to remove the unphysical high frequency components produced by Equation 2.11 in Chapter 2.2.3. It was on the other hand noted that these second order forces caused horizontal motions of the bridge girder with a period of about 40 seconds, which is close to the second eigenmode. Faltinsen (1990) statens that these unphysical

frequencies should not affect the response due to slowly-varying drift loads. Therefore if the second eigenmode is excited using the band-pass, it could indicate that one may get even larger response if frequencies in this range are not removed. Consequently the effect of using this approach should be studied more in depth. The method was used to make sure that the unphysical frequencies did not affect the linear components, but it may be more correct to filter out periods below a lower period than 50 seconds. Using for instance 20 seconds could be more appropriate.

9.5   Grid size for stochastic wind simulation

As noted by Moe (2016, p.106-107) the choice of location and size of the grid used to generate the stochastic wind in WindSim will affect the response of the bridge. Due to restrictions in the computer memory capacity the maximum amount of wind nodes was limited to a total of 240 nodes. Therefore some judgement had to be made in order to decide how these points should be distributed along the bridge. This as the stochastic and mean wind velocity are only calculated in these points, while in between the wind nodes the velocity is constant and equal to the nearest node (Moe, 2016, p.106). Thus, the selection of location of the wind grid in addition to the number of wind nodes in the three global coordinate axes will have influence on the final result. As the cable stayed part in the south end of the bridge is located higher than most of the floating part, it was focused on selecting points in the vertical direction such that the whole tower is captured. But if a course division in the vertical plane is used the low bridge part will experience a too large mean velocity giving unreasonably large horizontal displacement. As a consequence of this the first vertical wind node is located 30 meters above the free surface level, which is in between the location of the bridge girder in the cable stayed part and the floating part. Also the wind grid is only covering half of the bridge, meaning that the north end will experience fully correlated wind as the middle part of the bridge (Moe, 2016, p.106). As seen in connection with the wave analysis may correlation between the applied loads have large impact on the result, therefore if the wind field is handled differently it could affect the result.

9.6   Response from ship collision

The results from both collision scenarios showed that the bridge girder gets large utilization in some regions for the highest impact energies, which means that a considerable part of the cross section will experience yielding at these locations. This may not nec-

essarily be a problem as the structure is allowed to take local damage for this type of load (Statens vegvesen, 2015, p.168). Though it is required that global collapse of the bridge is prevented. A critical situation for collision scenario 1 could occur if the most utilized parts in the bridge girder are not able to maintain the stress level. Both the east and west side girder have similar plastic utilizations and if these fails simultaneously it could be questionable whether the global integrity is maintained. The floating part has no mooring system and an extreme situation where the bridge is cut in two due to failure at these locations could be critical, which will be discussed further in Chapter 9.7.

In addition to large utilization in the box girders the cross beams are also exposed to loads which are close to their maximum capacity. It may not be as critical if some of these fails compared to the box girders, but it appears that plastic rotation in the ends of these components could cause a permanent displacement of the bridge girder. As long as this is the only effect the cross beam's resistance are probably not critical with regard to the global integrity of the bridge. But as noted this result could be affected by the plastic section modulus which appears to be defined in a wrong manner. This may affect the permanent displacements that are observed for the first collision scenario. In order to study the effect of these discrepancies one should in general rerun some of the analysis, but this was not done as there was no time to perform new simulations.

The largest impact energy for collision scenario 1 and 2 was chosen to 1000 [MJ] and 1500 [MJ] respectively. The argument for doing this was to find the largest impact energy that did not cause large permanent damage of the bridge. Since a energy level of 1000 [MJ] gave permanent displacement of the bridge girder it was decided not to use larger impact energies. By reconsidering this one could argue that the same three impact energies should have been used for the parametric study of ship speed, as it could give a better basis for comparing the two collision scenarios. Especially as a permanent horizontal displacement may not impair the global integrity. It was tried to run collision scenario 1 for an impact energy of 1500 [MJ], but it was not studied in depth. One of the differences compared to 1000 [MJ] was that the largest utilization at one of the two critical points reached a value of approximately 1.15. A value of 1 indicates a fully plastic utilization of the cross section and should not be exceeded. One explanation for this large value could be numerical issues which may be solved by lowering the time step, but further studies should be made in order to confirm this.

It is important to note that the design impact energy for collision scenario 1, according to COWI et al. (2016), is 250 [MJ]. While for collision with the bridge girder the design impact energy is defined as an event where the ship dissipates a energy of 700 [MJ] (COWI et al., 2016, p.21). In comparison it was found that an impact energy of 1000 [MJ] gave a total of 614 [MJ] dissipated in the ship for collision scenario 2. Consequently an impact

energy of 1500 [MJ] may be somewhat larger than the design event for bridge girder impact. For pontoon collision it is found that even for a impact energy of 600 [MJ] the critical points have remaining capacity compared to fully plastic utilization, where the largest value is found in the box girder. For impact with the bridge girder an energy level of 1500 [MJ] gave utilization close to 1 at both the impacted region and the critical cross beam. Whether damage in the impacted region is critical will be discussed in Chapter 9.7, while a failure in one of the cross beams is expected to not impair the global integrity. Thus one may state that as long as the large utilizations do not result in a progressive failure of the structure, the bridge appears to have a large global capacity against ship collision.

9.7   Damaged condition

Statens vegvesen (2015, p.168) states that a floating bridge should be able to survive an accidental event, such as ship impact. This includes not only the impact it self, but it should also withstand a 100-year environmental condition after the impact. For this environmental condition it is required that the bridge do not turn into a global collapse (Statens vegvesen, 2015, p.168). As presented in Chapter 8 the latter was checked using 1000 seconds of a 100-year sea state for two different bridge damages.

For pontoon flooding there was only minor differences compared to the intact condition, which may indicate that the bridge has sufficient residual strength for this kind of damage. If three compartments at the end of a pontoon is filled it will give a reduction in the pontoon's roll stiffness. This can be illustrated by simplifying the pontoon geometry to a rectangular shape with similar water plane area. For this simplified geometry the roll stiffness of a pontoon will reduce from 5600 [MNm/m] to 3110 [MNm/m] due to the damage, i.e. approximately 56% of the intact value, and shows that the local change in roll stiffness is relatively large. But as no dramatic change in the global behaviour is observed close to the damage, it could indicate that the bridge girder itself has a relatively large stiffness against such motions. Another point is that the damage is applied close to the stay cables, which will carry some of the extra load. COWI et al. (2016) came to a similar conclusion, i.e. that pontoon damage is not critical, which was explained by the damage having little impact on the eigenperiods. As a result the dynamic behaviour should not be dramatically changed compared to intact condition, as also noted by COWI et al. (2016, p.80). It should on the other hand be noted that though the damage it self do not reduce the residual capacity, the most critical component is close to fully utilization. However, this is the same as in the intact condition, which indicates that the ULS condition is the critical for design and not the second step in the ALS. Thus if the intact bridge is

strengthened a pontoon damage at axis 3 is not expected to reduce the residual strength significantly. One should note that this damage was modelled as an applied force, not mass, which introduce some errors with regard to the inertia effect. This is expected to have minor impact on the result as the mass of the pontoon will have the largest contribution.

Contrary to the pontoon damage a damaged bridge girder, as analysed in Chapter 8.14, gives notably differences compared to the intact condition. The largest stress components at maximum utilization was from torsion and strong axis bending giving approximately 88% more utilized cross section than for the intact condition. This behaviour could be explained by the reduction in stiffness at this region when removing one beam element from the west side box girder. The reduction in strong axis stiffness could be explained as the cross section at the damaged bridge girder goes from two parallel box girders to a single. Loosing one of the two girders will therefore reduce the bending stiffness about the vertical axis, as a large contribution comes from the second term in the parallel axis theorem, see Equation 4.1 in Chapter 4.2.1. Further, since roll motion is one of the dominating response caused by waves it is natural that the remaining east side box girder has to take a much larger torsional moment at this location.

The largest utilization for the condition with damaged bridge girder is 0.90 during the 1000 seconds simulation, which is close to a fully utilized cross section. This means that a longer analysis could result in utilizations closer to a value of 1. As noted it is required that the global integrity is maintained during these extreme environmental loads, which may question whether this is fulfilled for damaged condition 2. If the box girder cross section at the critical location reaches fully plasticity it must be capable of maintaining the moments in order to meet the requirement. As an example Amdahl (2005, Ch.7, p.18) notes that a cross section exposed to plastic bending moment may fail due to local buckling if it is not designed to maintain these loads during plastic rotations. Since both torsional and bending moment is large for the critical location this may be of concern as the box girders are thin walled. This may set some limitations to whether it is proper to design for a fully utilization in this condition, as a failure of the critical part will turn the bridge into two cantilever beams. Since the bridge has no anchoring system this may give large moments at the supports. Therefore one should probably require that the global integrity is only kept as long as the capacity of the remaining box girder is well below fully utilized. In this case the results implies that the residual strength is not sufficient for such damage. One the other hand it was assumed that the damaged beam element could be totally removed, which may be too extreme. To get a better estimate of the actual residual capacity one has to know the resistance of the impacted bridge girder after the collision. This could be accounted for by performing a local analysis of the ship collision and use the resulting information to model the bridge girder resistance more properly.

In both damaged conditions the global integrity was assessed only one set of random phase angles, which may be too simple. According to Statens vegvesen (2015, p.168) the environmental loads in the second step of an ALS should corresponds to loads with a return period of 100-years. As a result using only 1000 seconds may not include the 100-year loads. Therefore, to get a more accurate estimate of the residual strength for such extreme environmental events one should probably run more and longer simulations. But the results presented in this thesis seems to imply that a situation where the bridge girder damage is so large that one part of the box girders can be regarded as removed, appears to be critical. For this situation the residual strength may not be sufficient to ensure the global integrity.

9.8 Results compared with those reported from use of alternative software

Some of the results have been compared with those presented by COWI et al. (2016) analysing the same bridge design. By comparing the four first eigenmodes obtained in this thesis with mode 1 to 4 in COWI et al. (2016, Appendix) it is evident that the shape of these appears to be similar. Mode 1 to 4 as presented by COWI et al. (2016, Appendix) are illustrated in Appendix K together with a table showing the eigenperiods. Thus it appears that the two bridge models behaves similarly for the largest eigenperiods. Though one should note that there are some differences in the eigenperiods, especially for the first two modes where the result in this thesis is approxemately 10 and 6 seconds larger. To check whether the single box girder model used by COWI et al. (2016, Appendix) have different stiffness properties, Equation 4.1 in Chapter 4 was used to calculate the total second moment of area for the parallel box girders used in this thesis. Two tables are included in Appendix L where these properties for bending about the weak and strong axis are compared against those in COWI et al. (2016). These tables illustrates that the second moment of area appears to be in the same range as the ones presented in COWI et al. (2016).

After updating the USFOS bridge model the results appears to be more in accordance with those presented in COWI et al. (2016) and COWI et al. (2016, Appendix) for waves from west. While for waves from north-west the differences is much larger compared to COWI et al. (2016, Appendix). One explanation could be that it is caused by differences in eigenperiods, where the model used in this thesis gets larger dynamic amplification. One may also note that one of the dominating behaviour, referred to as pendulum motion, was also reported in COWI et al. (2016). This behaviour was observed for all the four wave

condition, especially for condition 3 and 4. It was also noted similar absolute maximum and minimum distribution of the vertical displacements and accelerations as in COWI et al. (2016), see Chapter 8.5. These findings could be used to argue that the bridge models appears to behave similarly. Though one should note that there are differences when it comes to the size of these maximum and minimum displacements and accelerations. This may be result of how these values are measured on the bridge girder, as explained in Chapter 8.5.2. Another source of the differences in the result could be the applied wave forces, but as seen in Chapter 8.2 these appears to be almost identical as those reported by COWI et al. (2016). Where the largest deviations was found for the wave excitation roll moment.

By comparing the characteristic values calculated for the east side girder it is found that the bending moment about the weak axis in Chapter 8.8 is approximately 2.35 times larger than the characteristic value at the same bridge axis in COWI et al. (2016, Appendix). For the characteristic bending moment about the strong axis at the north support the situation is reversed, and the result in Chapter 8.8 is about 34% of the value in COWI et al. (2016, Appendix). The latter is expected as bending in the horizontal plane will be supported by both axial forces and bending moment for the two box girders in parallel, while it is taken as pure bending for a single box girder. While characteristic torsional moment between axis 3 and 4 is 2.4 times larger than in COWI et al. (2016, Appendix). These results shows that there are some notable deviations, but it was not found any good explanation for this except for the difference in modelling of the bridge girder. Though it could be mentioned that the characteristic responses are established in a different manner in the mentioned report, see COWI et al. (2016, p.24). One should also note that the software used by COWI et al. (2016) is different from the program used in this thesis, which could have impact on the results. As an example if the software can handle frequency dependent values such as added mass and potential damping, it may be a source to some of the differences. These are defined as constant values for the USFOS model in this thesis.

Chapter 10

Conclusion

The analysis of the bridge exposed to extreme environmental loads have showed that it is the linear wave loads that causes the largest load effects in the bridge girder, by means of bending and torsional moments. For this kind of loading the result implies a lack of capacity at the intersection between the bridge girder and columns. When using the resistance against yielding as criteria it was found that the bridge girder at this location has to be strengthened against bending moment about the weak axis. For the highest columns bending moment was also the critical component with regards to yielding.

The second order wave loads gives notable contribution to the horizontal displacement, though the dynamic amplification to the largest eigenmodes appears to be low. This could imply a large resistance against these loads, as a result of the relevant eigenmodes being below the dominating periods of the slowly-varying drift effects. The method using band-pass filter to remove unphysical frequencies for these loads should on the other hand be studied more in depth. Another point is that these loads seems to be more relevant for fully correlated conditions. Wind contributes mainly to the horizontal motions of the bridge girder in addition to being relevant for the tower response. This causes large bending moment about strong axis at the tower foundation. For the bridge girder moments the largest effect from wind is observed at the west side girder at the connection with tower.

The bridge girder response due to wave loads appears to exhibit similar behaviour as reported from a previous study of the same bridge design. This gives confidence to the method used for the wave loads in this thesis, where these are handled as time-varying load histories applied to the pontoons. Though one should note that the magnitude of these response tends to be larger for the results obtained in this thesis. Differences in how the bridge girder is modelled could be one of the sources to these deviations.

The collision analysis showed that critical components will experience highly utilized cross sections, for large impact energies. This do not necessarily mean that the global integrity is impaired, but they should probably be able to maintain the stress levels in order to prevent global collapse. If this is the case the bridge girder appears to have a large resistance against collision events. Collision with the pontoon showed that large forces had to be resisted locally in order to prevent local damage. Though a damage to the pontoon may not be critical with regard to design, according to the results for simulations with three flooded compartments. A damage to the bridge girder could on the other hand be more critical if a part of the a box girder is totally fractured. In this case the remaining box girder has to resist large utilizations when exposed to 100-year environmental loads since the stiffness against torsion and bending about the strong axis is reduced. Consequently this situation may inflict with the second step in the ALS requirement, but a better modelling of the residual strength of the damaged box girder could reveal a larger capacity for this damaged condition.

Chapter 11

Recommendations for Further Work

The results presented in this thesis implies that the bridge girder lacks capacity against weak axis moment, it could therefore be relevant to investigate this further. As an example it was found that that the response is affected by the correlation of the wave forces. Therefore it could be interesting to investigate whether using short crested sea instead of long crested, as used in this thesis, have impact on the behaviour. This because a short crested sea state may be more realistic at Bjørnafjorden. It could also be relevant to establish more stress components for both the box girders and columns in order to get a better estimate of the loads these components has to resist, in addition to evaluating these at other locations. The resistance criteria studied in this thesis was yielding, but other criteria such as buckling could be relevant for some components. Another point is that the sea state used in the characteristic response calculations exhibits drifting effects, which is something that could be studied in order to find the cause of it.

Since it was discovered that the properties of the cross beam appears to be defined incorrectly, the effect of this on both environmental loads and ship collision could be investigated.

It is also relevant to study the points in the problem description for this master thesis that were not covered. For description of these points it is referred to Chapter 1.2 and the problem description at the beginning of this thesis.

References

Aas Jakobsen, COWI, Global Maritim, & Johs. Holt. (2016). C*urved* B*ridge* - N*avigation* C*hannel in* S*outh* - A*ppendix*. Obtained from Professor Jørgen Amdahl.

Aas Jakobsen, COWI, & Johs. Holt. (2016a). Bjrnafjorden tegninger endeforankret bru 150216. Retrieved through Professor Jørgen Amdahl.

Aas Jakobsen, COWI, & Johs. Holt. (2016b). Design basis. Retrieved April 11, 2017, from http://www.vegvesen.no/_attachment/1605052/binary/1145248?fast_title=Bj%C3%B8rnafjorden+Flytebru+Design+Basis.pdf

Aas-Jakobsen. (2015). User manual windsim.

Aas-Jakobsen, K. & Strømmen, E. [E.]. (2001). Time domain buffeting response calculations of slender structures. *Journal of Wind Engineering and Industrial Aerodynamics*, *89*(5), 341–364. doi:https://doi.org/10.1016/S0167-6105(00)00070-2

Aas-Jakobsen, COWI, Johs. Holt, Moss Maritime, NGI, Plan, & TDA. (2016). Bjørnafjorden suspension bridge. design basis. Retrieved April 25, 2017, from http://www.vegvesen.no/_attachment/1607161/binary/1145773?fast_title=Bj%C3%B8rnafjorden+Suspension+Bridge+(TLP)+Design+Basis.pdf

Amdahl, J. (2005). TMR4205 - Buckling and Ultimate Strength of Marin Structures.

Baarholm, G. S., Haver, S., & Økland, O. D. (2010). Combining contours of significant wave height and peak period with platform response distributions for predicting design response. *Marine Structures*, *23*(2), 147–163. doi:http://dx.doi.org/10.1016/j.marstruc.2010.03.001

REFERENCES

Bell, K. (2011). *Matrisestatikk. statiske beregninger av rammekonstruksjoner.* Fagbokforlaget Vigmostad & Bjørke AS.

Cengel, Y. A. & Cimbala, J. M. (2009). *Fluid mechanics (si units): Si units: Fundamentals and applications.* McGraw-Hill Professional. Retrieved from https://www.amazon.com/Fluid-Mechanics-Units-Fundamentals-Applications/dp/0071284214?SubscriptionId=0JYN1NVW651KCA56C102&tag=techkie-20&linkCode=xm2&camp=2025&creative=165953&creativeASIN=0071284214

Chen, W.-L., Li, H., & Hu, H. (2014). An experimental study on the unsteady vortices and turbulent flow structures around twin-box-girder bridge deck models with different gap ratios. *Journal of Wind Engineering and Industrial Aerodynamics*, *132*, 27–36. doi:https://doi.org/10.1016/j.jweia.2014.06.015

COWI, Aas Jakobsen, Global Maritim, & Johs. Holt. (2016). Curved Bridge - Navigation Channel in South. (NOT-KTEKA-021 CURVED BRIDGE_SOUTH – SUMMARY OF ANALYSES.DOCX). Retrieved through Professor Jørgen Amdahl.

DNV. (2014a). Dnv-os-j101: Design of offshore wind turbine structures. Retrieved February 25, 2017, from https://rules.dnvgl.com/docs/pdf/DNV/codes/docs/2014-05/Os-J101.pdf

DNV. (2014b). Dnv-rp-c205: Environmental conditions and environmental loads. Retrieved February 25, 2017, from http://rules.dnvgl.com/docs/pdf/DNV/codes/docs/2014-04/RP-C205.pdf

DNV GL. (2015). Sesam user manual. Wadam. *Wave analysis by Diffraction and Morison theory.*

Faltinsen, O. M. (1990). *Sea loads on ships and offshore structures* (I. Dyer, R. E. Taylor, J. N. Newman, & W. G. Price, Eds.). Cambridge University Press.

Garathun, M. G. (2016). Ubåtteknologi skal bidra til å finne optimal bruløsning på ferjefri e39. Retrieved October 10, 2016, from http://www.tu.no/artikler/ferjefri-e39-ubatteknologi-skal-bidra-til-a-finne-optimal-brulosning/358715

Haver, S. K. (2013). Prediction of characteristic response for design purposes, Chapter 4. Compendium in TMR4195 Design of Offshore Structures.

Irgens, F. (1999). *Formelsamling (handbook of formulas).* Tapir Akademisk Forlag.

Jia, J. (2014). Investigations of a practical wind-induced fatigue calculation based on nonlinear time domain dynamic analysis and a full wind-directional scatter diagram. *Ships and Offshore Structures*, *9*(3), 272–296. doi:10.1080/17445302.2013.783453. eprint: http://dx.doi.org/10.1080/17445302.2013.783453

King, S. & Delatte, N. J. (2004). Collapse of 2000 commonwealth avenue: Punching shear case study. *Journal of Performance of Constructed Facilities*, *18*(1), 54–61. doi:10. 1061/(ASCE)0887-3828(2004)18:1(54). eprint: http://dx.doi.org/10.1061/(ASCE) 0887-3828(2004)18:1(54)

Kleiven, G. & Haver, S. (2004). Met-Ocean Contour Lines for Design; Correction for Omitted Variability in the Response Process. *Proceedings of The Fourteenth International Offshore and Polar Engineering Conference.*

Langen, I. & Sigbjörnsson, R. (1979). *Dynamisk analyse av konstruksjoner.* TAPIR.

Larsen, A. (1998). Advances in aeroelastic analyses of suspension and cable-stayed bridges. *Journal of Wind Engineering and Industrial Aerodynamics*, *74–76*, 73–90. doi:https: //doi.org/10.1016/S0167-6105(98)00007-5

Larsen, C. M. (2014). *Kompendium* TMR4182 *marin dynamikk* (Januar 2014). Kompendieforlaget.

Leira, B. J., Amdahl, J., Syvertsen, K., & Larsen, C. (2014). *Marine structures, basic course.* Compendium in TMR 4170 Marine Structures. Kompendieforlaget.

Levander, K. (2012). System based ship design. Compendium in TMR4254 - Marine Systems Design.

Marine Traffic. (2017). Color magic. Retrieved May 8, 2017, from http://www.marinetraffic. com/no/ais/details/ships/shipid:313685/mmsi:259222000/imo:9349863/vessel: COLOR_MAGIC

Moan, T. (2016). *Design of offshore structures.* Compendium in TMR4195 Design of Offshore Structures.

Moe, O. H. (2016). *Analysis and design of bjørnefjorden tlp supported suspension bridge subjected to large ship collisions and extreme environmental loads* (Master's thesis, Norwegian University of Science and Technology).

Myrhaug, D. (2007). *Uregelmessig Sjø (Irregular sea)*. Compendium in TMR4180 Marin Dynamics. Kompendieforlaget.

Naess, A. & Moan, T. (2012). *Stochastic dynamics of marine structures*. Cambridge University Press. doi:https://doi.org/10.1017/CBO9781139021364

Norrbin, N. H. (1971). *Theory and observations on the use of a mathematical model for ship manoeuvring in deep an confined waters* (tech. rep. No. 68). Statens Skeppsprovningsanstalt (The Swedish State Shipbuilding Experimental Tank).

Norsk Standard. (2005). Eurocode 1: Laster på konstruksjoner. del 1-4: Allmenne laster. vindlaster. ns-en 1991-1-4:2005+na:2009. (eurocode 1: Actions on structures. part 1-4: General actions. wind actions.)

Norsk Standard. (2006a). Eurocode 1: Aactions on structures - Part 1-7: General actions - Accidental actions NS-EN 1991-1-7-2006+NA:2008.

Norsk Standard. (2006b). Eurokode 3: Prosjektering av stålkonstruksjoner, Del 1-11: Kabler og strekkstag (Eurocode 3: Design of steel structures, Part 1-11: Design of structures with tension components). Retrieved April 3, 2017, from http://www. standard.no/nettbutikk/sokeresultater/?search=NS-EN+1993-1-11

NORSOK. (2004). Norsok standard n-004, design of steel structures. Retrieved August 27, 2016, from http://www.standard.no/pagefiles/1145/n-004.pdf

Pan, Z. Y., Vada, T., & Hanssen, F.-C. W. (2013). A mesh dependency study for the mean drift forces by pressure integration. *Proceedings of the ASME 2013 32nd International Conference on Oscean, Offshore and Artic Engineering (OMAE2013)*.

Panton, R. L. (2013). *Incompressible flow* (4th ed.). Wiley. Retrieved March 4, 2017, from http://ebookcentral.proquest.com/lib/ntnu/detail.action?docID=1273516

Pedersen, P. T. & Zhang, S. (1998). The mechanics of ship impact against bridges. In H. Gluver & D. Olsen (Eds.), (Chap. The mechanics of ship collision, pp. 41–51). Ship Collision Analysis. A.A. Balkema.

Pinkster, J. (1979). Mean and low frequency wave drifting forces on floating structures. *Ocean Engineering, 6*(6), 593–615. doi:http://dx.doi.org/10.1016/0029-8018(79) 90010-6

Raymond H. Myers, S. L. M. R. E. W., Keying E. Ye. (2010). *Probability & Statistics For Engineers and Scientists* (9th ed.). Pearson Education. Retrieved from https://www.amazon.com/Probability-Statistics-Engineers-Raymond-Walpole/dp/B007YXZPX8?SubscriptionId=0JYN1NVW651KCA56C102&tag=techkie-20&linkCode=xm2&camp=2025&creative=165953&creativeASIN=B007YXZPX8

Sha, Y. (2016). Bridge global response subjected to ship collision. Retrieved through Professor Jørgen Amdahl.

Sha, Y. & Amdahl, J. (2016a). Design of floating bridge girders against accidental ship collision loads. Retrieved through Professor Jørgen Amdahl. 19th Congress of IABSE. Stockholm, Sweden.

Sha, Y. & Amdahl, J. (2016b). Design of floating bridge pontoon subjected to ship collision load. Retrieved through Professor Jørgen Amdahl. 7th International Conference on Collision and Grounding of Ships. Ulsan, Korea.

Shipping Publications. (2017). Color magic. Retrieved May 8, 2017, from http://www.ship-info.com/prog/skip.asp?id=K137768

Standing, R., Brendling, W., & Wilson, D. (1987). Recent developments in the analysis of wave drift forces, low-frequency damping and response. Offshore Technology Conference (OTC 5456).

Statens vegvesen. (2015). Bruprosjektering. prosjektering av bruer, ferjekaier og andre bærende konstruksjoner. håndbok n400. Book. Retrieved August 27, 2016, from http://www.vegvesen.no/%5C_attachment/865860/binary/1030718?fast%5C_title=H%C3%A5ndbok+N400+Bruprosjektering.pdf

Statens vegvesen. (2016a). Fjordkryssing - Bjørnafjorden (Crossing of Bjørnafjorden). Retrieved June 5, 2017, from http://www.vegvesen.no/Europaveg/e39stordos/fjordkryssing-bjornafjorden

Statens vegvesen. (2016b). The E39 Coastal Highway Route. Retrieved October 10, 2016, from http://www.vegvesen.no/vegprosjekter/ferjefriE39/English

Storheim, M. & Amdahl, J. (2014). Design of offshore structures against accidental ship collisions. *Marine Structures*, *37*, 135–172. doi:10.1016/j.marstruc.2014.03.002

Strømmen, E. [Einar]. (2010, July 15). *Theory of bridge aerodynamics*. Springer Berlin Heidelberg. doi:10.1007/978-3-642-13660-3

Tabri, K. (2012). Influence of coupling in the prediction of ship collision damage. *Ships and Offshore Structures*, *7*(1), 47–54. doi:10.1080/17445302.2011.553812

Tipler, P. A. & Mosca, G. (2008). *Physics for scientists and engineers* (Sixth Edision) (C. Marshall, Ed.). Susan Finnemore Brennan.

USFOS. (1999). Usfos user's manual. *Modelling*. Retrieved April 14, 2017, from http://www.usfos.no/manuals/usfos/users/documents/Usfos_UM_03.pdf

USFOS. (2010). Usfos hydrodynamics. *Theory. Description of use. Verification*. Retrieved September 4, 2017, from http://www.usfos.no/manuals/usfos/theory/documents/Usfos_Hydrodynamics.pdf

USFOS. (2016). Usfos user's manual. Retrieved October 3, 2016, from http://usfos.no/manuals/usfos/users/documents/Usfos_UM_06.pdf

van Berlekom, W. B. & Goddard, T. A. (1972). *Maneuvering of large tankers*. The Society of Naval Architects and Marine Engineers. Advance copy of paper to be presented at the Annual Meetin, New York, N.Y., November 16 and 17, 1972.

Vejrum, T. (2016). Bjørnefjorden floating bridge, Norge. Retrieved October 9, 2016, from http://www.brodag.dk/Synopsis/2016/10%20Flydebro%20over%20Bj%C3%B8rnafjorden.pdf

Yu, Z. & Amdahl, J. (2016). Full six degrees of freedom coupled dynamic simulation of ship collision and grounding accidents. *Marine Structures*, *47*, 1–22. doi:http://dx.doi.org/10.1016/j.marstruc.2016.03.001

Appendix A

Pitch and roll stiffness

An illustration of the model used for studying the pitch and roll stiffness properties of the buoyancy element is presented in the figure below. The heeling moment is applied to the end node of a short vertical beam that is exaggerated in this figure. The red circle illustrates this node, which is also connected to a spring element with large rotational stiffness. Thus most of the force will go into this spring, while a minor part is used to rotate the pontoon. In this way the load is applied quasi-statically, and the moment-rotation curve is obtained by plotting the end moment in the vertical beam against the nodal rotation. The pontoon properties used in investigation is presented in the table below.

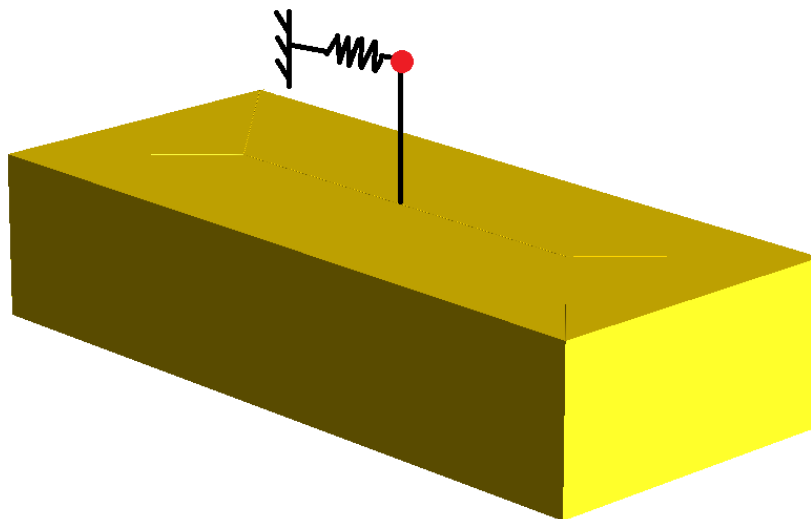**Figure A.1:** Illustration of the model used for studying pitch and roll stiffness of the buoyancy element.

Table A.1: Pontoon properties used for analysing pitch and roll stiffness.

	Value	Unit
L	64	[m]
B	28	[m]
T	10	[m]
Mass	$18.35E + 06$	[kg]

Appendix B

Added mass and damping study

The figure below illustrates the set up used for studying the added mass and damping properties of the buoyancy elements, where the arrow is the applied load. The orientation of the pontoon is defined by the sequence that is used when defining the pontoons. In this case it is defined that the pontoon element goes from node 1-2-3-4, which forces the local x-axis to be parallel to a line going from node 1 to node 2. The local y-axis is parallel to a line going from node 1 to node 4 in this case.
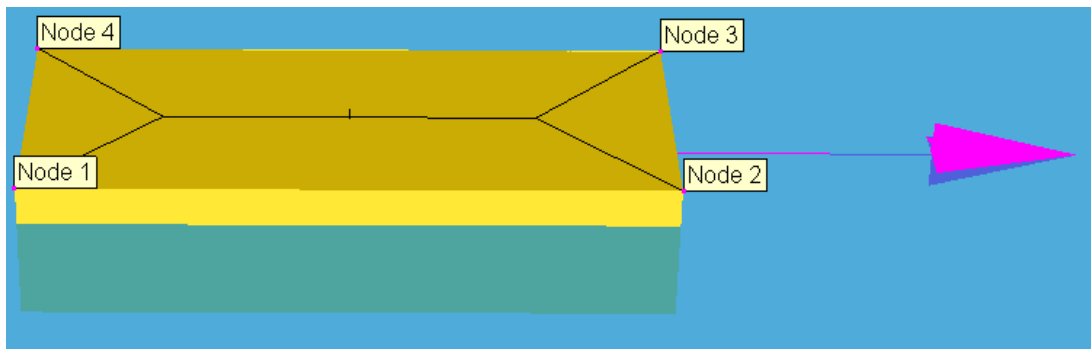
Figure B.1: Illustration of the model used for studying added mass and damping forces of the buoyancy element.

Appendix C

Elastic modulus and pretension of the stay cables

The tables below presents the effective elastic modulus that are used for the stay cables. In addition the resulting axial cable force that results from applying the temperature loads, for pretension of the stay cables, are also presented below. The latter is also compared against the values reported by COWI et al. (2016, p.115 - 116).

Table C.1: Effective modulus.

Material number	E_t	Unit
201	178.35	[GPa]
202	179.15	[GPa]
203	179.95	[GPa]
204	180.75	[GPa]
205	181.52	[GPa]
206	182.26	[GPa]
207	183.01	[GPa]
208	184.41	[GPa]
209	185.75	[GPa]
210	187.03	[GPa]
211	188.21	[GPa]
212	189.31	[GPa]
213	190.30	[GPa]
214	191.22	[GPa]
215	192.04	[GPa]
216	192.78	[GPa]
217	193.39	[GPa]
218	193.93	[GPa]
219	194.34	[GPa]
220	194.67	[GPa]
221	194.87	[GPa]

Table C.2: Cable forces in the side span on the west side of the bridge girder.

Element number,	Cable force [N]	COWI et. al. (2016, p. 115), cable force [N]	Ratio
440	5.98E+06	6.46E+06	0.93
442	5.73E+06	6.24E+06	0.92
444	5.53E+06	6.14E+06	0.90
446	5.63E+06	6.04E+06	0.93
448	5.34E+06	5.85E+06	0.91
450	5.40E+06	5.86E+06	0.92
452	5.09E+06	5.67E+06	0.90
454	5.10E+06	5.58E+06	0.92
456	4.84E+06	5.29E+06	0.92
458	4.59E+06	5.11E+06	0.90
460	4.35E+06	4.74E+06	0.92
462	4.12E+06	4.57E+06	0.90
464	4.03E+06	4.30E+06	0.94
466	3.80E+06	4.13E+06	0.92
468	3.58E+06	3.88E+06	0.92
470	3.65E+06	3.94E+06	0.93
472	3.86E+06	4.17E+06	0.93
474	3.54E+06	3.87E+06	0.91
476	3.72E+06	3.97E+06	0.94
478	3.97E+06	4.15E+06	0.96
480	4.44E+06	4.67E+06	0.95

Table C.3: Cable forces in the side span on the east side of the bridge girder.

Element number,	Cable force [N]	COWI et. al. (2016, p. 115), cable force [N]	Ratio
441	5.94E+06	6.40E+06	0.93
443	5.70E+06	6.19E+06	0.92
445	5.50E+06	6.09E+06	0.90
447	5.61E+06	5.99E+06	0.94
449	5.32E+06	5.79E+06	0.92
451	5.38E+06	5.80E+06	0.93
453	5.07E+06	5.61E+06	0.90
455	5.08E+06	5.51E+06	0.92
457	4.82E+06	5.23E+06	0.92
459	4.57E+06	5.05E+06	0.91
461	4.33E+06	4.68E+06	0.93
463	4.10E+06	4.52E+06	0.91
465	4.01E+06	4.25E+06	0.94
467	3.78E+06	4.09E+06	0.93
469	3.56E+06	3.85E+06	0.93
471	3.63E+06	3.90E+06	0.93
473	3.83E+06	4.15E+06	0.92
475	3.51E+06	3.87E+06	0.91
477	3.67E+06	3.98E+06	0.92
479	3.91E+06	4.18E+06	0.94
481	4.36E+06	4.72E+06	0.92

Table C.4: Cable forces in the main span on the west side of the bridge girder.

Element number,	Cable force [N]	COWI et. al. (2016, p. 116), cable force [N]	Ratio
482	4.13E+06	4.41E+06	0.94
484	4.28E+06	4.38E+06	0.98
486	3.69E+06	3.82E+06	0.97
488	4.04E+06	4.06E+06	0.99
490	3.95E+06	4.01E+06	0.98
492	3.63E+06	3.94E+06	0.92
494	3.95E+06	4.16E+06	0.95
496	3.99E+06	4.10E+06	0.97
498	3.53E+06	3.86E+06	0.92
500	4.00E+06	4.23E+06	0.94
502	4.18E+06	4.61E+06	0.91
504	4.38E+06	4.78E+06	0.92
506	4.86E+06	5.26E+06	0.92
508	5.11E+06	5.33E+06	0.96
510	5.39E+06	5.51E+06	0.98
512	5.80E+06	5.99E+06	0.97
514	5.58E+06	6.18E+06	0.90
516	6.04E+06	6.57E+06	0.92
518	5.82E+06	6.36E+06	0.91
520	5.90E+06	6.36E+06	0.93
522	5.68E+06	5.96E+06	0.95

Table C.5: Cable forces in the main span on the east side of the bridge girder.

Element number,	Cable force [N]	COWI et. al. (2016, p. 116), cable force [N]	Ratio
483	3.81E+06	4.06E+06	0.94
485	3.99E+06	4.23E+06	0.94
487	3.44E+06	3.65E+06	0.94
489	3.79E+06	4.01E+06	0.94
491	3.71E+06	3.93E+06	0.94
493	3.41E+06	3.69E+06	0.92
495	3.73E+06	3.74E+06	1.00
497	3.77E+06	3.98E+06	0.95
499	3.32E+06	3.53E+06	0.94
501	3.77E+06	3.99E+06	0.94
503	3.95E+06	4.18E+06	0.94
505	4.14E+06	4.38E+06	0.94
507	4.60E+06	4.85E+06	0.95
509	4.84E+06	5.10E+06	0.95
511	5.12E+06	5.37E+06	0.95
513	5.52E+06	5.77E+06	0.96
515	5.29E+06	5.84E+06	0.91
517	5.74E+06	6.00E+06	0.96
519	5.50E+06	5.76E+06	0.95
521	5.57E+06	5.84E+06	0.95
523	5.34E+06	5.61E+06	0.95

Linear transfer functions for 0° wave heading

The non-zero excitation forces and moment in the case of 0° wave heading are presented in the figures below.
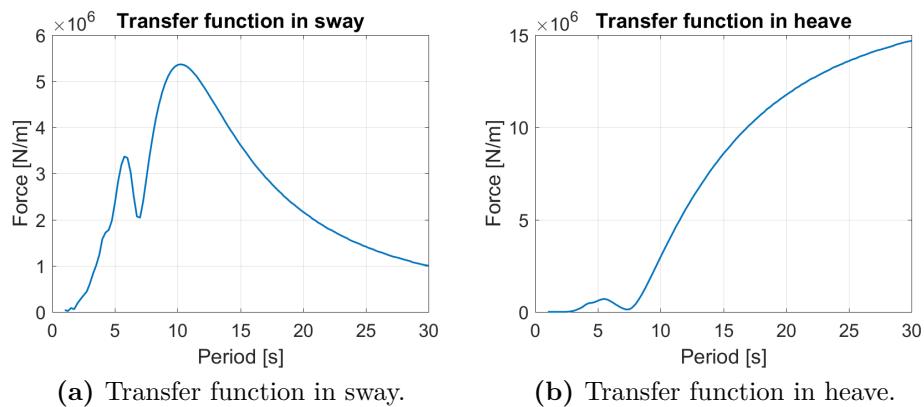

(a) Transfer function in sway. (b) Transfer function in heave.

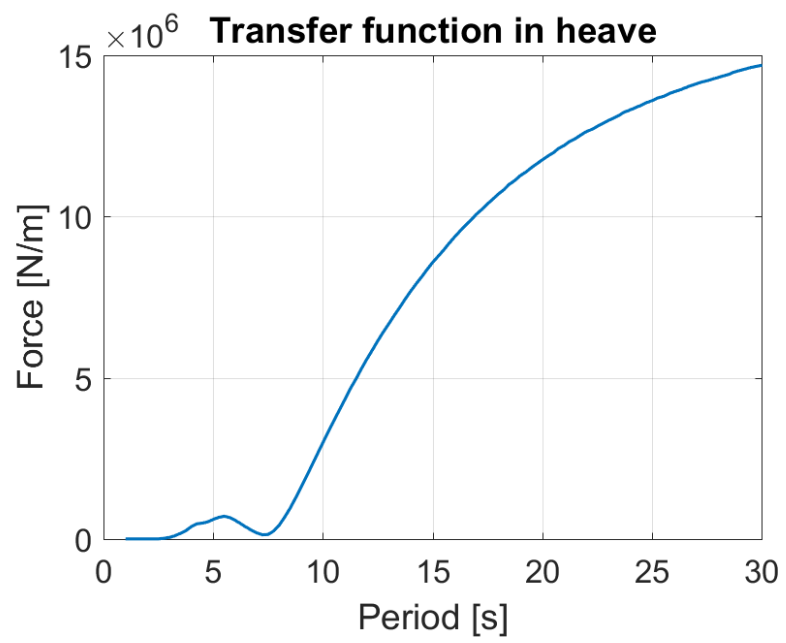**Figure D.1:** Transfer function for the excitation force in heave and sway, in the case of 0° heading.

Figure D.2: Transfer function for the excitation moment in roll, in the case of 0° heading.

Study of how the drag force from wind is calculated

A simple check was performed in order to verify how the drag forces due to incoming wind is calculated in USFOS. When using the USFOS command "Windpar" where the force coefficients are defend, one has to insert a height H and a width W. This check was also performed in order to verify how these values are used in the USFOS calculations. This to make sure that the input values where specified correctly. A single beam element was used in this study, and aligned horizontally with a incoming wind field profile defined by the red arrow in the Figure E.1. The wind filed was applied in the static domain in order to prevent dynamic effects. Furthermore, the beam is clamped in one end using one node springs with large stiffness in all 6 degrees of freedoms, while the other end is free to displace.
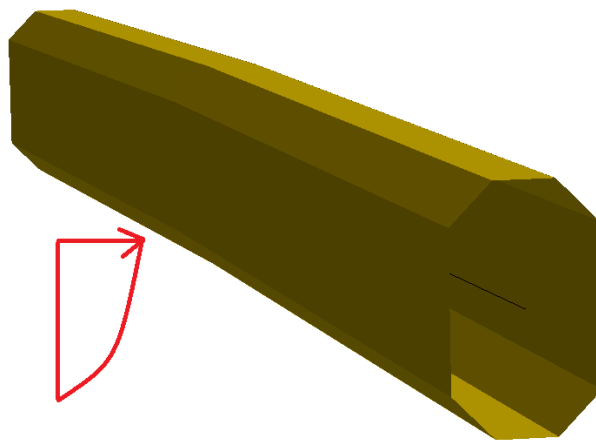

Figure E.1: Illustration of the orientation of the tower. The red arrow illustrates the profile and direction of the incoming mean wind velocity.

The parameters defining the wind properties of this beam element is presented in Table E.1 together with properties defining the mean wind speed. The mean wind speed is modelled using the formula in Chapter 5.3, and the wind forces extracted from USFOS are compared with the drag force formula in the same chapter, calculated by hand. For the hand calculations the drag force is integrated over the total length of 227 [m] of the beam element. The diameter in the drag force equation, see Equation 5.5 in Chapter 5.3, was set equal to the height H in Table E.1. By calculating the resulting drag force for this beam element one gets the value of 1.64E+06 [N]. This result corresponds well with the peak force at the final beam element tip displacement in Figure E.2. The vertical axis in this figure is the resulting force in the support, in the same direction as the applied wind field. From this study it appears that the H parameter defines the height projected normal to the incoming wind field of a beam that is oriented horizontally.

Table E.1: Aerodynamic properties of the beam element together with parameters defining the mean wind speed.

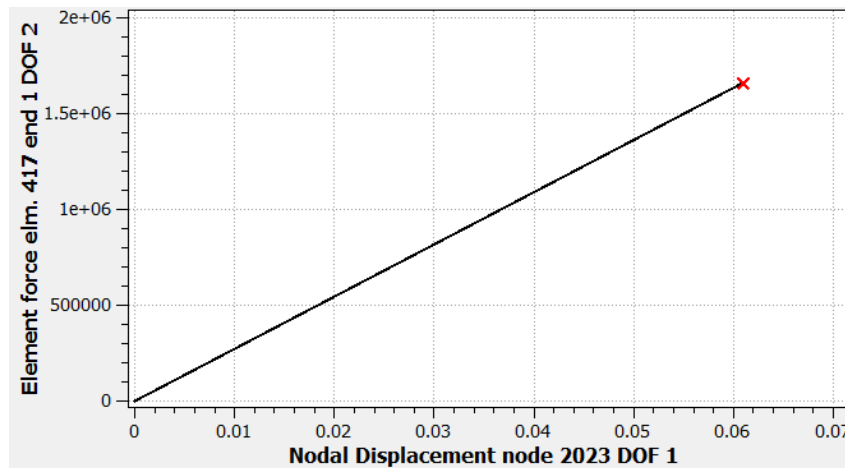| Parameter	Value
C_D	0.8
H	12
W	1
ρ_a	1.26 [kg/m^3]
U_{10min}	31.7 [m/s]
α	0.128

Figure E.2: Beam end displacement along the x-axis and support force in the same direction as the incoming wind field along the y-axis. The units along the vertical axis newton, while along the horizontal illustrates the displacement in meters.

Appendix F

Additional wave load time histories

The 3-hour wave force time histories in sway, surge, pitch and yaw are presented in the first four figures below for waves from north-west. The additional four figures illustrates the 3-hour time histories of the slowly-varying drift forces including high frequency components, in addition to a 3-hour time history for sway with band-pass filter.
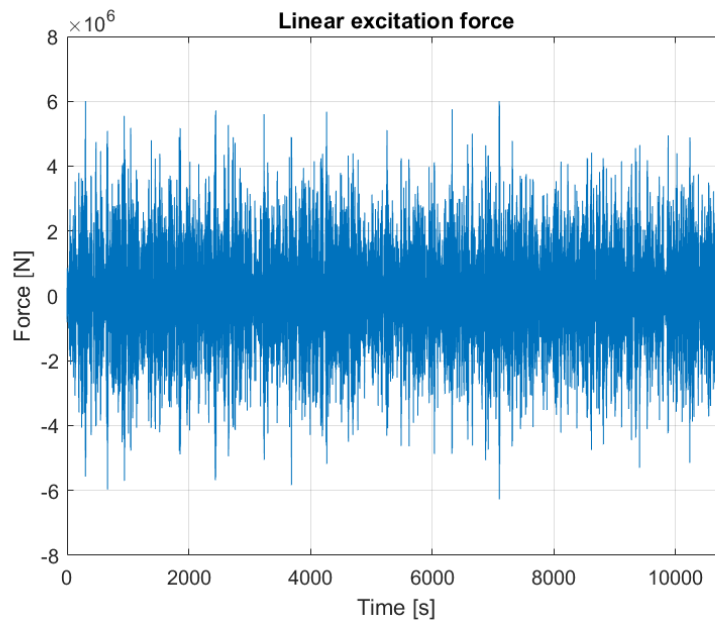

Figure F.1: Linear excitation force in sway direction due to wind generated waves from north-west.
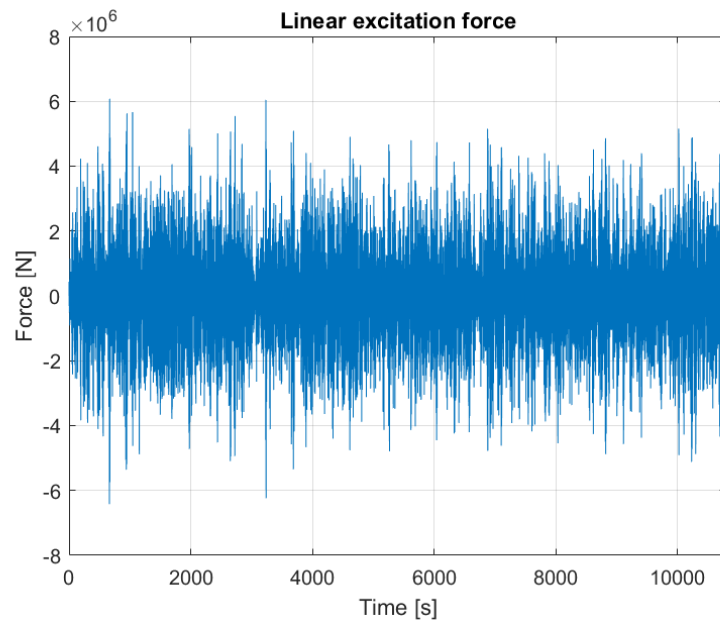
Figure F.2: Linear excitation force in surge direction due to wind generated waves from north-west.
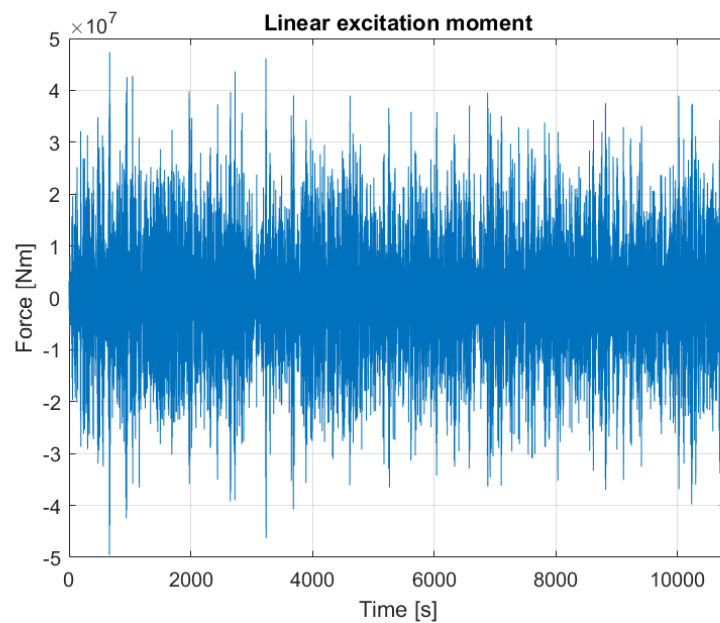

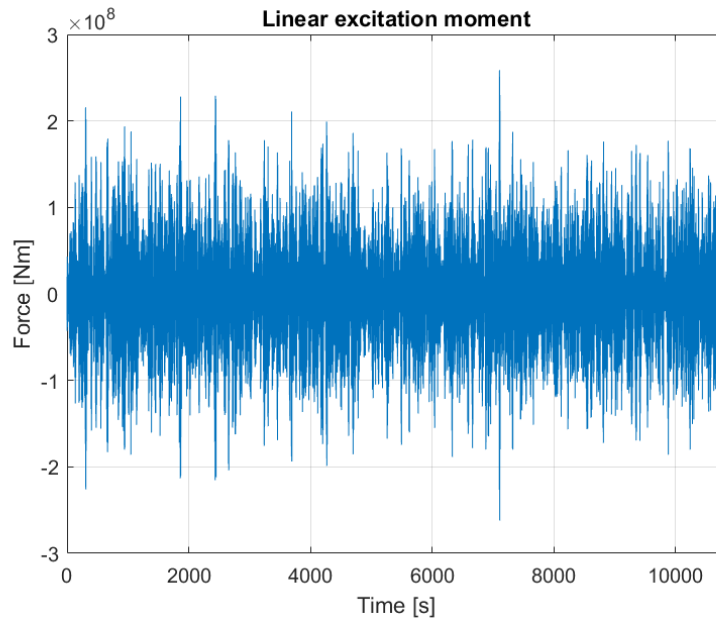**Figure F.3:** Linear excitation pitch moment due to wind generated waves from north-west.

Figure F.4: Linear excitation yaw moment due to wind generated waves from north-west.
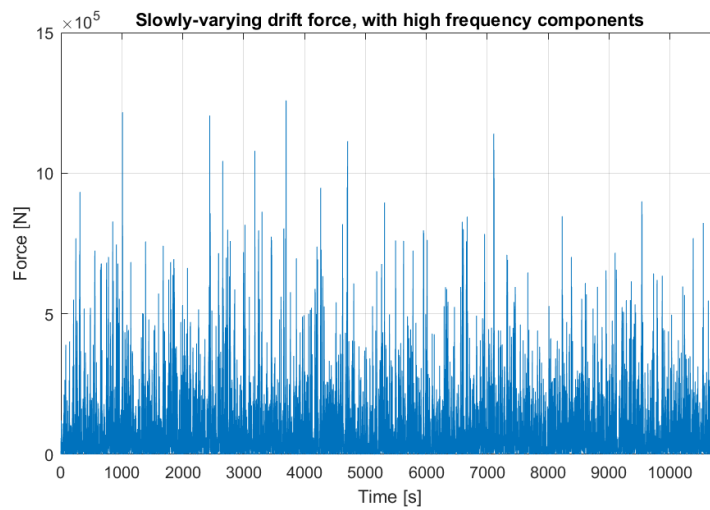

Figure F.5: Full three hour slowly-varying drift force time history in sway direction including the high frequency components for wind generated waves coming from west.
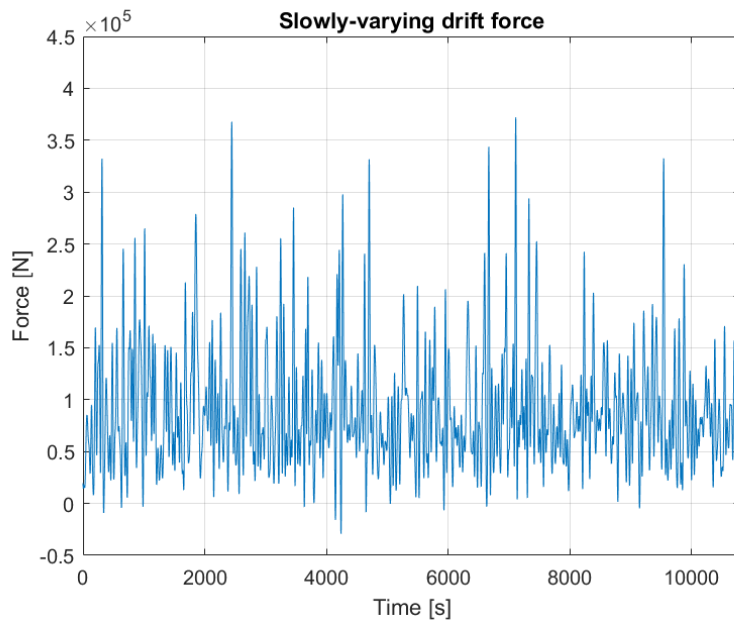
Figure F.6: Full three hour slowly-varying drift force time history in sway direction where the low wave periods are filtered out, for wind generated waves coming from west.
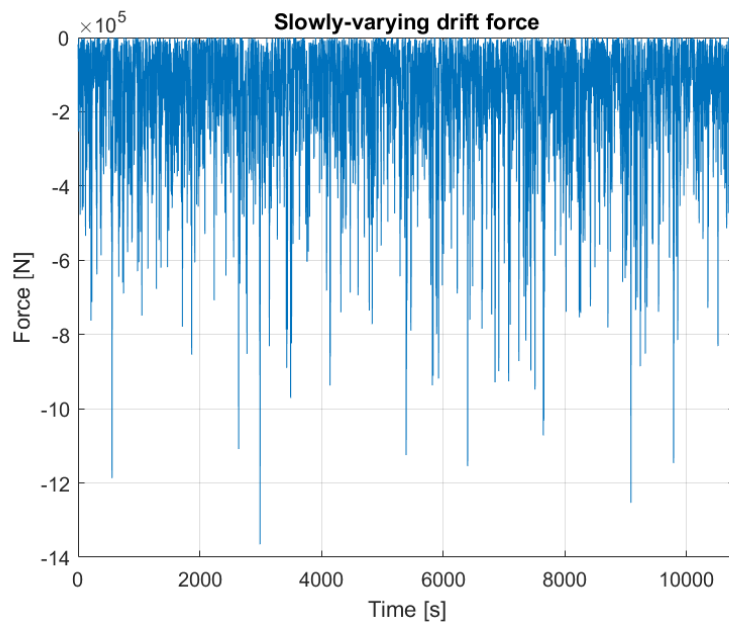

Figure F.7: Full three hour slowly-varying drift force time history in surge direction including the high frequency components for wind generated waves coming from north-west.
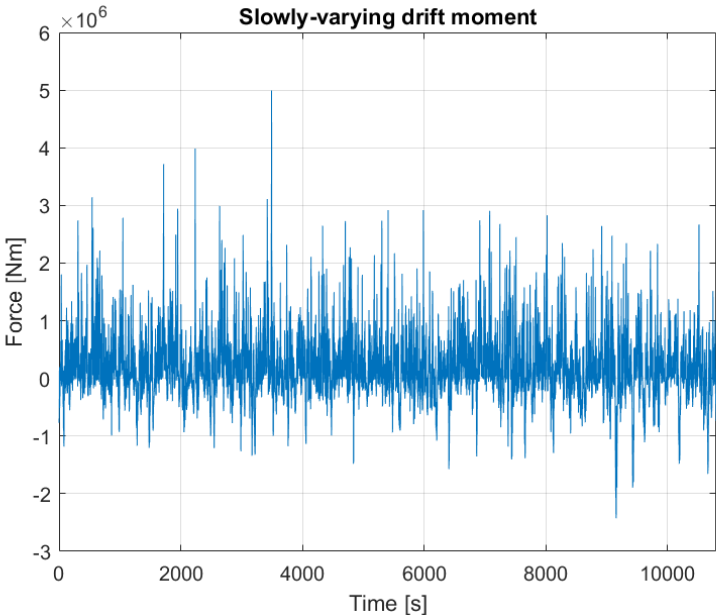
Figure F.8: Full three hour slowly-varying drift yaw moment time history including the high frequency components for wind generated waves coming from north-west.

Appendix G

Additional eigenvalues

Table G.1: The 30 highest eigenperiods.

Mode	Motion	Eigenperiod [s]
Mode 1	Horizontal	65.07
Mode 2	Horizontal	37.02
Mode 3	Horizontal and roll	22.65
Mode 4	Horizontal and roll	20.87
Mode 5	Horizontal and roll	15.65
Mode 6	Roll	13.52
Mode 7	Roll	13.13
Mode 8	Horizontal and roll	11.59
Mode 9	Vertical and roll	11.38
Mode 10	Vertical	11.31
Mode 11	Vertical	11.27
Mode 12	Vertical	11.26
Mode 13	Vertical	11.25
Mode 14	Vertical	11.18
Mode 15	Vertical	11.11
Mode 16	Vertical and roll	10.96
Mode 17	Roll	10.92
Mode 18	Vertical	10.75
Mode 19	Vertical	10.52
Mode 20	Vertical	10.22
Mode 21	Vertical	9.87
Mode 22	Vertical	9.51
Mode 23	Horizontal and roll	9.36
Mode 24	Roll	9.25
Mode 25	Vertical	9.10
Mode 26	Vertical	8.69
Mode 27	Vertical	8.30
Mode 28	Roll	7.98
Mode 29	Roll	7.91
Mode 30	Horizontal and roll	7.71

Table G.2: Eigenmode 31 to 50.

| Mode	Motion	Eigenperiod [s]
Mode 31	Vertical and horizontal	7.68
Mode 32	Vertical	7.52
Mode 33	Roll	6.95
Mode 34	Roll and horizontal	6.67
Mode 35	Vertical and roll	6.33
Mode 36	Roll and horizontal	6.04
Mode 37	Roll and horizontal	5.88
Mode 38	Roll and horizontal	5.82
Mode 39	Horizontal and roll	5.47
Mode 40	Roll and horizontal	5.16
Mode 41	Roll and horizontal	5.07
Mode 42	Roll and horizontal	4.70
Mode 43	Horizontal, vertical and roll	4.69
Mode 44	Roll	4.38
Mode 45	Pendulum, roll and bending of tower	4.16
Mode 46	Pendulum, roll and bending of tower	4.12
Mode 47	Pendulum, roll and bending of tower	4.08
Mode 48	Bending of tower and roll	4.01
Mode 49	Roll and bending of tower	3.96
Mode 50	Roll	3.84
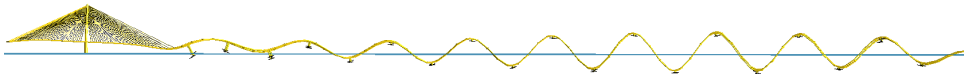
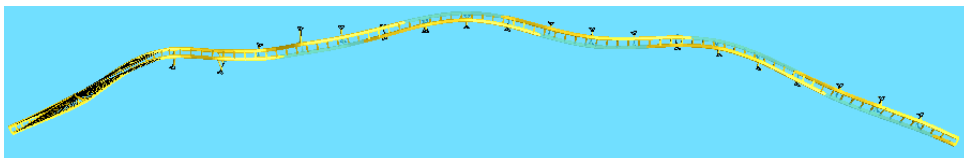**Figure G.1:** Mode 32

Figure G.2: Mode 33

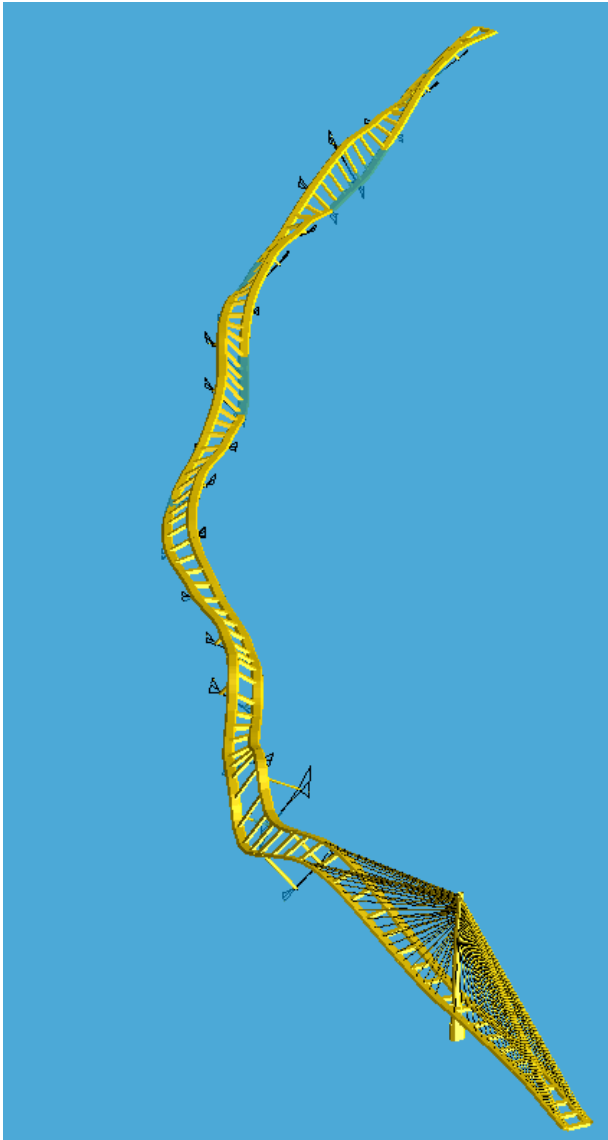**Figure G.3:** Mode 35

Figure G.4: Mode 36

Figure G.5: Mode 38

Appendix H

Selected eigenvalues for the early version of the bridge model.

Table H.1: Eigenmodes relevant for wave induces motions at axis 3 calculated using a bridge model with larger cable stiffness.

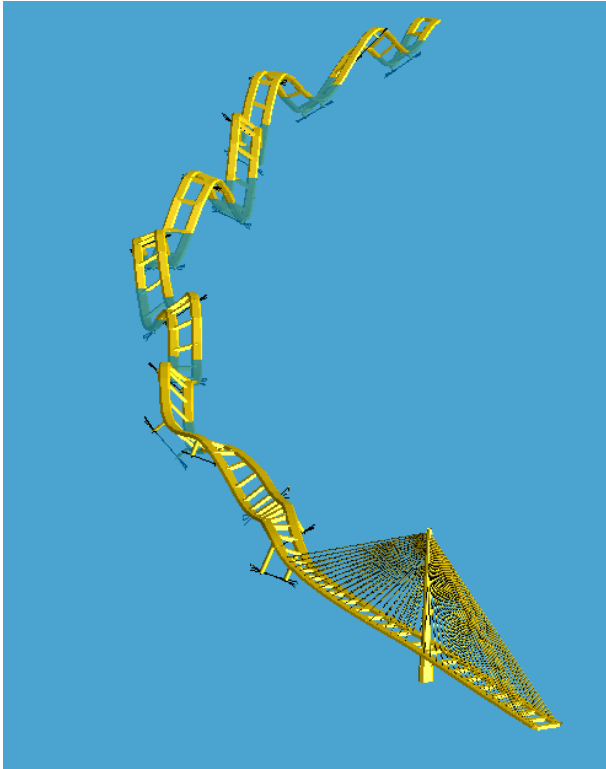| Mode	Motion at axis 3	Eigenperiod [s]
Mode 29	Horizontal and vertical	7.71
Mode 30	Vertical horizontal	7.70
Mode 31	Roll	7.21
Mode 32	Vertical and horizontal	7.02
Mode 33	Horizontal and roll	6.68
Mode 34	Roll	6.33
Mode 35	Roll and pendulum motion	5.94
Mode 36	Roll and pendulum motion	5.91
Mode 37	Roll	5.47
Mode 38	Roll and horizontal	5.37
Mode 39	Roll and horizontal	4.96

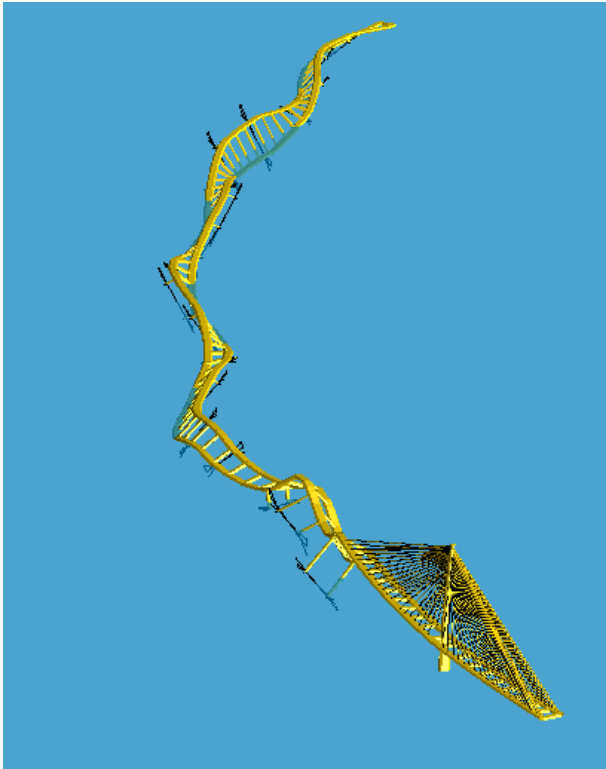**Figure H.1:** Mode 30 in the old version of the bridge model, the eigenperiod is 7.70 seconds.

Figure H.2: Mode 34 in the old version of the bridge model, the eigenperiod is 6.33 seconds.
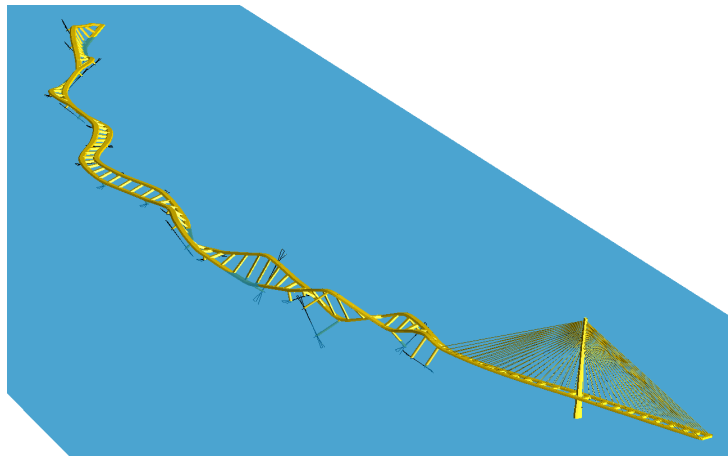
Figure H.3: Mode 38 in the old version of the bridge model, the eigenperiod is 5.37 seconds.

Appendix $\mathbf{I}$

Additional results for wave condition 1

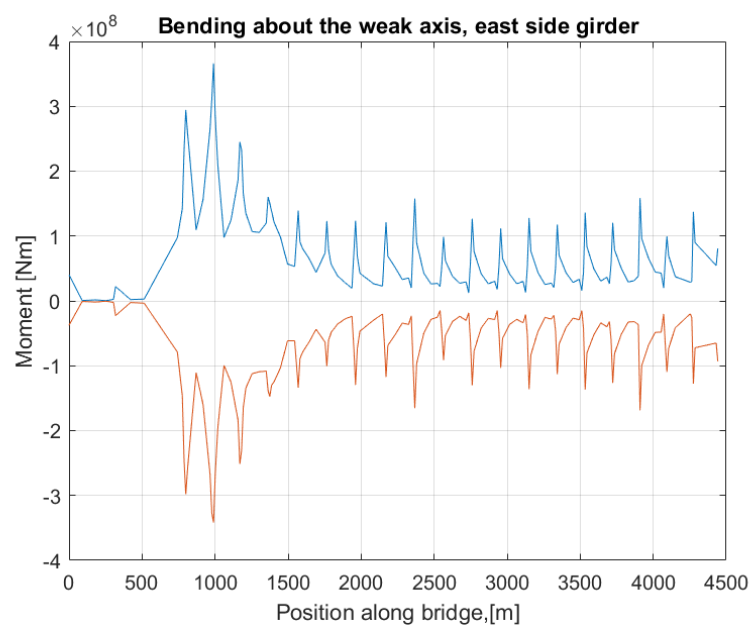The figure below shows the weak axis bending moment in the east side girder for wave condition 1.

Figure I.1: Absolute maximum and minimum weak axis bending moment at selected points along the east side girder.

Illustration of how the method using phase difference was verified

The figure below illustrates the setup used for verifying that the method used for calculating the phase difference behaved properly. The arrow indicates the direction the waves propagates. By adjusting the positions of pontoon 18 and 16 in this figure it is possible to obtain a situation where the regular waves hit one of the pontoons before the other, giving a phase shift in the wave loads. Thus the method using phase angles could be verified by position the pontoons such that one know what the resulting phase angle in forehand.
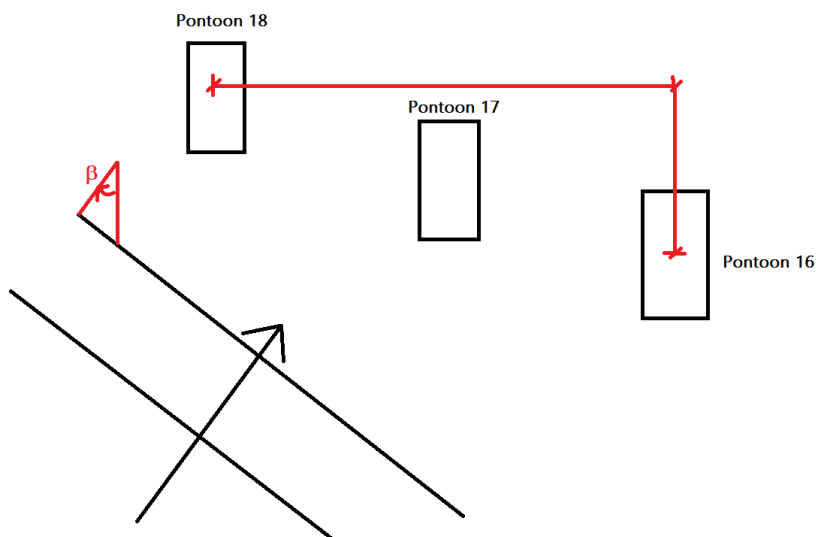
Figure J.1: Illustration of the wave heading and pontoon location that is used to verify the phase difference for regular waves.

Appendix K

Eigenvalue results reported by used of other software

The four figures below shows the shape of the largest eigenperiods reported by Aas Jakobsen, COWI, Global Maritim, and Johs. Holt (2016) in addition to the 32 largest eigenperiods.

Figure K.1: Mode 1 and 2 from COWI, Aas Jakobsen, Global Maritim, and Johs. Holt (2016, Appendix,p.57)

Mode 4

Figure K.2: Mode 3 and 4 from COWI, Aas Jakobsen, Global Maritim, and Johs. Holt (2016, Appendix,p.58)

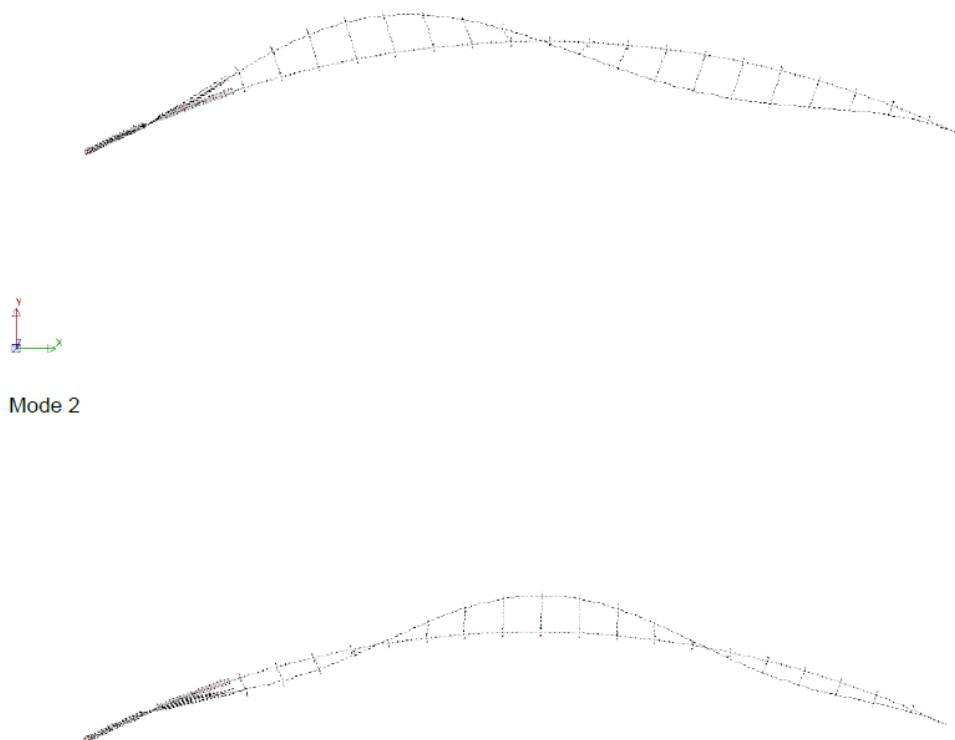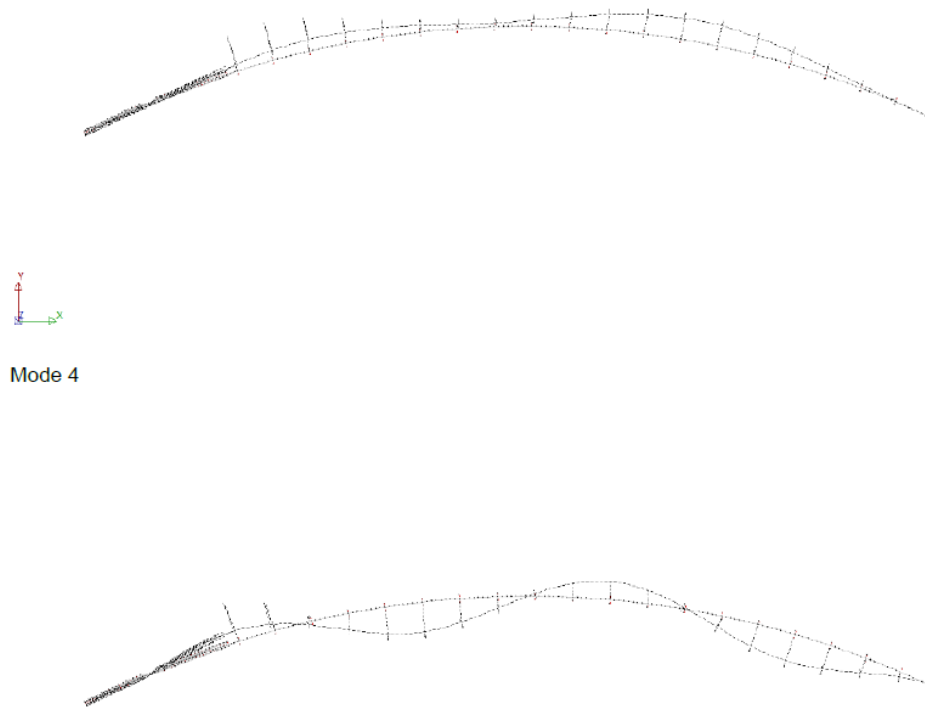| Mode	Period [s]	Frequenzy [Hz]	X [%]	Y [%]	Z [%]	RX [%]	RY [%]	RZ [%]	Dominating motion
1	56.72	0.0176	18	82	0	0	0	0	Y
2	31.69	0.0316	6	94	0	0	0	0	Y
3	22.68	0.0441	6	81	0	12	0	0	Y
4	18.62	0.0537	11	82	0	6	0	0	Y
5	14.33	0.0698	12	74	0	13	1	0	Y
6	11.90	0.0840	9	20	1	68	1	0	RX
7	11.48	0.0871	10	16	27	45	1	0	RX
8	11.48	0.0871	14	9	49	26	1	0	Z
9	11.02	0.0908	3	0	95	1	0	0	Z
10	10.95	0.0913	0	0	99	0	0	0	Z
11	10.95	0.0913	0	0	99	0	0	0	Z
12	10.94	0.0914	0	0	100	0	0	0	Z
13	10.92	0.0916	0	0	98	1	0	0	Z
14	10.89	0.0918	1	5	89	4	0	0	Z
15	10.81	0.0925	3	2	93	1	1	0	Z
16	10.71	0.0934	4	24	62	9	1	0	Z
17	10.64	0.0940	5	31	51	12	1	0	Z
18	10.48	0.0955	4	0	94	0	1	0	Z
19	10.21	0.0980	5	0	94	0	1	0	Z
20	9.88	0.1012	5	1	93	1	1	0	Z
21	9.68	0.1034	5	20	6	67	1	0	RX
22	9.54	0.1048	5	2	88	4	1	0	Z
23	9.19	0.1088	11	2	83	2	2	0	Z
24	8.81	0.1135	13	2	80	3	2	0	Z
25	8.55	0.1169	5	49	6	38	1	0	Y
26	8.38	0.1194	8	3	85	2	2	0	Z
27	8.07	0.1239	5	28	7	60	1	0	RX
28	7.99	0.1252	5	2	86	5	1	0	Z
29	7.68	0.1302	3	0	96	0	1	0	Z
30	7.47	0.1338	1	0	99	0	1	0	Z
31	7.13	0.1402	3	53	0	43	1	0	Y
32	6.51	0.1537	5	29	2	63	1	0	RX

Figure K.3: Eigenvalues from COWI, Aas Jakobsen, Global Maritim, and Johs. Holt (2016, Appendix,p.56)

Appendix L

Comparing second moment of area for the bridge girder

The two tables below shows the total second moment of area of the bridge girder used in this thesis calculated using the parallel axis theorem. These are aslo compared against those reported by COWI et al. (2016, p.6).

Table L.1: Second moment of area I_{tot} for bending about the strong axis of the bridge girder.

Cross section	I_{tot} using values from USFOS	I_{tot} used in COWI et.al.(2016,p.6)
H1	543.69	554.2
H2	786.31	809.1
H3	973.31	1011.4
F1	704.19	737.9
F1	771.96	806.5
S1	924.78	1037
S2*	1275.09	1445.68
S3	1233.37	1325.55
S3*	1572.08	1651.56

Table L.2: Second moment of area I_{tot} for bending about the weak axis of the bridge girder.

Cross section	I_{tot} using values from USFOS	I_{tot} used in COWI et.al.(2016,p.6)
H1	5.94	6.1
H2	8.94	9.38
H3	11.81	11.72
F1	12.95	13.16
F1	14.93	15.14
S1	17.55	18.34
S2*	22.75	24.06
S3	26.22	26.8
S3*	29.28	30.03